frontiers | Research Topics

Physics and modelling of landslides

Edited by
Eric Josef Ribeiro Parteli, Sabatino Cuomo, Irasema Alcántara-Ayala, Bianca Carvalho Vieira and Biswajeet Pradhan

Published in
Frontiers in Earth Science
Frontiers in Physics
Frontiers in Environmental Science

ISSN 1664-8714
ISBN 978-2-83251-687-4
DOI 10.3389/978-2-83251-687-4

About Frontiers

Frontiers is more than just an open access publisher of scholarly articles: it is a pioneering approach to the world of academia, radically improving the way scholarly research is managed. The grand vision of Frontiers is a world where all people have an equal opportunity to seek, share and generate knowledge. Frontiers provides immediate and permanent online open access to all its publications, but this alone is not enough to realize our grand goals.

Frontiers journal series

The Frontiers journal series is a multi-tier and interdisciplinary set of open-access, online journals, promising a paradigm shift from the current review, selection and dissemination processes in academic publishing. All Frontiers journals are driven by researchers for researchers; therefore, they constitute a service to the scholarly community. At the same time, the *Frontiers journal series* operates on a revolutionary invention, the tiered publishing system, initially addressing specific communities of scholars, and gradually climbing up to broader public understanding, thus serving the interests of the lay society, too.

Dedication to quality

Each Frontiers article is a landmark of the highest quality, thanks to genuinely collaborative interactions between authors and review editors, who include some of the world's best academicians. Research must be certified by peers before entering a stream of knowledge that may eventually reach the public - and shape society; therefore, Frontiers only applies the most rigorous and unbiased reviews. Frontiers revolutionizes research publishing by freely delivering the most outstanding research, evaluated with no bias from both the academic and social point of view. By applying the most advanced information technologies, Frontiers is catapulting scholarly publishing into a new generation.

What are Frontiers Research Topics?

Frontiers Research Topics are very popular trademarks of the *Frontiers journals series*: they are collections of at least ten articles, all centered on a particular subject. With their unique mix of varied contributions from Original Research to Review Articles, Frontiers Research Topics unify the most influential researchers, the latest key findings and historical advances in a hot research area.

Find out more on how to host your own Frontiers Research Topic or contribute to one as an author by contacting the Frontiers editorial office: frontiersin.org/about/contact

Physics and modelling of landslides

Topic editors

Eric Josef Ribeiro Parteli — University of Duisburg-Essen, Germany
Sabatino Cuomo — University of Salerno, Italy
Irasema Alcántara-Ayala — National Autonomous University of Mexico, Mexico
Bianca Carvalho Vieira — University of São Paulo, Brazil
Biswajeet Pradhan — University of Technology Sydney, Australia

Citation

Parteli, E. J. R., Cuomo, S., Alcántara-Ayala, I., Vieira, B. C., Pradhan, B., eds. (2023). *Physics and modelling of landslides*. Lausanne: Frontiers Media SA.
doi: 10.3389/978-2-83251-687-4

Table of contents

frontiers | Frontiers in Physics

TYPE Editorial
PUBLISHED 01 February 2023
DOI 10.3389/fphy.2023.1146166

OPEN ACCESS

EDITED AND REVIEWED BY
Alex Hansen,
Norwegian University of Science and Technology, Norway

*CORRESPONDENCE
Irasema Alcántara-Ayala,
ialcantara@geografia.unam.mx

SPECIALTY SECTION
This article was submitted to Interdisciplinary Physics, a section of the journal Frontiers in Physics

RECEIVED 17 January 2023
ACCEPTED 24 January 2023
PUBLISHED 01 February 2023

CITATION
Alcántara-Ayala I, Ribeiro Parteli EJ, Pradhan B, Cuomo S and Vieira BC (2023), Editorial: Physics and modelling of landslides.
Front. Phys. 11:1146166.
doi: 10.3389/fphy.2023.1146166

Editorial: Physics and modelling of landslides

Irasema Alcántara-Ayala[1]*, Eric Josef Ribeiro Parteli[2], Biswajeet Pradhan[3], Sabatino Cuomo[4] and Bianca Carvalho Vieira[5]

[1]Institute of Geography, National Autonomous University of Mexico, Mexico city, Mexico, [2]Faculty of Physics, University of Duisburg-Essen, Duisburg, Germany, [3]School of Civil and Environmental Engineering, Faculty of Engineering, and Information Technology, The University of Technology Sydney, Ultimo, NSW, Australia, [4]Civil Engineering Department, University of Salerno, Fisciano, Italy, [5]Department of Geography, University of São Paulo, São Paulo, Brazil

KEYWORDS

landslides, physics, modelling, dynamics, inter and multidisciplinary, disaster risk reduction

Editorial on the Research Topic
Physics and modelling of land slides

Disasters triggered by landslides cause life losses and substantial devastation to communities in terms of effects on the economy, livelihoods, and infrastructure every year across the world. However, the causative factors and mechanisms underlying landslide initiation and dynamics must be better understood, as accurate modelling of landslide risk is an essential prerequisite for developing reliable control and mitigation strategies [1]. Landslide susceptibility is influenced by a broad range of factors [2], such as soil physics and geochemistry, geological setting, climate, atmospheric dynamics, biogenic feedbacks, and anthropogenic influences, which have profound interlinkages with each other over a broad period- and length-scales. Moreover, landslide risk assessment further hinges on correctly understanding communities' local vulnerability and exposure [3].

This Research Topic of articles on the *Physics and Modelling of Landslides* presents leading-edge work into the quantitative understanding of landslide processes and dynamics.

A series of numerical simulations were carried out by Wang et al. for a better understanding of the dynamic response and failure modes of rock slopes containing weak interlayers subjected to earthquake excitation. They used the continuum-discontinuum element method considering the influence of seismic amplitude and weak interlayer inclination, to shed light on the formation mechanism of rock landslides with weak interlayers. Accordingly, the acceleration waveform and peak ground displacement amplification coefficient characteristics strongly contradict the landslide failure process. The combination of weak interlayers and seismic load causes multiple failure landslide modes.

Aiming at understanding the influence of water content on the characteristics of long-term deformations and stability of soil-rock mixtures of the Dahua landslide located on the right bank of Lancang River, China, Jiang et al., and Wang et al. performed multi-stage shear creep tests of SRM samples with different water contents. Based on their analysis, it was suggested that there are three stages of creep deformation: transient, steady-state, and accelerated. Moreover, shear-creep deformation is controlled by fractures of large particles at low water content but by large particles at high water content rotations.

By looking at the combined effects of the debris-flow impact force and lateral Earth pressure through finite element analysis, Eu et al. modelled internal stresses experienced during debris flow and sediment deposition from the 2011 Mt. Umyeon landslide, Seoul, the Republic of Korea. This approach provided valuable insights for the structural analysis and safety

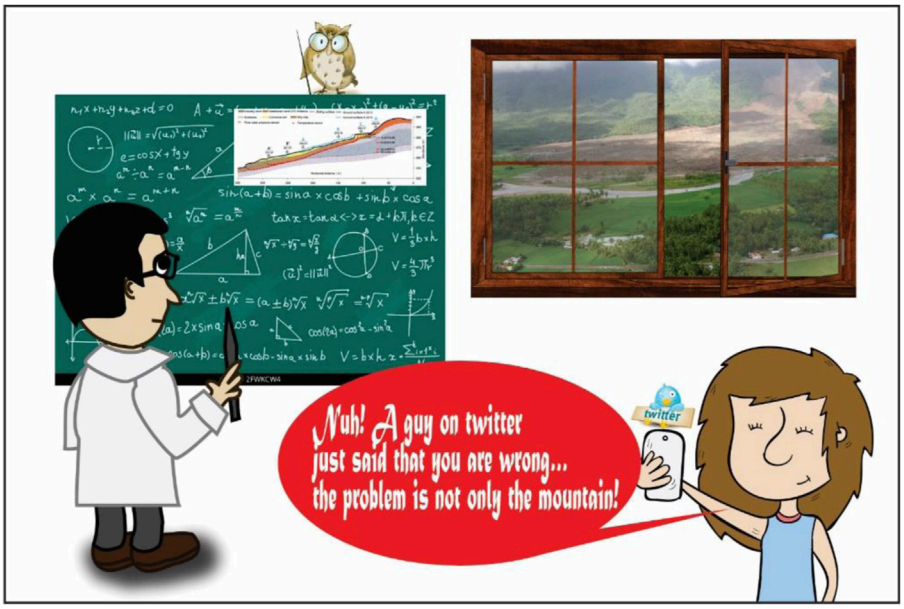

FIGURE 1
Landslide disaster risk reduction requires a sustained dialogue between the various disciplines on the physics of landslides, their causes and dynamics, and their socio-environmental interactions (Cartoon courtesy of Irasema Alcántara-Ayala).

assessment of check dams. It offered practical guidance for check-dam design and maintenance, considering sediment deposition and debris-flow impact force.

Zhang et al. used the Drucker–Prager model and the smooth particle hydrodynamics method to simulate soil slope failure and determine the slip surface with and without the effect of potential earthquakes. This study contributed to this growing area of research by exploring the relationships between sliding material volume, influence range, and slope angle. That being the case, the horizontal displacement of the slope under the effect of an earthquake increased non-linearly with the increase of slope incline angle.

He et al. and colleagues examined the mechanical property of typical residual soils from a landslide zone in Chenzhou city, China, by conducting direct shear tests. Mineral composition and microstructures of soil samples analysis through X-ray diffraction and scanning electron microscope tests showed rich clay minerals, including pyrophyllite, illite, kaolinite, and montmorillonite. The shear strength of soils gradually decreased with increasing water content under constant vertical load by a linear function, but the soil types influenced the trend of shear strength.

The fuzzy point estimation method and physical-based model were combined with the local factor of safety theory by Yang et al. to calculate the hillslope's internal local factor of safety for the hillslope of the Babaoliao collapse site in Chiayi County, Taiwan. The results indicated that the boundary flux controls the overall infiltration of water into the slope and affects the change in soil water content, which in turn causes slope instability. Moreover, delayed rainfall causes early slope instability; thus, evaluating shallow soils' hydraulic behavior and failure mechanisms is critical.

Li et al. used the fuzzy set assessment method to assess the risk level of landslide hazards in the Badong section of Three Georges in China. The stratigraphic lithology, degree of weathering, relationship between the structural plane and slope direction, cohesive force, angle of internal friction, severity, average slope degree, the height of slope, and type of landslide were considered as the assessment indices. Despite drawbacks, such as complicated calculation and necessary multiple variable parameters, results suggested that the variable fuzzy set model could offer an alternate route to evaluate the landslide hazards.

Conventional Machine Learning and Multi-Criteria Decision-Making techniques were used to compare performance for the development of susceptibility mapping of landslides in Muzaffarabad district, lower Himalayas of Northern Pakistan. Following this perspective, Khalil et al. found 85% accuracy when using Support Vector Machine, 83% with Linear Regression, 80% with Analytical Hierarchy Process, 79% with Logistic Regression, and 78% with Technique for Order of Preference by Similarity to Ideal Solution. The study offered a baseline for decision-makers for effective landslide countermeasures and long-term monitoring.

Yildiz et al. drew attention to uncertainty quantification, a computationally demanding task for designing and developing a model-based landslide risk assessment. Using a synthetic case involving simple topography and the Acheron rock avalanche near Canterbury, New Zealand, they demonstrated how uncertainty quantification workflow can be set up effectively and how this affects the model-based landslide risk assessment. GP emulation-based Monte Carlo Simulations can significantly improve computational efficiency, making GP-integrated MCS applicable for landslide run-out modelling.

A significant contemporary Research Topic of landslide hazard assessment is that socioterritorial drivers, particularly in urban areas, have intensified their impact [4,5]. Non-etheless, inter and multidisciplinary efforts [6] that combine physical, engineering, and computer sciences with geological, geographical, and social sciences required to advance the quantitative understanding of landslide processes, are still incipient.

This Research Topic focused on the *physics and modelling of landslides*. It provided a platform for the dialogue between the various disciplines on the physics of landslides, their causes and dynamics, and their socio-environmental interactions (Figure 1). This dialogue is essential to enhance landslide forecasting and management capabilities and produce novel insights by the science and technology community to contribute to implementing the Sendai Framework through future integrated disaster risk reduction policy formulation and practice [7].

Author contributions

All authors listed have made a substantial, direct, and intellectual contribution to the work and approved it for publication.

Conflict of interest

The authors declare that the research was conducted in the absence of any commercial or financial relationships that could be construed as a potential conflict of interest.

Publisher's note

References

1. Rafiei Sardooi E, Azareh A, Mesbahzadeh T, Soleimani Sardoo F, Parteli EJ, Pradhan B. A hybrid model using data mining and multi-criteria decision-making methods for landslide risk mapping at Golestan Province, Iran. *Environ Earth Sci* (2021) 80(15): 487–25. doi:10.1007/s12665-021-09788-z

2. Dias HC, Gramani MF, Grohmann CH, Bateira C, Vieira BC. Statistical-based shallow landslide susceptibility assessment for a tropical environment: A case study in the southeastern Brazilian coast. *Nat Hazards* (2021) 108(1):205–23. doi:10.1007/s11069-021-04676-y

3. Alcántara-Ayala I. Integrated landslide disaster risk management (ILDRiM): The challenge to avoid the construction of new disaster risk. *Environ Hazards* (2021) 20(3): 323–44. doi:10.1080/17477891.2020.1810609

4. Adler CE, Wester P, Bhatt I, Huggel C, Insarov G, Morecroft MD, Muccione V, Prakash A, Alcántara-Ayala I, et al. Cross-chapter paper 5: Mountains. In: HO Pörtner, DC Roberts, M Tignor, ES Poloczanska, K Mintenbeck, A Alegría, et al. editors. *IPCC [intergovernmental panel on climate change]*. Climate change 2022: Impacts, adaptation, and vulnerability. Contribution of working group II to the sixth assessment Report of the intergovernmental Panel on climate change. Cambridge, United Kingdom: Cambridge University Press (2022).

5. Alcántara-Ayala I, Geertsema M. Construction of disaster risk in mountain systems and its integrated management. In: FO Sarmiento, editor. *Montology palimpsest. Montology*, 1 Cham: Springer (2022). doi:10.1007/978-3-031-13298-8_19

6. Cascini L, Cuomo S, Di Mauro A, Di Natale M, Di Nocera S, Matano F. Multidisciplinary analysis of combined flow-like mass movements in a catchment of Southern Italy. *Georisk: Assess Manag Risk Engineered Syst Geohazards* (2021) 15(1): 41–58. doi:10.1080/17499518.2019.1674339

7. Kirsch-Wood J, Katsanakis R, Hieber Girardet L, Kumar A, Mena R, Cook R, et al. *Global assessment report 2022*. Geneva, Switzerland: United Nations Office for Disaster Risk Reduction (2022).

frontiers in Earth Science

ORIGINAL RESEARCH
published: 23 December 2021
doi: 10.3389/feart.2021.791458

Numerical Investigation on Dynamic Response and Failure Modes of Rock Slopes with Weak Interlayers Using Continuum-Discontinuum Element Method

Chengwen Wang, Xiaoli Liu, Danqing Song, Enzhi Wang and Jianmin Zhang*

Department of Hydraulic Engineering, State Key Laboratory of Hydroscience and Engineering, Tsinghua University, Beijing, China

OPEN ACCESS

Edited by:
Eric Josef Ribeiro Parteli, University of Duisburg-Essen, Germany

Reviewed by:
Yang Yu, Zhejiang University, China
Huan Sun, Hainan University, China
Weimin Yang, Shandong University, China

***Correspondence:**
Xiaoli Liu
xiaoli.liu@tsinghua.edu.cn

Specialty section:
This article was submitted to Geohazards and Georisks, a section of the journal Frontiers in Earth Science

Received: *08 October 2021*
Accepted: *07 December 2021*
Published: *23 December 2021*

Citation:
Wang C, Liu X, Song D, Wang E and Zhang J (2021) Numerical Investigation on Dynamic Response and Failure Modes of Rock Slopes with Weak Interlayers Using Continuum-Discontinuum Element Method. Front. Earth Sci. 9:791458. doi: 10.3389/feart.2021.791458

In order to better understand the dynamic response and failure modes of rock slopes containing weak interlayers subjected to earthquake excitation, a series of numerical simulations were carried out using the continuum-discontinuum element method (CDEM), considering the influence of seismic amplitude and weak interlayers inclination. The seismic response characteristics of slopes were systematically analyzed according to the waveform characteristics, amplification effect, equivalent crack ratio, etc. The numerical results show that the acceleration waveform characteristics and peak ground displacement (PGD) amplification coefficient have good correspondence with the dynamic failure process of landslides. Comprehensive analysis of waveform characteristics and PGD amplification coefficient can determine the damage time, damage location, and damage degree of landslides. The landslide process can be divided into three stages according to the equivalent crack ratio: rapid generation of a large number of microcracks, expansion and aggregation of microcracks, and penetration of micro-cracks and the formation of slip surfaces. The equivalent crack ratio provides a new idea for evaluating slope stability. In addition, under the combination of different amplitudes and weak interlayers, these earthquake-induced landslides exhibit different failure modes: the failure of the gentle-dip slope is mainly local rockfall; The mid-dip and steep-dip slopes with small amplitudes experience “tensile cracking-slip-collapsing” failure; The steep-dip slopes under strong earthquake failed in the form of “tensile cracking-slip-slope extrusion-collapsing”. The research results are of great significance for a deeper understanding of the formation mechanism of rock landslides with weak interlayers and the prevention of such landslide disasters.

Keywords: earthquake, dynamic response, failure modes, weak interlayers, continuum-discontinuum element method (CDEM)

INTRODUCTION

Rock landslide is one of the most common geological disasters in mountainous areas (Wasowski et al., 2011; Kawamura et al., 2019; Luo et al., 2019). Earthquake-induced landslides pose huge threats to human activities and facility construction (Song et al., 2021). Take the Wenchuan earthquake in Sichuan Province, China in 2008 as an example, this earthquake caused 3314 landslides and 1656 unstable slopes (Dai et al., 2011). The volume of Daguangbao landslide induced by the Wenchuan earthquake reached $1.16 \times 109\ m^3$, which is by far the largest earthquake-induced landslide recorded in the world (Cui et al., 2020). Therefore, special attention should be paid to the dynamic response of rock slopes under earthquakes.

Among the many landslide-inducing factors, weak interlayers are one of the most prominent (Huang et al., 2007). The slope with weak interlayers is a common geological body. The weak interlayers in the rock mass often have an unfavorable influence on the engineering projects due to their relatively weak mechanical properties, which is an important factor affecting the deformation and instability of slopes. In recent years, scholars have paid great attention to the seismic stability of weak sandwich slopes (Huang et al., 2013; Huang et al., 2017). At present, the research on the dynamic stability of weak sandwich slopes is only carried out from one aspect (Xu et al., 2020). However, the complexity of weak interlayers in actual landslides and the immeasurability of their influence on the stability of slopes require confirmation and analysis from many aspects. The rock slopes slid suddenly and quickly along the weak structural plane under the action of the earthquake, which induced huge disasters, causing traffic paralysis, economic losses, and casualties. However, the failure mechanism of rock slopes with weak interlayers under earthquake action is still unclear. Therefore, it is necessary to reveal the dynamic response and failure modes of rock slopes with weak interlayers under seismic excitation to provide guidance for the prevention and control of landslides.

At present, the methods of investigation on earthquake-induced landslides mainly include theoretical analysis, field investigation, geological model test and numerical simulation methods (Tang et al., 2009; Lin et al., 2018). The quasi-static method (Terzaghi and Paige, 1950) and the Newmark method (Newmark, 1965) are commonly used in theoretical analysis. The theoretical analysis methods are simple and practical, and can give clear evaluation indicators, so they are widely used in the analysis of landslide engineering (Xu and Yang, 2018; Delgado et al., 2020; Yiğit, 2020), but it is difficult to analyze complex geological structures (Lin et al., 2018). Field investigation and geological model test are the most commonly used methods to study the dynamic stability of slopes. Based on field investigations, the characteristics of landslides can be observed (Zhao et al., 2018; Montgomery et al., 2020), but the gradual failure process of landslides is lacking and it is time-consuming and expensive (Tang et al., 2020). To supplement the shortcomings of field investigations, geological model tests have become a hot topic in the research field of slope dynamic stability. As an important method of slope stability evaluation, the geological model test has been widely recognized for its practicality and professionalism (Seisdedos et al., 2012; Yang et al., 2018). The geological model test can directly reflect the stability of the rock slopes under earthquake, and provide a basis for the verification of the results (Li et al., 2016). However, this method is affected by factors such as size effect, a similar design of the model structure, boundary conditions, and the level of experimenters. There is a certain gap of dynamic response between the test results and the actual landslides (Xu and Dong, 2021). Therefore, numerical simulation has been becoming a powerful method to research rock landslides under earthquakes (Deng et al., 2020). Numerical simulation has become the mainstream method for the stability analysis of earthquake-induced landslides under complex geological structures due to its advantages such as realistic reflection of the landslide process, easy modeling of complex geological structures, and reproducibility (Zhu et al., 2011; Liu et al., 2018; Song et al., 2020). The common numerical simulation methods are mainly based on the continuum and discontinuum-based methods. Continuum-based methods can simulate the actual dynamic motion of landslides. For example, the finite element method (Martino et al., 2018; Yu et al., 2019; Sangirardi et al., 2020) and finite difference method (Marcato et al., 2012; Yu et al., 2014) are applied to the study of slope dynamic stability. However, the continuous method is difficult to simulate large deformation and cracking, and cannot give the failure evolutional process of sliding initiation and expansion to large-scale sliding. For discontinuous geological bodies, large deformation, and stress concentration, the continuum-based method has great limitations (Chen and Song, 2021). Discontinuum-based methods, since the separation and displacement of the elements are not restricted, can simulate the gradual progressive development process of landslides. Benefiting from the above advantages of the discontinuous method, the application of it to landslides simulation has received widespread attention. The discrete element method (Wu et al., 2018; Donati et al., 2020) and discontinuous block analysis method (Lin et al., 2016; Liu et al., 2019; Do and Wu, 2020) have been extensively used in the field of rock slope dynamic failure research. However, discontinuum-based methods can not reflect the continuous state of material before failure. And the low computational efficiency is a common problem with discontinuum-based methods, which makes it time-consuming to perform large-scale simulations (Bao et al., 2019). The whole failure process of rock slope from continuum to discontinuum needs more in-depth study. Continuum-discontinuum element method (CDEM) is a new numerical method suitable for the analysis of geological hazards that has emerged in recent years (Feng et al., 2014). CDEM method can not only simulate the deformation and movement characteristics of the material but also realize the transformation of the material from the continuum to the discontinuum. Previous studies have shown that the CDEM method has unique advantages in simulating geological disasters such as landslides (Feng et al., 2014; Li et al., 2015).

In this study, based on field investigations and laboratory rock mechanics tests, accurate rock physicomechanical parameters

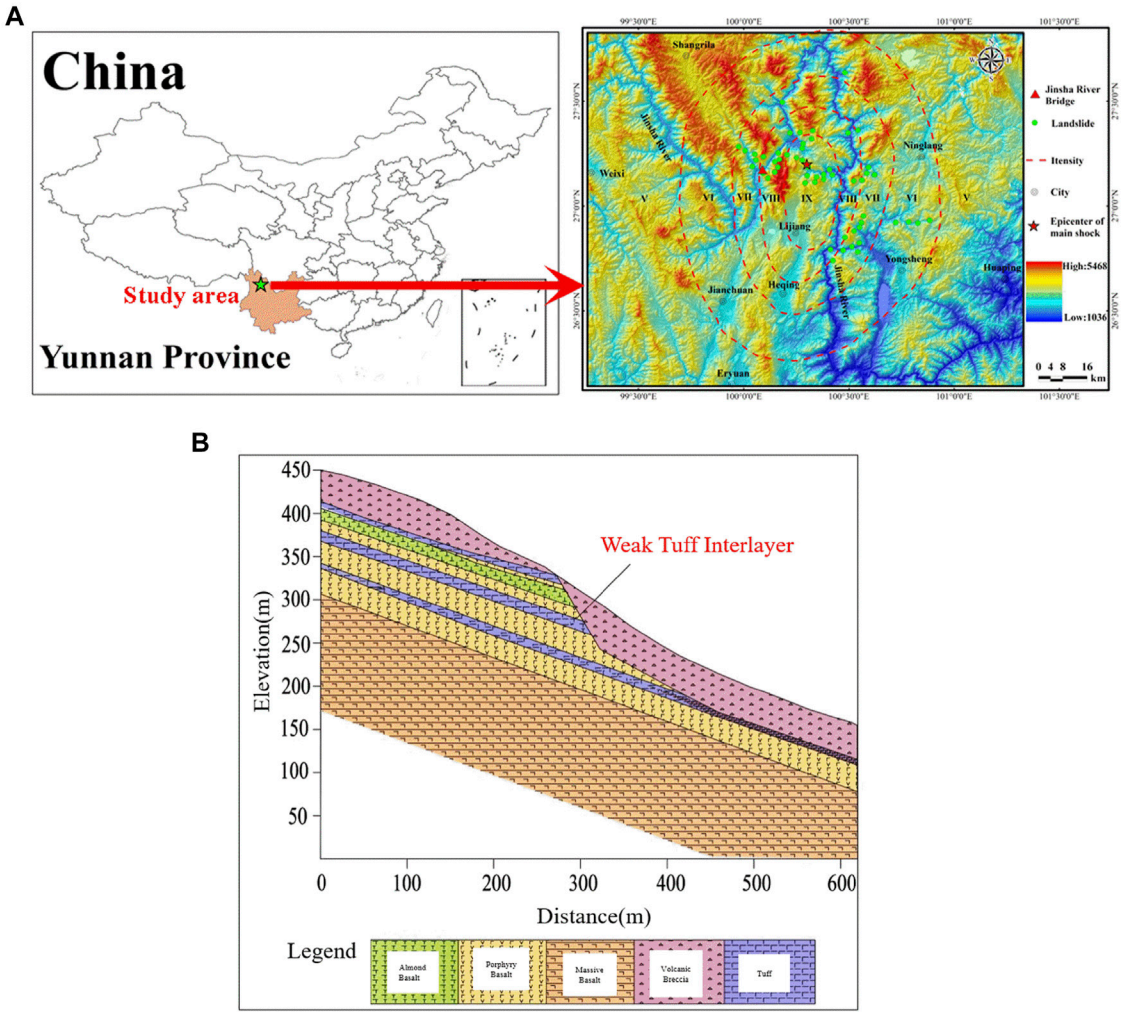

FIGURE 1 | (A) Location of the landslide, Yunnan Province, China, **(B)** The longitudinal geological profile of the landslide.

were obtained, which provides a basis for numerical simulation. Considering the influence of the amplitudes and the weak interlayers dips, we carried out a series of numerical tests with the CDEM method. The waveform characteristics, PGD amplification effect, and equivalent crack ratio are analyzed according to the numerical simulation results, and the failure modes and dynamic development process of rock slopes with weak interlayers under earthquake action are studied, which provides a scientific basis for a deeper understanding of the dynamic characteristics of rock landslides with weak interlayers. As such, the simulation results presented here can provide a reference for related future research and guidance for the seismic design of this type of landslide.

Study Area

The study area is located in the northwestern part of Yunnan Province, China (**Figure 1A**). Due to the close proximity to the suture zone where the Indian plate and the Asia-Europe plate collide, the tectonic movement in this area is unusually intense, and many active faults have developed as a result. Under the influence of violent tectonic movement and surface biodynamics, various geological phenomena such as landslides, avalanches, and rock weathering have appeared here. As shown in **Figure 1B**, the rock slope in this area is stepped with a gradient of 30–40°. The surface is exposed to tight basalt, almond basalt, and volcanic breccia lava. There are many weak tuff layers, which are broken owing to structural dislocation, scattered in the rock mass. The rock slope studied is a bedding slope, mainly composed of basalt. And there are three sets of weak tuff interlayers with steep dip angles on the slope. Based on the surveyed engineering geological conditions, the main factors affecting the stability of slopes are topographic conditions, rock properties, rock mass structural planes, weak interlayers, and external loads. The slope remains relatively stable under natural conditions, but the stability under seismic loads needs further research. Especially the combined effect of seismic load and weak interlayers is the principal factor controlling slope stability.

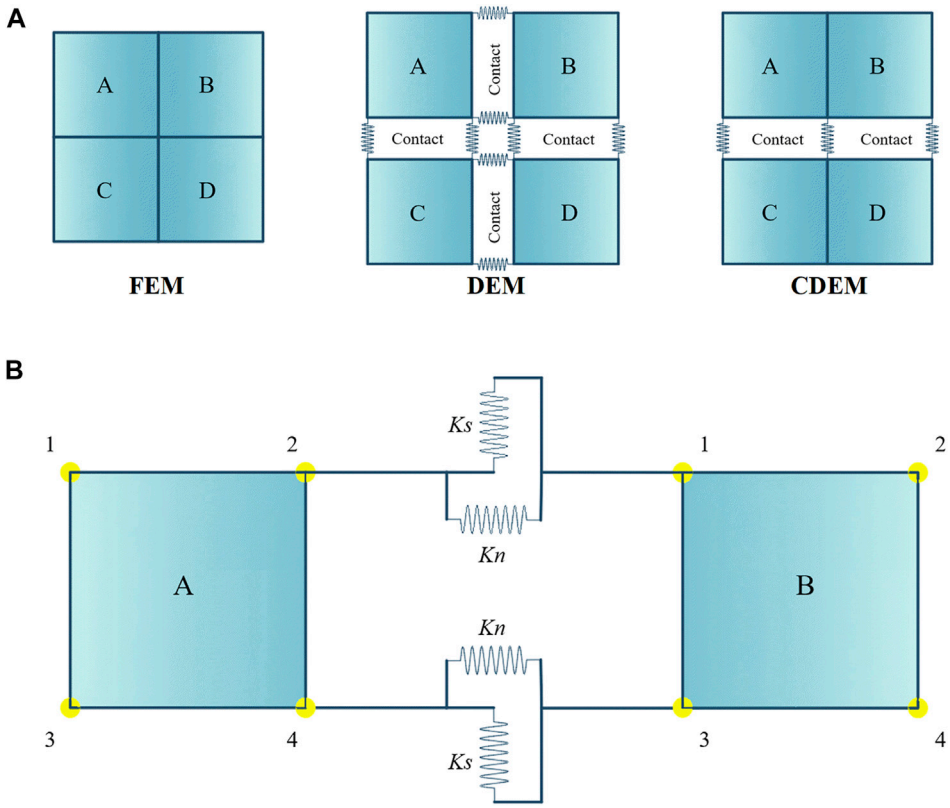

FIGURE 2 | (A) Comparison of computational domains FEM, DEM, and CDEM; **(B)** 2D contacts in CDEM contacts A2 - B1 and A4 - B3.

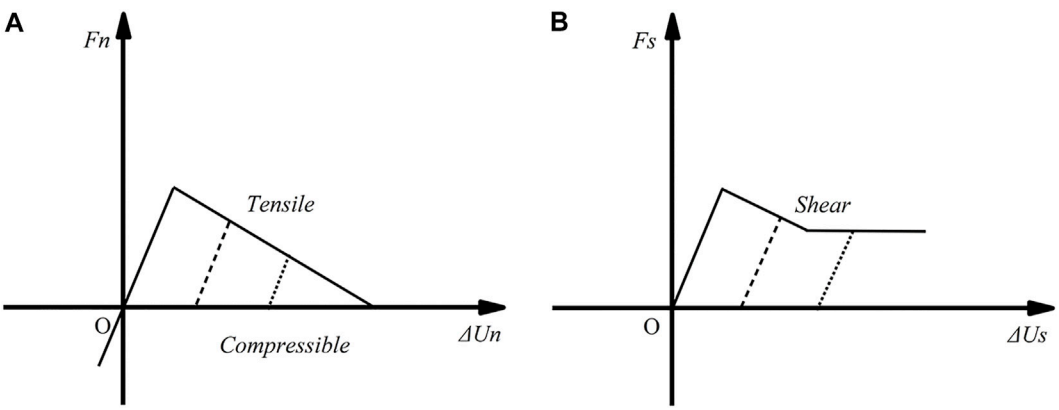

FIGURE 3 | Relationship between the bonding stress and opening sliding displacement **(A)** under compression and tension conditions; **(B)** under shear and sliding conditions.

NUMERICAL MODEL

Principle of CDEM

Continuum-Discontinuum Element Method (CDEM) is a new type of numerical method developed on the basis of the rigid block discrete element method. In the numerical simulation, the computational domain is generally discretized into units for calculation. For these elements, they can be continuous(corresponding to the finite element method), discontinuous(corresponding to the discrete element method), and partially continuous(corresponding to the CDEM method), as shown in **Figure 2A** (springs include normal and tangential springs). The finite element method is used to solve completely continuous problems, while the discrete element method is

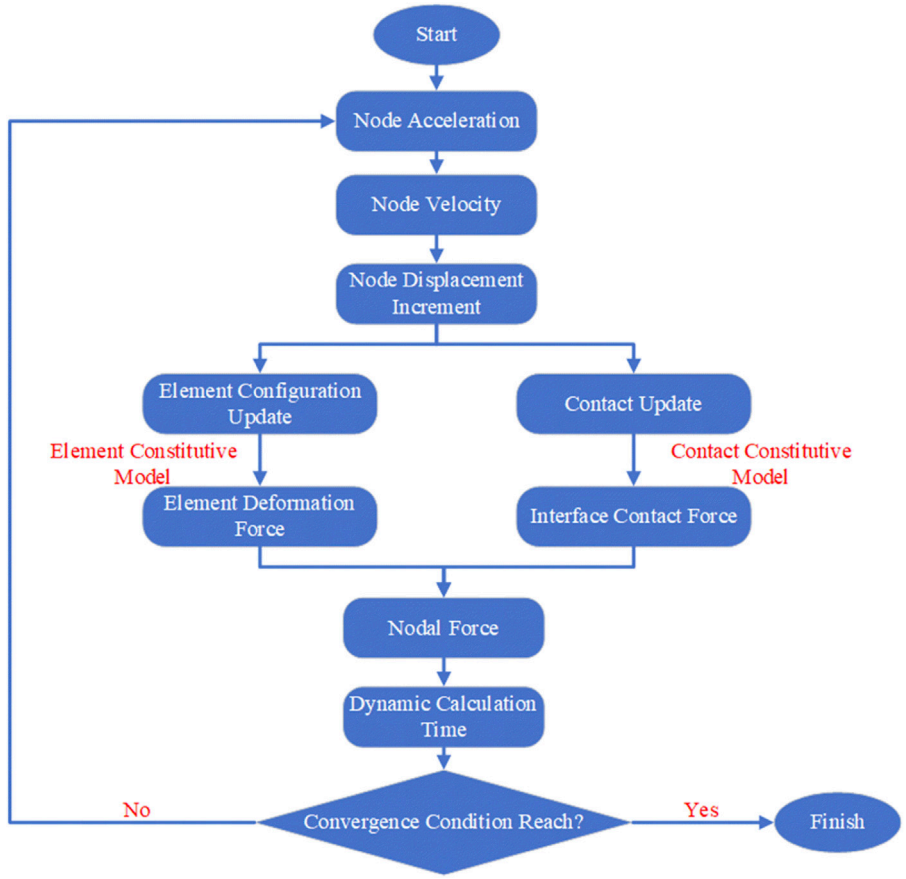

FIGURE 4 | Flowchart of the iteration process in CDEM.

suitable for fully discontinuous problems, generally. CDEM combines the advantages of continuous calculation and discrete calculation, that is, finite element calculation in the block and discrete element calculation at the boundary to realize the progressive failure process of the rock mass. As shown in **Figure 2B**, the computational domain in CDEM is composed of blocks and virtual interfaces. The blocks, composed of finite element, is used to calculate the elastic, plastic and other continuous properties of rocks. The virtual interfaces refer to the common boundaries between blocks, which are composed of normal penalty springs and tangential penalty springs, and their cracking and sliding can characterize the discontinuous features of rocks.

In the CDEM calculation, the constitutive of the tensile-shear composite interface based on the fracture energy is used to calculate the fracture of the rock virtual interface. Use the following equations to calculate the contact forces at the next time step on the interface:

$$F_{\mathrm{n}}(t_1) = F_{\mathrm{n}}(t_0) - k_n A_c \Delta u_{\mathrm{n}} \tag{1}$$

$$F_{\mathrm{s}}(t_1) = F_{\mathrm{s}}(t_0) - k_{\mathrm{s}} A_c \Delta u_{\mathrm{s}} \tag{2}$$

where F_{n} and F_{s} are contact forces of the normal and tangential penalty spring, respectively; k_{n} and k_{s} are contact stiffness of the normal and tangential penalty spring (Pa/m), respectively; A_{c} is the contact area; Δu_{s} and Δu_{n} are the relative displacement increment in tangential and normal directions, respectively.

The tensile failure criterion is expressed as follows:

$$\text{If} - F_{\mathrm{n}}(t_1) \geq \sigma_{\mathrm{t}}(t_0) A_c \tag{3}$$

$$\text{then } F_{\mathrm{n}}(t_1) = -\sigma_{\mathrm{t}}(t_0) A_c \tag{4}$$

$$\sigma_t(t_1) = -(\sigma_{t0})^2 \Delta u_{\mathrm{n}} / (2G_{\mathrm{ft}}) + c_0 \tag{5}$$

where σ_{t0}, $\sigma_{\mathrm{t}}(t_0)$ and $\sigma_{\mathrm{t}}(t_1)$ are the tensile strengths at the initial moment, this moment and the next moment, respectively; G_{ft} is the tensile fracture energy (Pa·m).

The shear failure criterion is expressed as follows:

$$\text{If } F_{\mathrm{s}}(t_1) \geq F_{\mathrm{n}}(t_1) \tan \Phi + c(t_0) A_c \tag{6}$$

$$\text{then } F_{\mathrm{s}}(t_1) = F_{\mathrm{n}}(t_1) \tan \Phi + c(t_0) Ac \tag{7}$$

$$c(t_1) = -c_0^2 \Delta u_{\mathrm{s}} / (2G_{\mathrm{fs}}) + c_0 \tag{8}$$

where c_0, $c(t_0)$, and $c(t_1)$ are the cohesion at the initial moment, this moment and the next moment, respectively; Φ is the internal friction angle of the virtual interface; G_{fs} is the shear fracture energy (Pa·m).

According to the above description, the tensile-shear constitutive curve considering the fracture energy is drawn as shown in **Figure 3**.

TABLE 1 | Calculation conditions in numerical simulation.

No	Weak interlayer dip angles (°)	Amplitude (g)
1	15	0.3
2		0.5
3		0.8
4		1.0
5	30	0.3
6		0.5
7		0.8
8		1.0
9	45	0.3
10		0.5
11		0.8
12		1.0

CDEM is a dynamic explicit solution algorithm based on breakable elements under the Lagrangian system, and is solved by the explicit Euler forward difference method based on the incremental method. The solution is divided into three steps: (1) calculate the deformation force and damping force of the blocks by cycling each finite element; (2) cycle each contact surface to calculate the connection force and damping force of the contact surface; (3) cycle all nodes to calculate the joint external force, acceleration, velocity, and displacement. The specific calculation process is shown in **Figure 4**.

Numerical Modeling

In the numerical simulation, the effects of different weak interlayer dip angles and amplitudes are considered. Three groups of weak interlayer dip angles, i.e. 15°, 30°, and 45°, are analyzed; and four groups of input amplitudes, i.e. 0.3, 0.5, 0.8, and 1.0 g, are studied. **Table 1** shows the specific calculation scheme.

Figure 5 shows the slope geometry, monitoring point layout, and grid division in the numerical simulation. All of the slope height is 450 m. For dynamic calculations, to eliminate the influence of artificial boundaries, the bottom of the model adopts a viscous boundary, and the normal displacement of the bottom is fixed. Use free field boundaries on the left and right sides of the model to absorb false vibrations. Apply sine waves of different amplitudes at the bottom of the model, and **Figure 6** shows the amplitude time history curve. In CDEM, to impose a dynamic load of stress-time history on the viscous boundary, it is necessary to integrate the acceleration time history into a velocity-time history and then convert it into a stress-time history. The conversion expression is as follows:

$$\sigma_n = 2(\rho \cdot C_p)v_n \tag{9}$$

$$\sigma_s = 2(\rho \cdot C_s)v_s \tag{10}$$

where C_p is P-wave velocity and C_s is S-wave velocity; v_n and v_s represent normal and tangential velocity, respectively. In the numerical calculation, 12 monitoring points are set up on the slope surface and in the slope, to monitor the acceleration of the slope. The test results can be used to study the acceleration change characteristics and amplification effects, so as to analyze the dynamic response.

In CDEM, the selection of material parameters is important content. The material parameters in CDEM include bulk parameters that characterize continuity and numerical spring parameters that characterize discontinuity. In this study, the block parameters are obtained based on experiments. **Table 2** shows the rock block parameters used in numerical simulation, and **Table 3** gives the numerical springs parameters. The micro-parameters parameters used in the numerical modelling can be determined by the method in the published papers (Li et al., 2006; Feng et al., 2014; Li et al., 2015). Among them, use the following equation to calculate the normal stiffness and tangential stiffness:

$$K = AE_r/(2T_0) \tag{11}$$

where A is the contact area, E_r denotes the young's modulus, T_0 denotes the thickness of the structural layer, and its size is usually 1% of the size of the block.

The expressions of tensile fracture energy and shear fracture energy are as follows:

$$G_{ft} = K_{IC}^2/E \tag{12}$$

$$G_{fs} = (1 - \nu^2)K_{IIC}^2/E \tag{13}$$

where K_{IC} and K_{IIC} are tensile and shear fracture toughness.

To ensure the correctness of the numerical calculation results, the validity of the parameters used is verified by a uniaxial compression test. **Figure 7** shows the geometric model and results of the uniaxial compression test.

ANALYSIS OF SIMULATION RESULTS

The failure modes of landslides are studied by analyzing the failure process, waveform characteristics, amplification effect, and crack ratio in this section.

Analysis of Landslide Failure Process

The dynamics failure process of the landslide is shown in **Figure 8**. **Figure 8A**; **Figure 8B** show the displacement distributions ((A) 0.5 g amplitude; (B) 1.0 g amplitude) of the failure process of the slope with 15°-dip-angle weak interlayers. **Figure 8A**; **Figure 8B** shows that the slope with 15° inclination angle weak interlayers is only partially damaged under the action of earthquakes with different amplitudes, but does not reach the overall instability slip. This kind of slope has similar failure disciplines under the effect of earthquakes of different amplitudes: (1) The contact surface of weak interlayers was damaged and broken (t = 0.1–4.0 s); (2) Vertical tension cracking occurred on the back edge of the slope. The rock mass on the slope surface, meanwhile, was damaged to generate micro-cracks since the amplification effect of the seismic wave (t = 8.0-12.0 s); (3) The tensile crack at the trailing edge of the slope widened and continued to spread downward, but it never penetrated the fracture surface produced by the weak interlayers. This is the reason why the overall slip failure did not occur under these conditions. In addition, for the damaged weak interlayers that have a

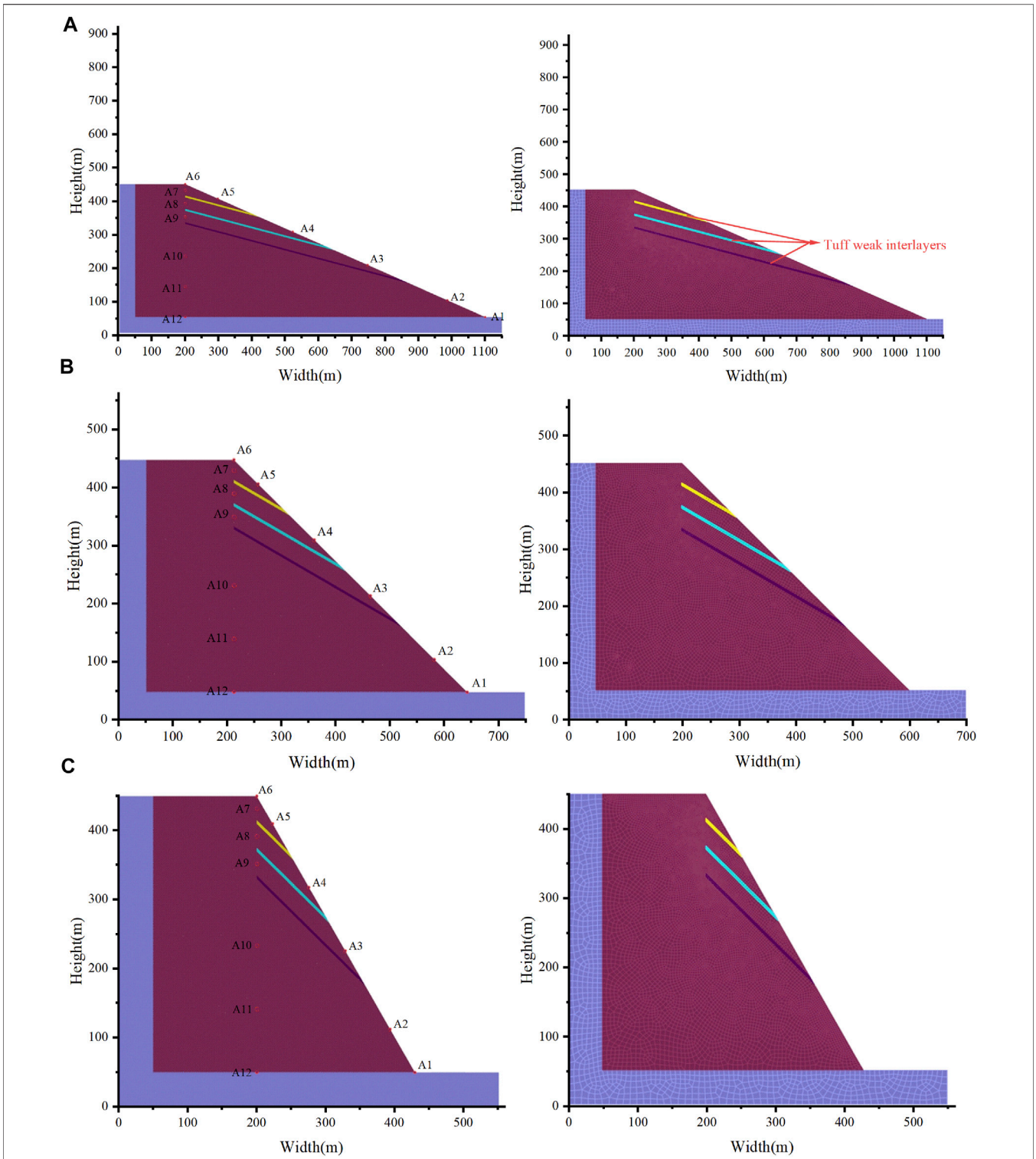

FIGURE 5 | Model geometry, monitoring point layout and grid division **(A)** weak interlayers dip is 15°, **(B)** weak interlayers dip is 30°, **(C)** weak interlayers dip is 45°.

downward sliding trend, the broken rock blocks were driven to slide downward, forming a small number of falling rocks (t = 16.0-19.8 s). It is noted that when the amplitude is small (0.3–0.8 g), the slope failure mainly occurs above the third weak interlayer, and the weak interlayers play a principal role in slope failure. As for large amplitude (1.0 g), the slope toe was damaged (**Figure 8B**), indicating that the effect of strong earthquakes is greater than that of weak interlayers. The toe of

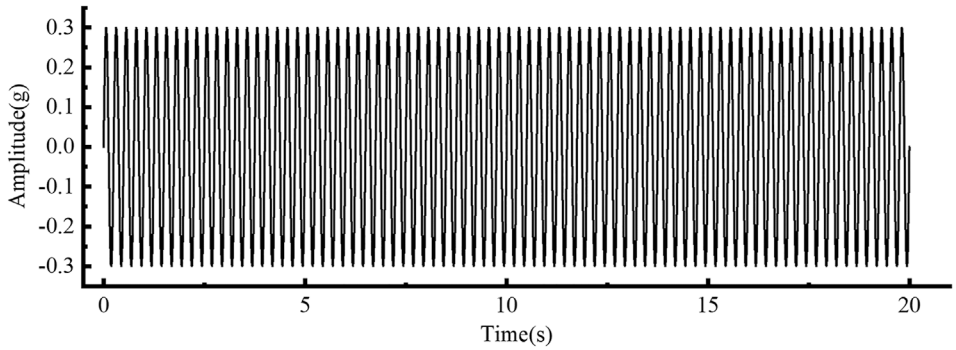

FIGURE 6 | Harmonic waves used as input base excitations.

TABLE 2 | Parameters of block elements in the numerical calculation.

Name	ρ (kg/m^3)	E (GPa)	ν (-)	c (MPa)	T (MPa)	Φ (°)
Basalt	3000	20	0.23	1.5	1.3	43
Tuff	2500	8	0.3	0.5	0.45	38

the slope was squeezed out under the action of strong earthquakes due to stress concentration.

Figure 8C; **Figure 8D** show the displacement distributions ((C) 0.5 g amplitude; (D) 1.0 g amplitude) of the failure process of the slope with 30° dip angle weak interlayers. From **Figure 8C**; **Figure 8D**, the slopes with 30°-dip-angle weak interlayers are completely destroyed under the action of earthquakes, and the final slip surface is mainly controlled by the third weak interlayer. Under different amplitudes, the failure process of slopes shows similar disciplines: (1) Damage and cracking occurred on the contact surfaces of the weak interlayers (t = 0.2 s); (2) Vertical tension cracks occurred on the back edge of the slope. At the angle between the fractured surfaces and the weak interlayers, the rock masses were destroyed due to stress concentration, and a small amount of rock fell (t = 4.0 s); (3) The tensile cracks on the back edge widened and expanded downwards, intersecting with the first weak intercalation, and the rock masses above the first weak interlayer slipped downward (t = 8.0 s); (4) The trailing edge cracks continued to propagate downward, and successively penetrated the second and third weak interlayers (t = 12.0 s and t = 16.0 s), causing the rock masses above the third weak interlayer to collapse. Finally, the overall collapse was formed (t = 19.9 s). It is worth mentioning that when the amplitude is small (0.3 and 0.5 g), no damage occurs at the slope toe, and the third weak interlayer is the control sliding surface, where in the case of large amplitude (0.8 and 1.0 g), the slope toe is damaged. The rock mass below the third weak interlayer appears buckling failure, but no new slip surface is formed.

Figure 8E; **Figure 8F** show the displacement distributions ((E) 0.5 g amplitude; (F) 1.0 g amplitude) of the failure process of the slope with 45°-dip-angle weak interlayers. From **Figure 8E**; **Figure 8F**, the slope with weak interlayers with an inclination angle of 45° has overall instability and destructiveness. The failure process is expressed: (1) The contact surfaces of the weak interlayers were damaged and cracked (t = 0.4 s); (2) Vertical tension cracks occurred on the back edge of the slope. The rock mass above the third weak interlayer, meanwhile, slipped as a whole (t = 2.6 s); (3) The cracks on the trailing edge were widened and extended downwards to penetrate the weak interlayers. The slope top blocks collapsed (t = 6.1–8.6 s); (4) Under the control of the weak interlayers, the slope fell as a whole. There are different final failure modes under different amplitudes. Under the condition of an amplitude of 0.3 g, the slope toe does not damage, and the final slip surface is controlled by the third weak interlayer; In the case of an amplitude of 0.5 g, the slope toe undergoes extrusion failure and the rock masses below the third weak interlayer buckle, but no new slip surface is formed; The rock masses below the third weak interlayer are destroyed as a whole and penetrates through the upper slip surface to form a new integral slip surface when the amplitude is above 0.8 g.

Analysis of Waveform Characteristics

In the numerical simulation, 12 monitoring points are arranged (**Figure 5**). Obtain the acceleration time-history curve from the acceleration data of the monitoring points. **Figure 9** shows the acceleration time-history curves with weak interlayers inclination of 15° under the input wave of amplitude 0.5 g. According to **Figure 9**, the waveform fluctuates uniformly throughout the entire process without obvious discrete points at the two monitoring blocks A1 and A2, indicating that there is no damage at the two places, that is, no damage occurs below the third weak interlayer. The waveforms of A3-A6 produced different degrees of fluctuation dispersion phenomenon at different moments. After the first fluctuation dispersion, there will still be multiple wave dispersion phenomena in a relatively short period, and then enter the relatively uniform fluctuation phase. The reason for this phenomenon is that: when discrete fluctuations appear for the first time, it indicates that the connection of the monitoring block is broken and microcracks are generated, which leads to a sharp change in acceleration. However, the constraints between the monitoring block and the adjacent blocks have not been completely lifted, and the collision between the blocks makes the acceleration change drastically. After the connection between the monitoring block and the adjacent blocks is completely broken, the monitoring block

TABLE 3 | Parameters of the contact elements in the numerical calculation.

Name	k_n (GPa/m)	k_s (GPa/m)	Φ (°)	c (MPa)	T (MPa)	G_{fI} (Pa·m)	G_{fII} (Pa·m)
Basalt	200	20	43	1.5	1.3	120	40
Tuff	80	8	38	0.5	0.45	600	130
Interface	1.2	0.12	35	0.15	0.15	3	11

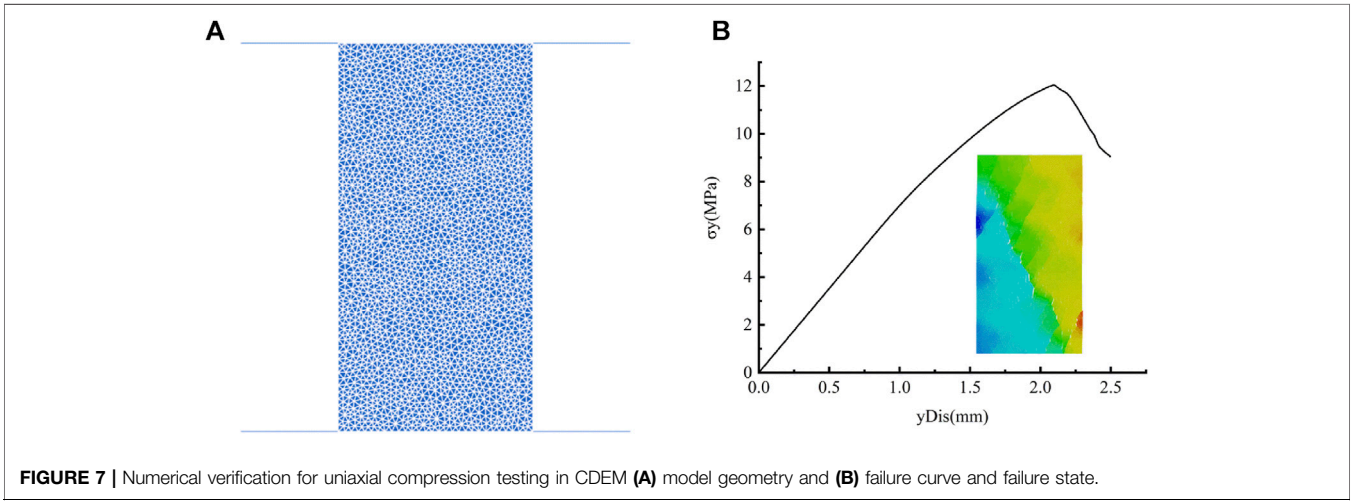

FIGURE 7 | Numerical verification for uniaxial compression testing in CDEM **(A)** model geometry and **(B)** failure curve and failure state.

slides out or flies out, and the acceleration fluctuates uniformly, that is, the waveform is uniformly distributed. As shown in **Figure 9**, A7-A12 monitoring blocks all have discrete waveform fluctuations at different times, indicating that damage occurs inside the slope at different times. After damage, the waveform fluctuates uniformly or discretely again. The reason is that: the A7-A12 monitoring blocks are located inside the slope. After the damage occurs, the damaged monitoring block cannot slide due to the constraints of the surrounding blocks, so the waveform is evenly distributed. However, the damaged block may suffer connection damage again, causing discrete fluctuations in the waveform again.

According to the above analysis, for the calculation condition with weak interlayers inclination of 15° and an amplitude of 0.5 g, no damage occurs at A1-A2, that is, no damage occurs below the third weak interlayer. The different degrees of damage occurred at A3-A6, indicating that under the influence of the weak interlayers, the upper part of the slope appears to be damaged and slipped, and the weak interlayers are the key cause of slope instability. Different degrees of damage occurred in A7-A12, indicating that the earthquake will cause internal damage to the slope and produce more micro-cracks. These micro-cracks are unstable factors that threaten the safety of the slope. More, the sequence of a slope failure can be determined by using the time when the discrete waveform appears. The time sequence of slope failure is A6, A5, A4, A3 at the slope surface, indicating that with the effort of the weak interlayers, the upper weak interlayer is destroyed first, driving the rock above the upper weak interlayer to slip, and then the lower rock layer is successively destroyed. In the interior of the slope, A7-A10 are destroyed first, A11 and A12 are destroyed in sequence, and the order of destruction is from the top to the bottom of the slope.

Other calculation conditions show similar disciplines. It is worth mentioning that under these two conditions, the slope toe (A1) and the lower part of the weak interlayer (A2) were damaged, and the third weak interlayer (A3) was the first to fail and slip. This is because when the inclination angle is relatively large, seismic action is no longer the only dominant factor in slope failure. The combined effort of the earthquake and geological structure makes the third weak interlayer break out first, and then drive the upper rock formation to slide.

Dynamic Amplification Effect Analysis

The amplification effect of the slopes takes into account the influence of the weak interlayers dip and the amplitude of the seismic load. Here use the peak ground displacement (PGD) to describe the dynamic response of the slopes. Introduce the PGD amplification coefficient, i.e. the ratio of the PGD of any monitoring point to the PGD at the slope toe (A1), and the relative height (h/H), i.e. the ratio of the height of any monitoring point to the height of the slope. **Figure 10** shows the PGD amplification coefficient under various calculation conditions. As the height increases, the PGD amplification coefficient increases first and then decreases overall.

From **Figure 10A**, for a slope with weak interlayers inclination of 15°, the PGD amplification coefficient increases sharply in the middle of the slope (A3, A4, and A5), indicating that this is the main area of slope failure, that is, the slope failure is mainly controlled by the weak interlayers under this calculation condition. Note that the slope toe is not damaged when the

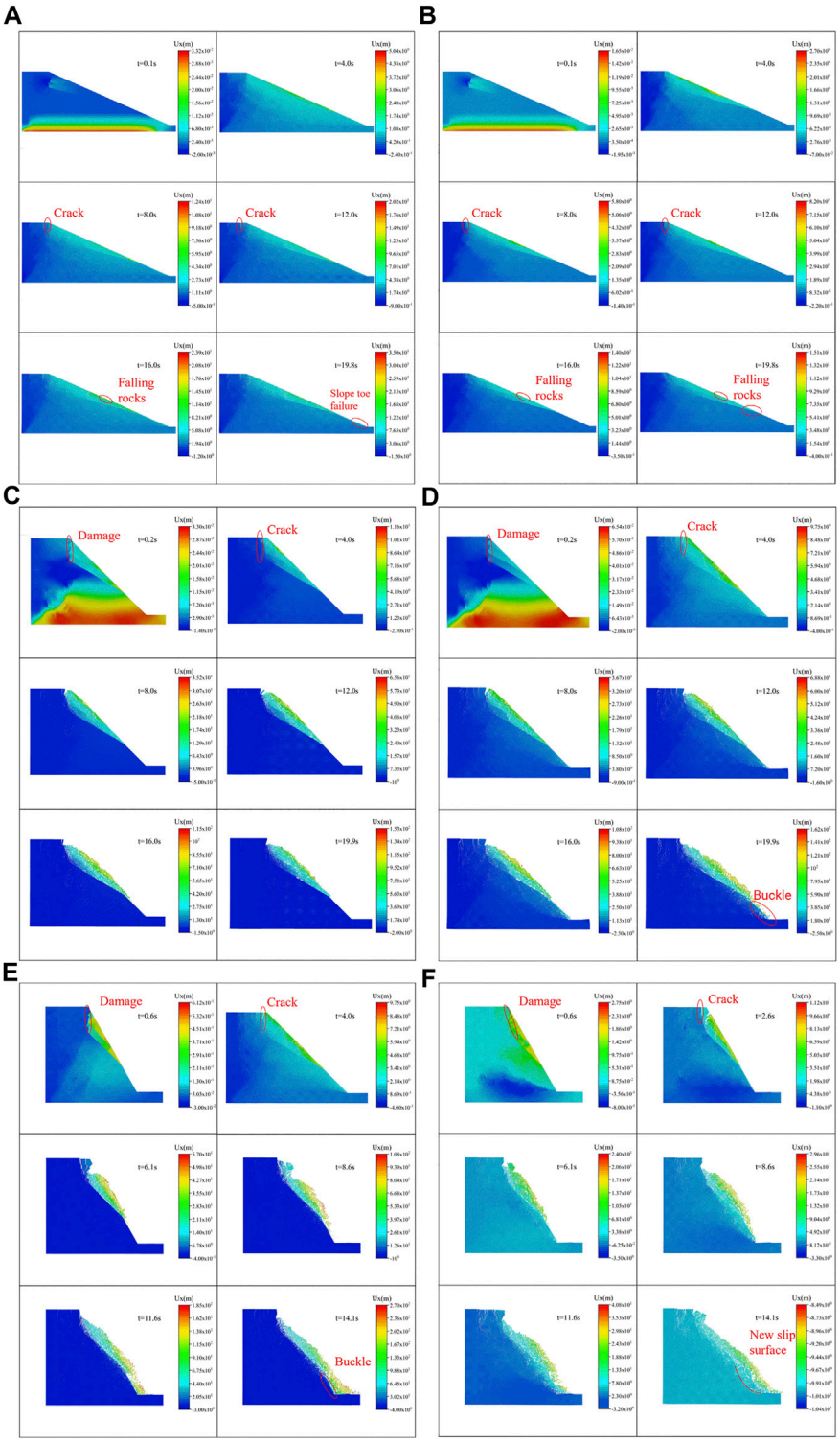

FIGURE 8 | The failure process of the slope **(A)** 0.5 g-15˚, **(B)** 1.0 g-15˚, **(C)** 0.5 g-30˚, **(D)** 1.0 g-30˚, **(E)** 0.5 g-45˚, **(F)** 1.0 g-45˚.

amplitude is below 0.5 g, and the PGD amplification coefficient of the slope lower part (A2) is very small; and when the amplitude is above 0.8 g, the slope toe is damaged. The slope lower part (A2) produces a large displacement, and its PGD amplification coefficient also increases. **Figure 10B** shows the PGD amplification coefficient of slopes with weak interlayers

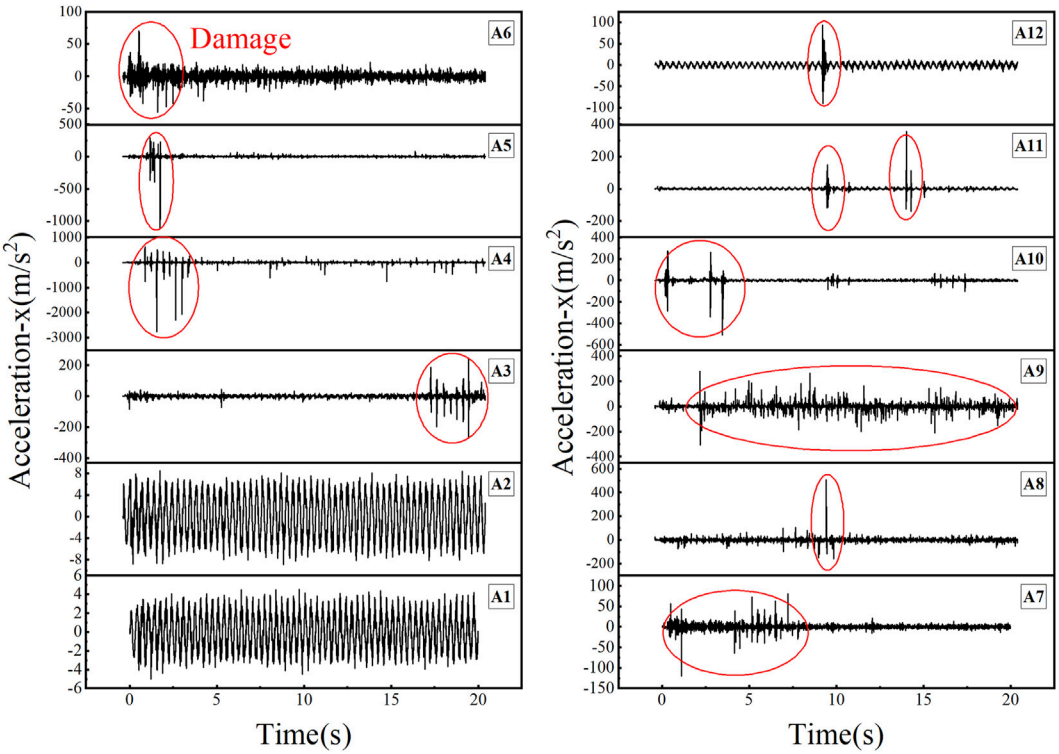

FIGURE 9 | Acceleration time-history curve of calculation condition with weak interlayers of 15° and amplification of 0.5 g.

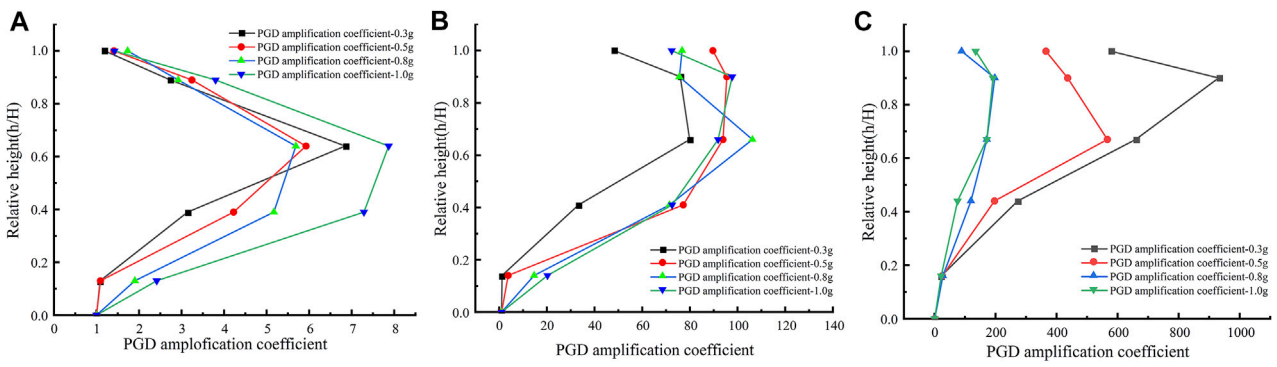

FIGURE 10 | Variation of PGD amplification coefficient with relative height **(A)** weak interlayers dip is 15°, **(B)** weak interlayers dip is 30°, **(C)** weak interlayers dip is 45°.

inclination of 30°. Similar to the inclination angle of 15°, the amplification coefficient of PGD in the middle and upper part of the slope increases sharply. The slope toe is not damaged when the amplitude is 0.3 g, and the PGD amplification coefficient is small, and when the amplitude is greater than 0.5 g, the PGD amplification coefficient of the lower slope is increased due to the damage of the slope toe. The slope with an inclination angle of 30°, different from the slope with an inclination angle of 15°, has an overall slippage above the weak interlayers, so the overall PGD amplification coefficient is very large. And the slope top (A6) has a large slippage, where the PGD amplification coefficient is large. **Figure 10C** shows the PGD amplification coefficient of the slope with weak interlayers inclination angle of 45°. Under these conditions, the slope toe is damaged. Because the slope toe does not have a large slip as the amplitude of the slope is below 0.5 g, its PGD is small, making the middle and upper

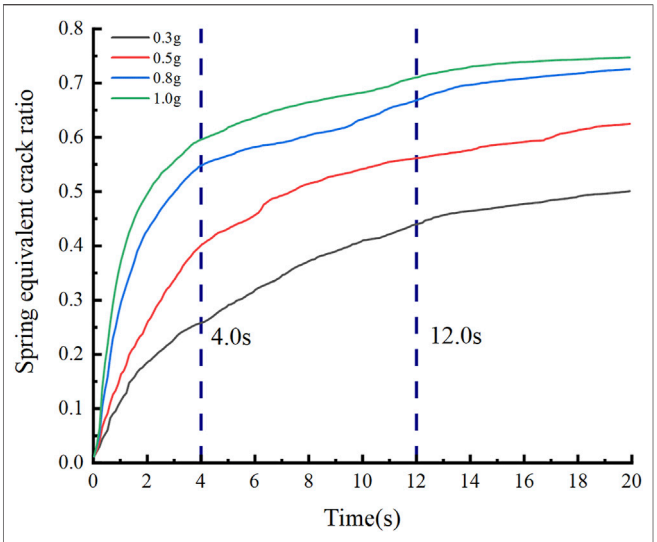

FIGURE 11 | Variation of spring equivalent crack ratio with amplifications (weak interlayers dip is 45°).

PGD amplification coefficient very large. When the amplitude is greater than 0.8g, the slope toe slides out, and its PGD is larger, making the overall PGD amplification factor smaller. From **Figure 10C**, the slope damage is mainly concentrated in the middle and upper part for the effect of the weak interlayers.

Comparing the above results, the slope damage, when the inclination angle is small (15°), mainly occurs in the middle and upper part, especially in the middle part, indicating that the failure of this type of slopes is mainly controlled by the weak interlayers, and the third weak interlayer has the most obvious effect. When the inclination angle is large (30° and 45°), the slopes are damaged by sliding as a whole, even the slope toe fails, too. In terms of the damage degree, the middle part of the slope is the most serious, followed by the top and toe of the slope, indicating that the weak interlayers still play an important part in the damage to this type of slope. However, with the increase of inclination angle and amplitude, the slope toe is squeezed out under the dynamic loads, and the failure control surface of the slopes change from the weak interlayers to the combination of weak interlayers and slope toe.

Equivalent Crack Ratio Analysis

The concept of spring equivalent crack ratio is introduced to characterize the slope failure degree. The definition formula of spring equivalent crack ratio is:

$$R = S_1/S_0 \tag{14}$$

where R is the spring equivalent crack ratio, S_1 is the cumulative value of the product of the spring damage factor and the area, and S_0 is the total contact area of the blocks. The equivalent crack ratio under different calculation conditions is shown in **Figure 11**. As the loading time increases, the equivalent crack ratio first increases sharply and then gradually stabilizes. According to **Figure 11**, the development of the equivalent crack ratio is divided into three stages: (1) Rapid growth stage (t = 0–4.0 s). At this stage, a large number of micro-cracks are rapidly generated under seismic loads, providing basic conditions for the subsequent failure of the slope. (2) Slowly increasing stage (t = 4.0–12.0 s). The increase in the equivalent crack ratio at this stage is mainly due to the aggregation of the microcracks generated in the previous stage, accompanied by a small number of new micro-cracks, and the growth rate slows down. The aggregation of micro-cracks promotes the failure of slopes. (3) Stable stage (t = 12.0–20.0 s). The equivalent crack ratio increases little at this stage, mainly because the aggregated cracks in the previous stages gradually penetrate and form slip surfaces, which makes the slope instability and failure. After the landslide failure occurs, the accumulated energy is released, and no new microcracks are generated, so the equivalent crack ratio gradually stabilizes.

Figure 12A shows the variation of the final spring equivalent crack ratio with the weak interlayers dip. When the amplitude is small (0.3 and 0.5 g), as the inclination angle increases, the final spring equivalent crack ratio gradually increases, and when the amplitude is large (0.8 and 1.0 g), the final spring equivalent crack ratio changes little as the inclination angle increases. This is because when the amplitude is not large, the weak interlayers have an important influence on slope failure. The seismic load, with the amplitude increasing, becomes the dominant factor for slope failure. As shown in **Figure 12B**, the final spring equivalent crack ratio has a positive correlation with the amplitude. When the amplitude is greater than 0.8 g, the final spring equivalent crack ratio reaches about 0.7, and the slope reaches failure. It can be seen that earthquakes, especially strong earthquakes, have a devastating effect on slopes.

Seismic Failure Mechanism of Landslides

Based on the previous analysis, the numerical results reveal the failure mechanism of landslides with different inclination angles and amplitudes. When the inclination angle of the weak interlayers is 15°, the slope is partially damaged without overall slippage. The main form of slope failure is local rockfall. When the inclination of the weak interlayers is 30°, the slope will slip as a whole. The failure process of the slope can be described as the weak interlayers cracking - tensile cracks appearing on the trailing edge - the tensile cracks widening and expanding downward - the tensile cracks penetrate the weak surfaces and the sliding surface formed, and the landslide is destroyed as a whole. The failure mode can be summarized as "tensile cracking-slip-collapsing". It is noticed that the slope toe undergoes extrusion failure, but the overall slip surface is not formed as the amplitude reaches 1.0 g. The failure mode of a slope with weak interlayers inclination angle of 45° and an amplitude of less than 0.5 g is akin to that of a slope with an inclination angle of 30°. When the amplitude is equal to or greater than 0.8 g, the failure process is weak interlayer cracking–tensile cracks on the trailing edge–tensile cracks widening and extending downwards - slope toe extrusion–slipping surface penetration, and the overall failure of the landslide. The failure mode can be summarized as "tensile cracking-slip-slope extrusion-collapsing". Therefore, it can be seen that under different geological conditions, the leading factors of landslide are different, and the combination of weak

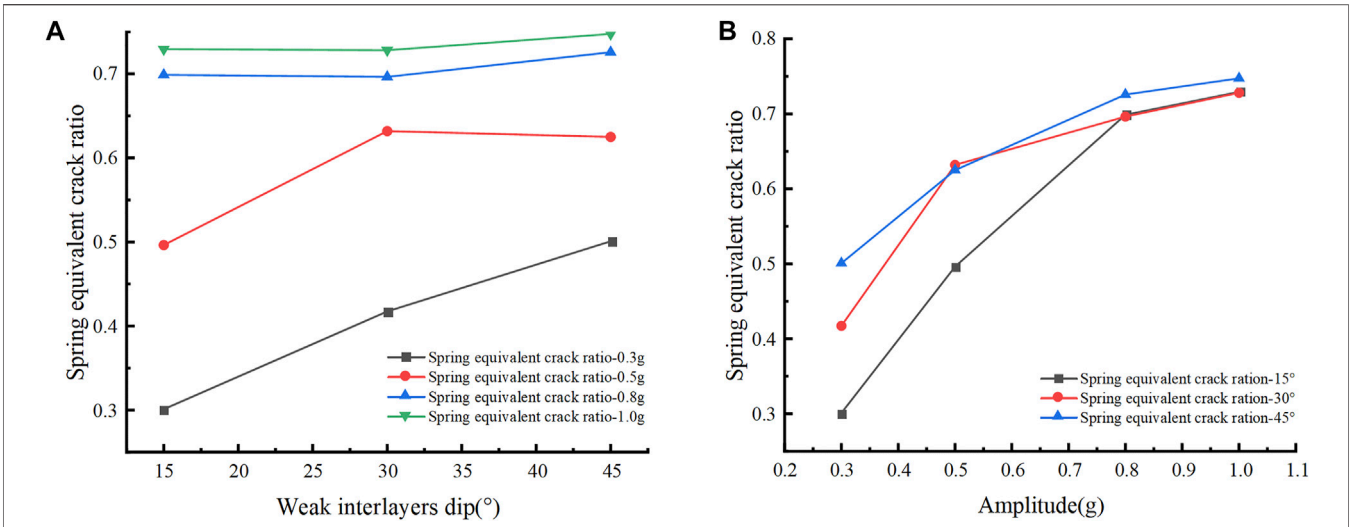

FIGURE 12 | Variation of final spring equivalent crack ratio **(A)** with weak interlayers dips, **(B)** with amplitudes.

interlayers and seismic load creates complex landslide failure modes.

DISCUSSION

Research on the stability of weak interbedded rock slopes is a hot issue. Many scholars have carried out research on this issue through field investigation, geological model test, and numerical simulation. Field investigation and geological model test have their own limitations. As computer technology developing rapidly, numerical simulation has become a good choice for studying the progressive failure process of landslides with complex geological structures.

The traditional numerical simulation methods, including the finite element method (FEM) and discrete element method (DEM), are widely used in calculating slope stability. The finite element method usually cannot simulate the large deformation and failure of rock slopes, especially the dynamic slip process accompanied by the seismic load of complex geological structures. The discrete element method can simulate the large deformation and the entire failure process of the slope, but due to its complex contact detection and low calculation efficiency, large-scale calculations are time-consuming. The CDEM method combines the advantages of the two traditional numerical methods and can realize the transformation of rock materials from continuum to discontinuum. Studies have shown that it is an effective method for simulating geological disasters such as landslides.

The CDEM simulation results show that different failure modes occur under different weak interlayers and seismic load combinations: local rockfall occurs in a gentle slope, “tensile cracking-slip-collapsing” failure occurs in mid-dip slope, and “tensile cracking-slip-slope extrusion-collapsing” failure occurs in a steep slope. Besides, the waveform characteristics, PGD amplification coefficient, and spring equivalent crack ratio have consistent correspondence with the failure process of landslides. The discrete fluctuations of the acceleration waveform indicate the cracking failure of the rock blocks, and the characteristics of the waveform reveal the failure location and failure time of landslides. The sudden change of the PGD amplification coefficient reflects the damaged location and damage degree of landslides. It is worth mentioning that the slope failure process can be divided into three stages according to the spring equivalent crack ratio: equivalent crack ration rapid increase stage, equivalent crack ration slow increase stage, and equivalent crack ration stable stage. This reveals the failure mechanism of landslides: under the action of the earthquake, a large number of micro-cracks are rapidly generated first, and then the micro-cracks are expanded and aggregated, and finally the cracks penetrate to form a slip surface and cause a landslide. The failure process of landslides can be divided and the failure mechanism of landslides can be explained based on the analysis of the equivalent crack ratio, which provides a reference for the criterion of landslides.

However, CDEM numerical simulation in this study has its own limitations. The real geological structure is in a three-dimensional state, and it is difficult for two-dimensional numerical simulation to accurately reflect the three-dimensional motion characteristics of landslides. Also, the variation of parameters that is not considered in this paper will be an important factor for the failure modes. We will try to carry out three-dimensional related research and parameters discussion in future work. In addition, some laboratory experiments contain important information for understanding the mechanism of earthquake-induced landslides, which are of high value for simulation and verification(Burridge and Knopoff, 1967; Parteli et al., 2005). We will consider these experimental information in the future research. Although the simulation has limitations, a reference to reveal the failure process and failure mechanism of rock slopes under the combined action of weak interlayers and earthquakes is provided. In addition, CDEM

method is not only suitable for earthquake-induced landslides simulation, but also applied to model a broader range of landslide types, for example, cumulative perturbations due to soil instability processes(Feng et al., 2014; Yongbo et al., 2016). CDEM method provides new ideas for studying geological disasters such as landslides.

CONCLUSIONS

The CDEM method is used to numerically simulate the failure modes and dynamic response of weak interbedded rock slopes under earthquakes. Some conclusions can be drawn as follows:

1. The characteristics of acceleration waveform and PGD amplification coefficient have strong consistency with the landslide failure process. The discrete fluctuation of the waveform reflects the damage location and time of the landslide. The sharp change of the PGD amplification coefficient reveals the landslide damage location and damage degree.
2. The concept of spring equivalent crack ratio is introduced, and the landslide development process can be divided into three stages by using the change of spring equivalent crack ratio over time: rapid generation of a large number of microcracks, expansion, and aggregation of microcracks, and penetration of micro-cracks and the formation of slip surfaces.
3. The combination of weak interlayers and seismic load causes multiple failure modes of the landslide. For the gentle slope (15°), local damage occurs on the slope, and the main form of damage is rockfall. For a mid-dip slope (30°), the slope has an overall failure, and the failure mode is "tensile cracking-slip-collapsing". For the steep slope (45°), "tensile cracking-slip-collapsing" failure occurs when the amplitude is small, and "tensile cracking-slip-slope extrusion-collapsing" failure occurs when the amplitude is large.

DATA AVAILABILITY STATEMENT

Publicly available datasets were analyzed in this study. This data can be found here: http://www.civil.tsinghua.edu.cn/he/essay/340/956.html.

AUTHOR CONTRIBUTIONS

XL designed the research; CW performed the research; DS, EW, and JZ wrote sections of the manuscript; and CW and XL organized and wrote the paper. All authors read and approved the manuscript.

FUNDING

This work was supported by the National Key R&D Program of China (Grant No. 2018YFC1504902), the National Natural Science Foundation of China (Grant No. 52079068), and the State Key Laboratory of Hydroscience and Hydraulic Engineering (Grant No. 2021-KY-04).

ACKNOWLEDGMENTS

Special thanks to Gdem Technology, Beijing, Co., Ltd. for its technical support.

REFERENCES

Bao, Y., Han, X., Chen, J., Zhang, W., Zhan, J., Sun, X., et al. (2019). Numerical Assessment of Failure Potential of a Large Mine Waste Dump in Panzhihua City, China. *Eng. Geology.* 253, 171–183. doi:10.1016/j.enggeo.2019.03.002

Burridge, R., and Knopoff, L. (1967). Model and Theoretical Seismicity. *Bull. Seismological Soc. America* 57, 341–371. doi:10.1785/bssa0570030341

Chen, Z., and Song, D. (2021). Numerical Investigation of the Recent Chenhecun Landslide (Gansu, China) Using the Discrete Element Method. *Nat. Hazards* 105, 717–733. doi:10.1007/s11069-020-04333-w

Cui, S., Yang, Q., Pei, X., Huang, R., Guo, B., and Zhang, W. (2020). Geological and Morphological Study of the Daguangbao Landslide Triggered by the Ms. 8.0 Wenchuan Earthquake, China. *Geomorphology* 370, 107394. doi:10.1016/j.geomorph.2020.107394

Dai, F. C., Xu, C., Yao, X., Xu, L., Tu, X. B., and Gong, Q. M. (2011). Spatial Distribution of Landslides Triggered by the 2008 Ms 8.0 Wenchuan Earthquake, China. *J. Asian Earth Sci.* 40, 883–895. doi:10.1016/j.jseaes.2010.04.010

Delgado, J., Rosa, J., Peláez, J. A., Rodríguez-Peces, M. J., Garrido, J., and Tsigé, M. (2020). Newmark Displacement Data for Low to Moderate Magnitude Events in the Betic Cordillera. *Data in Brief* 32, 106097. doi:10.1016/j.dib.2020.106097

Deng, Z., Liu, X., Liu, Y., Liu, S., Han, Y., Liu, J., et al. (2020). Model Test and Numerical Simulation on the Dynamic Stability of the Bedding Rock Slope under Frequent Microseisms. *Earthq. Eng. Eng. Vib.* 19, 919–935. doi:10.1007/s11803-020-0604-8

Do, T. N., and Wu, J.-H. (2020). Simulating a Mining-Triggered Rock Avalanche Using DDA: A Case Study in Nattai North, Australia. *Eng. Geology.* 264, 105386. doi:10.1016/j.enggeo.2019.105386

Donati, D., Stead, D., Stewart, T. W., and Marsh, J. (2020). Numerical Modelling of Slope Damage in Large, Slowly Moving Rockslides: Insights from the Downie Slide, British Columbia, Canada. *Eng. Geology.* 273, 105693. doi:10.1016/j.enggeo.2020.105693

Feng, C., Li, S., Liu, X., and Zhang, Y. (2014). A Semi-spring and Semi-edge Combined Contact Model in CDEM and its Application to Analysis of Jiweishan Landslide. *J. Rock Mech. Geotechnical Eng.* 6, 26–35. doi:10.1016/j.jrmge.2013.12.001

Huang, M., Fan, X., and Wang, H. (2017). Three-dimensional Upper Bound Stability Analysis of Slopes with Weak Interlayer Based on Rotational-Translational Mechanisms. *Eng. Geology.* 223, 82–91. doi:10.1016/j.enggeo.2017.04.017

Huang, M., Wang, H., Sheng, D., and Liu, Y. (2013). Rotational-translational Mechanism for the Upper Bound Stability Analysis of Slopes with Weak Interlayer. *Comput. Geotechnics* 53, 133–141. doi:10.1016/j.compgeo.2013.05.007

Huang, R., Xiao, H., Ju, N., and Zhao, J. (2007). Deformation Mechanism and Stability of a Rocky Slope. *J. China Univ. Geosciences* 18, 77–84. doi:10.1016/s1002-0705(07)60021-1

Kawamura, S., Kawajiri, S., Hirose, W., and Watanabe, T. (2019). Slope Failures/landslides over a Wide Area in the 2018 Hokkaido Eastern Iburi Earthquake. *Soils and Foundations* 59, 2376–2395. doi:10.1016/j.sandf.2019.08.009

Li, C., Wu, J., Tang, H., Hu, X., Liu, X., Wang, C., et al. (2016). Model Testing of the Response of Stabilizing Piles in Landslides with Upper Hard and Lower Weak Bedrock. *Eng. Geology.* 204, 65–76. doi:10.1016/j.enggeo.2016.02.002

Li, S. H., Wang, J. G., Liu, B. S., and Dong, D. P. (2006). Analysis of Critical Excavation Depth for a Jointed Rock Slope Using a Face-To-Face Discrete Element Method. *Rock Mech. Rock Engng.* 40, 331–348. doi:10.1007/s00603-006-0084-9

Li, Z., Wang, J. a., Li, L., Wang, L., and Liang, R. Y. (2015). A Case Study Integrating Numerical Simulation and GB-InSAR Monitoring to Analyze Flexural Toppling of an Anti-dip Slope in Fushun Open Pit. *Eng. Geology.* 197, 20–32. doi:10.1016/j.enggeo.2015.08.012

Lin, C.-H., Li, H.-H., and Weng, M.-C. (2018). Discrete Element Simulation of the Dynamic Response of a Dip Slope under Shaking Table Tests. *Eng. Geology.* 243, 168–180. doi:10.1016/j.enggeo.2018.07.005

Lin, P., Liu, X., Hu, S., and Li, P. (2016). Large Deformation Analysis of a High Steep Slope Relating to the Laxiwa Reservoir, China. *Rock Mech. Rock Eng.* 49, 2253–2276. doi:10.1007/s00603-016-0925-0

Liu, C., Liu, X., Peng, X., Wang, E., and Wang, S. (2019). Application of 3D-DDA Integrated with Unmanned Aerial Vehicle-Laser Scanner (UAV-LS) Photogrammetry for Stability Analysis of a Blocky Rock Mass Slope. *Landslides* 16, 1645–1661. doi:10.1007/s10346-019-01196-6

Liu, X., Han, G., Wang, E., Wang, S., and Nawnit, K. (2018). Multiscale Hierarchical Analysis of Rock Mass and Prediction of its Mechanical and Hydraulic Properties. *J. Rock Mech. Geotechnical Eng.* 10, 694–702. doi:10.1016/j.jrmge.2018.04.003

Luo, J., Pei, X., Evans, S. G., and Huang, R. (2019). Mechanics of the Earthquake-Induced Hongshiyan Landslide in the 2014 Mw 6.2 Ludian Earthquake, Yunnan, China. *Eng. Geology.* 251, 197–213. doi:10.1016/j.enggeo.2018.11.011

Marcato, G., Mantovani, M., Pasuto, A., Zabuski, L., and Borgatti, L. (2012). Monitoring, Numerical Modelling and hazard Mitigation of the Moscardo Landslide (Eastern Italian Alps). *Eng. Geology.* 128, 95–107. doi:10.1016/j.enggeo.2011.09.014

Martino, S., Lenti, L., and Bourdeau, C. (2018). Composite Mechanism of the Büyükçekmece (Turkey) Landslide as Conditioning Factor for Earthquake-Induced Mobility. *Geomorphology* 308, 64–77. doi:10.1016/j.geomorph.2018.01.028

Montgomery, J., Candia, G., Lemnitzer, A., and Martinez, A. (2020). The September 19, 2017 Mw 7.1 Puebla-Mexico City Earthquake: Observed rockfall and Landslide Activity. *Soil Dyn. Earthquake Eng.* 130, 105972. doi:10.1016/j.soildyn.2019.105972

Newmark, N. M. (1965). Effects of Earthquakes on Dams and Embankments. *Géotechnique* 15, 139–160. doi:10.1680/geot.1965.15.2.139

Parteli, E. J., Gomes, M. A., and Brito, V. P. (2005). Nontrivial Temporal Scaling in a Galilean Stick-Slip Dynamics. *Phys. Rev. E Stat. Nonlin Soft Matter Phys.* 71, 036137. doi:10.1103/PhysRevE.71.036137

Sangirardi, M., Amorosi, A., and De Felice, G. (2020). A Coupled Structural and Geotechnical Assessment of the Effects of a Landslide on an Ancient Monastery in Central Italy. *Eng. Structures* 225, 111249. doi:10.1016/j.engstruct.2020.111249

Seisdedos, J., Ferrer, M., and González de Vallejo, L. I. (2012). Geological and Geomechanical Models of the Pre-landslide Volcanic Edifice of Güímar and La Orotava Mega-Landslides (Tenerife). *J. Volcanology Geothermal Res.* 239-240, 92–110. doi:10.1016/j.jvolgeores.2012.06.013

Song, D., Chen, Z., Chao, H., Ke, Y., and Nie, W. (2020). Numerical Study on Seismic Response of a Rock Slope with Discontinuities Based on the Time-Frequency Joint Analysis Method. *Soil Dyn. Earthquake Eng.* 133, 106112. doi:10.1016/j.soildyn.2020.106112

Song, D., Liu, X., Huang, J., and Zhang, J. (2021). Energy-based Analysis of Seismic Failure Mechanism of a Rock Slope with Discontinuities Using Hilbert-Huang Transform and Marginal Spectrum in the Time-Frequency Domain. *Landslides* 18, 105–123. doi:10.1007/s10346-020-01491-7

Tang, C.-L., Hu, J.-C., Lin, M.-L., Angelier, J., Lu, C.-Y., Chan, Y.-C., et al. (2009). The Tsaoling Landslide Triggered by the Chi-Chi Earthquake, Taiwan: Insights from a Discrete Element Simulation. *Eng. Geology.* 106, 1–19. doi:10.1016/j.enggeo.2009.02.011

Tang, C., Tang, J., Van Westen, C. J., Han, J., Mavrouli, O., and Tang, C. (2020). Modeling Landslide Failure Surfaces by Polynomial Surface Fitting. *Geomorphology* 368, 107358. doi:10.1016/j.geomorph.2020.107358

Terzaghi, K., and Paige, S. (1950). "Mechanism of Landslides," in *Application of Geology to Engineering Practice* (Boulder, USA: Geological Society of America).

Wasowski, J., Keefer, D. K., and Lee, C.-T. (2011). Toward the Next Generation of Research on Earthquake-Induced Landslides: Current Issues and Future Challenges. *Eng. Geology.* 122, 1–8. doi:10.1016/j.enggeo.2011.06.001

Wu, J.-H., Lin, W.-K., and Hu, H.-T. (2018). Post-failure Simulations of a Large Slope Failure Using 3DEC: The Hsien-Du-Shan Slope. *Eng. Geology.* 242, 92–107. doi:10.1016/j.enggeo.2018.05.018

Xu, J., Tang, X., Wang, Z., Feng, Y., and Bian, K. (2020). Investigating the Softening of Weak Interlayers during Landslides Using Nanoindentation Experiments and Simulations. *Eng. Geology.* 277, 105801. doi:10.1016/j.enggeo.2020.105801

Xu, J., and Yang, X. (2018). Seismic Stability Analysis and Charts of a 3D Rock Slope in Hoek-Brown media. *Int. J. Rock Mech. Mining Sci.* 112, 64–76. doi:10.1016/j.ijrmms.2018.10.005

Xu, W.-J., and Dong, X.-Y. (2021). Simulation and Verification of Landslide Tsunamis Using a 3D SPH-DEM Coupling Method. *Comput. Geotechnics* 129, 103803. doi:10.1016/j.compgeo.2020.103803

Yang, G., Qi, S., Wu, F., and Zhan, Z. (2018). Seismic Amplification of the Anti-dip Rock Slope and Deformation Characteristics: A Large-Scale Shaking Table Test. *Soil Dyn. Earthquake Eng.* 115, 907–916. doi:10.1016/j.soildyn.2017.09.010

Yiğit, A. (2020). Prediction of Amount of Earthquake-Induced Slope Displacement by Using Newmark Method. *Eng. Geology.* 264, 105385. doi:10.1016/j.enggeo.2019.105385

Yongbo, F., Shihai, L., Yang, Z., Zhiyong, F., and Xiaoyu, L. (2016). Lessons Learned from the Landslides in Shengli East Open-Pit Mine and North Open-Pit Mine in Xilinhot City, Inner Mongolia Province, China. *Geotech Geol. Eng.* 34, 425–435. doi:10.1007/s10706-015-9954-9

Yu, Y., Shen, M., Sun, H., and Shang, Y. (2019). Robust Design of Siphon Drainage Method for Stabilizing Rainfall-Induced Landslides. *Eng. Geology.* 249, 186–197. doi:10.1016/j.enggeo.2019.01.001

Yu, Y., Wang, E., Zhong, J., Liu, X., Li, P., Shi, M., et al. (2014). Stability Analysis of Abutment Slopes Based on Long-Term Monitoring and Numerical Simulation. *Eng. Geology.* 183, 159–169. doi:10.1016/j.enggeo.2014.10.010

Zhao, S., Chigira, M., and Wu, X. (2018). Buckling Deformations at the 2017 Xinmo Landslide Site and Nearby Slopes, Maoxian, Sichuan, China. *Eng. Geology.* 246, 187–197. doi:10.1016/j.enggeo.2018.09.033

Zhu, D., Yan, E., Hu, G., and Lin, Y. (2011). Revival Deformation Mechanism of Hefeng Landslide in the Three Gorges Reservoir Based on FLAC3D Software. *Proced. Eng.* 15, 2847–2851. doi:10.1016/j.proeng.2011.08.536

Conflict of Interest: The authors declare that the research was conducted in the absence of any commercial or financial relationships that could be construed as a potential conflict of interest.

Publisher's Note: All claims expressed in this article are solely those of the authors and do not necessarily represent those of their affiliated organizations, or those of the publisher, the editors and the reviewers. Any product that may be evaluated in this article, or claim that may be made by its manufacturer, is not guaranteed or endorsed by the publisher.

frontiers | Frontiers in Earth Science

ORIGINAL RESEARCH
published: 14 June 2022
doi: 10.3389/feart.2022.925636

Effects of Rainfall on Mechanical Behaviors of Residual-Soil Landslide

Yong He[1,2,3], *Zhi-Peng Yu*[1,2], *Zhao Zhang*[1,2,3]*, *Bin Chen*[4] *and Ke-Neng Zhang*[1,2]

[1]Key Laboratory of Metallogenic Prediction of Nonferrous Metals and Geological Environment Monitoring (Central South University), Ministry of Education, Changsha, China, [2]School of Geosciences and Info-Physics, Central South University, Changsha, China, [3]Key Laboratory of Geotechnical and Underground Engineering of Ministry of Education and Department of Geotechnical Engineering, Tongji University, Shanghai, China, [4]Hunan Provincial Key Laboratory of Geomechanics and Engineering Safety, Xiangtan University, Xiangtan, China

Rainfall-induced landslides commonly occur in residual-soil layers of Chenzhou city, China. Slope failure induced by rainfall is intimately related to changes in the mechanical property and microstructures of residual soils. In this study, series of direct shear tests were respectively conducted on four typical residual soils from the area of Chenzhou to study influences of rainwater on their mechanical behaviors. Meanwhile, X-ray diffraction (XRD) tests and scanning electron microscope (SEM) tests were also performed to investigate microstructure characteristic of several types of soils. Experimental results revealed that the shear strength of soils decreased with increasing water content and its development trends were obviously influenced by the types of residual soils. Meanwhile, the shear strength of soils increased with the increase of vertical loads, and the relationship between them could be well expressed by a linear function. As water content increased, the calculated cohesions and internal friction angles both decreased. XRD observations implied that several residual soils showed rich clay minerals, including pyrophyllite, illite, kaolinite and montmorillonite, etc. Microstructures of these soils presented a sheet-structure system which was composed of various-sized clay particles. During hydration, these clay minerals gradually transferred from a face-face arrangement to face-edge or even edge-edge one, leading to the softening of clay particles and the reduction of the contact force between soil particles.

Keywords: landslide, shear strength, residual soil, microstructure, mechanical behavior

OPEN ACCESS

Edited by:
Irasema Alcántara-Ayala, National Autonomous University of Mexico, Mexico

Reviewed by:
Luqi Wang, Chongqing University, China
Bing Bai, Beijing Jiaotong University, China

***Correspondence:**
Zhao Zhang
zhangzhaozn@163.com

Specialty section:
This article was submitted to Geohazards and Georisks, a section of the journal Frontiers in Earth Science

Received: *21 April 2022*
Accepted: *30 May 2022*
Published: *14 June 2022*

Citation:
He Y, Yu Z-P, Zhang Z, Chen B and Zhang K-N (2022) Effects of Rainfall on Mechanical Behaviors of Residual-Soil Landslide. Front. Earth Sci. 10:925636. doi: 10.3389/feart.2022.925636

1 INTRODUCTION

China is a country with frequent landslide activities. Landslide will seriously threaten the safety of human life and property, e.g., Sugarwumei landslide in 2018, Shuicheng landslide in 2019 and Manisales landslide in 2019, etc. The occurrence of landslides is normally related to mechanical properties of sliding-surface soils, especially for the soil layers with poor properties (Zhang et al., 2016; Xiao et al., 2021; Yin et al., 2022). Large number of studies demonstrated that landslides commonly happen in rainy seasons because the rainfall causes the deterioration in the mechanical property of slope soils. Wen et al. (2019) studied the triggering mechanism of rainfall on slow-dip red-bed rock landslide and concluded that the formation process of landslides could be closely classified into four stages: 1) the fracture development stage resulted from the rainfall infiltration; 2) the shear-strength decreasing stage in the weak zone; 3) the rising stage of the pore water pressure and uplift pressure; and 4) the instability and sliding process of slopes. Zhu et al. (2019) conducted

laboratory model tests on the loess-mudstone slope under two heavy rainfall patterns, and results revealed that the slope instability both occurred on the loess-mudstone contact surface. The creeping-fracturing instability happened under a continuous strong rainfall, while a sliding-fracturing instability occurred in an intermittent strong rainfall, which depended on the infiltration rates of rainwater. Moreover, Miščević and Vlastelica (2014) investigated the influences of weathering on the stability of soft-rock slope and pointed out that the instability modes of marl slope were primarily controlled by a weak surface generated during the weathering process. Khan et al. (2017) explored the failure mechanism of the shallow expansive soil slope. Experimental results demonstrated that as rainwater infiltrated along the surface cracks, shear strength of the soils in the sliding zone obviously decreased, which was the main reason of landslides. Therefore, it is necessary to study the mechanical behavior of sliding-zone soils and its sensitivity to water changes for assessment of the slope stability.

It is well recognized that the rainfall infiltration can cause a dissipation of the soil suction and a reduction of the shear strength when the unsaturated soil slopes are subjected to rainfall (De Vita et al., 1998; Patuti et al., 2017). Farooq et al. (2004) and Orense et al. (2004) pointed out that the pore pressure inside slope soil gradually increased from a negative value to a higher one with the infiltration of rainwater, and the effective stress accordingly decreased until the failure occurred. The strength of soil actually originates from frictional resistance and bonding force between soil particles, which are associated with fabric changes. Studies demonstrated that the shear strength of unsaturated soils normally decreased with increasing water content, and its reduction was intimately related to the soil property, e.g., microstructure, mineral composition, the stress history and the original fabric (Fredlund et al., 1996; He et al., 2020, 2021; Zhang et al., 2021). For unsaturated sandy soils, the capillary force between soil particles reduces and the cohesion generated by the capillary water decreases during the infiltration of rainwater. Meanwhile, small sand particles are likely to transport through large inter-particle pores under high groundwater pressure (Bai et al., 2021a; 2021b). While for unsaturated clayey soils, the interaction between clay particles was controlled by the absorptive force of absorbed water and the capillary force of capillary water. The shear strength of soil was dominated by the absorptive force in low water contents (or high suctions), while in high water contents (or low suctions), the change of shear strength was primarily influenced by the capillary water (Mitchell and Soga, 2005; Lu, 2016). Therefore, the rainfall-induced strength changes for clayey soil appear to be more complicate due to complex mineral composition and fabric changes.

In this study, several typical residual soils were extracted from the landslide zones in Chenzhou, Hunan province. Series of shear tests, X-ray diffraction (XRD) tests and scanning electron microscope (SEM) tests were carried out to investigate mechanical property and microstructures of several soils at varied water contents, respectively. The changes of strength parameters (e.g., shear strength, cohesion and internal friction angle) with water content were analyzed and the corresponding mechanisms were clarified through microstructural observations. These findings provide useful information for deeply understanding the failure mechanism of residual-soil slopes.

2 MATERIALS AND METHODS

2.1 Materials

A western North Pacific Ocean severe tropical storm "Bilis" made landfall on the southeastern coast of mainland China on 14 July 2006. The heavy rainfalls induced by Bilis attacked the Chenzhou city in Hunan province and caused more than 8,000 landslides and mudslides, which killed at least 394 people and left 97 people missing (Ma and Tan, 2009). Field investigation found that most of the landslide sliding zones are in residual soil layers. **Figure 1** presents several typical residual soils widely distributed in this area, including white silty-clay layer (WSC), gray coal-soil layer (GCS) and red-clay layers (RC-I and RC-II). These soil layers are normally considered as the main slip formations of landslides. In this work, four types of residual soils above were selected and remolded. Basic physical properties of these soils are listed in **Table 1**. It can be seen that the natural water contents of four types of soils are all lower than their liquid limits, with a highest water content for the gray coal soil. Two kinds of red clay had high liquid limits and initial void ratios. **Figure 2** shows particle size distribution curves of several soil samples. It can be found that the fine-particles (<0.075 mm) content for all samples is over than 80 %. Red clay sample has the highest clay content, corresponding to a high specific surface area.

The preparation procedure of remodeled samples was carried out with reference to the method proposed by GB/T 50123-2019. The dry density of soil samples was 1.72 ± 0.2 g/cm^3 and the designed moister content range was between 16%–41%.

2.2 Test Instrument and Method

2.2.1 Direct Shear Test

According to the test method (Ministry of Housing and Urban-Rural Development of the People's Republic of China, 2019), a strain-controlled direct shear apparatus was employed for conducting direct shear tests. Four vertical loads (i.e., 100, 200, 300, and 400 kPa) were respectively applied on the soil samples and a shear rate of 0.8 mm/min was adopted for a fast direct shear. Meanwhile, direct shear tests were separately performed on soil samples at various water contents to study effects of water content on shear behavior. There were totally 84 samples for four types of soils in the direct shear test, where 24 for WSC samples, 16 for GCS samples, 20 for RC-I samples and 24 for RC-II samples.

2.2.2 X-Ray Diffraction Measurement

The soil samples were dried at 50°C in oven, finely ground and screened through a 200-mesh sieve to obtain powders for mineralogy characterizations. Characterization by XRD was carried out using the random powder method (Sun et al., 2019). The XRD measurement was carried out by D8 FOCUS (Germany, Bruker) with CuKα radiation (λ = 0.15418 nm) at the ambient temperature of 25°C, operating at 30 mA and 40 kV. The

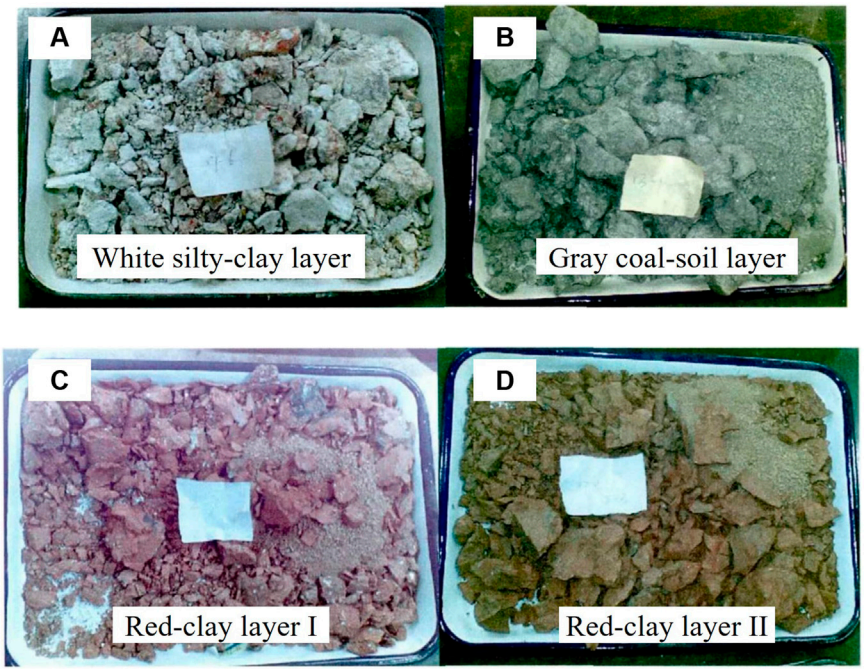

FIGURE 1 | Typical residual soils in Chenzhou area: **(A)** WSC; **(B)** GCS; **(C)** RC-I and **(D)** RC-II.

TABLE 1 | Basic physical properties of typical residual soils.

Number	Sample name	Specific gravity	Water content (%)	Void ratio	Liquid limit (%)	Plastic limit (%)
1	White silty clay	2.69	17.7	0.476	32.3	16.2
2	Gray coal soil	2.72	25.7	0.536	32.9	20.3
3	Red clay I	2.73	20.6	1.098	54.1	19.4
4	Red clay II	2.69	22.4	1.379	49.6	20.2

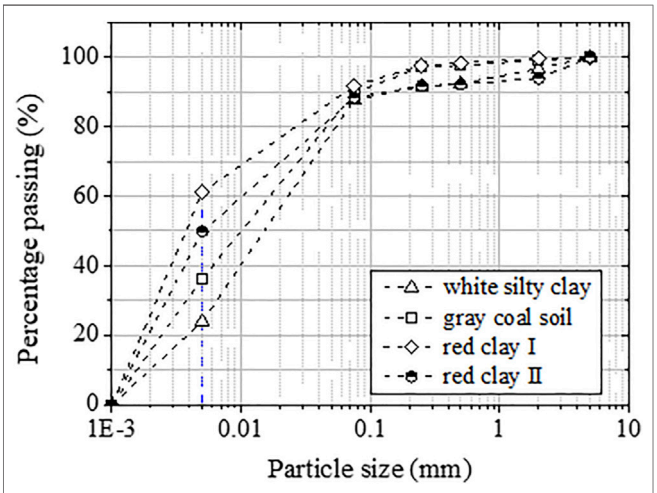

FIGURE 2 | Particle size distribution curves of several residual soils.

measured range was 3°–70° and the 2θ-scanning rate was 2°/min. The JCPDS PDF database was used for the phase identification of the XRD results.

2.2.3 Scanning Electron Microscope Test

To prepare samples of SEM tests, the soil samples were firstly cut into small pieces with dimensions of 10 × 10 × 5 mm (length × width × height) and then rapidly immersed in the previously vacuum-cooled liquid nitrogen. After that, the frozen samples were freeze-dried for 24 h in a vacuumed chamber. SEM tests were performed on the freeze-dried samples using a JSM-6490LV electron microscope scanner.

3 RESULTS AND DISCUSSION

3.1 Shear Property of Residual Soils

Figure 3 shows the changes of shear strength with water content for four soil samples. On the whole, the shear strength of all soil

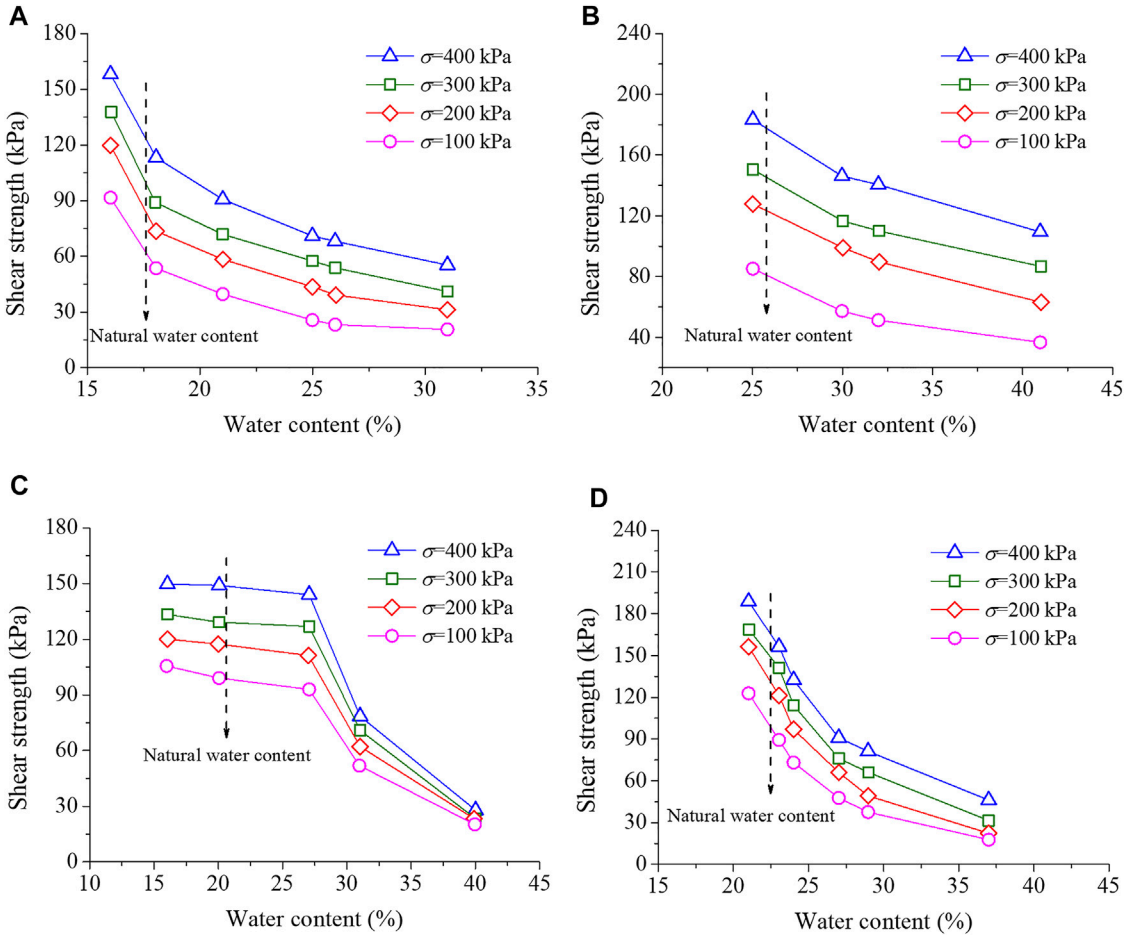

FIGURE 3 | Variations of shear strength with water content for **(A)** WSC samples; **(B)** GCS samples; **(C)** RC-I samples and **(D)** RC-II samples.

samples decreased with increasing water content, but the shear strength for each soil shows different developing trends. For WSC samples, the shear strength firstly decreased quickly with increasing water content and then gradually tended to a stabilization, as shown in **Figure 3A**. At a given water content, the shear strengths of samples increased with the increase of vertical loads. Similar phenomenon was also observed from the curves of gray coal soil (**Figure 3B**). Results in **Figure 3C** demonstrated that the shear strength of RC-I samples slightly reduced as water content increased from 16% to 26%, whereas it obviously decreased with a further increase of water content. Different from RC-I samples, the strength changes for RC-II samples were significant in low water contents, whereas the reducing rate of shear strength became slower in high water contents. According to the natural water contents of several soils, the increases of water content nearby the natural value will cause an obvious reduce of shear strength for WSC, GCS and RC-II samples, excepting for RC-I sample.

Figure 4 presents changes of shear strength with vertical load for soil samples at different water contents. Generally, the relationship between shear strength and vertical load can be described by a linear equation in **Eq. 1**. According to experimental results in **Figure 4**, the fitting curves between shear strength and vertical load could be obtained, and the corresponding parameters ϕ and c are listed in **Table 3**, respectively.

$$\tau_s = \sigma \tan \phi + c \tag{1}$$

where τ_s is the shear strength (kPa) of soil samples; σ is the applied vertical load (kPa) on samples; ϕ is internal friction angle (°) and c is cohesion (kPa). It is noted that for unsaturated soils, the parameters ϕ and c in **Eq. 1** are influenced by the water contents, which is also confirmed from **Table 2**.

Figure 5 shows variations of cohesion c and internal friction angle ϕ with water content, respectively. Results indicated that the c values for WSC, GCS and RC-II samples firstly reduced obviously and then gradually tended to a stable state, but it appeared that the opposite developing trend was observed in RC-I samples. An exponential function (**Eq. 2**) can be tried to describe the relationship between the cohesion and water content, and the corresponding fitting parameters are summarized in **Table 3**. Comparison reveals that this fitting function could give high correlation coefficients (R^2), suggesting a good fitting

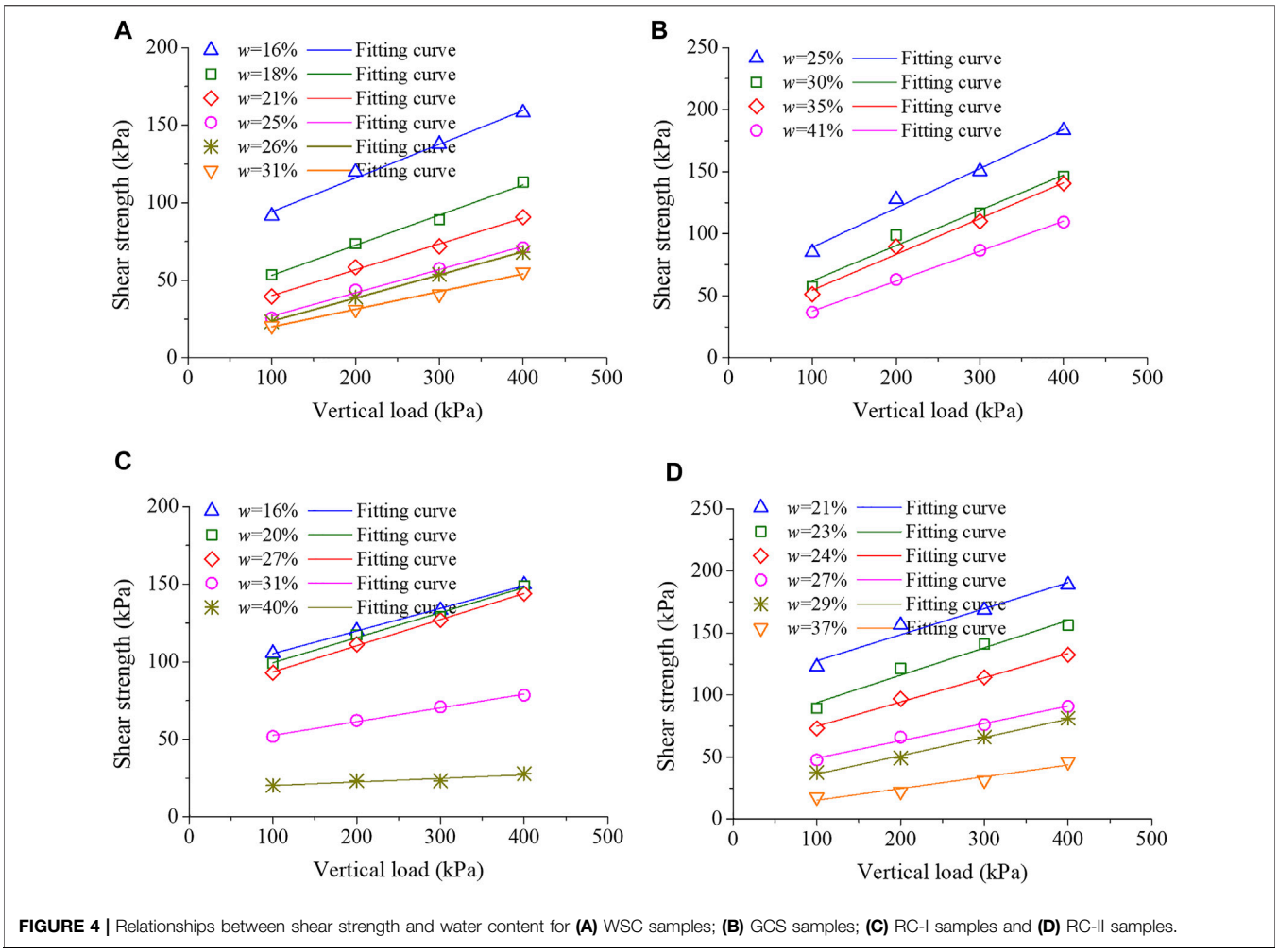

FIGURE 4 | Relationships between shear strength and water content for **(A)** WSC samples; **(B)** GCS samples; **(C)** RC-I samples and **(D)** RC-II samples.

TABLE 2 | Fitting results for relationship between shear strength and vertical load.

Samples	Water content (%)	ϕ	C	R^2	Samples	Water content (%)	ϕ	c	R^2
WSC	16	12.298	72.403	0.986	RC-I	16	8.306	90.710	0.997
	18	10.979	33.786	0.990		20	9.146	83.287	0.987
	21	9.425	23.514	0.994		27	9.592	76.624	0.999
	25	8.531	11.996	0.992		31	5.086	43.693	0.993
	26	8.475	8.707	0.999		40	1.318	17.995	0.824
	31	6.504	8.596	0.989	RC-II	21	11.860	106.600	0.943
GCS	25	17.589	57.42	0.980		23	12.462	71.828	0.956
	30	15.855	33.713	0.963		24	11.034	55.330	0.992
	32	16.066	25.805	0.980		27	7.970	32.279	0.983
	41	13.604	13.585	0.998		29	8.419	21.573	0.993
						37	5.370	5.830	0.918

relationship. Observations from **Figure 5B** showed that the internal friction angle ϕ nearly decreased linearly with the increase of water content. A linear function (**Eq. 3**) was used to represent the relationship between ϕ and water content. Results in **Table 4** implied that this linear equation can well describe the variation of ϕ values with water content, excepting for RC-I samples.

$$c = \alpha e^{\beta w} + \chi \tag{2}$$

$$\phi = aw + b \tag{3}$$

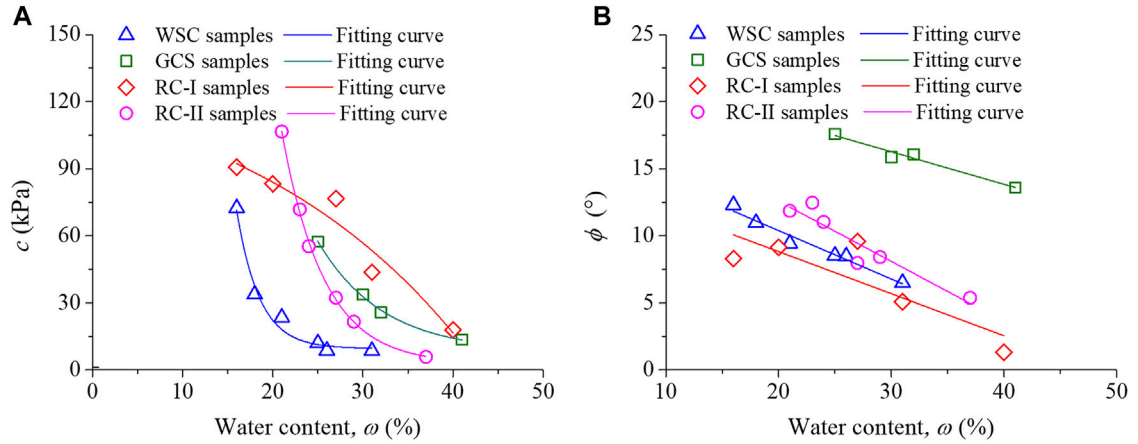

FIGURE 5 | Variations of cohesion c and internal friction angle ϕ with water content for several residual-soil samples.

TABLE 3 | Fitting results for relationship between the cohesion and water content.

Samples	Fitting parameters			R^2
	A	*B*	*X*	
WSC	34945.338	−0.396	9.599	0.972
GCS	1,583.817	−0.139	8.035	0.994
RC-I	-26.089	0.039	140.964	0.888
RC-II	9,309.764	−0.214	2.663	0.998

TABLE 4 | Fitting results for relationship between internal friction angle and water content.

Samples	Fitting parameters		R^2
	A	*B*	
WSC	−0.361	17.619	0.960
GCS	−0.242	23.514	0.951
RC-I	−0.314	15.092	0.625
RC-II	−0.449	21.574	0.866

where α, β, χ, a and b are fitting parameters, respectively; w is water content.

3.2 Mineral Composition and Microstructure of Residual Soils

3.2.1 Mineral Composition Analysis

Figure 6 shows X-ray diffraction results of WSC, GCS and RC-I samples. The mineral contents of soils are summarized in **Table 5**. It can be seen from **Table 5** and **Figure 6** that the white silty clay sample include rich clay minerals, especially pyrophyllite and illite. Similar observations were also found in gray coal soil, corresponding to 36% for pyrophyllite and 27% for illite. Differently, the main mineral compositions of red clay were kaolinite and quartz, as well as low montmorillonite (12%). Moreover, X-ray diffraction spectra implied that the mineral diffraction peaks for WSC and GCS soils were sharp due to a high content of pyrophyllite, while those of RC-I soil were relatively flat.

3.2.2 Microstructural Analysis

The SEM photos of white silty clay, gray coal soil and red clay (RC-I) are illustrated in **Figure 7**. The microstructure of WSC sample was composed of various-sized aggregates (1–30 μm), which were consisted of clay particles. These clay particles exhibited a loose arrangement with identified inter-particle pores and a poor orientation with face-face and face-edge connections, as shown in **Figure 7B**. Meanwhile, these large-size pores (1–10 μm) between clay particles promoted the connection of air or fluid inside soil, thus resulting in a high permeability. Observations from **Figures 7C,D** revealed that the

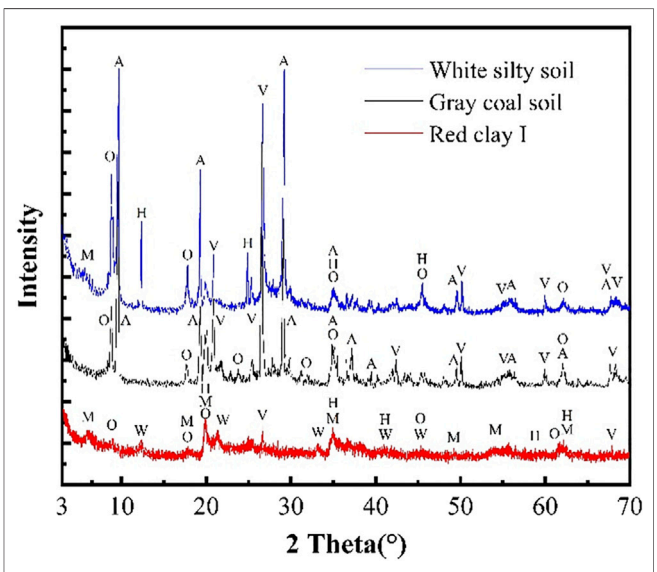

FIGURE 6 | X-ray diffraction spectra of soils in the study area.

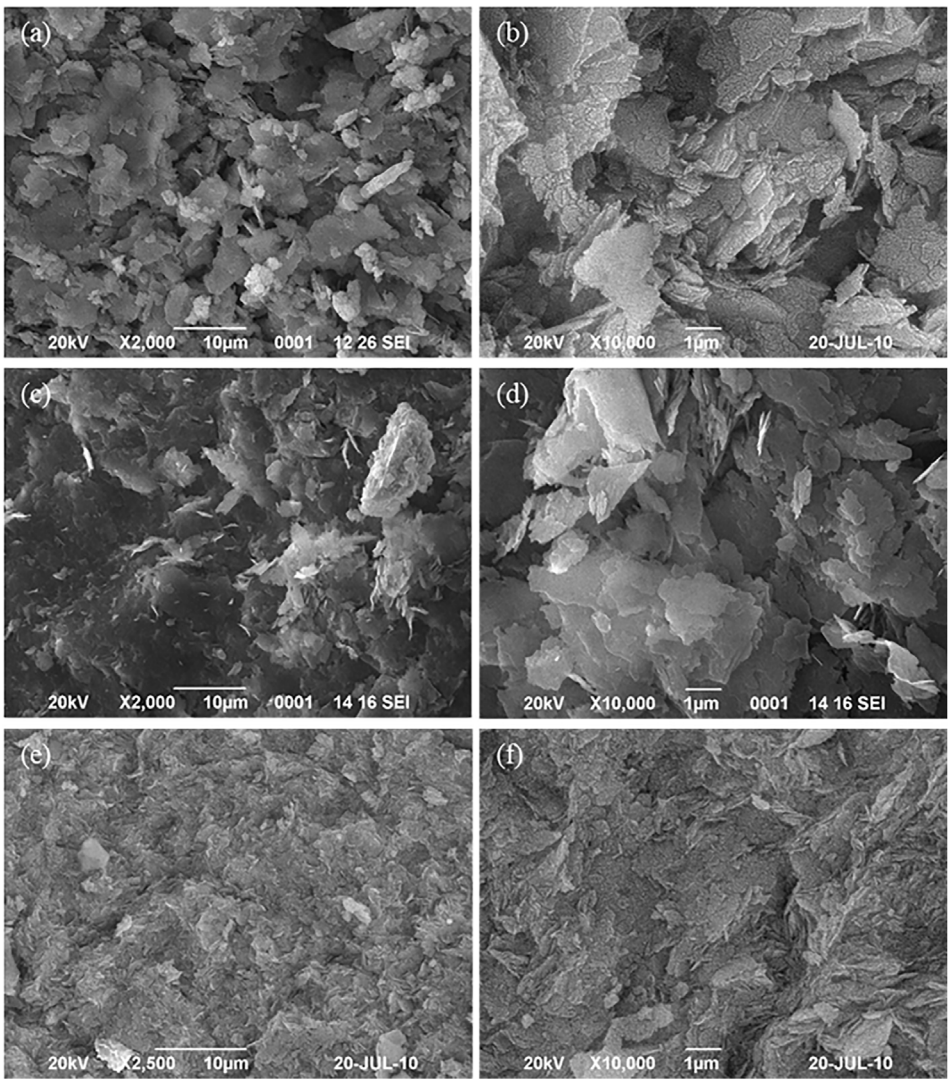

FIGURE 7 | SEM photographs for **(A) (B)** WSC samples; **(C) (D)** GCS samples and **(E) (F)** RC-I samples.

TABLE 5 | Mineral compositions of typical residual soils.

Samples	A	V (%)	O (%)	H	M	W	L	N
WSC	41%	17	20	12%	4%	—	—	Rest
GCS	36%	21	27	—	—	—	—	Rest
RC-I	—	25	7	32%	12%	11%	3%	Rest

A, pyrophyllite; V, quartz; O, illite; H, kaolinite; M, montmorillonite; W, limonite; L, anatase; N, others.

coal-soil structure exhibited a sheet-structure system with an orderly face-face arrangement and a strong orientation between clay particles. Compared with WSC samples, the GCS samples had smaller sized pores and a tighter structure. Thus, the permeability for GCS samples was lower and the anisotropy in mechanical property was more obvious. Similarly, red clay also possessed a face-face structure. The soil particles were arranged in an orderly manner with an obvious orientation. The stratification between particles was discernible, but the boundaries and edges between clay particles could not be clearly identified.

The residual-soil landslide induced by rainfall is substantially due to the reduction in shear strength of the sliding-zone soils. Results in **Figure 3** have demonstrated that the shear strength of soils decreased with increasing water content, indirectly confirming that the rainfall process will cause a decrease in shear strength of slope soils in the field environment. Actually, the reduction of shear strength was actually attributed to microstructural changes inside the soils. Several residual soils studied in this study contained abundant clay minerals, e.g., illite, kaolinite and montmorillonite. During hydration process, these clay minerals would absorb water molecules, generating water films on the surface of clay particles (He et al., 2019; Zhang et al., 2020; He et al., 2022). As the thickness of water films increased,

clay particles separate from each other and the cohesiveness between them gradually reduced. Correspondingly, the clay structure underwent softening and degradation, and the clay minerals transferred from a tightly face-face arrangement to a loosely face-edge or even edge-edge one, leading to a reduction in mechanical strength (Zhang et al., 2016; Lu et al., 2021).

4 CONCLUSION

In this study, the mechanical property of typical residual soils from a landslide zone was investigated by conducting direct shear tests. Meanwhile, mineral composition and microstructures of soil samples were also analyzed through XRD and SEM tests. The obtained results allowed the following conclusions to be drawn:

The shear strength of soils gradually decreased with increasing water content under constant vertical load, but the developing trends of shear strength were influenced by the soil types. At a given water content, the shear strength of all soil samples nearly linearly increased with the increase of vertical loads. The soil cohesion reduced with increasing water content and this change could be well described by an exponential function. Simultaneously, as water content increased, the internal friction angle of soils nearly linearly decreased.

XRD analysis results implied that the main mineral components for white silty clay and gray coal soil were pyrophyllite and illite, corresponding to sharp mineral diffraction peaks. Different from these two samples, red clay had rich kaolinite and montmorillonite and its mineral diffraction peaks were low. SEM observations revealed that white silty clay was consisted of various-sized aggregates. The clay particles inside aggregates exhibited a loose arrangement and a poor orientation. Compared with white silty clay samples, the gray coal soil samples showed an orderly face-face arrangement and a strong orientation between clay particles. In red clay, the soil particles were arranged in an orderly manner, but the boundaries and edges between clay particles could not be clearly identified. The clay minerals inside residual soils absorbed water molecules upon hydration, generating water films on the surface of clay particles. Clay particles separated from each other and gradually transferred from a tightly face-face arrangement to a loosely face-edge or even edge-edge one, resulting in a reduction in the cohesive force between them.

DATA AVAILABILITY STATEMENT

The original contributions presented in the study are included in the article/Supplementary Material, further inquiries can be directed to the corresponding author.

AUTHOR CONTRIBUTIONS

ZZ: Investigation, Writing review and editing YH: Resources, Supervision, Project administration Z-PY: Writing original draft, Methodology BC: Conceptualization, Formal analysis K_NZ: Visualization, Supervision.

FUNDING

The authors thank the National Natural Science Foundation of China (Projects: 42072318 & 41807253) and the Natural Science Foundation of Hunan Province, China (Project 2019JJ50763) for their financial support. The authors also thank the Science and Technology Innovation Program of Hunan Province (Project 2021RC 2004) and the Open Research Fund Program of Key Laboratory of Metallogenic Prediction of Nonferrous Metals and Geological Environment Monitoring (Central South University), Ministry of Education (Project 2021YSJS17).

REFERENCES

Bai, B., Nie, Q., Zhang, Y., Wang, X., and Hu, W. (2021b). Cotransport of Heavy Metals and SiO_2 Particles at Different Temperatures by Seepage. *J. Hydrol.* 597. doi:10.1016/j.jhydrol.2020.125771

Bai, B., Zhou, R., Cai, G. Q., Hu, W., and Yang, G. C. (2021a). Coupled Thermo-Hydro-Mechanical Mechanism in View of the Soil Particle Rearrangement of Granular Thermodynamics. *Comput. Geotech.* 137. doi:10.1016/j.compgeo.2021.104272

De Vita, P., Reichenbach, P., Bathurst, J. C., Borga, M., Crosta, G., Crozier, M., et al. (1998). Rainfall-triggered Landslides: a Reference List. *Environ. Geol.* 35 (2), 219–233. doi:10.1007/s002540050308

Farooq, K., Orense, R., and Towhata, I. (2004). Response of Unsaturated Sandy Soils under Constant Shear Stress Drained Condition. *Soils Found.* 44 (2), 1–13. doi:10.3208/sandf.44.2_1

Fredlund, D. G., Xing, A., Fredlund, M. D., and Barbour, S. L. (1996). The Relationship of the Unsaturated Soil Shear Strength to the Soil-Water Characteristic Curve. *Can. Geotech. J.* 33 (3), 440–448. doi:10.1139/t96-065

He, Y., Hu, G., Wu, D.-Y., Zhu, K.-F., and Zhang, K.-N. (2022). Contaminant Migration and the Retention Behavior of a Laterite–Bentonite Mixture Engineered Barrier in a Landfill. *J. Environ. Manage.* 304, 114338. doi:10.1016/j.jenvman.2021.114338

He, Y., Li, B.-b., Zhang, K.-n., Li, Z., Chen, Y.-g., and Ye, W.-m. (2019). Experimental and Numerical Study on Heavy Metal Contaminant Migration and Retention Behavior of Engineered Barrier in Tailings Pond. *Environ. Pollut.* 252, 1010–1018. doi:10.1016/j.envpol.2019.06.072

He, Y., Wang, M.-m., Wu, D.-y., Zhang, K.-n., Chen, Y.-g., and Ye, W.-m. (2021). Effects of Chemical Solutions on the Hydromechanical Behavior of a Laterite/bentonite Mixture Used as an Engineered Barrier. *Bull. Eng. Geol. Environ.* 80 (2), 1169–1180. doi:10.1007/s10064-020-02003-6

He, Y., Ye, W.-m., Chen, Y.-g., Zhang, K.-n., and Wu, D.-y. (2020). Effects of NaCl Solution on the Swelling and Shrinkage Behavior of Compacted Bentonite under One-Dimensional Conditions. *Bull. Eng. Geol. Environ.* 79 (1), 399–410. doi:10.1007/s10064-019-01568-1

Khan, M. S., Hossain, S., Ahmed, A., and Faysal, M. (2017). Investigation of a Shallow Slope Failure on Expansive Clay in Texas. *Eng. Geol.* 219, 118–129. doi:10.1016/j.enggeo.2016.10.004

Lu, N. (2016). Generalized Soil Water Retention Equation for Adsorption and Capillarity. *J. Geotech. Geoenviron. Eng.* 142 (10), 04016051. doi:10.1061/(asce)gt.1943-5606.0001524

Lu, P.-H., He, Y., Zhang, Z., and Ye, W.-M. (2021). Predicting Chemical Influence on Soil Water Retention Curves With Models Established Based on Pore

Structure Evolution of Compacted Clay. *Comput. Geotech.* 138, 104360. doi:10.1016/j.compgeo.2021.104360

Ma, L.-M., and Tan, Z.-M. (2009). Improving the Behavior of the Cumulus Parameterization for Tropical Cyclone Prediction: Convection Trigger. *Atmos. Res.* 92 (2), 190–211. doi:10.1016/j.atmosres.2008.09.022

Ministry of Housing and Urban-Rural Development of the People's Republic of China (2019). *Standard for Geotechnical Testing Method. GB / T 50123-2019*. Beijing: China Architecture & Building Press.

Miščević, P., and VlastUelica, G. (2014). Impact of Weathering on Slope Stability in Soft Rock Mass. *J. Rock Mech. Geotech.* 6 (3), 240–250. doi:10.1016/j.jrmge.2014.03.006

Mitchell, J. K., and Soga, K. (2005). *Fundamentals of Soil Behavior*. New York: John Wiley & Sons.

Orense, R., Farooq, K., and Towhata, I. (2004). Deformation Behavior of Sandy Slopes during Rainwater Infiltration. *Soils Found.* 44 (2), 15–30. doi:10.3208/sandf.44.2_15

Patuti, I. M., Rifa'i, A., and Suryolelono, K. B. (2017). Mechanism and Characteristics of the Landslides in Bone Bolango Regency, Gorontalo Province, Indonesia. *Int. J. GEOMATE* 12 (29), 1–8. doi:10.21660/2017.29.79901

Sun, Z., Chen, Y.-g., Cui, Y.-j., Ye, W.-m., and Chen, B. (2019). Effect of Synthetic Beishan Site Water and Cement Solutions on the Mineralogy and Microstructure of Compacted Gaomiaozi(GMZ) Bentonite. *Soils Found.* 59 (6), 2056–2069. doi:10.1016/j.sandf.2019.11.006

Wen, M., Chen, A. Q., and Dong, R. (2019). Analysis of the Mechanism of Rain-Induced Slow-Inclination Red Bed Rock Landslide. *Eng. Constr. Des.* 402 (04), 68–70. (In Chinese). doi:10.13616/j.cnki.gcjsysj.2019.02.231

Xiao, T., Yu, L. B., Tian, W. M., Zhou, C., and Wang, L. Q. (2021). Reducing Local Correlations Among Causal Factor Classifications as a Strategy to Improve Landslide Susceptibility Mapping. *Front. Earth Sci.* 9, 997. doi:10.3389/feart.2021.781674

Yin, Y., Wang, L., Huang, B., Zhang, Z., and Dai, Z. (2022). Evolution Analysis of the Banbiyan Dangerous Rock Mass in the Three Gorges Reservoir Area, China. *Georisk Assess. Manag. Risk Eng. Syst. Geohazards* 81 (3), 1–11. doi:10.1080/17499518.2022.2062776

Zhang, C., Li, J. Z., and He, Y. (2021). Impact of the Loading Rate on the Unsaturated Mechanical Behavior of Compacted Red Clay Used as an Engineered Barrier. *Environ. Earth Sci.* 80 (4), 1–12. doi:10.1007/s12665-021-09436-6

Zhang, S., Xu, Q., and Hu, Z. (2016). Effects of Rainwater Softening on Red Mudstone of Deep-Seated Landslide, Southwest China. *Eng. Geol.* 204, 1–13. doi:10.1016/j.enggeo.2016.01.013

Zhang, Z., Ye, W.-M., Liu, Z.-R., Wang, Q., and Cui, Y.-J. (2020). Mechanical Behavior of GMZ Bentonite Pellet Mixtures over a Wide Suction Range. *Eng. Geol.* 264, 105383. doi:10.1016/j.enggeo.2019.105383

Zhu, J. D., Yan, H., Li, S. H., and Wu, L. Z. (2019). Laboratory Model Experiment of Landslides along Loess Mudstone Interface Induced by Rainfall Patterns. *J. Eng. Geo.* 27 (03), 623–631. (In Chinese). doi:10.13544/j.cnki.jeg.2018-139

Conflict of Interest: The authors declare that the research was conducted in the absence of any commercial or financial relationships that could be construed as a potential conflict of interest.

Publisher's Note: All claims expressed in this article are solely those of the authors and do not necessarily represent those of their affiliated organizations, or those of the publisher, the editors and the reviewers. Any product that may be evaluated in this article, or claim that may be made by its manufacturer, is not guaranteed or endorsed by the publisher.

frontiers | Frontiers in Earth Science

ORIGINAL RESEARCH
published: 20 June 2022
doi: 10.3389/feart.2022.887102

Influence of Debris-Flow Impact on the Structural Stability of Check Dams

Song Eu[1] *and Sangjun Im*[2]*

[1]Division of Forest Fire and Landslide, Department of Forest Environment and Conservation, National Institute of Forest Science, Seoul, South Korea, [2]Department of Agriculture, Forestry and Bioresources, Research Institute of Agriculture and Life Sciences, Seoul National University, Seoul, South Korea

Small check dams are widely used in the Republic of Korea to mitigate and prevent sediment-driven damages by mountain torrents. This study aimed to quantify the combined effects of debris-flow impact forces and earth pressures from dam sedimentations on the structural stability of a dam by incorporating the change in the longitudinal profile of the channel bed owing to sediment deposition. A debris-flow simulation model (Hyper Kanako) was used to reproduce the debris-flow behavior from the 2011 Mt. Umyeon landslide (Seoul, The Republic of Korea). Finite element analysis was conducted to analyze the structural stability of the check dam under various debris discharge and sedimentation scenarios. The magnitudes of impact forces that were exerted on the check dam ranged from 81.76 kPa under a non-deposition scenario to 123.04 kPa under a 100% deposition scenario. The resultant tensile and compressive stresses were found to be up to 0.80 and 0.35 MPa, respectively, which were lower than the maximum allowable strengths of the dam, securing sufficient strength for the dam stability. Overall, the proposed approach can be applied to obtain a better understanding of the resultant internal stresses experienced during debris flow and sediment deposition, thereby providing valuable information for the structural analysis and safety assessment of check dams.

Keywords: check dam, debris-flow impact force, structural stability, sediment deposition, finite element method

OPEN ACCESS

Edited by:
Eric Josef Ribeiro Parteli, University of Duisburg-Essen, Germany

Reviewed by:
Carlo Gregoretti, University of Padua, Italy
Yutaka Gonda, Niigata University, Japan

***Correspondence:**
Sangjun Im
junie@snu.ac.kr

Specialty section:
This article was submitted to Geohazards and Georisks, a section of the journal Frontiers in Earth Science

Received: *01 March 2022*
Accepted: *17 May 2022*
Published: *20 June 2022*

Citation:
Eu S and Im S (2022) Influence of Debris-Flow Impact on the Structural Stability of Check Dams. Front. Earth Sci. 10:887102. doi: 10.3389/feart.2022.887102

1 INTRODUCTION

Debris flows, which are fast-flowing and sediment-laden flows, represent a severe geological hazard that occur in mountain streams worldwide. In the Republic of Korea, sediment-related disasters can occasionally occur in high-gradient mountain streams, which cause catastrophic consequences and thereby, threatening people living in downstream regions (Chae et al., 2017). Sediment-related hazards can usually be managed by the establishment of sediment-retaining structures in the upper or intermediate reaches of the stream of interest. In terms of torrent control structures, check dams are basic transversal structures that effectively control the sediment and debris discharges of mountain torrents over long periods of time (Hübl and Fiebiger, 2005; Marchelli and De Biagi, 2019). Dams perform an additional function of stabilizing a channel by trapping coarse sediment particles and weakening the longitudinal gradient of streams (Seo et al., 2016; Bernard et al., 2019).

Check dams require special consideration from the perspective of structural stability to be implemented successfully in steep terrains. According to previous studies of geomorphic changes around check dams (Victoriano et al., 2018; Cucchiaro et al., 2019a; Cucchiaro et al., 2019b), inadequate design of check dams can accelerate stream erosion, especially around the foundations

and wings of the dams, and can result in long-term instability of debris flow barrier structures. Thus, forest engineers or professionals should consider sliding and overturning failure modes in the stability assessment of check dams (Hübl et al., 2009).

Additionally, a certain level of safety in check dams is necessitated in their response to the external forces exerted by the direct impact of debris flows. However, check dams often experience structural failure or damage as a result of fast debris flows accompanied by large stones, as highlighted by Baggio and D'agostino (2022). Therefore, check dams must be designed to endure high impact forces from debris flows (Chen et al., 2019).

Engineering concerns regarding the impact of debris flows on structural design of check dams have increasingly attracted the attention of researchers over recent decades (Hungr et al., 1984; Hübl and Holzinger, 2003; Chen et al., 2019). Many studies have been conducted to elucidate the dynamic interaction between debris flows and check dams, including flow dynamics and corresponding impact-force studies using real-time observations (Hu et al., 2011) or flume experiments (Hübl and Holzinger, 2003; Scheidl et al., 2013; Rossi and Armanini, 2019; Sanvitale et al., 2021).

Some countries, such as Japan, Austria, and Hong Kong, have formulated technical guidelines on considering the impact force of debris flows in engineering design. Austria has established a simple design method (ONR 24801 and 24802) that accounts for the impact force, which is empirically derived from the debris-flow velocity and its density (Huebl et al., 2017). Japan (NILIM, 2016a) considered both overflow and non-overflow conditions in dam designing and proposed check criteria for the potential of sliding failure due to internal and external forces, which are exerted by hydrostatic pressure, earth pressure, and debris-flow impact force. Similarly, Hong Kong (Kwan, 2012) evaluated structural stability against sliding, overturning, and distress failure. Hong Kong regulations imply that the lateral earth pressure, derived from sediment deposition, is regarded as an additional external force in the stability analysis. However, the influence of debris flows on dam stability in the Republic of Korea is poorly understood.

Japan (NILIM, 2016a) and Austria (Huebl et al., 2017) have used empirical approaches to reflect the influence of debris flows, which provide efficient solutions for robust check-dam designs. Hong Kong (Kwan, 2012) used numerical models to simulate flow behavior and quantified impact forces based on the simulated flow characteristics. The maximum stress, driven by debris-flow impact, represents an essential variable for dam stability. Notably, the maximum stress varies because the location of debris collisions can change with ongoing sediment deposition. Moreover, changing spatiotemporal patterns of sedimentation hamper the accurate estimation of the location and magnitude of the maximum stress, which are often induced by debris flows over the lifespan of the dam.

Various numerical approaches have been applied previously to examine the structural behavior of debris-flow barriers under different external forces (Bernard et al., 2019; Chen et al., 2019; Song et al., 2019; Wendeler et al., 2019; Leonardi and Pirulli, 2020; Brighenti et al., 2021). Recently, finite element analysis has been applied to estimate changes in sediment discharge and deposition near check dams by examining debris-flow behavior (Law et al., 2016; Shen et al., 2020). Chen et al. (2019) conducted a study on dam stability by analyzing the collapse of a dam, given that the structural displacement was caused by a debris flow. However, their analysis did not examine the stability of individual dams and only focused on determining the most suitable location and number of dams. Bernard et al. (2019) used hydraulic analysis to quantify the influence of debris-flow discharge and its corresponding impact force on an open-type check dam. They analyzed the debris-flow impact force on the fins of a check dam, but the structural behavior of the check dam was rarely discussed in terms of variable debris-flow discharges.

Meanwhile, closed-type check dams are characterized by a higher risk of damage when subjected to unplanned external forces compared to open-type structures; such forces are inflicted by debris-flow impact and sedimentation (Mizuyama, 1979). Owing to this, an accurate design of check dams requires a precise investigation of the distribution and magnitude of potential internal stresses in the context of debris-flow behavior and sediment deposition conditions.

This study examined the structural stability of check dams, subjected to external forces that were induced by debris flows and lateral earth pressure from sediment deposition. To this end, a debris-flow simulation model (Hyper Kanako) was used to reproduce the debris-flow behavior in the 2011 Mt. Umyeon landslide (Seoul, The Republic of Korea). To pursue the main aim of the study, we 1) incorporated the impact force, derived from the hydraulic characteristics of the simulated debris flow, and 2) analyzed the dam stability using different sedimentation scenarios.

2 MATERIALS AND METHODS

2.1 Study Site

Before assessing the stability of the check dam, we simulated the debris flow in the Hyoungchon watershed of Mt. Umyeon (Seoul, the Republic of Korea), as shown in **Figure 1**. The area of the analyzed watershed was 34.1 ha, while the main channel was approximately 663 m long with an inclination of 13.6° of the mean longitudinal slope (SMG, 2012). A fatal debris-flow event occurred on 27 July 2011, in Mt. Umyeon and its surrounding areas, resulting in 17 fatalities and causing extensive damage, including mud flooding and the collapse of houses.

A field investigation shortly after this 2011 event revealed that the debris flow in the watershed was a runoff-generated debris flow, the type of which was reported by Imaizumi et al. (2006) and Coe et al. (2008). It was initiated by surface runoff, which caused the erosion of soil materials on a steep slope at the uppermost part of the channel (SMG, 2012). The eroded soil mixtures were transported down steep channels and entrained sediments in the channel bed. The initiation process is similar to that of runoff-generated debris flow reported by Simoni et al. (2020). Approximately 3,800 m^3 of sediment was discharged from eroded slopes in the source area and several tributary branches. After the debris-flow disaster, various

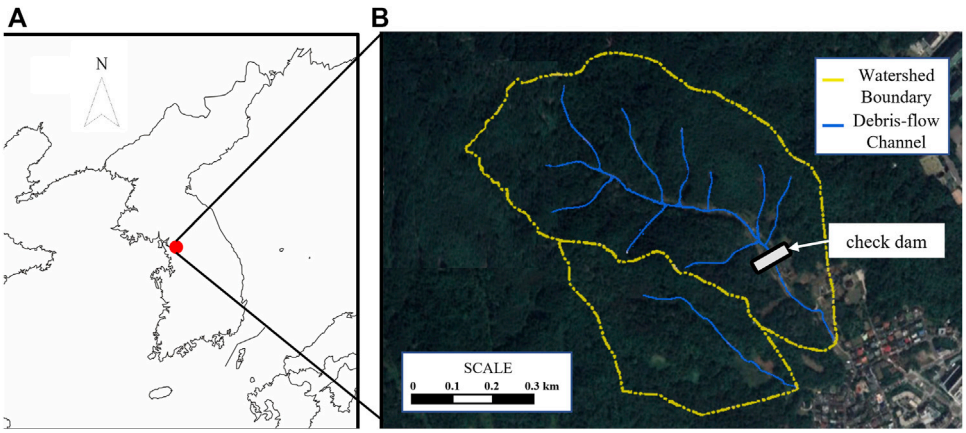

FIGURE 1 | (A) Location of the Hyoungchon watershed. **(B)** Boundary (yellow line) and debris flow channel (blue line) network of the watershed. The gray block in the downstream region is the check dam analyzed in this study.

countermeasures, including a series of check dams, were implemented to protect steep streams and unstable hillslopes from subsequent rainfall.

2.2 Debris-Flow Simulation

2.2.1 Debris-Flow Simulator

An accurate debris-flow simulation is essential for quantifying debris-flow behavior and for assessing its influence on structural stability with countermeasures designed in areas prone to sediment-related disasters. The debris-flow event in the Hyoungchon watershed in 2011 was quantitatively reproduced using a debris-flow simulation model. Although various models have been developed, Hyper Kanako (Horiuchi et al., 2012) was utilized in this study to simulate the debris-flow behavior. Kanako, initially developed in Japan, is a physical-based one-dimensional computational model that evaluates the influence of engineering structures on debris-flow propagation with a graphical user interface (GUI) (Nakatani et al., 2008). The updated release of Kanako, Hyper Kanako, embeds an integrated system with one- and two-dimensional (2-D) models to simulate debris flows with a GUI in a geographic information system (Uchida et al., 2013).

Kanako simulates debris-flow propagation in a channel and deposition forming an alluvial fan by using the mass and momentum conservation and entrainment rates. Notably, Kanako is advantageous because it can simulate the flow characteristics of a debris flow, which are affected by the installation of check dams (Nakatani et al., 2008; Nakatani, 2010). The model is fundamentally based on the following governing equations: the continuity equation (see **Eq. 1**), the mass conservation equation of sediment concentration (**Eq. 2**), the momentum conservation equation in the x-(**Eq. 3**) and y-directions (**Eq. 4**), and the entrainment sub-model (**Eq. 5**). The expressions for each equation in the 2-D simulations are shown below:

$$\frac{\partial h}{\partial t} + \frac{\partial uh}{\partial x} + \frac{\partial vh}{\partial y} = i \tag{1}$$

$$\frac{\partial Ch}{\partial t} + \frac{\partial Cuh}{\partial x} + \frac{\partial Cvh}{\partial y} = iC_* \tag{2}$$

$$\frac{\partial u}{\partial t} + u\frac{\partial u}{\partial x} + v\frac{\partial u}{\partial y} = -g\frac{\partial H}{\partial x} - \frac{\tau_x}{\rho h} \tag{3}$$

$$\frac{\partial v}{\partial t} + u\frac{\partial v}{\partial x} + v\frac{\partial v}{\partial y} = -g\frac{\partial H}{\partial x} - \frac{\tau_y}{\rho h} \tag{4}$$

$$i = \frac{\partial z}{\partial t} = \begin{cases} \delta_d \dfrac{C_\infty - C}{C_*}\sqrt{u^2+v^2} & (i<0,\ deposition) \\ \delta_e \dfrac{C_\infty - C}{C_* - C_\infty}\sqrt{u^2+v^2} & (i\geq 0,\ erosion) \end{cases} \tag{5}$$

where h is the flow depth, z is the height of the channel bed, H is the flow elevation ($h + z$), C is the volumetric sediment concentration, t is time, g is the gravitational acceleration, and ρ is the density of the interstitial fluids comprising the debris flow. u is the flow velocity in the flow direction, denoted as x, and v is the flow velocity in the lateral direction, represented by y.

The component i in **Eq. 5** reflects the entrainment rate, proposed by Takahashi and Nakagawa (1991). They assumed that the entrainment of debris flows was mainly governed by sediment concentration and mobility, and the empirical formula for the entrainment was derived through a flume experiment; δ_d and δ_e are empirically derived coefficients of deposition and erosion, respectively.

C_* is the sediment concentration in the movable bed layer, and C_∞ is the equilibrium sediment concentration of the debris flow on the current channel slope, determined by **Eq. 6**:

$$C_\infty = \frac{\rho \tan\theta}{(\sigma - \rho)(\tan\phi - \tan\theta)} \tag{6}$$

where ϕ is the internal friction angle, and the range of C_∞ is $0.3 \leq C_\infty \leq 0.9C_*$.

The rheological terms, τ_x and τ_y, reflect the shear stress that acts on the channel bed in the respective direction based on the dilatant model, introduced by Takahashi and Nakagawa (1991). The dilatant model, commonly used for stony debris flows where

TABLE 1 | Summary of parameters and values used in Hyper Kanako.

Input parameter [unit]	Value
Number of nodes along the channel	42
Spacing between nodes along the channel [m]	14.74
Simulation time [s]	1,200
Calculation time interval [s]	0.1
Mean debris particle diameter [m]	0.2
Particle density of channel bed sediments [kg m^{-3}]	2,665
Density of interstitial fluids [kg m^{-3}]	1,260
Internal friction angle [°]	29.2
Sediment volumetric concentration of channel bed (C*)	0.600
Erosion rate constant	0.0007
Deposition rate constant	0.05

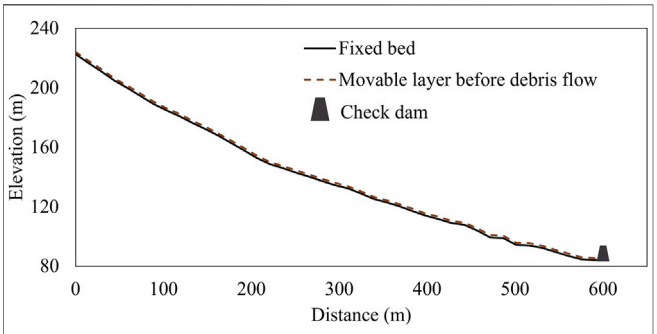

FIGURE 2 | Schematic design of the debris flow channel. The black solid line is the fixed channel bed, and the brown dashed line is the erodible layer. The location of the check dam is represented as a black trapezoid.

shear stress is dominated by the inertial grain stress (Takahashi, 2014), stipulates that the dissipation of kinetic energy, expressed as the shear stress, is dramatically increased due to particle collision in the debris flow when its velocity increases. Takahashi et al. (1992) conducted field investigations alongside flume experiments and introduced a 2-D rheological model with the coefficient K_d, dependent on the grain size and sediment concentration, as indicated by **Eqs 7**, **8**:

$$\tau_x = \frac{\rho d^2}{8\left\{C + (1-C)\frac{\rho}{\sigma}\right\}\left\{\left(\frac{C_*}{C}\right)^{\frac{1}{3}} - 1\right\}^2} \frac{u\sqrt{u^2+v^2}}{h^2} \tag{7}$$

$$\tau_y = \frac{\rho d^2}{8\left\{C + (1-C)\frac{\rho}{\sigma}\right\}\left\{\left(\frac{C_*}{C}\right)^{\frac{1}{3}} - 1\right\}^2} \frac{v\sqrt{u^2+v^2}}{h^2} \tag{8}$$

2.2.2 Model Parameters

Model parameters that describe debris-flow behavior should be adjusted to reconstruct the given debris-flow phenomenon. In this study, parameters were determined by referring to the geological and soil characteristics, such as density, internal friction angle, and mean coarse particle diameter, retrieved from the field investigation at the time of the debris-flow incident (SMG, 2014). As the values of the erosion and deposition coefficients were not obtained directly from the field investigation, we used estimates from previous studies. The parameters used in Hyper Kanako execution are listed in **Table 1**.

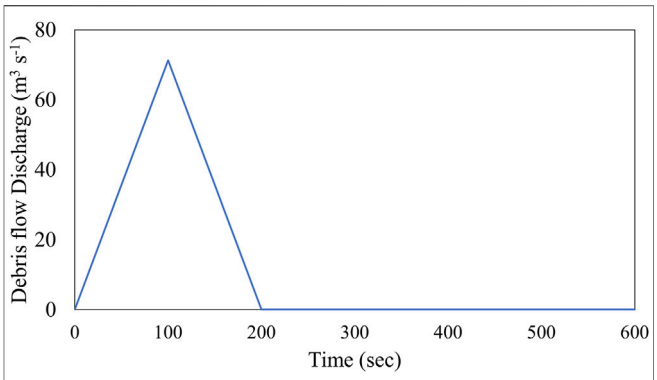

FIGURE 3 | Hydrograph of simulated debris flow discharge.

2.2.3 Channel Geometry

One of the important datasets for debris-flow simulation is the topographic features of channels. However, due to the lack of topographic data prior to the 2011 debris-flow event, the channel geometry of the Hyoungchon watershed was derived from the 10 m × 10 m digital elevation model (DEM) extracted from the 2009 National Digital Topographic Map of the National Geographic Information Institute (NGII, 2019). The National Topographic Map was generated by combining aerial photographs and ground survey data, and had a 1:5000 scale (NGII, 2019). The geometry of the channel used in this study is shown in **Figure 2**. Meanwhile, Hyper Kanako assumes a uniform channel with a rectangular cross-section in a given portion of stream. The debris-flow channel width was set to 10 m according to the average width of the field investigation results (SMG, 2014). As the erodible layer depth had a broad range of 0.5–2.0 m according to field measurements, an average value of 1.5 m was applied to all sections for the simulation.

2.2.4 Input Hydrograph

The empirical formulae, expressed in **Eqs 9**–**11** (NILIM, 2016b), derived from the initial volume of discharged sediment were utilized to generate the input hydrograph of the debris flow, as shown below:

$$\sum Q = \frac{V_{dpq} \cdot C_*}{C_d} \tag{9}$$

$$Q_{sp} = 0.01 \cdot \sum Q \tag{10}$$

$$C_d = \frac{\rho \cdot \tan\theta_0}{(\sigma - \rho)(\tan\Phi - \tan\theta_0)} \tag{11}$$

where Q is the total discharged amount of debris flow (m^3), V_{dpq} is the initial volume (m^3), C_* is the volumetric sediment concentration of the channel bed, and Q_{sp} is the maximum discharge rate of the debris flow (m^3 s^{-1}). C_d, the volumetric sediment concentration of debris flow on the mean channel slope

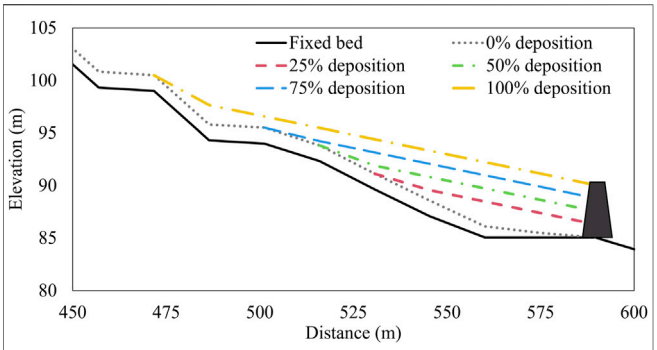

FIGURE 4 | Changes in the gradient of the upstream reaches of the dam according to the deposit scenario. The location of the check dam is represented as a black trapezoid.

(θ_0), was proposed by Takahashi and Nakagawa (1991), with the range of $0.3 \leq C_d \leq 0.9C_*$. Here, θ_0 is the mean slope of the channel that is calculated on the portion of the channel from the dam location to 200 m upstream (NILIM, 2016b), and specified as 8.39°. ρ is the density of the interstitial fluid of the debris flow (kg m^{-3}), σ is the particle density of the debris in the debris flow (kg m^{-3}), and ϕ is the internal friction angle.

Figure 3 shows how the hydrograph was set, representing a C_d of 0.32, Q of 7,127.49 m^3, and Q_{sp} of 71.27 m^3 s^{-1}, with a duration of 200 s. These estimates were based on the initial volume of the debris flow (3,800 m^3), approximated at the contributing source area in the Hyoungchon watershed.

2.3 Estimation of Debris-Flow Impact Force

The external force exerted by a debris flow is generally considered as a temporally variable dynamic load. Note that the time-dependent interaction between debris flow and structure is a significant concern in stability analysis. Specifically, some studies on a single debris-flow surge (Scheidl et al., 2013; Lee et al., 2019; Wang et al., 2020) have reported that the impact force was substantially triggered by the collision of the first flow surge. Subsequently, the preceding surge of debris flow was sequentially deposited along the upstream reach of a dam, which acted as a buffering barrier against the following sediment flow (Shen et al., 2018; Ng et al., 2021). These results indicated that the maximum impact force exerted by the debris-flow surge seemingly represents the most important trigger for dam stability.

Various estimation methods have been used to quantify debris-flow impact force (Hungr et al., 1984; Armanini, 1997; Hübl and Holzinger, 2003; Scheidl et al., 2013). In this study, the empirical model, developed by Hübl and Holzinger (2003), was applied to quantify the debris-flow impact force (**Eq. 12**). This model reflects the hydrodynamic behavior of debris flows (Proske et al., 2011; Scheidl et al., 2013; Koo et al., 2017) and, most importantly, it can be applied to a wide range of Froude number conditions (Hübl et al., 2009; Suda et al., 2009), thereby reflecting variations in the empirical coefficient in the model according to Froude numbers (Proske et al., 2011; Scheidl et al., 2013). The maximum debris-flow impact force was estimated from the

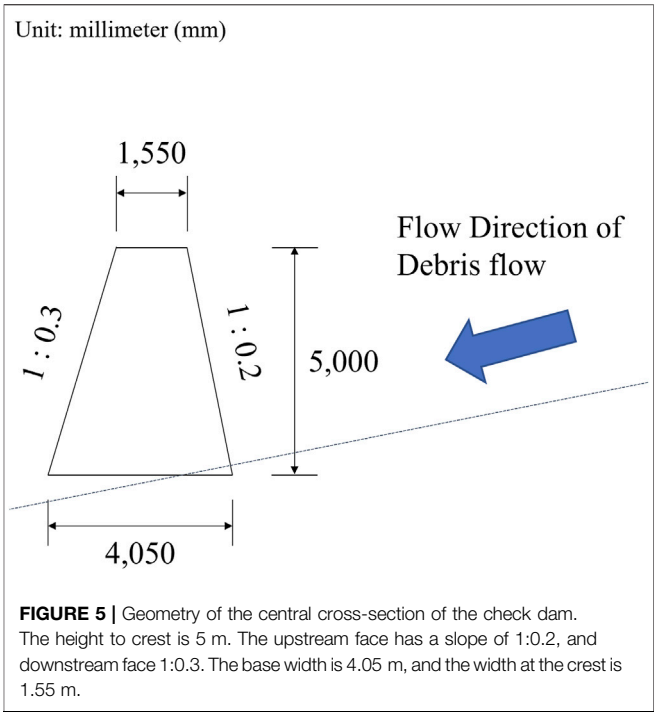

FIGURE 5 | Geometry of the central cross-section of the check dam. The height to crest is 5 m. The upstream face has a slope of 1:0.2, and downstream face 1:0.3. The base width is 4.05 m, and the width at the crest is 1.55 m.

maximum velocity and depth of the debris flow approaching the check dam using **Eq. 12**:

$$P_{max} = 4.5\rho_m u^{0.8} (gh)^{0.6} \quad (12)$$

where P_{max} is the maximum impact force (kN m^{-2}), ρ_m is the density of the debris-flow mixture (kg m^{-3}), u is the debris-flow velocity in the flow direction (m s^{-1}), g is the gravitational acceleration (9.807 m s^{-2}), and h is the flow depth (m). To calculate the impact force on the check dam, ρ_m, u, and h are taken at the position of the check dam where the impact force reaches the maximum value.

2.4 External Load Scenarios With Sedimentation

As sediment particles are continuously deposited in the upstream reaches of check dams over a long period, the stress distribution applied on a check dam varies with sediment deposition. In this study, five sedimentation scenarios were introduced, ranging from the no-deposit condition immediately after dam construction to the entire-deposit condition. In other words, this study considered heights of sediment deposits of 0%, 25%, 50%, 75%, and 100% in relation to the dam height. Sediment deposition in the upstream reach causes a change in the longitudinal profile of streams, thereby modifying the flow characteristics, such as flow velocity. Seo et al. (2016) indicated that the channel bed slope became gentle at one-half to two-thirds of the mean channel slope gradient (in percent) due to the sediment storage effect of the check dam. Given this concept, we assumed that the channel bed slope decreased to half of the mean channel bed slope in the 200 m section upstream

TABLE 2 | Summary of parameters and values used in COMSOL Multiphysics.

Parameter [unit]	Value
Density [kg m^{-3}]	2,350
Modulus of elasticity [GPa]	25
Poisson's ratio	0.2
Compressive strength [MPa]	21
Tensile strength [MPa]	2.89

of the dam (**Figure 4**). Consequently, the debris-flow impact force was quantified by considering the mitigated channel bed slope for each deposit scenario.

2.5 Structural Stability Analysis

A finite element analysis was applied to examine the structural stability of the Hyoungchon watershed check dam against simulated debris flows, where the sediment deposition and debris-flow impact force were considered. The check dam stability was estimated using a 2-D plane for the central cross-section under a prismatic debris-flow impact force. The geometry of the central cross-section of the check dam is shown in **Figure 5**.

Two-dimensional finite element analysis was performed using the COMSOL Multiphysics 5.3 software (COMSOL AB, 2017). COMSOL is a finite element solver, which is widely used in single and multi-physics simulations. We further utilized the Structure Mechanics Module in COMSOL to perform a principal stress analysis. In this way, the tensile and compressive stresses were quantified using the linear elastic model.

Furthermore, the structural stability was scrutinized by comparing the estimated tensile and compressive stresses with the allowable strengths of the check dam. The allowable strength (21 MPa, **Table 2**) of the concrete material (KMLIT, 2012) was applied as the compressive strength. As the analyzed dam is a plain concrete structure without rebars, the tensile strength induced by debris-flow impact force should be considered in stability analysis. The tensile strength of the check dam was estimated to be 2.89 MPa (**Table 2**) by considering the relationship between the compressive strength and the tensile strength ($f_t = 0.63\sqrt{f_{ck}}$, where f_t is the tensile strength and f_{ck} is the compressive strength) from KMLIT (2012). Moreover, the common properties of concrete materials were applied by referring to KFS (2014) for assigning the physical properties of density, modulus of elasticity, and Poisson's ratio.

We compared the allowable strengths and maximum stresses acting on check dams through structural analysis. The uncertainty in the load estimation was considered by multiplying the respective factors of predefined loads. The load factors of 1.2 and 1.6 were utilized for the dead and live loads, respectively. The hydrostatic pressure, sediment earth pressure, and debris-flow impact force were regarded as live loads (KMLIT 2012).

Generally, concrete structures, including check dams, suffer from time-dependent degradation of their mechanical properties. However, it is difficult to define the age degradation rate of strength induced by various environmental conditions. Therefore, this study simply considered structural stability with the strength reduction set at 0%, 25%, and 50% to ensure the long-term stability of the structure.

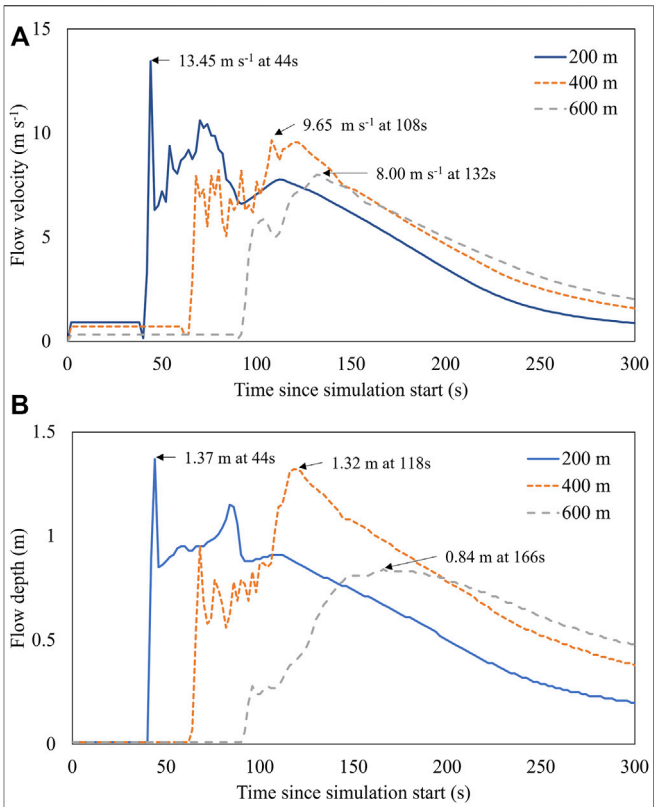

FIGURE 6 | Time-series profiles of flow velocity **(A)** and depth **(B)** at 200 m (blue solid line), 400 m (orange dotted line), and 600 m (gray dashed line) from the source area.

3 RESULTS

3.1 Simulation of Debris Flow and Impact Force

Figure 6 shows the overall profiles of simulated flow velocity and depth at 200, 400, and 600 m. Simulations revealed a maximum flow velocity of 14.15 m s^{-1} that occurred 177 m from the source area after 42 s of flow. The maximum flow depth of 1.81 m was found to be 236 m from the source area at 46 s of runtime. On the channel reaching 200 m downstream from the source area, where the channel slope dramatically changed (from 33% to 16%), the flow velocity decreased, and sediment deposition occurred owing to the gentle slope (**Figure 7A**). The design input for the sediment discharge exhibited a peak discharge of 71.27 m^3 s^{-1}, resulting in the highest flow 400 m downstream from the source area, with a velocity of 9.72 m s^{-1} and depth of 1.32 m. It was found that, after the peak flow passed, sediment mixtures started to deposit in the 200–250 m reach and consequently accumulated in the dam reservoir and deposit fan (**Figure 7B**).

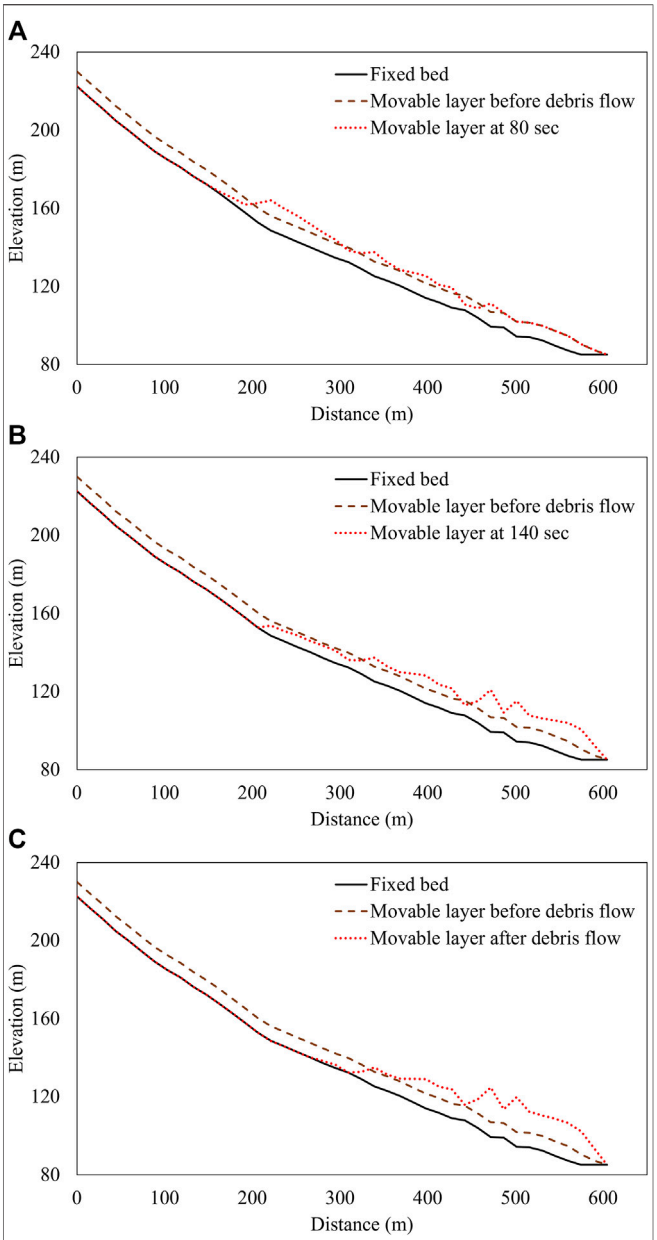

FIGURE 7 | Change in the erodible layer after debris flow simulation without a dam after **(A)** 80 s, **(B)** 140 s, and **(C)** post-simulation. The black line is the fixed channel bed; the brown dashed and red dotted lines represent the movable layer before and after debris flow, respectively. Note that movable layers (brown dashed and red dotted lines) are not drawn at a realistic scale; they are exaggerated by five times their actual values for visibility.

The simulated debris flow entirely eroded the active layer in the upper reach, and in-stream sediment was deposited 280 m upstream from the dam site (**Figure 7C**). Note that the 2011 field observations had previously indicated that sediment deposition occurred approximately 300 m upstream of the dam (SMG, 2012). Therefore, Hyper Kanako can accurately reproduce the location and the type of sediment deposition along the stream. Moreover, the model is applicable for simulating the entrainment pattern of debris flow in steep mountain streams. Close agreement of the observed and simulated debris volumes was discerned for the 2011 event. The simulation results revealed that the debris flow immediately filled the dam reservoir and then overflowed to the downstream channel. This was identical to the debris-flow tracks, estimated by the airborne image taken after the disaster, as shown in **Figure 8**. Moreover, although the simulated deposit area was discontinuous because of the coarse spatial resolution (10 m × 10 m) of the computations, the extent of the deposit pixels was comparable to that of the actual deposit area in the 2011 event (**Figure 9**). During the simulation with 3,800 m^3 of sediment input, 4,898.21 m^3 of sediment was eroded along the channel. The total deposit amounts of sediments were estimated to be 8,434.13 m^3, comprising 4,216.43 m^3 deposited in the channel and 4,217.70 m^3 in the deposit fan. Reflecting that some parts of the debris flow were discharged beyond the simulation boundary, the simulated debris flow satisfied the sediment balance within the dam–channel network.

Regarding the trace of the debris flow, the Hyper Kanako result seemingly exhibited close comparison to the actual 2011 debris-flow event, despite some parameters being indirectly derived from previous studies without adjustment. However, due to the lack of data on the volume and area of erosional and depositional areas, the model results could not be validated quantitatively against the observed data.

The flow characteristics and impact force exhibited considerable differences across the different deposit condition scenarios (**Table 3**). The simulations with no dam condition revealed that the maximum impact force was approximately 132 kPa at a depth of 0.81 m, and the velocity was 7.17 m s^{-1}. When the check dam was installed along the reach, the simulated depth, velocity of debris flow, and associated impact force all decreased, to 0.59 m, 5.36 m s^{-1}, and 81.76 kPa, respectively, for the no-deposit scenario. The simulation under the entire-deposition (100%) scenario indicated that the flow depth, velocity, and resultant maximum impact force increased, to 0.77 m, 6.99 m s^{-1}, and 123.04 kPa, respectively (**Figure 10**).

Under the no-deposit condition, sedimentation occurred at two gentle sections with a gradient of less than 4%. Because of the deposition in these sections, the sediment concentration could have been decreased, which potentially affected the flow characteristics of the debris flow. However, when sedimentation scenarios were applied, the gradient of these sections was 7%, which was steeper than the initial slope due to sedimentation, as shown in **Figure 4** in **Section 2.4**. As a result, the debris flow could run downstream with a faster flow velocity and less sediment deposition.

The flow depth was also affected by the deposition induced by a gentle slope gradient. If sediment deposition in the check dam reservoir was suppressed owing to a steeper slope, compared with the original channel slope, the debris flow would contain more sediment with increased flow rate, thereby deepening the flow.

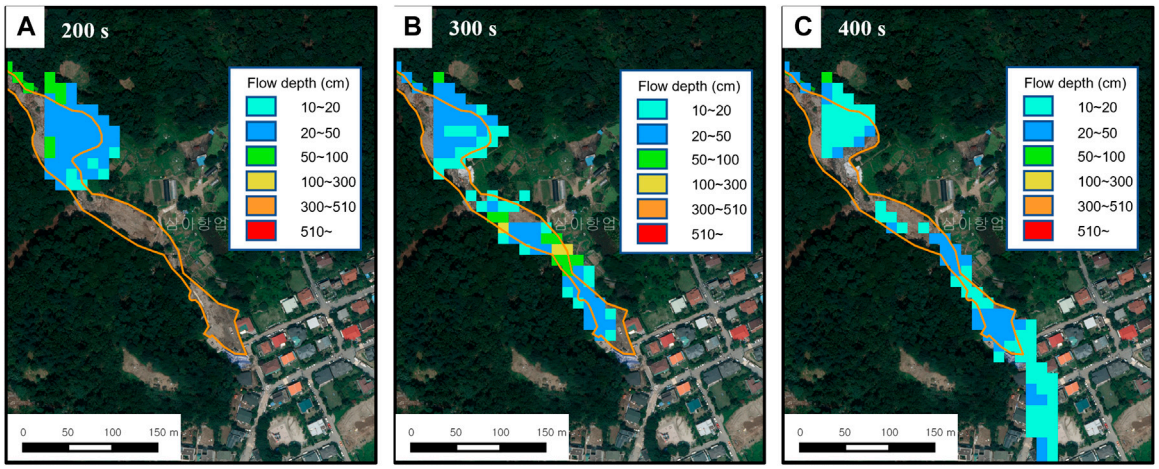

FIGURE 8 | Result of debris flow simulation using Hyper Kanako. Flow depth at **(A)** 200 s, **(B)** 300 s, and **(C)** 400 s shows that the simulated flow path in the deposit fan is similar to the observed damaged area (orange line).

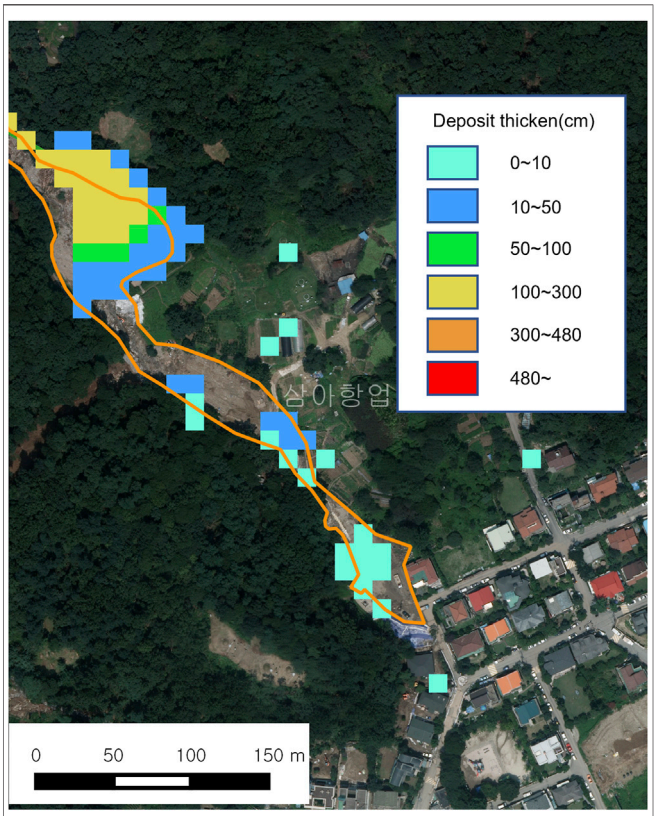

FIGURE 9 | Result of simulated sediment using Hyper Kanako at 1,200 s. Although the simulated deposit fan is discontinuous, the sediment deposition in the reservoir (yellow deposition pixels) was well simulated; the total extent of deposition is also comparable to the actual deposit area in the 2011 event (orange line).

Moreover, increasing the deposit height seemingly induces changes in the flow characteristics and sediment concentration, thereby affecting the debris-flow impact force.

3.2 Check Dam Stability

The results of the dam stability analysis, which elucidates the influence of sedimentation and debris flow, are shown in **Table 4**. This shows that the maximum tensile and compressive stress values were lowest in the no-deposit condition, at 0.38 and 0.14 MPa, respectively. As the deposited depth increased, the resultant tensile and compressive stresses increased to 0.80 and 0.35 MPa, respectively. The point at which the maximum compressive stress was produced varied with the sediment deposition; it was exerted on the middle of the collision section in the face of the dam until 50% deposition was achieved; under deposition conditions of more than 75% it was exerted at the collision section of the debris flow and the bottom of the downstream face (**Figure 11**).

Figure 11 shows that the maximum tensile stress occurred at the bottom of the upstream face for all the deposition scenarios. Our results demonstrated that the check dam had sufficient strength against the maximum compressive and tensile stresses, even under a 50% strength reduction by aging degradation. Notably, this finding indicates that the check dam satisfies the stability criteria for distress failure under the combined conditions of sediment deposition and debris-flow impact (**Table 4**).

4 DISCUSSION

Sediment deposition and debris-flow discharge are essential for producing the external load to check dams; however, it is inherently challenging to accurately reproduce debris-flow characteristics by using numerical models. As a debris flow approaches a dam, the flow velocity is attenuated because of the rip current of the debris flow. When a debris flow reaches a rigid wall, such as a check dam, it immediately runs up in the vertical direction along the slope of the dam body (Iverson et al., 2016; Koo et al., 2017; Shen et al., 2018; Ng et al., 2021).

TABLE 3 | Simulation result for debris flow characteristics and impact force in each deposit scenario.

Deposit condition	Flow depth [m]	Flow velocity [m s^{-1}]	Maximum impact force [kPa]
No dam	0.81	7.17	132.64
0% deposit	0.59	5.36	81.76
25% deposit	0.58	6.61	96.02
50% deposit	0.65	6.00	95.68
75% deposit	0.65	6.88	105.96
100% deposit	0.77	6.99	123.04

TABLE 4 | Results of structural stability analysis.

Stress type	Deposit condition	Maximum stress [MPa]	Factor of safety[a] (FS) considering strength reduction		
			100% strength	75% strength	50% strength
Tensile	0% deposit	0.38	7.63	5.72	3.81
	25% deposit	0.25	11.75	8.81	5.87
	50% deposit	0.45	6.48	4.86	3.24
	75% deposit	0.73	3.94	2.96	1.97
	100% deposit	0.80	3.61	2.71	1.80
Compressive	0% deposit	0.14	151.71	113.78	75.86
	25% deposit	0.16	127.78	95.83	63.89
	50% deposit	0.19	111.52	83.64	55.76
	75% deposit	0.35	60.27	45.21	30.14
	100% deposit	0.31	66.87	50.15	33.44

[a]*Factor of Safety (FS) = Strength/Stress (stable when FS > 1.0).*

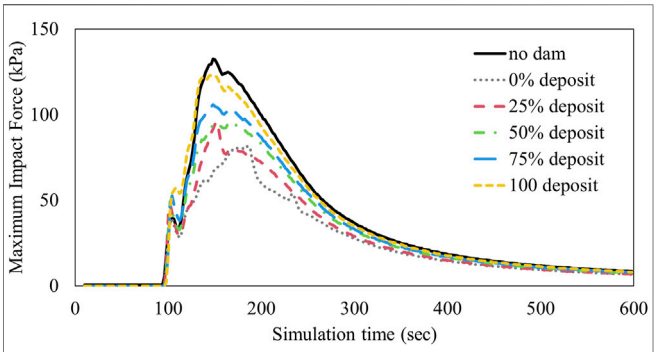

FIGURE 10 | Changes in debris flow impact force according to different deposit scenarios.

According to Sanvitale et al. (2021), the vertical jet of debris discharge might overflow the check dam in an inertial-dominated condition (higher Froude number); it falls down and becomes a reflected wave into the upstream direction in a low Froude number condition. This reflected wave induces a reduction in the kinetic energy of the subsequent flow. Consequently, debris materials are sequentially deposited in the upstream face of check dams, which acts as a buffering barrier to reduce subsequent debris-flow impact forces. However, as the deposit depth increases, the piled-up debris extends to the top of the check dam, and subsequent debris flows can overflow the dam. Reflected wave and debris buffer effects can be somewhat prolonged until the overflow occurs. Sediment deposition in the check dam reservoir decreases the effective height of the dam on the upstream side, thereby reducing the storage capacity for sediment trapping and shortening the time to overflow. Therefore, the dissipated impact energy may be weakened as the deposit height increases, thus exacerbating the debris-flow impact force.

This study had several limitations, including: 1) the reproducibility of Hyper Kanako; 2) coarse spatial resolution; 3) simplicity of the entrainment model; and 4) difficulties in simulating strict physical processes.

In terms of the reproducibility, the results of numerical simulations should be quantitatively validated by comparisons with observed data, including the area and volume of entrainment (Gregoretti et al., 2019). This comparison was achieved with the help of 3-D topographic data obtained from airborne photogrammetry or LiDAR (Cucchiaro et al., 2019a; Cucchiaro et al., 2019b; Gregoretti et al., 2019). In this study, only airborne orthoimage was available to trace debris-flow movement; therefore, the erosional and depositional areas in the channel could not be quantified. Although a digital topographic map was taken within a month of the debris-flow event, most debris–sediment mixtures in the deposit fan had already been removed because they covered public roads and residence areas.

The spatial resolution of the DEM obtained from the digital topographic map was also a critical limitation of this study. When a debris-flow impacts a check dam, the impact force distribution continuously varies owing to the debris-flow impact dynamics, such as the hydraulic processes of run-up

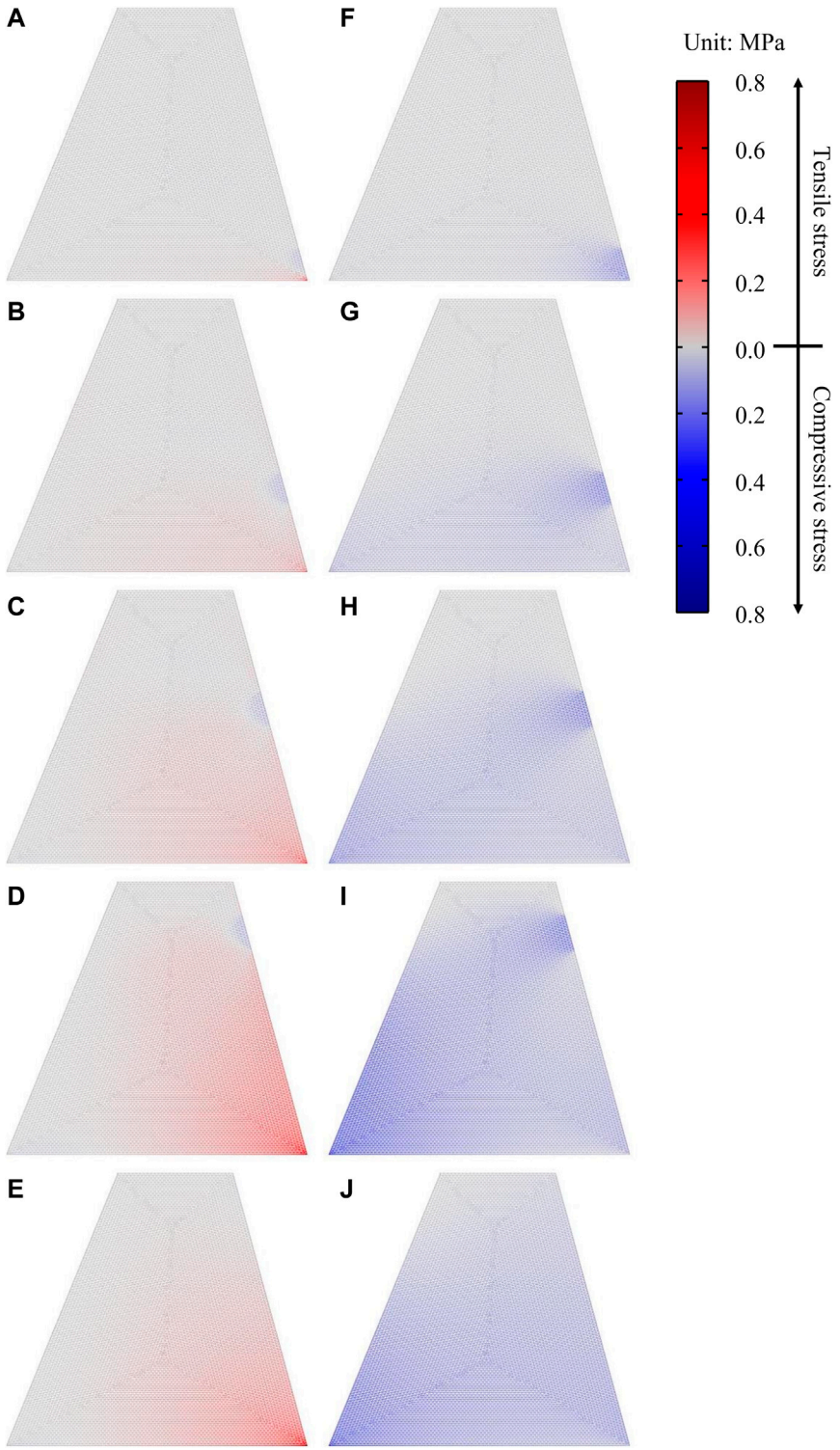

FIGURE 11 | Results of tensile and compressive stress for each deposit scenario. Tensile stress distribution at **(A)** 0%, **(B)** 25%, **(C)** 50%, **(D)** 75%, and **(E)** 100% deposition conditions; compressive stress distribution at **(F)** 0%, **(G)** 25%, **(H)** 50%, **(I)** 75%, and **(J)** 100% deposition conditions.

or reflected waves. As these dynamic phenomena only occur locally, the spatial resolution for addressing the impact dynamics should be sufficiently high to consider the interaction between the debris flow and the check dam. However, the spatial resolution of the DEM used in this study was 10 m × 10 m, and the interval between spatial

nodes in the channel area was approximately 15 m. Given a dam width of 4 m and height of 5 m, the data used in the simulation were insufficient to reproduce the local dynamics of debris-flow impact. Owing to this, we suggest that further studies should analyze the debris-flow impact force exerted on the check dam with higher precision and at a higher spatial resolution, using data taken before and after a debris-flow event, compared to those herein.

Moreover, the entrainment process in Hyper Kanako, which is represented as an empirical relationship between the flow velocity and sediment concentration, is likely insufficient to simulate the impact dynamics. When Hyper Kanako simulates a debris flow under the installation of check dams, this model assumes that the momentum of the debris flow instantaneously becomes zero with rapid sediment deposition until overflow occurs to avoid numerical errors induced by discontinuous flow phenomena, such as run-up or hydraulic jump when debris-flow impacts (Nakatani, 2010). This simplification ensures stable numerical solutions for deposit fans situated downstream of check dams. However, it could reduce the accuracy of the estimation of the debris-flow impact load.

Further analysis is needed to ensure the long-term stability of a check dam by considering several factors. First, the impact force can be set to reflect an extreme debris-flow event in the watershed. In this context, KFS (2014) and NILIM (2016a) suggest that design flood discharge should be quantified based on a return period of 100 years. The debris-flow evidence from 2011 has a 20-years recurrence interval, which is rather short to embrace an extreme disaster within the Hyoungchon watershed. Second, check dams suffer from aging and lose their strength over time (Lee, 2015). Thus, check dams with reduced strength are vulnerable to debris-flow impact forces. To address this issue, check dams need to be designed considering time-dependent strength reduction for providing long-term protection against debris flows.

5 CONCLUSION

In this study, we simulated a debris flow and the associated impact force in a small mountain stream to examine the structural stability of a check dam. The combined effects of the debris-flow impact force and lateral earth pressure were considered through finite element analysis. This analysis revealed that the check dam would be stable under all the simulations considering sediment deposition on the upstream face and debris-flow impact force. The debris-flow impact force resulted in concentrated tensile stress on the upstream face of the dam foundation.

These results were achieved for a specific debris-flow event, thereby constraining us from providing a broader conclusion that similar stress distributions can be observed in various other watershed environments. Nevertheless, our proposed framework for distress stability analysis of check dams will be more widely applicable. With a reasonable estimation method for debris-flow magnitude, the methods and results of this study can provide practical guidance for check-dam design and maintenance, taking into account sediment deposition and debris-flow impact force.

DATA AVAILABILITY STATEMENT

The raw data supporting the conclusion of this article will be made available by the authors, without undue reservation.

AUTHOR CONTRIBUTIONS

All authors contributed to conception and design of the study. SE organized the database. SE performed the numerical and statistical analysis. SE wrote the first draft of the manuscript. All authors contributed to manuscript revision, read, and approved the submitted version.

REFERENCES

Armanini, A. (1997). "On the Dynamic Impact of Debris Flows," in *Recent Developments on Debris Flows*. Editors A. Armanini and M. Michiue (Berlin/Heidelberg: Springer), 208–226.

Baggio, T., and D'agostino, V. (2022). Simulating the Effect of Check Dam Collapse in a Debris-Flow Channel. *Sci. of Total Environ.* 816, 151660. doi:10.1016/j.scitotenv.2021.151660

Bernard, M., Boreggio, M., Degetto, M., and Gregoretti, C. (2019). Model-Based Approach for Design and Performance Evaluation of Works Controlling Stony Debris Flows with an Application to a Case Study at Rovina di Cancia (Venetian Dolomites, Northeast Italy). *Sci. of Total Environ.* 688, 1373–1388. doi:10.1016/j.scitotenv.2019.05.468

Brighenti, R., Spaggiari, L., Segalini, A., Savi, R., and Capparelli, G. (2021). Debris Flow Impact on a Flexible Barrier: Laboratory Flume Experiments and Force-Based Mechanical Model Validation. *Nat. Hazards* 106, 735–756. doi:10.1007/s11069-020-04489-5

Chae, B.-G., Park, H.-J., Catani, F., Simoni, A., and Berti, M. (2017). Landslide Prediction, Monitoring and Early Warning: A Concise Review of State-of-The-Art. *Geosci. J.* 21, 1033–1070. doi:10.1007/s12303-017-0034-4

Chen, H.-X., Li, J., Feng, S.-J., Gao, H.-Y., and Zhang, D.-M. (2019). Simulation of Interactions Between Debris Flow and Check Dams on Three-Dimensional Terrain. *Eng. Geol.* 251, 48–62. doi:10.1016/j.enggeo.2019.02.001

Chun, K. W., Chun, K. W., and Song, D. G. (2016). Estimation of Sediment Discharge Controlled by Sediment-Filled Check-Dam in a Forested Catchment. *J. Korean For. Soc* 105, 321–329. (in Korean). doi:10.14578/jkfs.2016.105.3.321

Coe, J. A., Kinner, D. A., and Godt, J. W. (2008). Initiation Conditions for Debris Flows Generated by Runoff at Chalk Cliffs, Central Colorado. *Geomorphology* 96, 270–297. doi:10.1016/j.geomorph.2007.03.017

COMSOL AB (2017). *COMSOL Multiphysics®. V. 5.3*. Stockholm: COMSOL AB.

Cucchiaro, S., Cavalli, M., Vericat, D., Crema, S., Llena, M., Beinat, A., et al. (2019a). Geomorphic Effectiveness of Check Dams in a Debris-Flow Catchment Using Multi-Temporal Topographic Surveys. *Catena* 174, 73–83. doi:10.1016/j.catena.2018.11.004

Cucchiaro, S., Cazorzi, F., Marchi, L., Crema, S., Beinat, A., and Cavalli, M. (2019b). Multi-Temporal Analysis of the Role of Check Dams in a Debris-Flow Channel: Linking Structural and Functional Connectivity. *Geomorphology* 345, 106844. doi:10.1016/j.geomorph.2019.106844

Gregoretti, C., Stancanelli, L. M., Bernard, M., Boreggio, M., Degetto, M., and Lanzoni, S. (2019). Relevance of Erosion Processes When Modelling In-Channel Gravel Debris Flows for Efficient Hazard Assessment. *J. of Hydrology* 568, 575–591. doi:10.1016/j.jhydrol.2018.10.001

Horiuchi, S., Iwanami, E., Nakatani, K., Satofuka, Y., and Mizuyama, T. (2012). Development of "Hyper KANAKO", a Debris Flow Simulation System Using with Laser Profiler Data. *J. Jpn. Soc. Eros. Control Eng.* 64, 25–31. (In Japanese). doi:10.11475/sabo.64.6_25

Hu, K., Wei, F., and Li, Y. (2011). Real-Time Measurement and Preliminary Analysis of Debris-Flow Impact Force at Jiangjia Ravine, China. *Earth Surf. Process. Landforms* 36, 1268–1278. doi:10.1002/esp.2155

Hübl, J., and Fiebiger, G. (2005). "Debris-Flow Mitigation Measures," in *Debris-Low Hazards and Related Phenomena*. Editors M. Jakob and O. Hungr (Berlin/Heidelberg: Springer), 445–487.

Hübl, J., and Holzinger, G. (2003).Kleinmassstaebliche Modellversuche zur Wirkung von Murbrechern. *WLS Report 50:3*. Vienna: University of Natural Resources and Life Sciences. (In German).

Hübl, J., Suda, J., Proske, D., Kaitna, R., and Scheidl, C. (2009). "Debris Flow Impact Estimation," in Proceedings of the 11th International Symposium on Water Management and Hydraulic Engineering(Ss. Ohrid: Cyril and Methodius University), 137–148.

Huebl, J., Nagl, G., Suda, J., and Rudolf-miklau, F. (2017). Standardized Stress Model for Design of Torrential Barriers Under Impact by Debris Flow (According to Austrian Standard Regulation 24801). *Int. J. of Eros. Control Eng.* 10, 47–55. doi:10.13101/ijece.10.47

Hungr, O., Morgan, G. C., and Kellerhals, R. (1984). Quantitative Analysis of Debris Torrent Hazards for Design of Remedial Measures. *Can. Geotech. J.* 21, 663–677. doi:10.1139/t84-073

Imaizumi, F., Sidle, R. C., Tsuchiya, S., and Ohsaka, O. (2006). Hydrogeomorphic Processes in a Steep Debris Flow Initiation Zone. *Geophys. Res. Lett.* 33, L10404. doi:10.1029/2006GL026250

Iverson, R. M., George, D. L., and Logan, M. (2016). Debris Flow Runup on Vertical Barriers and Adverse Slopes. *J. Geophys. Res. Earth Surf.* 121, 2333–2357. doi:10.1002/2016JF003933

[KFS] Korea Forest Service (2014). *Erosion Control Technical Manual*. Daejeon: Korea Forest Service. (In Korean).

[KMLIT] Korea Ministry of Land, Infrastructure and Transport (2012). *Concrete Structure Design Code*. Seoul: Korea Ministry of Land, Infrastructure and Transport. (in Korean).

Koo, R. C. H., Kwan, J. S. H., Ng, C. W. W., Lam, C., Choi, C. E., Song, D., et al. (2017). Velocity Attenuation of Debris Flows and a New Momentum-Based Load Model for Rigid Barriers. *Landslides* 14, 617–629. doi:10.1007/s10346-016-0715-5

Kwan, J. (2012). *Supplementary Technical Guidance on Design of Rigid Debris-Resisting Barriers*, Hong Kong. *GEO Report No.270*. Hong Kong: Geotechnical Engineering Office.

Law, R. P. H., Choi, C. E., and Ng, C. W. W. (2016). Discrete-Element Investigation of Influence of Granular Debris Flow Baffles on Rigid Barrier Impact. *Can. Geotech. J.* 53, 179–185. doi:10.1139/cgj-2014-0394

Lee, J.-H. (2015). Analysis of Condition Assessment and Damage Patterns of Concrete Check Dam. Ph.D. Dissertation. Chuncheon (South Korea): Kangwon National University. (In Korean).

Lee, K., Kim, Y., Ko, J., and Jeong, S. (2019). A Study on the Debris Flow-Induced Impact Force on Check Dam With- and Without-Entrainment. *Comput. and Geotechnics* 113, 103104. doi:10.1016/j.compgeo.2019.103104

Leonardi, A., and Pirulli, M. (2020). Analysis of the Load Exerted by Debris Flows on Filter Barriers: Comparison Between Numerical Results and Field Measurements. *Comput. and Geotechnics* 118, 103311. doi:10.1016/j.compgeo.2019.103311

Marchelli, M., and De Biagi, V. (2019). Dynamic Effects Induced by the Impact of Debris Flows on Protection Barriers. *Int. J. of Prot. Struct.* 10, 116–131. doi:10.1177/2041419618798378

Mizuyama, T. (1979). Calculation and its Problem of Debris Flow Impact Force Acting on Sabo Dam. *Shin-Sabo* 32, 40–43. (in Japanese). doi:10.11475/sabo1973.31.4_26

Nakatani, K. (2010). Development and Application of General-Purpose Debris Flow Numerical Simulation System with GUI. Ph.D. Dissertation. Kyoto (Japan): Kyoto University. (In Japanese).

Nakatani, K., Satofuka, Y., and Mizuyama, T. (2008). Development of "Kanako Ver.1.10", a Wide Use One Dimensional Debris Flow Simulator Equipped with GUI. *J. Jpn. Soc. Eros. Control Eng.* 61, 41–46. (In Japanese). doi:10.11475/sabo.61.2_41

Ng, C. W. W., Liu, H., Choi, C. E., Kwan, J. S. H., and Pun, W. K. (2021). Impact Dynamics of Boulder-Enriched Debris Flow on a Rigid Barrier. *J. Geotech. Geoenviron. Eng.* 147, 04021004. doi:10.1061/(ASCE)GT.1943-5606.0002485

[NGII] National Geographic Information Institute (2019). National Geospatial Information Platform. Available at: http://map.ngii.go.kr/mn/mainPage.do (Accessed April 1, 2022).

[NILIM] National Institute for Land and Infrastructure Management (Japan) (2016a). *Manual of Technical Standard for Designing Sabo Facilities Against Debris Flow and Driftwood. Technical Note of NILIM No. 905*. Tsukuba: National Institute for Land and Infrastructure Management. (In Japanese).

[NILIM] National Institute for Land and Infrastructure Management (Japan) (2016b). *Manual of Technical Standard for Establishing Sabo Master Plan for Debris Flow and Driftwood. Technical Note of NILIM No. 904*. Tsukuba: National Institute for Land and Infrastructure Management. (In Japanese).

Proske, D., Suda, J., and Hübl, J. (2011). Debris Flow Impact Estimation for Breakers. *Georisk Assess. and Manag. of Risk Eng. Syst. and Geohazards* 5, 143–155. doi:10.1080/17499518.2010.516227

Rossi, G., and Armanini, A. (2019). Impact Force of a Surge of Water and Sediments Mixtures against Slit Check Dams. *Sci. of Total Environ.* 683, 351–359. doi:10.1016/j.scitotenv.2019.05.124

Sanvitale, N., Bowman, E., and Cabrera, M. A. (2021). Experimental Investigation on the Impact Dynamics of Saturated Granular Flows on Rigid Barriers. *Environ. Eng. Geosci.* 27, 127–138. doi:10.2113/EEG-D-20-00033

Scheidl, C., Chiari, M., Kaitna, R., Müllegger, M., Krawtschuk, A., Zimmermann, T., et al. (2013). Analysing Debris-Flow Impact Models, Based on a Small Scale Modelling Approach. *Surv. Geophys.* 34, 121–140. doi:10.1007/s10712-012-9199-6

Shen, W., Li, T., Li, P., and Lei, Y. (2020). Numerical Assessment for the Efficiencies of Check Dams in Debris Flow Gullies: A Case Study. *Comput. and Geotechnics* 122, 103541. doi:10.1016/j.compgeo.2020.103541

Shen, W., Zhao, T., Zhao, J., Dai, F., and Zhou, G. G. D. (2018). Quantifying the Impact of Dry Debris Flow against a Rigid Barrier by DEM Analyses. *Eng. Geol.* 241, 86–96. doi:10.1016/j.enggeo.2018.05.011

Simoni, A., Bernard, M., Berti, M., Boreggio, M., Lanzoni, S., Stancanelli, L. M., et al. (2020). Runoff-Generated Debris Flows: Observation of Initiation Conditions and Erosion-Deposition Dynamics Along the Channel at Cancia (Eastern Italian Alps). *Earth Surf. Process. Landforms* 45, 3556–3571. doi:10.1002/esp.4981

[SMG] Seoul Metropolitan Government (2012). *Mt. Umyeon Lansdlide Recovery Plan. Lot No.3: Hyoungchon Area*. Seoul: Seoul Metropolitan Goverment. (In Korean).

[SMG] Seoul Metropolitan Government (2014). *Supplimentary Investigation of Cause of Mt. Umyeon Landslide*. Seoul: Seoul Metropolitan Goverment. (In Korean).

Song, D., Choi, C. E., Ng, C. W. W., Zhou, G. G. D., Kwan, J. S. H., Sze, H. Y., et al. (2019). Load-Attenuation Mechanisms of Flexible Barrier Subjected to Bouldery Debris Flow Impact. *Landslides* 16, 2321–2334. doi:10.1007/s10346-019-01243-2

Suda, J., Strauss, A., Rudolf-Miklau, F., and Hübl, J. (2009). Safety Assessment of Barrier Structures. *Struct. and Infrastructure Eng.* 5, 311–324. doi:10.1080/15732470701189498

Takahashi, T. (2014). *Debris Flow: Mechanics, Prediction and Countermeasures*. Leiden: CRC Press.

Takahashi, T., Nakagawa, H., Harada, T., and Yamashiki, Y. (1992). Routing Debris Flows with Particle Segregation. *J. Hydraul. Eng.* 118, 1490–1507. doi:10.1061/(asce)0733-9429(1992)118:11(1490)

Takahashi, T., and Nakagawa, H. (1991). Prediction of Stony Debris Flow Induced by Severe Rainfall. *J. Jpn. Soc. Eros. Control Eng.* 44, 12–19. (In Japanese). doi:10.11475/sabo1973.44.3_12

Uchida, T., Nishiguchi, Y., Nakatani, K., Satofuka, Y., Yamakoshi, T., Okamoto, A., et al. (2013). New Numerical Simulation Procedure for Large-Scale Debris Flows (Kanako-LS). *Int. J. of Eros. Control Eng.* 6, 58–67. doi:10.13101/ijece.6.58

Victoriano, A., Brasington, J., Guinau, M., Furdada, G., Cabré, M., and Moysset, M. (2018). Geomorphic Impact and Assessment of Flexible Barriers Using

Multi-Temporal LiDAR Data: The Portainé Mountain Catchment (Pyrenees). *Eng. Geol.* 237, 168–180. doi:10.1016/j.enggeo.2018.02.016

Wang, Y., Liu, X., Yao, C., and Li, Y. (2020). Debris-Flow Impact on Piers with Different Cross-Sectional Shapes. *J. Hydraul. Eng.* 146, 04019045. doi:10.1061/(ASCE)HY.1943-7900.0001656

Wendeler, C., Volkwein, A., Mcardell, B. W., and Bartelt, P. (2019). Load Model for Designing Flexible Steel Barriers for Debris Flow Mitigation. *Can. Geotech. J.* 56, 893–910. doi:10.1139/cgj-2016-0157

Conflict of Interest: The authors declare that the research was conducted in the absence of any commercial or financial relationships that could be construed as a potential conflict of interest.

Publisher's Note: All claims expressed in this article are solely those of the authors and do not necessarily represent those of their affiliated organizations, or those of the publisher, the editors and the reviewers. Any product that may be evaluated in this article, or claim that may be made by its manufacturer, is not guaranteed or endorsed by the publisher.

frontiers | Frontiers in Physics

BRIEF RESEARCH REPORT
published: 21 June 2022
doi: 10.3389/fphy.2022.819709

Study on Shear Creep Characteristics and Creep Model of Soil-Rock Mixture Considering the Influence of Water Content

*Zihua Jiang and Huanling Wang**

Geotechnical Research Institute, Hohai University, Nanjing, China

Water content has a significant effect on the creep properties of soil-rock mixtures (SRM). Multi-loading shear creep tests are carried out on SRM samples with different water contents. The test results show that deformation gradually increase with increasing water content, while long-term strength gradually decrease with increasing water content. The deformation mechanism shows that increasing of water content causes the change of rock particles at on the shear surface from fracture to rotation. Based on the creep test results, a modified Burgers model considering the water content is proposed by the empirical relationship between the parameters of the traditional Burgers model and the water content. And the results predicted by the modified Burgers model agree well quite well with the experimental creep data.

Keywords: deposit landslide, soil-rock mixture, moisture content, time-dependent deformation, creep constitutive model, long-term strength

OPEN ACCESS

Edited by:
Eric Josef Ribeiro Parteli, University of Duisburg-Essen, Germany

Reviewed by:
Bei Han, Beijing University of Technology, China
Fuguo Tong, China Three Gorges University, China

****Correspondence:***
Huanling Wang
wanghuanling@hhu.edu.cn

Specialty section:
This article was submitted to Interdisciplinary Physics, a section of the journal Frontiers in Physics

Received: *22 November 2021*
Accepted: *01 June 2022*
Published: *21 June 2022*

Citation:
Jiang Z and Wang H (2022) Study on Shear Creep Characteristics and Creep Model of Soil-Rock Mixture Considering the Influence of Water Content. Front. Phys. 10:819709. doi: 10.3389/fphy.2022.819709

INTRODUCTION

A large number of deposit landslides of soil-rock mixtures (SRM) exhibit the characteristics of long-term and creep deformation under the action of rainfall and other internal and external geological forces [1,2]. The creeping deposit landslide in the reservoir area is a threat to the long-term safe operation of power stations. Therefore, it is necessary to study on the creep characteristics and long-term stability of large-scale deposit landslides.

There have been many studies on the mechanical properties of SRM, mainly through laboratory tests[3,4], numerical simulations [5,6], and *in-situ* tests [7,8]. Furthermore, there are a number of studies on the creep properties of SRM strength [9,10], which were not considering the effect of water content on the creep properties of SRM. However, water content of SRM in the deposit landslide changes under the action of rainfall or reservoir water. Although there is a body of work which focused on the effect of rainfall and other environmental factors from remote sense observations and statistical modelling [11,12], the effect of creep behavior on the SRM in the deposit landslide evolutional process under different water contents is poorly understood.

In order to study the influence of water content on the characteristics of long-term deformations and stability of SRM, multi-stage shear creep tests of SRM samples with different water contents are conducted. The creep characteristics of SRM are analyzed, the long-term strengths of SRM with different water contents are obtained, and a modified Burgers model considering water content is developed based on the results of the shear creep test.

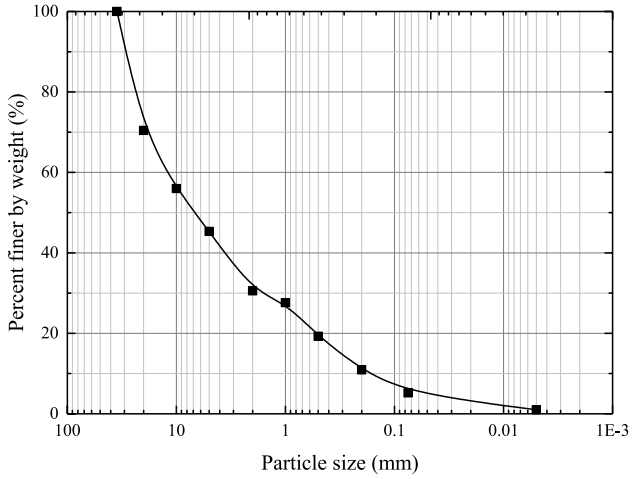

FIGURE 1 | Particle size distribution of SRM.

TESTING PROCEDURE

The Dahua landslide located on the right bank of Lancang River is a typical deposit landslide[13]. The main components of the landslide are a mixture of soil and rock debris. The filed displacement monitoring data show that the landslide is still in the creeping state and has the characteristics of time-dependent deformation. The density of the selected SRM is 2.2 g/cm^3, the distribution of particle size is shown in **Figure 1**. The water contents of SRM samples are determined to be ranging from 3.9% to 16.4%.

Shear creep tests are conducted using a shear creep test system. The sample is a cube with a side length of 150 mm. Tests are conducted in the laboratory environment with constant temperature (20 ± 0.5°C) and humidity. Considering the depth of SRM at the sampling site, a normal pressure of 300 kPa is applied to represent the confining pressure at the sampling site. The shear stress loading scheme for the creep test is listed in **Table 1**. Procedure of shear creep test is as follows:

1. Place the sample into the test platform and adjust the initial setting of the LVDTs.
2. Apply the normal pressure to the desired value (300 kPa) under displacement-controlled conditions with a rate of 0.2 mm/min and keep it constant throughout the test.
3. Increase the shear stress to the desired value under displacement-controlled conditions with a rate of 0.2 mm/min and keep it for approximately 72 h.
4. Apply multiple shear stress loadings following the loading scheme in **Table 1** until the sample fails.

SHEAR CREEP TEST RESULTS AND ANALYSIS

Creep Strain Behavior

The multi-loading deformations of the samples with water contents of 3.8%, 7.9%, 12.2%, and 16.4% are presented in **Figure 2**. It can be seen that shear creep deformations are observed from all SRM samples. For the same shear stress, the higher the water contents, the greater the creep deformation. Taking shear stress of 80 kPa as an example, the strains after stabilization of the SRM samples with water contents of 3.8%, 7.9%, 12.2%, and 16.4% are 2.14%, 3.52%, 4.25%, and 5.08%, respectively. The presence of water has a significant softening effect on SRM, weakening the mechanical properties of SRM and increasing the SRM deformability [14].

It is also seen that the creep deformation of SRM experiences three creep stages: transient creep, steady-state creep, and accelerated creep. Instantaneous deformation occurs at the beginning of each loading process. The higher water content, the greater instantaneous deformation. The strain then remains constant in the steady-state creep stage. Before the final shear stress level, the SRM undergoes the transient creep and steady-state creep stages. In the transient creep, the strain rate is relatively high but decreases with time, showing that strain rate approaches a fixed value. Accelerated creep occurs at the final shear stress level.

The shear strain and strain-rate versus time at the final shear stress level are shown in **Figure 2**. Compared to the results of preceding stress levels, the transient creep stage at the final stress level is less apparent. During this stage, the strain-rate decreases rapidly in a very short time, then remains almost constant, and finally increases rapidly. The final stress levels of SRM samples with four levels of water content are maintained for 54.73, 51.02, 39.33, and 32.86 h, respectively. The higher the water content, the longer the duration of the accelerated creep.

Long-Term Strength

The isochronic curve method is an effective method to determine the long-term strength [15,16]. The isochronic curves are drawn by the following method:

TABLE 1 | Shear stress loading scheme for the creep test.

Sample Number	Water Content (%)	Normal Stress (kPa)	Shear Stress (kPa)	Creep Time (h)
S-1	3.8	300	80-120-140-160-180-200-240-280-320	72-72-72-72-72-72-72-72-54.73
S-2	7.9	300	80-120-140-160-180-200-240-280-320	72-72-72-72-72-72-72-72-51.02
S-3	12.2	300	80-120-140-160-180-200-240-280-320	72-72-72-72-72-72-72-72-39.33
S-4	16.4	300	80-120-140-160-180-200-240-280-320	72-72-72-72-72-72-72-72-32.86

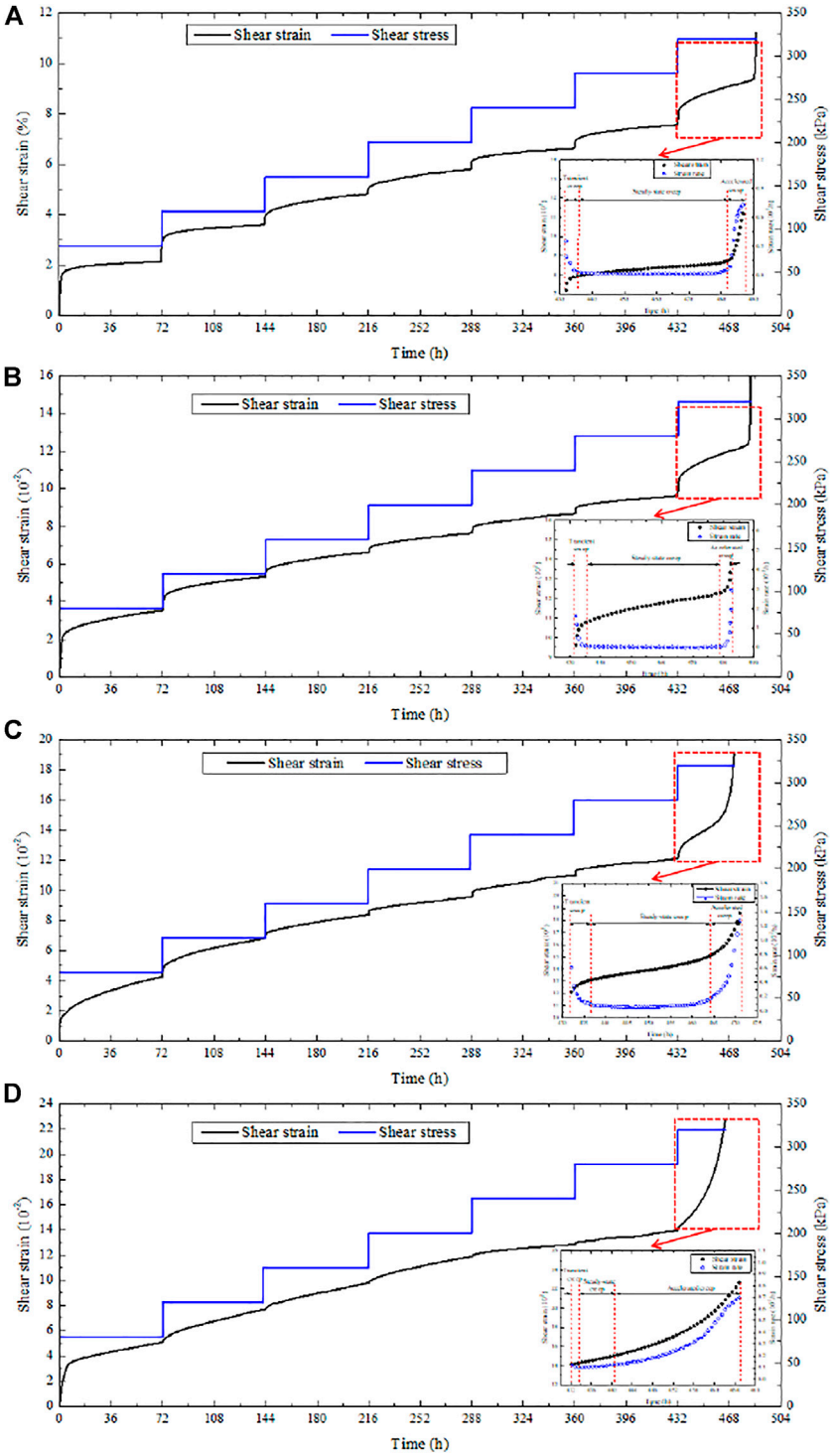

FIGURE 2 | Shear creep of samples with different water contents **(A)** 3.8%, **(B)** 7.9%, **(C)** 12.2%, and **(D)** 16.4%.

- Draw the shear creep strain versus time under various loading conditions according to the Boltzmann linear superposition principle.
- Select a series of time points in the creep curves under different shear stresses. Draw vertical lines at the selected time instances, which intersect the creep strain curves to

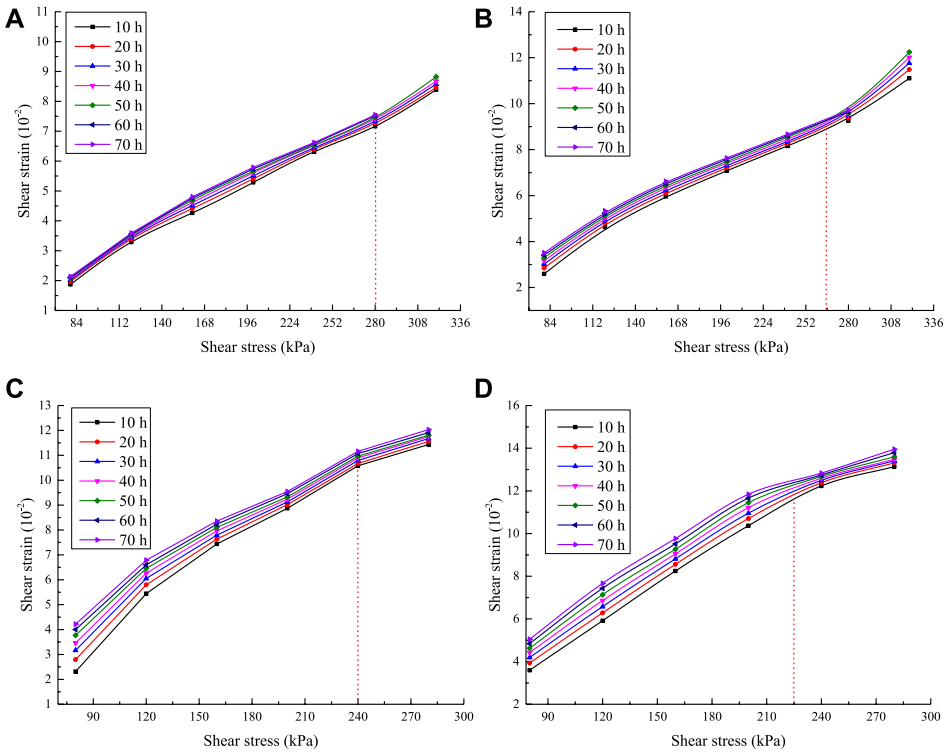

FIGURE 3 | Isochronous curves with different water contents **(A)** 3.8%, **(B)** 7.9%, **(C)** 12.2%, and **(D)** 16.4%.

give a series of shear stress and strain values. The shear strains are then plotted versus the shear stresses.

The isochronous curves are shown in **Figure 3**. The shear stress corresponding to the inflection point on the isochronous curve is considered to be the long-term strength [16]. Furthermore, inflection point may not be unique [17]. When there are two inflection points in an isochronous stress-strain curve, the shear stress value corresponding to the second inflection point is considered to be long-term strength. That is because, within a period of time after the second inflection point, the sample will be more likely to fail. From **Figure 3**, the long-term strengths of the four SRM samples are approximately 280, 266, 240, and 220 kPa, respectively, which show a trend of decrease with the increase of water content.

CREEP CONSTITUTIVE MODEL CONSIDERING WATER CONTENT

A modified Burgers model, which considers the effect of water content but not the accelerated creep phase, is developed.

Burgers Model

A Burgers model consists of a Kelvin model and a Maxwell model in series [17]. It is capable of describing the characteristics in the attenuation and steady-state creep stages of SRM.

The total creep strain ε of a Burgers model consists of the instantaneous elastic strain ε_1 corresponding to the spring in Maxwell model, the constant velocity strain ε_2 corresponding to the viscous damper in Maxwell model, and the creep strain ε_3 corresponding to the Kelvin model:

$$\varepsilon = \varepsilon_1 + \varepsilon_2 + \varepsilon_3 = \frac{\sigma}{E_1} + \frac{\sigma}{\eta_1}t + \frac{\sigma}{E_2}\left[1 - \exp\left(-\frac{E_2}{\eta_2}t\right)\right] \quad (1)$$

In a shear creep test, for each fixed shear stress τ, **Eq. 1** can be rewritten as

$$\varepsilon = \frac{\tau}{G_1} + \frac{\tau}{\eta_1}t + \frac{\tau}{G_2}\left[1 - \exp\left(-\frac{G_2}{\eta_2}t\right)\right] = A + B \times t + C \times \left[1 - \exp\left(-D \times t\right)\right] \quad (2)$$

where $A = \tau/G_1, B = \tau/\eta_1, C = \tau/G_2, D = \tau/\eta_2$.

TABLE 2 | Parameters of the Burgers model.

Shear Stress (kPa)	G_1 (kPa)	η_1 (kPa h)	G_2 (kPa)	η_2 (kPa ? h)	R^2
80	80836.35	1.78×10^6	4430.78	4.58×10^3	0.937
120	4847.82	2.44×10^6	15092.82	2.34×10^4	0.966
160	4077.23	2.21×10^6	40959.48	3.47×10^5	0.993
200	3619.06	3.08×10^6	65591.81	4.49×10^5	0.996
240	3946.91	5.32×10^6	48371.49	5.94×10^5	0.930
280	4073.68	5.28×10^6	87265.47	3.18×10^5	0.952

Note: R^2 is the coefficient of determination.

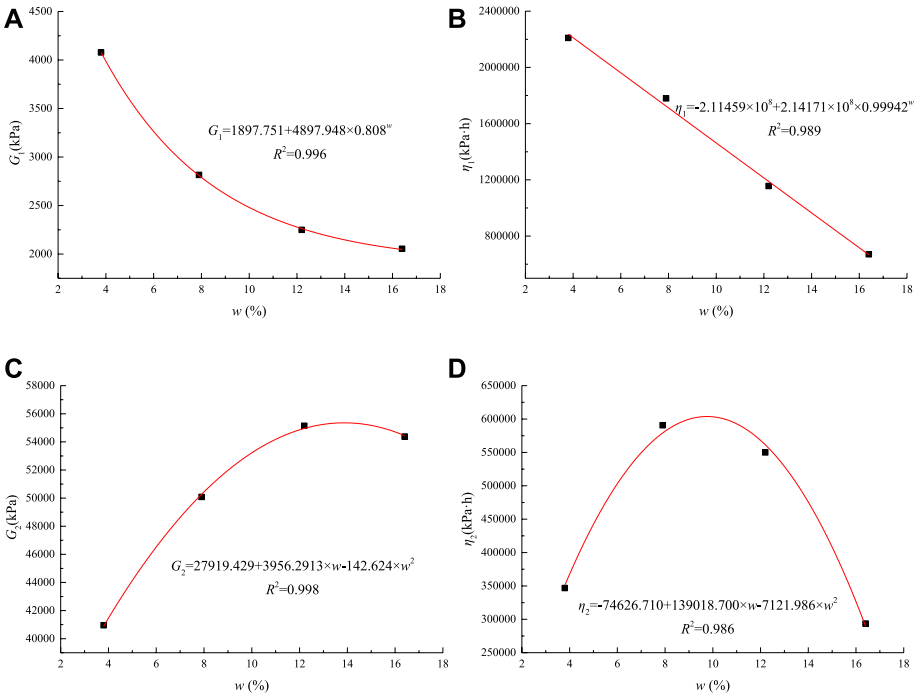

FIGURE 4 | Correlation between model parameters and water content.

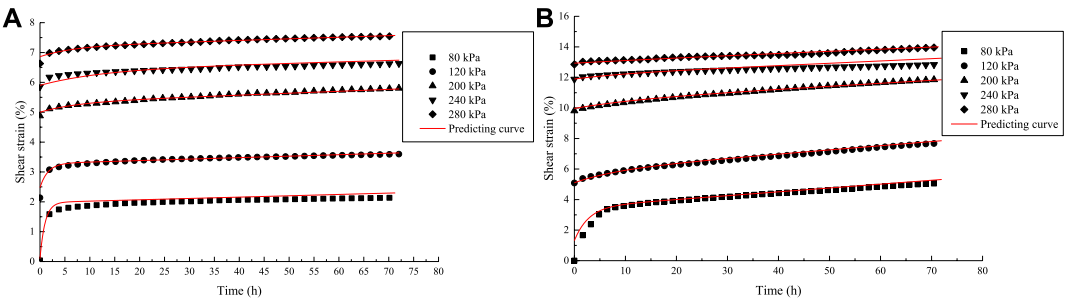

FIGURE 5 | Prediction results of the Burgers model **(A)** w = 3.8%, **(B)** w = 16.4%.

Parameters in the Burgers model of **Eq. 2** can be determined from regression analysis by fitting the creep process curves. Results for the case with water content of 3.8% are listed in **Table 2**.

Modified Burgers Model Considering Water Content

Having obtained the four parameters G_1, η_1, G_2, and η_2 of the Burgers model given by **Eq. 2**, the relationships between these model parameters and water content are shown in **Figure 4**. It can be seen that parameters G_1, η_1 and the water content follow an exponential relationship, whereas parameters G_2, η_2 and the water content follow a parabolic relationship. Regression analysis is performed to obtain the following empirical relationships between the four parameters and the water content. Substituting **Eq. 3** into **Eq. 2**, the Burgers model considering the effect of water content can be obtained.

$$\begin{cases} G_1 = 1897.751 + 4897.948 \times 0.808^{w} \\ \eta_1 = -2.11459 \times 10^8 + 2.14171 \times 10^8 \times 0.99942^{w} \\ G_2 = 27919.429 + 3956.2913 \times w - 142.624 \times w^2 \\ \eta_2 = -74626.710 + 139018.700 \times w - 7121.986 \times w^2 \end{cases} \tag{3}$$

In order to verify the accuracy of the proposed Burgers model, the model is applied to predict the shear creep curves of SRM and the results are shown in **Figure 5**. As can be seen, the results obtained using the Burgers creep model agree very well with the shear creep test data.

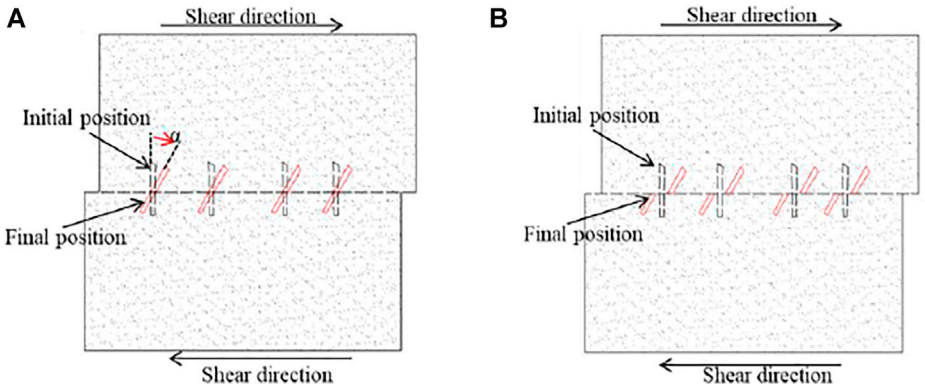

FIGURE 6 | Schematic diagram of deformation mechanisms **(A)** low water content, **(B)** high water content.

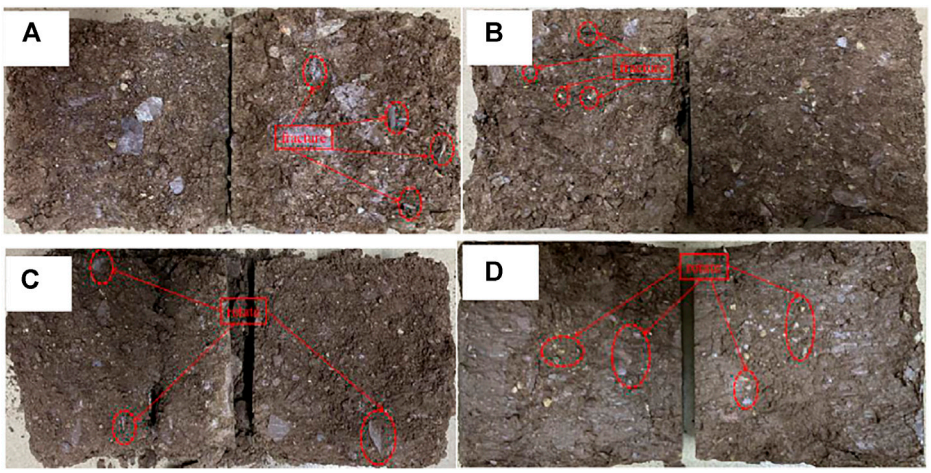

FIGURE 7 | Deformation characteristics of SRM samples **(A)** w = 3.9%, **(B)** w = 7.8%, **(C)** w = 12.2%, **(D)** w = 16.4%.

DISCUSSION

There are mainly two mechanisms affecting the shear deformations of SRM:

1. Rock particles continue to rotate and shift with time under the action of the shear load (**Figure 6A**). In this case, rock particles on the shear surface will rotate and squeeze the surrounding soil particles under the action of the shear stress;
2. Rock particles, especially the flake rock particles on the shear surface, undergo time-related fatigue fracture under the continuous application of loading (**Figure 6B**).

In the shear creep tests, it is observed that many of the flake rock particles on the shear surface are fractured in SRM sample with low water content, as shown in **Figure 7A**. Rock particles rotate with time under the action of shear stress in SRM sample with high water content, as shown in **Figure 7D**. In shear creep test of SRM, the deformation of the SRM is contributed by both deformation mechanisms. Mechanism one can affect the creep properties of soil at high and low shear stress values, while Mechanism 2 characterizes the creep deformation of SRM with low water content. Similar phenomena are also observed by Hu et al. [9] and Wei et al. [19]. Discrete element method could resolve the motion of every single grain in the system under consideration of a model for the inter-particle forces [20–22]. Therefore, focusing on particle-based simulations of the processes that are investigated in our experiments is necessary in future work [23].

CONCLUSION

Multi-loading shear creep tests are performed on SRM samples obtained from the Dahua landslide with different water contents. Based on the test results, the following conclusions can be drawn:

1) There are three stages of creep deformation in a shear creep test of SRM including transient creep, steady-state creep, and

accelerated creep. The shear strain accumulated after stabilization increases with water content under the same shear stress.
2) The long-term strength of SRM can be obtained using the isochronous curve method. The long-term strength of SRM decreases with the increase of water content.
3) Based on the results of the shear creep tests, a modified Burgers model is proposed, which takes into account of the effect of water content on the creep behavior of SRM. The creep curves of SRM with different water contents predicted using the Burgers model developed agree well with the test data.
4) Shear creep deformation is dominated by fractures of large particles at low water content, but by rotations of large particles at high water content.

DATA AVAILABILITY STATEMENT

The raw data supporting the conclusions of this article will be made available by the authors, without undue reservation.

AUTHOR CONTRIBUTIONS

All authors listed have made a substantial, direct, and intellectual contribution to the work and approved it for publication.

FUNDING

Financial supports from the National Key R&D Program of China (2017YFC1501100), the National Natural Science Foundation of China (Grant Nos. 11772116), and the Qinglan project are gratefully acknowledged.

REFERENCES

1. Pánek T, Klimeš J. Temporal Behavior of Deep-Seated Gravitational Slope Deformations: A Review. *Earth-Science Rev* (2016) 156:14–38. doi:10.1016/j.earscirev.2016.02.007
2. Kang Y, Lu Z, Zhao C, Xu Y, Kim J-w., Gallegos AJ. InSAR Monitoring of Creeping Landslides in Mountainous Regions: A Case Study in Eldorado National Forest, California. *Remote Sensing Environ* (2021) 258:112400. doi:10.1016/j.rse.2021.112400
3. Liu SQ, Hong BN, Cheng T, Liu X. Models to Predict the Elastic Parameters of Soil-Rock Mixture. *J Food Agric Environ* (2013) 11(2):1272–6.
4. Huang S, Ding X, Zhang Y, Cheng W. Triaxial Test and Mechanical Analysis of Rock-Soil Aggregate Sampled from Natural Sliding Mass. *Adv Mater Sci Eng* (2015) 2015:1–14. doi:10.1155/2015/238095
5. Xu W-J, Wang S, Zhang H-Y, Zhang Z-L. Discrete Element Modelling of a Soil-Rock Mixture Used in an Embankment Dam. *Int J Rock Mech Mining Sci* (2016) 86:141–56. doi:10.1016/j.ijrmms.2016.04.004
6. Wang H, Sha C, Xu W, Meng Q. Research on Strength of Soil-Rock Mixture Based on Particle Discrete Element Method. *China Civil Eng J* (2020) 53:106–14. doi:10.15951/j.tmgcxb.2020.09.012
7. Xu W-J, Hu R-L, Tan R-J. Some Geomechanical Properties of Soil-Rock Mixtures in the Hutiao Gorge Area, China. *Géotechnique* (2007) 57:255–64. doi:10.1680/geot.2007.57.3.255
8. Zhang Z-L, Xu W-J, Xia W, Zhang H-Y. Large-scale *In-Situ* Test for Mechanical Characterization of Soil-Rock Mixture Used in an Embankment Dam. *Int J Rock Mech Mining Sci* (2016) 86:317–22. doi:10.1016/j.ijrmms.2015.04.001
9. Hu X, Sun M, Tang H, Xie N, Guo J. Creep Tests of Gravel-Soil of Majiagou Landslide in Three Gorges Reservoir Area. *Rock Soil Mech* (2014) 35(11):3163–9+3190. doi:10.16285/j.rsm.2014.11.028
10. Guo H, Guo R, Nan Y, Zhang P, Liu K. Burgers Model of Creep Properties of Colluvial Soil-Rock Mixture. *Acta Scientiarum Naturalium Universitatis Sunyatseni* (2020) 59:64–69. doi:10.13471/j.cnki.acta.snus.2020.05.13.2020d019
11. Abraham MT, Satyam N, Lokesh R, Pradhan B, Alamri A. Factors Affecting Landslide Susceptibility Mapping: Assessing the Influence of Different Machine Learning Approaches, Sampling Strategies and Data Splitting. *Land* (2021) 10:989. doi:10.3390/land10090989
12. Rafiei Sardooi E, Azareh A, Mesbahzadeh T, Soleimani Sardoo F, Parteli EJR, Pradhan B. A Hybrid Model Using Data Mining and Multi-Criteria Decision-Making Methods for Landslide Risk Mapping at Golestan Province, Iran. *Environ Earth Sci* (2021) 80:1–25. doi:10.1007/s12665-021-09788-z
13. Jiang Z, Wang H, Xie W. Deformation Mechanism of deposit Landslide Induced by Fluctuations of Reservoir Water Level Based on Physical Model Tests. *Environ Earth Sci* (2021) 80:1–13. doi:10.1007/s12665-021-09673-9
14. Wang H, Sun G, Sui T. Landslide Mechanism of Waste Rock Dump on a Soft Gently Dipping Foundation: a Case Study in China. *Environ Earth Sci* (2021) 80:1–10. doi:10.1007/s12665-021-09407-x
15. Tang H, Li H, Duan Z, Liu C, Wu G, Luo J. Direct Shear Creep Characteristics and Microstructure of Fiber-Reinforced Soil. *Adv Civil Eng* (2021) 2021:1–12. doi:10.1155/2021/8836293
16. Wang X, Wang J, Zhan H, Li P, Qiu H, Hu S. Moisture Content Effect on the Creep Behavior of Loess for the Catastrophic Baqiao Landslide. *Catena* (2020) 187:104371. doi:10.1016/j.catena.2019.104371
17. Yao W, Hu B, Zhan H, Ma C, Zhao N. A Novel Unsteady Fractal Derivative Creep Model for Soft Interlayers with Varying Water Contents. *KSCE J Civ Eng* (2019) 23:5064–75. doi:10.1007/s12205-019-1820-5
18. Mansouri H, Ajalloeian R. Mechanical Behavior of Salt Rock under Uniaxial Compression and Creep Tests. *Int J Rock Mech Mining Sci* (2018) 110:19–27. doi:10.1016/j.ijrmms.2018.07.006
19. Wei H, Xu W, Xu X, Meng Q-S, Wei C-F. Mechanical Properties of Strongly Weathered Rock – Soil Mixtures with Different Rock Block Contents. *Int J Geomechanics* (2018) 18:1–12. doi:10.1061/(ASCE)GM.1943-5622.0001131
20. Gladkyy A, Schwarze R. Comparison of Different Capillary Bridge Models for Application in the Discrete Element Method. *Granular Matter* (2014) 16:911–20. doi:10.1007/s10035-014-0527-z
21. Zhang Y, Shao J, Liu Z, Shi C, De Saxcé G. Effects of Confining Pressure and Loading Path on Deformation and Strength of Cohesive Granular Materials: a Three-Dimensional DEM Analysis. *Acta Geotech.* (2019) 14:443–60. doi:10.1007/s11440-018-0671-4
22. Elekes F, Parteli EJR. An Expression for the Angle of Repose of Dry Cohesive Granular Materials on Earth and in Planetary Environments. *Proc Natl Acad Sci U.S.A* (2021) 118, e2107965118. doi:10.1073/pnas.2107965118
23. Sun M, Tang H, Wang M, Shan Z, Hu X. Creep Behavior of Slip Zone Soil of the Majiagou Landslide in the Three Gorges Area. *Environ Earth Sci* (2016) 75:1–12. doi:10.1007/s12665-016-6002-x

Conflict of Interest: The authors declare that the research was conducted in the absence of any commercial or financial relationships that could be construed as a potential conflict of interest.

Publisher's Note: All claims expressed in this article are solely those of the authors and do not necessarily represent those of their affiliated organizations, or those of the publisher, the editors and the reviewers. Any product that may be evaluated in this article, or claim that may be made by its manufacturer, is not guaranteed or endorsed by the publisher.

frontiers | Frontiers in Physics

ORIGINAL RESEARCH
published: 14 July 2022
doi: 10.3389/fphy.2022.892566

SPH Analysis of Sliding Material Volume and Influence Range of Soil Slope Under Earthquake

Weijie Zhang[1], *Ruihua Yu*[2]*, *Yu Chen*[2] *and Shuxin Chen*[2]

[1]Key Laboratory of Geomechanics and Embankment Engineering of Ministry of Education, Hohai University, Nanjing, China, [2]College of Civil and Transportation Engineering, Hohai University, Nanjing, China

The post-failure process of soil slope triggered by earthquake is usually characterized by large deformation, which can be properly addressed by SPH simulation. Meanwhile, it is of engineering significance to evaluate the sliding volume and influence range after the failure of soil slope. The simulation method is based on the Drucker–Prager constitutive model and the SPH method. The fixity boundary and free boundary particles are adopted to realize the application of ground motion and the simulation of free field boundary, and this study proposes a dynamic analysis model for the whole-failure process simulation of soil slope under earthquakes. By comparing the PGA amplification coefficients obtained from the model test and numerical simulation, the accuracy of ground motion input and ground motion response simulation is verified. Then, the proposed dynamic analysis method is used to simulate a shaking table test of soil slope in the literature. The results of the deformation of the soil slope after the test are compared to verify the accuracy of the analysis method in the soil slope displacement and the influence range under the earthquake action. Finally, by comparing the SPH results of slopes under different angles with and without vibration, this study obtains the variation rules of sliding material volume and the influence range of soil slope under seismic vibration. The greater the slope angle is, the greater the displacement of the slope will be with vibration, and the sliding material volume will present different trends under different displacement thresholds. Moreover, the horizontal displacement of the slope under the effect of an earthquake increases nonlinearly with the increase of slope incline angle.

Keywords: SPH, soil slope, earthquake, sliding material volume, influence range

OPEN ACCESS

Edited by:
Eric Josef Ribeiro Parteli, University of Duisburg-Essen, Germany

Reviewed by:
Wuwei Mao, Tongji University, China
Cheng Liu, Nanjing Forestry University, China

***Correspondence:**
Ruihua Yu
191304010009@hhu.edu.cn

Specialty section:
This article was submitted to Interdisciplinary Physics, a section of the journal Frontiers in Physics

Received: *09 March 2022*
Accepted: *30 May 2022*
Published: *14 July 2022*

Citation:
Zhang W, Yu R, Chen Y and Chen S (2022) SPH Analysis of Sliding Material Volume and Influence Range of Soil Slope Under Earthquake. Front. Phys. 10:892566. doi: 10.3389/fphy.2022.892566

INTRODUCTION

Landslide disaster is a very important part of the post-earthquake disaster, which has brought significant threat to peoples life and property safety. For example, the M_L 8.0 Wenchuan earthquake in 2008 triggered more than 60,000 landslides [1], among which the sliding distance of the Tangjiashan landslide reached 900 m [2], the Wangjiayan landslide reached 550 m [3], and the Donghekou landslide reached 2,400 m [4]. In 2017, the M_L 7.0 earthquake in Jiuzhaigou County, Sichuan Province, triggered more than 4,800 landslides, affecting a total area of 9.6 km^2, including a typical landslide in the Wuhuahai–Shamo section with a horizontal distance of about 200 m and the influence area about 12,000 m^2 that completely blocked the road with a blocking length about 70 m [5]. According to the investigation, these landslides have the characteristics of fast speed, long sliding distance, and large impact [6], showing the characteristics of large deformation. Previous studies [7,

8] have found that the catastrophic consequences caused by landslides are often quantified by the volume of sliding soil [7], and the number of affected bodies and possible damage degree can be quantitatively determined only by determining the size of the influence range [8]. Therefore, it is of great significance to analyze the sliding material volume and influence range of soil slope failures caused by the earthquake.

From the historical perspective, there have been some experiments on the sliding of blocks on surfaces subjected to different types of excitation aiming at modeling the input of energy from earthquakes. Such experiments used a slider on a hard surface and have both reproduced the Gutenberg–Richter's law or the Omori's law and brought groundbreaking insights into the physics of landslides triggered by earthquakes [9, 10]. In addition to these experiments, some numerical methods have also been developed to simulate the physical process of slope failure under the energy from earthquakes. The commonly used methods for slope analysis under earthquakes in geotechnical engineering include limit analysis, the permanent displacement method (Newmark method), the finite element analysis (FEM), the finite difference method (FDM), and so on. However, the limit analysis method [11, 12] relies on the location of the assumed slip surface and cannot determine the influence range of landslides after slope failure. The permanent displacement method (Newmark method) [13, 14] is only used to judge whether the slope fails under an earthquake, and the calculated displacement is not the real flow distance of the slope. In addition, the slope failure process triggered by earthquakes is often characterized by large deformation. Therefore, it is difficult to use the FEM [15, 16] and FDM [17, 18] to simulate the post-failure process of soil slope. At the same time, the FEM and FDM combined with the shear strength reduction procedure produce misleading results for the determination of slope slip surface [7]. Therefore, it is necessary to adopt appropriate approaches to simulate soil slope failure and determine the slip surface [7]. The newly developed meshless method is one of the means to address this problem, among which the smooth particle hydrodynamics (SPH) method is the most widely used [19]. The SPH method has some unique advantages in simulating the large deformation process, the free interface problem, and the deformation boundary of materials, so it has been widely applied in geotechnical engineering [20].

Some researchers have adopted the SPH method in the dynamic stability analysis and post-failure process simulation of slopes under the action of an earthquake. For example, Huang Yu et al. [21, 22] conducted the flow process simulations for landslides induced by the Wenchuan earthquake. He et al. [23] studied the influence of initial slope shape on the convection-slip process by using the SPH model. Chen et al. [24] simulated the deformation of soil slope under the earthquake action with the three-dimensional SPH model. Bao et al. [6, 25] used an SPH method based on the elasto-plastic model and the fluid model to simulate the startup process, solid–liquid change process, and large deformation sliding process of landslides. These research studies mainly focused on the failure process simulation of soil slopes under the earthquake, the verification of the dynamic analysis methods, and their applicability. However, the influences of related parameters, such as slope size and slope angle, on the sliding material volume and the influence range are not clearly revealed.

In this article, based on the Drucker–Prager model and the SPH method for the solid phase, the fixity boundary particles and free boundary particles were used to apply the ground motion and simulate the free-field boundary, and a dynamic analysis method was proposed for the soil slope under earthquake. In addition, the Linked list searching method was used as the Nearest Neighbor Particle Search (NNPS) method, and the SPH dynamic analysis method is established based on the OpenMP parallel framework that can improve computational efficiency. The proposed method was used to analyze a model test and a shaking table test of a soil slope in literature, and herein, the results were compared to validate the accuracy of the proposed method. Finally, by comparing the SPH simulation results of slopes with different angles and with or without earthquakes, the variation rule of sliding material volume and the influence range of soil slope under the earthquake were analyzed and discussed.

PRINCIPLE OF THE SPH DYNAMIC ANALYSIS METHOD

SPH Fundamentals

The basic idea of SPH is to discretize a continuous entity in the space into a series of particles. All information, such as mass, velocity, stress, and deformation, is carried by these particles without any link between them. During the whole simulation process, the SPH method tracks the movement information of each particle at each moment. The characteristics of no mesh and interaction between particles make it easier to deal with the large-deformation problem by eliminating the mesh distortion and distortion in the traditional Lagrangian methods [26].

The core ideas of the SPH method include the smooth approximation and particle approximation of a function. The smooth approximation means that a macroscopic physical function is represented by the integral form. Particle approximation means that the movement information of a particle is replaced by the weight-averaged summation of the movement information of all nearby particles within the influence domain. The radius of the influence domain, defined as the smooth length, is determined artificially according to the accuracy of a specific problem [27]. The smooth approximation can be expressed in the following form

$$< f(x) > = \int_{\Omega} f(x') W(x - x', h) dx', \tag{1}$$

where W is the smooth kernel function, h is the smooth length, and x is the coordinate of a particle.

The smooth particle approximation of a physical function and its derivatives can be expressed as

$$< f(x) > = \sum_{j=1}^{N} m_j \frac{f_i(x')}{\rho_j} W(x - x', h), \tag{2}$$

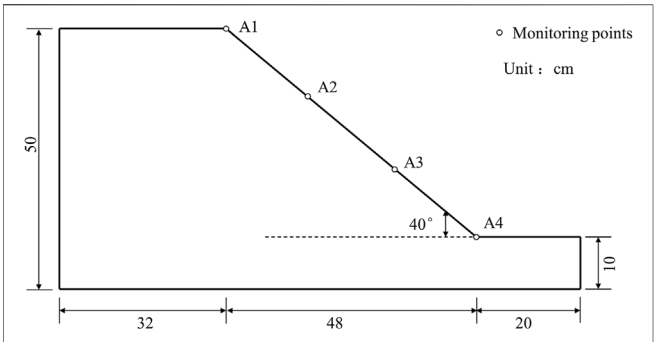

FIGURE 1 | Slope dimension and monitoring point locations.

$$\frac{\partial < f(x) >}{\partial x} = \sum_{j=1}^{N} m_j \frac{f_i(x')}{\rho_j} \frac{\partial W(x - x', h)}{\partial x}, \tag{3}$$

where m is the mass, ρ is the density, and j is the particle number. In this study, the cubic B-spline function was selected as the smooth function to calculate the value of W [6].

Governing Equations and Constitutive Model

For the geotechnical engineering problem, the governing equations in the SPH method include the continuity equation and the momentum conservation equation, combined with a specific elasto-plastic constitutive model [27]. According to the conservation of mass, the SPH approximate format of the continuous equation is as follows

$$\frac{d\rho_i}{dt} = \rho_i \sum_{j=1}^{N} \frac{m_j}{\rho_j} \left(v_i^a - v_j^a\right) \frac{\partial W_{ij}}{\partial x_i^a}, \tag{4}$$

where t is time, W_{ij} is the smooth kernel function of particle j evaluated at particle i, v is the velocity, a is the coordinate index, and i and j are particle numbers.

The momentum equation is derived from Newton's second law as follows,

$$\frac{dv_i^a}{dt} = \sum_{j=1}^{N} m_j \left(\frac{\sigma_i^{ab}}{\rho_i^2} + \frac{\sigma_j^{ab}}{\rho_j^2} - \delta^{ab} \Pi_{ij}\right) \frac{\partial W_{ij}}{\partial x_i^b} + \frac{F_i^a}{\rho_i}, \tag{5}$$

where σ is the stress of soil particles, a and b are coordinate indexes, δ^{ab} is the Dirac function, and F_i is the external force. The artificial viscosity term Π_{ij} is used to prevent the non-physical penetration of particles. The calculation method of Π_{ij} is given in Ref. [28].

The stress–strain relationship of soil can be described by a specific constitutive model. Currently, many constitutive models have been introduced into the framework of the SPH method, such as the elastic model [29], the Drucker–Prager model [30], the unsaturated soil model [28], and the unified constitutive model of granular materials [31]. Among them, the Drucker–Prager model is a widely used model in the SPH method. Therefore, it is adopted as the constitutive model of soil in this study. Bui and Fukagawa described this model with unassociated flow rules in detail in the literature [32]. According to their work, the incremental form of this model is

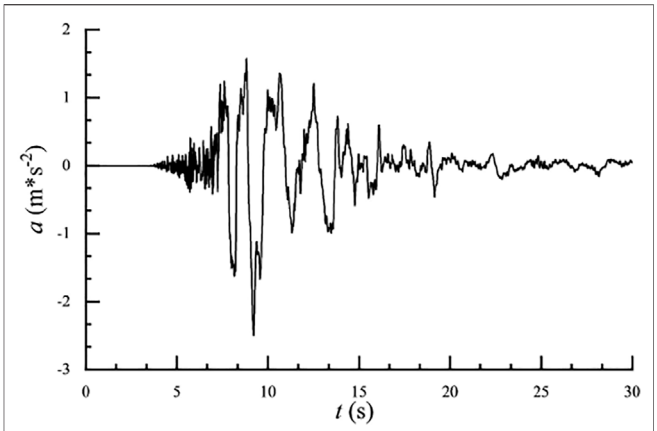

FIGURE 2 | Acceleration time series of KOBE wave.

TABLE 1 | Table of parameters in SPH simulation of the model test.

Parameter	Value	Parameter	Value
Elastic module (MPa)	5.0	Cohesion (Pa)	1,800
Poisson's ratio	0.25	Friction angle (°)	32.0
Soil skeleton density (kg/m^3)	2,650	Initial void ratio	0.75

$$\begin{pmatrix} d\sigma_{xx} \\ d\sigma_{yy} \\ d\sigma_{zz} \\ d\sigma_{xy} \end{pmatrix} = \left\{ \begin{bmatrix} \lambda_e + 2\mu_e & \lambda_e & 0 \\ \lambda_e & \lambda_e + 2\mu_e & 0 \\ \lambda_e & \lambda_e & 0 \\ 0 & 0 & \mu_e \end{bmatrix} - \frac{1}{C} \begin{bmatrix} A_{xx}^g A_{xx}^f & A_{xx}^g A_{yy}^f & A_{xx}^g A_{xy}^f \\ A_{yy}^g A_{xx}^f & A_{yy}^g A_{yy}^f & A_{yy}^g A_{xy}^f \\ A_{zz}^g A_{xx}^f & A_{zz}^g A_{yy}^f & A_{zz}^g A_{xy}^f \\ A_{xy}^g A_{xx}^f & A_{xy}^g A_{yy}^f & A_{xy}^g A_{xy}^f \end{bmatrix} \right\} \begin{pmatrix} d\epsilon_{xx} \\ d\epsilon_{yy} \\ d\epsilon_{xy} \end{pmatrix}, \tag{6}$$

where λ_e and μ_e are Ramet constants, which can be calculated by the elastic modulus E and Poisson's ratio υ, and $d\varepsilon_{ij}$ is the total strain increment. Other components can be calculated as follows:

$$A_{ij}^f = \lambda_e f_{kk} + 2\mu_e f_{ij}. \tag{7}$$

$$A_{ij}^g = \lambda_e g_{kk} + 2\mu_e g_{ij}. \tag{8}$$

$$C = \lambda_e f_{kk} g_{ll} + 2\mu_e f_{kl} g_{kl} + g_{kk}. \tag{9}$$

f is the yield function that can be found in the work of Bui et al [32], as shown in the formula below

$$f(I_1, J_2) = \sqrt{J_2} + \alpha_\phi I_1 - K_c = 0, \tag{10}$$

where $I_x = \sigma^{xx} + \sigma^{yy} + \sigma^{zz}$ and $J_2 = \frac{1}{2} s^{\alpha\beta} s^{\alpha\beta}$ are the first and second invariants of the stress tensor, respectively. The constants α_ϕ and K_c can be obtained from the internal friction angle and the cohesion [33].

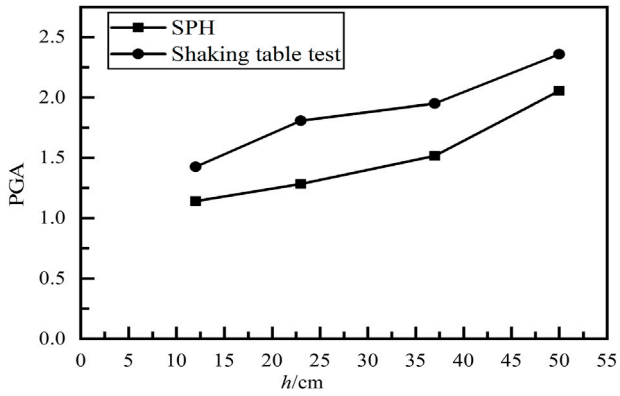

FIGURE 3 | Comparison of PGA amplification coefficient between SPH simulation and the model test.

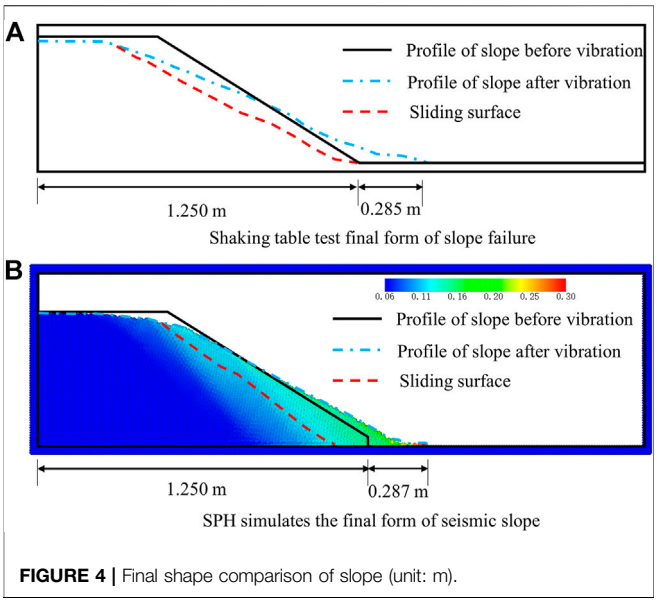

FIGURE 4 | Final shape comparison of slope (unit: m).

TABLE 2 | Table of parameters in SPH simulation of a soil slope vibration table test.

Parameter	Value	Parameter	Value
Elastic module (MPa)	5.0	Cohesion (Pa)	500
Poisson's ratio	0.25	Friction angle (°)	40.0
Soil skeleton density (kg/m^3)	2,650	Initial void ratio	0.80

Boundary Treatment Approach

The boundary in this study comprises several layers of virtual boundary particles, which have different particle types compared with the moving particles (soil particles). It is assumed that the boundary particle has a virtual velocity, and the influence of the boundary particle on the moving particle is determined according to the relative distance between the boundary particle and the moving particle. In addition, the boundary effect is calculated only when the moving particle approaches the boundary particle. The dynamic load is applied by applying acceleration to the bottom boundary particles. The principle is similar to the fixity boundary proposed by Hiraoka et al. [34], where the virtual velocity of boundary particles can be expressed as follows:

$$V_B = (1-\beta)V_A + \beta V_{seismic}, \tag{11}$$

where V_A, V_B, and $V_{seismic}$ are the soil particle velocity, the boundary virtual velocity, and the seismic wave velocity, respectively. $\beta = min(\beta_{max}, 1 + d_B/d_A)$ is related to the distance between the soil particle and the boundary particle.

In order to reduce the reflection of seismic waves, the left and right boundaries are set to the free-field boundary and the particles are assigned to a different particle type. In the SPH simulation, the free-field boundary is forced to move, and the outward waves generated by soil particles in the calculation area are appropriately absorbed. To achieve this goal, soil particles and free-field particles are simultaneously calculated under the earthquake and gravity, and at the same time, the unbalanced force of free-field particles is applied to soil particles for satisfying the displacement and stress conditions in the lateral boundary.

Implementation of the Dynamic Analysis Method

The linked-list searching method is used as the Nearest Neighbor Particle Search (NNPS) method [35]. At first, grids or cells are placed in the problem domain. Then, given the total number of cells at each coordinate (*nXm*, *nYm,* and *nZm*), the adjacent cell ID can be determined. When searching, only particles in the adjacent grids or cells are selected as candidate particles. For efficiency improvement, the initialization of global linked-list grid variables and the searching of adjacent grids are only performed in the first step, without repeated calculations. In addition, the subroutines of neighboring particle search are carried out at the beginning of each loop so that each step only needs to perform the neighboring particle searching once. These two improvements greatly improve computational efficiency.

Combined with the characteristics of this study, the OpenMP parallel framework [36] was used to optimize the SPH model. The difficulties of parallel optimization rely on the reasonable allocation of data storage, the reasonable storing of the physical quantities of particles to avoid excessive memory accessing, and the scheduled control of data access to avoid access conflict between different threads. Aiming at the first difficulty, the class in object-oriented programming is used to abstract the particle data, which simplifies the process of memory access. Aiming at the second difficulty, this study sets some local variables belonging to different threads in the linked-list search method and performs the local threads in parallel. Then, a global function is used to realize the summarization of local variables on different threads, complete the updating of global variables, and avoid access conflict. Zhang et al. [27] have verified the high efficiency of this parallel scheme by comparing the calculation time of slope stability analysis with different number of threads.

TABLE 3 | Table of SPH simulating cases of conceptual slope.

Case	Angle (°)	Working condition	Case	Angle (°)	Working condition
1–1	30	Without vibration	1–2	30	With vibration
2–1	40	Without vibration	2–2	40	With vibration
3–1	50	Without vibration	3–2	50	With vibration
4–1	60	Without vibration	4–2	60	With vibration

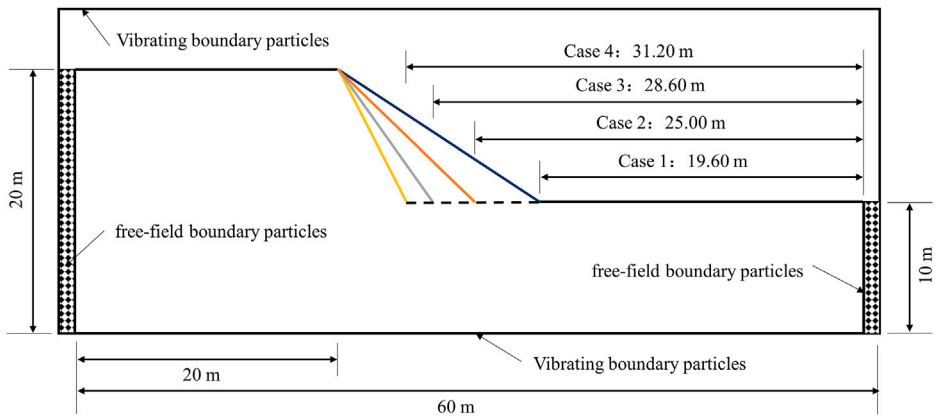

FIGURE 5 | Size chart of different slopes.

TABLE 4 | Table of parameters in SPH simulation of soil slopes.

Parameter	Value	Parameter	Value
Elastic module (MPa)	5.0	Cohesion (Pa)	500
Poisson's ratio	0.25	Friction angle (°)	20.0
Soil skeleton density (kg/m^3)	2,650	Initial void ratio	0.80

VALIDATION OF THE DYNAMIC SPH METHOD

Validation of the Seismic Response of Soil Slope

In order to verify the applicability of the dynamic SPH method in the seismic response analysis that is an outcome of the vibration applied, this study applies it to the seismic analysis of a conceptual slope in the research of Tang et al [37]. The size and monitoring point's location of the two-dimensional slope are shown in **Figure 1**. In this case, the total number of particles is 4,167, with an initial spacing of 0.01 m, including 438 free-field boundary particles, 315 fixity boundary particles, 3,412 soil particles on the soil slope, and two particles used to define the vibration space. In the initial state, the slope particles are stationary and can move under the action of gravity and earthquake after the calculation begins. The incremental time step in the SPH simulation is 4.0×10^{-5} s, and the total number of steps is 1.0×10^{6} steps, so the total simulation time for slope is 40 s. In this simulation, the time for the initialization of geostatic stress is set as 5 s, and the applying time of ground vibration is 30 s. In addition, after the application of ground vibration, the slope model is still moving, and it takes 5 s for the slope to reach the static state. Herein, the KOBE wave with a peak acceleration of 2.5 m/s^2 is used for dynamic analysis, and the loading time is 30 s, from 5 to 35 s in the simulation. The specific time history of ground acceleration is shown in **Figure 2**. The specific calculation parameters are shown in **Table 1**. On the workstation equipped with a dual Intel Xeon E5 2520V4 processor, 64 GB DDR4 memory, and Windows Server 2016 operating system, it takes nearly 2.3 h to finish one simulation by using eight threads.

Figure 3 shows a comparison of the PGA amplification coefficient between the SPH simulation and the model test. At the elevation of 10 cm, the amplification coefficient of PGA obtained by SPH simulation is around 1.2, which is slightly smaller than 1.4 in the model test. In addition, both the PGA amplification coefficient increases with the height and the PGA amplification coefficient of the SPH simulation is increased from 1.2 to 2.0, which is close to the model test. Although the results of the numerical simulation have a few differences from the results of the test, which is because the soil model used in the SPH simulation is the elastic model, the PGA amplification coefficient of the slope at the top is close to 2.0, which is consistent with existing research studies [38–40]. Therefore, the method in this article can well-input the ground motion and analyze the dynamic response of soil slope.

Validation of the Slope Deformation Under the Earthquake

In order to validate the applicability of the dynamic SPH method in the deformation analysis of soil slope, it is applied to a shaking table test, and the results are compared with the test results [41].

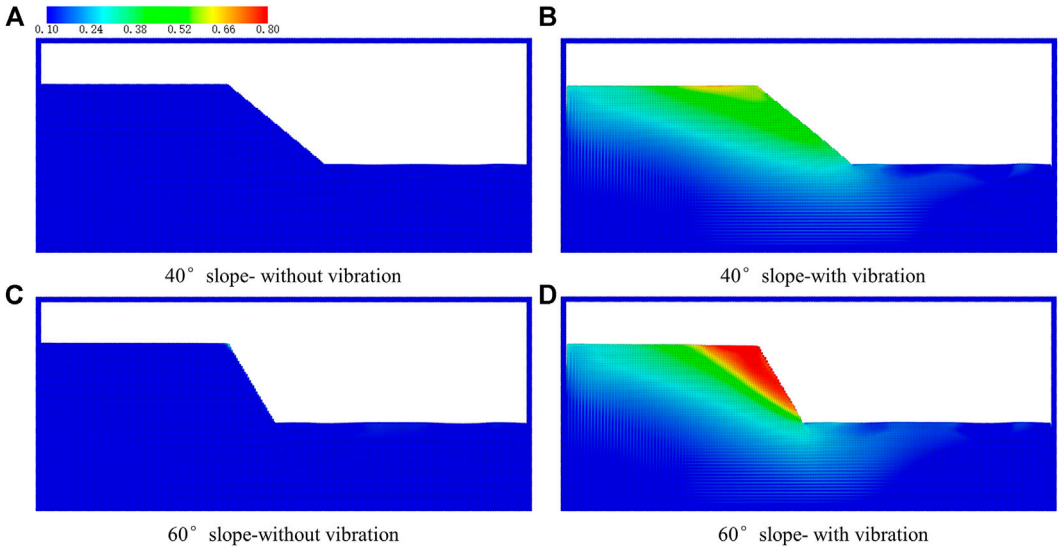

FIGURE 6 | Horizontal deformation diagram of 40°and 60°slopes with or without vibration (unit: m).

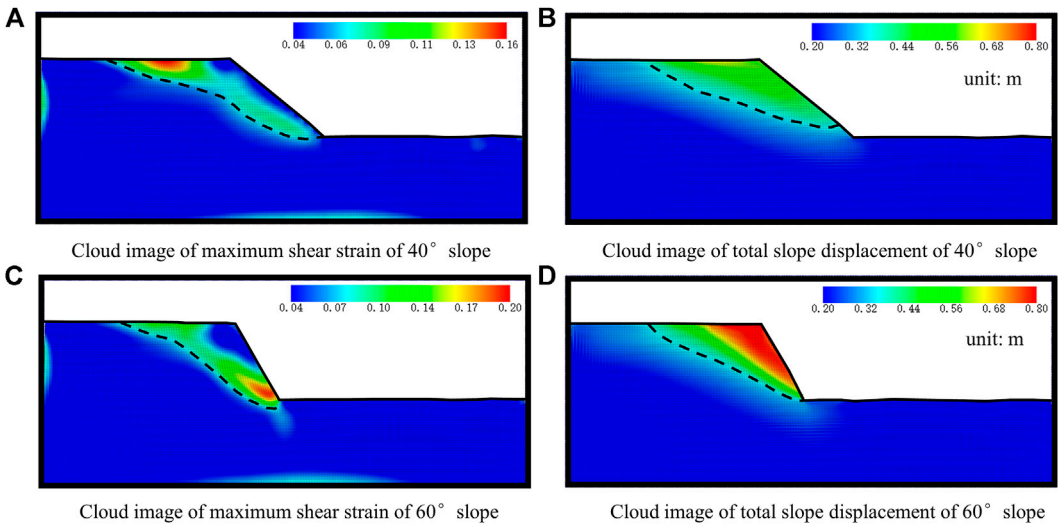

FIGURE 7 | Cloud image of shear strain and a total displacement of 40° and 60° slope with vibration.

The total number of particles in the numerical model was 6,977, with 2,118 boundary particles and 4,857 soil particles. The initial spacing of the particles was 0.01 m. Meanwhile, the left boundary is set to the free-field boundary. At the initial stage, the soil slope is still and begins to move under the action of gravity and earthquake. The incremental time in the SPH simulation is 2.5×10^{-5} s, and the total steps are 1.21×10^{7}; thus, the total time is 302.5 s. In this simulation, the time for the generation of initial geostatic stress is set as 1 s, and the applying time of ground vibration is 300 s. In addition, after the application of ground vibration, the slope model is still moving, and it takes 1.5 s for the slope to reach the static state. The model parameters are shown in **Table 2**. **Figure 4** shows the final deposit form between the SPH simulation and the shaking table test. The final shapes are basically consistent, and the maximum sliding distance of SPH simulation is very close to the test result. Therefore, the method in this article has high accuracy in the deformation analysis of soil slope under vibration loads.

APPLICATION EXAMPLE—DYNAMIC ANALYSIS OF SOIL SLOPES WITH DIFFERENT SLOPE ANGLES

Simulating Case

In order to analyze the sliding material volume and the influence range of soil slope failure with different angles under the action of

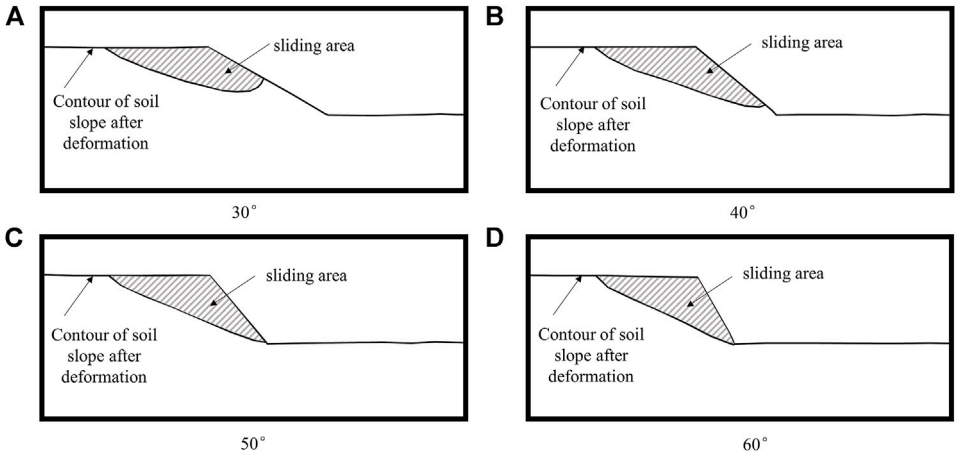

FIGURE 8 | Sliding material volume comparison when the threshold is 0.20 m.

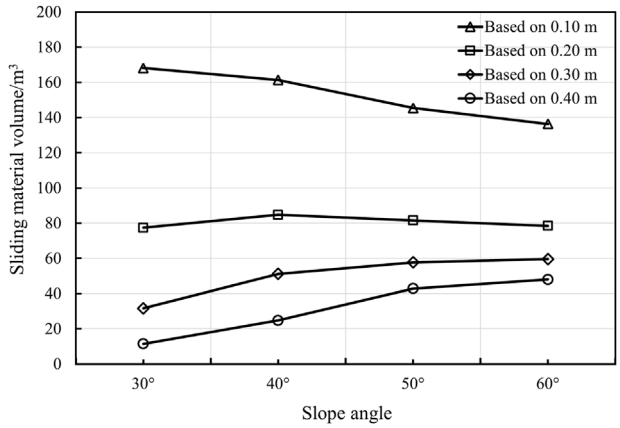

FIGURE 9 | Sliding material volume change curves of slopes with slope angles under different deformation thresholds (The longitudinal length of the slope is assumed to be 1.00 m).

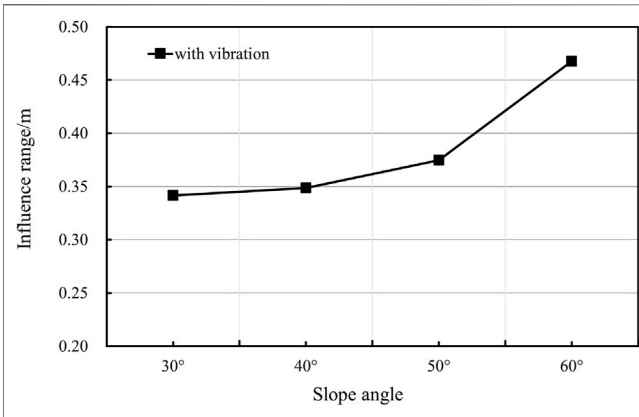

FIGURE 10 | Change curves of the influence range of slopes with slope angles.

the earthquake, this section shows four conceptual soil slopes with different angles, including 30°, 40°, 50°, and 60°. The simulating cases are shown in **Table 3**. The slope size is shown in **Figure 5**, and the locations of fixity boundary particles and free-field boundary particles are also shown in **Figure 5**. The safety factors of each slope calculated by the stability analysis method are all greater than 1.0, that is, each slope can remain stable under gravity. In this part, the total number of particles changes with slope angles, and the initial spacing of particles is uniformly set as 0.20 m. At the initial stage, the soil slope particles are stationary and can move under the action of gravity and earthquake after the calculation begins. The incremental time spacing in the SPH simulation was 5.0×10^{-5} s, the total number of steps is 6.4×10^{5} steps, and the simulation time was 32 s. In this simulation, the time for the generation of initial geostatic stress is set as 1 s, and the applying time of ground vibration is 30 s. In addition, after the application of ground vibration, the slope model is still moving, and it takes 1 s for the slope to reach the static state. As a summary, the calculation parameters are shown in **Table 4**.

In the simulation, the geostatic stress is generated by the elastic model within 1.00 s, and thereafter, the behavior of soil is described by the Drucker–Prager model. Here, the KOBE wave as shown in **Figure 2** is used for the dynamic analysis, and the loading time is 30 s, from 1.00 to 31.00 s. It takes about 2.0 h to complete a simulation using 16 threads on the same computing platform as in the previous section.

Discussion of Sliding Material Volume and Influence Range

The SPH simulations obtained the deformation of slopes with different angles under static and seismic conditions. Due to space limitation, **Figure 6** only shows the total displacement distributions of slopes with 40° and 60°. It can be seen that each slope has no obvious displacement under the geostatic condition. Under the action of the earthquake, the slope surface has obvious deformation and eventually forms an obvious slip surface. In addition, with the increase of slope

angle, the total displacement also increases, so with the same soil parameters, the greater the slope angle, the worse the stability.

At present, the shear strain is commonly used to determine the potential slip surface, while Li et al. [7] have checked the accuracy of using a displacement threshold to determine the slip surface of the slope. Herein, this study compares the potential slip surfaces of 40° and 60° slopes under the seismic action determined by shear strain and total displacement, as shown in **Figure 7**. The potential slip surface of the slope determined by the maximum shear strain has a certain degree of coincidence with the potential slip surface determined by the total displacement. The slip surface starts from the toe of the slope, and the sliding surface area determined by the two is similar. Therefore, it is proved once again that the displacement threshold can be used to determine the potential slip surface of soil slope.

In addition, 0.10, 0.20, 0.30, and 0.40 m are selected as the displacement thresholds in this study. By simplifying the deformation distribution map with the displacement threshold, a clearer distribution of the slide material can be obtained. **Figure 8** shows the sliding material volume of each slope with a displacement threshold of 0.20 m, which indicates that each slope has an obvious and regular sliding material volume.

Then, the sliding material volume of each slope under different displacement thresholds is calculated in detail, and the change curve of sliding material volume with slope angles was drawn, as presented in **Figure 9**. It can be seen that the potential sliding volume will decrease with the increase of slope angles at a small displacement threshold, but the potential sliding volumes are very close. Under the larger displacement threshold, the sliding area will increase with the increase of slope angles, but the increase is very slow. The sliding material volume decreases greatly with the increase of slope angles, but the potential sliding volume of the 60° slope still increases with a larger displacement threshold.

The maximum horizontal displacement of soil slope is regarded as the sliding distance of soil slopes under an earthquake, namely, the influence range, and the variation curve of influence range with slope angles is plotted in **Figure 10**. It can be seen that the influence range of soil slope increases linearly with the slope angle, and the angle has a significant effect on the sliding distance.

CONCLUSION

In this study, a dynamic SPH method is applied to a model test and a shaking table test of soil slopes in literature. By setting slopes of different angles and comparing the results of SPH simulation with or without an earthquake, the sliding material volume and influence range of soil slope under the action of the earthquake are analyzed, and the relationships between sliding material volume, influence range, and slope angle are obtained and discussed. Some conclusions can be derived as follows:

1) The acceleration time history and PGA amplification coefficient obtained from the dynamic SPH simulation are compared with the test results, which proves that the proposed dynamic SPH method can be used to analyze the dynamic response of soil slope.
2) Aiming at the deformation analysis of soil slope under earthquakes, the SPH simulation results of a shaking table test are compared with the test results, and the proposed method can be applied to the deformation analysis of slope under earthquakes.
3) In the analysis of sliding material volume under different slope angles, the sliding volume of the slope will decrease with the increase of slope angles at a small displacement threshold, but the sliding material volume of each slope is very similar. At the larger displacement threshold, the sliding material volume will increase with the increase of slope angles, but the increase is very slow.
4) In the analysis of influence range with different slope angles, the maximum horizontal displacement of slope under earthquakes presents a trend of nonlinear increase with the increase of slope angles.

DATA AVAILABILITY STATEMENT

The original data presented in the study are all included in the article and further inquiries can be directed to the corresponding author.

AUTHOR CONTRIBUTIONS

WZ wrote, checked, and revised this manuscript. RY wrote and revised this manuscript. YC provided revision recommendations for this manuscript. SC provided revision recommendations for this manuscript.

FUNDING

This study was supported by the National Natural Science Foundation of China (No. 51808192), the Fundamental Research Funds for the Central Universities (Grant No. B210202039), and the Natural Science Foundation of Jiangsu Province (No. BK20211575).

REFERENCES

1. Huang RQ. Mechanism and Geomechanical Modes of Landslide Hazards Triggered by Wenchuan 8.0 Earthquake. *Chin J Rock Mech Eng* (2008) 28(6): 1239–49. doi:10.1002/9780470611807.ch2
2. Hu XW, Huang RQ, Shi YB, Lv XP, Zhu HY, Wang XR. Analysis of Blocking River Mechanism of Tangjiashan Landslide and Dam-Breaking Mode of its Barrier Dam. *J Hohai Univ (Natural Sciences)* (2009) 28(1):181–9. CNKI:SUN: YSLX.0.2009-01-027.
3. Yin Y, Wang F, Sun P. Landslide Hazards Triggered by the 2008 Wenchuan Earthquake, Sichuan, China. *Landslides* (2009) 6(2):139–52. doi:10.1007/s10346-009-0148-5
4. Xu Q, Huang RQ. Kinetics Charateristics of Large Landslides Triggered by May 12th Wenchuan Earthquake. *J Eng Geology* (2008) 16(6):721–9. doi:10.3969/j.issn.1004-9665.2008.06.001

5. Xu C, Tang XB, Wang SY, Xu XW, Zhang H, Tian YY, et al. A Panorama of Landslides Triggered by the 8 August 2017 Jiuzaigou, Sichuan MS7.0 Earthquake. *Seismology Geology* (2018) 40(01):232–60. doi:10.3969/j.issn.0253-4967.2018.01.017
6. Bao Y, Huang Y, Liu GR, Wang G. SPH Simulation of High-Volume Rapid Landslides Triggered by Earthquakes Based on a Unified Constitutive Model. Part I: Initiation Process and Slope Failure. *Int J Comput Methods* (2020) 17(04):1850150–890. doi:10.1142/S0219876218501505
7. Li L, Wang Y. Identification of Failure Slip Surfaces for Landslide Risk Assessment Using Smoothed Particle Hydrodynamics. *Georisk: Assess Manag Risk Engineered Syst Geohazards* (2020) 14(2):91–111. doi:10.1080/17499518.2019.1602877
8. Wu Y, Liu DS, Zhou ZH. Mobility Assessment Model for Landslide Mass Considering Disintegration Energy Consumption in Slipping Process. *Chin J Geotechnical Eng* (2015) 37(01):35–46. doi:10.11779/CJGE201501003
9. Burridge R, Knopoff L. Model and Theoretical Seismicity. *Bull Seis Soc Amer* (1967) 57(3):341–71. doi:10.1785/bssa0570030341
10. Parteli E, Gomes M, Montarroyos E, Brito VP. Omori Law for Slidings of Blocks on Inclined Rough Surfaces. *Physica A: Stat Mech its Appl* (2001) 292(1-4):536–44. doi:10.1016/S0378-4371(00)00629-4
11. Zhou Y, Zhang F, Wang J, Gao Y, Dai G. Seismic Stability of Earth Slopes with Tension Crack. *Front Struct Civ Eng* (2019) 13(4):950–64. doi:10.1007/s11709-019-0529-3
12. Xia ZX, Li P, Cao B, Li T, Shen W, Kang H. Bayesian Estimation and Posterior Robustness of Slope Reliability. *J Hohai Univ (Natural Sciences)* (2020) 48(3):238–44. doi:10.3876/j.issn.1000-1980.2020.03.008
13. Yin X, Wang L. Block Limit Analysis Method for Stability of Slopes during Earthquakes. *J Shanghai Jiaotong Univ (Sci.)* (2018) 23(6):764–9. doi:10.1007/s12204-018-1997-7
14. Zhou Z, Zhang F, Gao Y-f., Shu S. Nested Newmark Model to Estimate Permanent Displacement of Seismic Slopes with Tensile Strength Cut-Off. *J Cent South Univ* (2019) 26(7):1830–9. doi:10.1007/s11771-019-4137-0
15. Cui Y, Liu A, Xu C, Zheng J. A Modified Newmark Method for Calculating Permanent Displacement of Seismic Slope Considering Dynamic Critical Acceleration. *Adv Civil Eng* (2019) 2019(3):1–10. doi:10.1155/2019/9782515
16. Li K, Chen GR. Finite Element Analysis of Slope Stability Based on Theory of Slip Line Field. *J Hohai Univ (Natural Sciences)* (2010) 38(2):191–5. doi:10.3876/j.issn.1000-1980.2010.02.014
17. Wang L, Li N, Wang P, Wang H. Study on Dynamic Stability of High-Steep Loess Slope Considering the Effect of Buildings. *Soil Dyn Earthquake Eng* (2020) 134:106146. doi:10.1016/j.soildyn.2020.106146
18. Zhao L, Huang Y, Chen Z, Ye B, Liu F. Dynamic Failure Processes and Failure Mechanism of Soil Slope under Random Earthquake Ground Motions. *Soil Dyn Earthquake Eng* (2020) 133:106147–7. doi:10.1016/j.soildyn.2020.106147
19. Mao Z, Liu GR, Huang Y. A Local Lagrangian Gradient Smoothing Method for Fluids and Fluid-like Solids: A Novel Particle-like Method. *Eng Anal boundary Elem* (2019) 107:96–114. doi:10.1016/j.enganabound.2019.07.003
20. Cuomo S, Pastor M, Capobianco V, Cascini L. Modelling the Space-Time Evolution of Bed Entrainment for Flow-like Landslides. *Eng Geology* (2016) 212:10–20. doi:10.1016/j.enggeo.2016.07.011
21. Huang Y, Zhang W, Xu Q, Xie P, Hao L. Run-out Analysis of Flow-like Landslides Triggered by the Ms 8.0 2008 Wenchuan Earthquake Using Smoothed Particle Hydrodynamics. *Landslides* (2012) 9(2):275–83. doi:10.1007/s10346-011-0285-5
22. Huang Y, Dai Z. Large Deformation and Failure Simulations for Geo-Disasters Using Smoothed Particle Hydrodynamics Method. *Eng Geology* (2014) 168(1):86–97. doi:10.1016/j.enggeo.2013.10.022
23. He X, Liang D, Bolton MD. Run-out of Cut-Slope Landslides: Mesh-free Simulations. *Géotechnique* (2018) 68(1):50–63. doi:10.1680/jgeot.16.P.221
24. Chen W, Qiu T. Simulation of Earthquake-Induced Slope Deformation Using SPH Method. *Int J Numer Anal Meth Geomech* (2014) 38(3):297–330. doi:10.1002/nag.2218
25. Bao Y, Huang Y, Liu GR, Zeng W. SPH Simulation of High-Volume Rapid Landslides Triggered by Earthquakes Based on a Unified Constitutive Model. Part II: Solid-liquid-like Phase Transition and Flow-like Landslides. *Int J Comput Methods* (2020) 17(04):1850149. doi:10.1142/S0219876218501499
26. Huang Y, Dai ZL, Zhang WJ. *Geo-disaster Modeling and Analysis: An SPH-Based approach[M]*. Berlin: Springer (2014).
27. Zhang W, Zheng H, Jiang F, Wang Z, Gao Y. Stability Analysis of Soil Slope Based on a Water-Soil-Coupled and Parallelized Smoothed Particle Hydrodynamics Model. *Comput Geotechnics* (2019) 108:212–25. doi:10.1016/j.compgeo.2018.12.025
28. Zhang W, Maeda K, Saito H, Li Z, Huang Y. Numerical Analysis on Seepage Failures of dike Due to Water Level-Up and Rainfall Using a Water-Soil-Coupled Smoothed Particle Hydrodynamics Model. *Acta Geotech.* (2016) 11(6):1401–18. doi:10.1007/s11440-016-0488-y
29. Huang Y, Zhang W, Dai Z, Xu Q. Numerical Simulation of Flow Processes in Liquefied Soils Using a Soil-Water-Coupled Smoothed Particle Hydrodynamics Method. *Nat Hazards* (2013) 69(1):809–27. doi:10.1007/s11069-013-0736-5
30. Bui HH, Fukagawa R. An Improved SPH Method for Saturated Soils and its Application to Investigate the Mechanisms of Embankment Failure: Case of Hydrostatic Pore-Water Pressure. *Int J Numer Anal Meth Geomech* (2013) 37:31–50. doi:10.1002/nag.1084
31. Peng C, Guo X, Wu W, Wang Y. Unified Modelling of Granular media with Smoothed Particle Hydrodynamics. *Acta Geotech.* (2016) 11(6):1231–47. doi:10.1007/s11440-016-0496-y
32. Bui HH, Sako K, Fukagawa R. Numerical Simulation of Soil-Water Interaction Using Smoothed Particle Hydrodynamics (SPH) Method. *J Terramechanics* (2007) 44(5):339–46. doi:10.1016/j.jterra.2007.10.003
33. Peng C, Wang S, Wu W, Yu H-s., Wang C, Chen J-y. LOQUAT: an Open-Source GPU-Accelerated SPH Solver for Geotechnical Modeling. *Acta Geotech.* (2019) 14(5):1269–87. doi:10.1007/s11440-019-00839-1
34. Hiraoka N, Oya A, Rajeev P, Fukagawa R. Seismic Slope Failure Modelling Using the Mesh-free SPH Method. *Int J GEOMATE* (2013) 5(1):660–5. doi:10.21660/2013.9.3318
35. Zhang WJ, Zheng H, Wang ZB, Gao YF. Study on Flowing Behavior of Soil Based on Three Dimensional and Parallelized SPH Model. *J Eng Geology* (2018) 26(5):1279–84. doi:10.13544/j.cnki.jeg.2018114
36. Zhang WJ, Gao YF, Huang Y, Maeda K. Normalized Correction of Soil-Water-Coupled SPH Model and its Application. *Chin J Geotechnical Engineer* (2018) 40(2):262–9. doi:10.11779/CJGE201802006
37. Tang WM, Ma SZ, Liu XL, Zhao X. Influence of Topographic and Geomorphic Conditions on the Dynamic Response of Slope Acceleration. *J Yangtze River Scientific Res Inst* (2019) 36(11):98–103. doi:10.11988/ckyyb.20180443
38. Sun Z, Kong L, Guo A, Xu G, Bai W. Experimental and Numerical Investigations of the Seismic Response of a Rock-Soil Mixture deposit Slope. *Environ Earth Sci* (2019) 78(24):716. doi:10.1007/s12665-019-8717-y
39. Sun Z, Kong L, Guo A, Alam M, Mohammad A. Centrifuge Model Test and Numerical Interpretation of Seismic Responses of a Partially Submerged deposit Slope. *J Rock Mech Geotechnical Eng* (2020) 12(2):381–94. doi:10.1016/j.jrmge.2019.06.012
40. Huang Q, Jia X, Peng J, Liu Y, Wang T. Seismic Response of Loess-Mudstone Slope with Bedding Fault Zone. *Soil Dyn Earthquake Eng* (2019) 123:371–80. doi:10.1016/j.soildyn.2019.05.009
41. Huang D, Qiao JP, Zhang XG, Chen YL. Experimental Research of the Topographic Effects of Slopes in Earthquake. *Chin J Rock Mech Eng* (2017) 36(3):587–98. doi:10.13722/j.cnki.jrme.2016.0952

Conflict of Interest: The authors declare that the research was conducted in the absence of any commercial or financial relationships that could be construed as a potential conflict of interest.

Publisher's Note: All claims expressed in this article are solely those of the authors and do not necessarily represent those of their affiliated organizations, or those of the publisher, the editors, and the reviewers. Any product that may be evaluated in this article, or claim that may be made by its manufacturer, is not guaranteed or endorsed by the publisher.

frontiers | Frontiers in Environmental Science

TYPE Original Research
PUBLISHED 16 September 2022
DOI 10.3389/fenvs.2022.1028373

OPEN ACCESS

EDITED BY
Biswajeet Pradhan,
University of Technology Sydney, Australia

REVIEWED BY
Yacine Achour,
University of Bordj Bou Arréridj, Algeria
Hong Haoyuan,
University of Vienna, Austria

*CORRESPONDENCE
Aqil Tariq,
at2139@msstate.edu
Shujing Qin,
Shujing.qin@whu.edu.cn

†These authors have contributed equally to this work

SPECIALTY SECTION
This article was submitted to Environmental Informatics and Remote Sensing, a section of the journal Frontiers in Environmental Science

RECEIVED 25 August 2022
ACCEPTED 05 September 2022
PUBLISHED 16 September 2022

CITATION
Khalil U, Imtiaz I, Aslam B, Ullah I, Tariq A and Qin S (2022), Comparative analysis of machine learning and multi-criteria decision making techniques for landslide susceptibility mapping of Muzaffarabad district.
Front. Environ. Sci. 10:1028373.
doi: 10.3389/fenvs.2022.1028373

Comparative analysis of machine learning and multi-criteria decision making techniques for landslide susceptibility mapping of Muzaffarabad district

Umer Khalil[1], Iqra Imtiaz[2], Bilal Aslam[3], Israr Ullah[4], Aqil Tariq[5,6*†] and Shujing Qin[7*†]

[1]ITC Faculty of Geo-information Science and Earth Observation, University of Twente, Enschede, Netherlands, [2]COMSATS University Islamabad, Islamabad Campus, Islamabad, Pakistan, [3]School of Informatics, Computing and Cyber Systems, Northern Arizona University, Flagstaff, AZ, United States, [4]Division of Earth Sciences and Geography, RWTH Aachen University, Aachen, Germany, [5]Department of Wildlife, Fisheries and Aquaculture, Mississippi State University, Mississippi State, MS, United States, [6]State Key Laboratory of Information Engineering in Surveying, Mapping and Remote Sensing, Wuhan University, Wuhan, China, [7]State Key Laboratory of Water Resources and Hydropower Engineering Science, Wuhan University, Wuhan, China

Landslides are natural disasters deliberated as the most destructive among the others considered. Using the Muzaffarabad as a case study, this work compares the performance of three conventional Machine Learning (ML) techniques, namely Logistic Regression (LGR), Linear Regression (LR), Support Vector Machine (SVM), and two Multi-Criteria Decision Making (MCDM) techniques, namely Analytical Hierarchy Process (AHP) and Technique for Order of Preference by Similarity to Ideal Solution (TOPSIS) for the susceptibility mapping of landslides. Most of these techniques have been used in the region of Northern Pakistan before for the same purpose. However, this study for landslide susceptibility assessment compares the performance of various techniques and provides additional insights into the factors used by adopting multicollinearity analysis. Landslide-inducing factors considered in this research are lithology, slope, flow direction, fault lines, aspect, elevation, curvature, earthquakes, plan curvature, precipitation, profile curvature, Normalized Difference Water Index (NDWI), Normalized Difference Vegetation Index (NDVI), roads, and waterways. Results show that SVM performs better than LGR and LR among ML models. On the other hand, the performance of AHP was better than TOPSIS. All the models rank slope, precipitation, elevation, lithology, NDWI, and flow direction as the top three most imperative landslide-inducing factors. Results show 80% accuracy in Landslide Susceptibility Maps (LSMs) from ML techniques. The accuracy of the produced map from the AHP model is 80%, but for TOPSIS, it is less (78%). In disaster planning, the produced LSMs can significantly help the decision-makers, town planners, and local management take necessary measures to decrease the loss of life and assets.

KEYWORDS

disaster planning, landslide susceptibility maps, machine learning techniques, multi-criteria decision making techniques, weight determining method

1 Introduction

Considerable life and economic losses, and harmful influences on communities, environment, and infrastructure, relentlessly disturbing land use and urban development are caused by landslides, which are common natural hazards (Shahabi and Hashim, 2015; Flentje and Chowdhury, 2018; Zhu et al., 2018; Bragagnolo et al., 2020). Due to the increasing deforestation rates, unrestrained urbanization, and rising population density, the dangers of landslides have grown (Flentje and Chowdhury, 2018; Froude and Petley, 2018; Bragagnolo et al., 2020). To reduce and manage disasters related to landslides, it is vital to appraise zones susceptible to landslides (Hong et al., 2016a; Chen et al., 2018b). A widespread assumption that future landslide locations are linked to past and present landslides is based on all the prediction-related studies involving different techniques (Capitani et al., 2013). In other words, the failures of slopes are ascertained by a specified set of regulating factors, and impending failures are anticipated to happen under identical circumstances.

Landslides usually occur in those areas where few factors, such as mountains, steep slopes, higher precipitations, and higher seismicity, are substantially found (Hong et al., 2016a; Chen et al., 2018b; Maqsoom et al., 2021; Aslam et al., 2022). Mapping of landslide susceptibility is also of eminent value for land use planning and facilitates planners in making potential development-related decisions (Erener et al., 2016; Bragagnolo et al., 2020; Aslam et al., 2022). Consequently, in current times, appraising different models for landslide susceptibility has become a key research topic globally.

Formerly many studies have used several methods aiming at the susceptibility mapping of landslides in different regions of the world. These different methods can be largely categorized as Qualitative and Quantitative methods. Different researchers extensively utilized qualitative methods until the late 1970s. Qualitative techniques weigh each landslide-causing factor based on researchers' expertise. These methods have been utilized broadly to evaluate landslide susceptible areas (Yoshimatsu and Abe, 2006; Abella and Van Westen, 2007) and are considered subjective in nature (Fall et al., 2006). Quantitative techniques, which have been developed and used frequently in recent years, comprise approaches to evaluate the associations among causes of landslides based on probabilistic models (Raghuvanshi et al., 2014). They are considered objective in nature (Girma et al., 2015). The development of computer and Geographic Information System (GIS) technology has assisted in the application of these approaches, and they have become prevalent in recent times (Shano et al., 2020).

Additionally, methods to map landslide susceptibility can be classified into four groups, namely statistical, physical-based, heuristic, and data-driven or Machine Learning (ML) methods (Chen et al., 2018b; Zhang et al., 2018). Statistical methods are used to choose and examine landslide-causing factors in areas with environmental situations like those where past landslides have been reported. Statistical methods such as the Weight of Evidence (Baeza et al., 2010; Tsangaratos et al., 2017), the Certainty Factors (Devkota et al., 2013; Azareh et al., 2019), the Frequency Ratio (Youssef et al., 2015; Chen et al., 2016a), the Analytical Hierarchy Process (AHP) (Pourghasemi et al., 2012; Shahabi et al., 2014; Kanwal et al., 2017), the Evidential Belief Function (Chen et al., 2019a), and the Technique for Order of Preference by Similarity to Ideal Solution (TOPSIS) (Najafabadi et al., 2016; Razavi and Shirani, 2019), are easy to manage and simple to comprehend and therefore have been used frequently for mapping landslide susceptibility in different areas of the world. The physical-based models handle complex parameters effectively, but these parameters can only be established by executing problematic experiments to apply to larger areas (Pradhan and Kim, 2016; Bui et al., 2017). Heuristic approaches are used by geomorphologists to examine aerial photographs or to perform site surveys. Heuristic models are usually indelicately scaled (Ruff and Czurda, 2008).

Due to the enhancement of GIS technology and easier access to land surface remote sensing images and digital earth surface elevation models, data-driven or ML models are extensively applied in landslide susceptibility mapping. The most frequently used models include the Multivariate Adaptive Regression Spline (Wang et al., 2015), the Naïve Bayes Tree (Tsangaratos and Ilia, 2016), the Adaptive Neuro-Fuzzy Inference System (Chen et al., 2019b), Random Forests (Hong et al., 2016b), Kernel Logistic Regression (Bui et al., 2016), Artificial Neural Networks (Pradhan and Lee, 2010; Pham et al., 2016b; Wang et al., 2016), Logistic Regression (LGR) (Süzen and Kaya, 2012; Umar et al., 2014; Trigila et al., 2015), Decision Trees (Saito et al., 2009; Pradhan, 2013), Support Vector Machine (SVM) (Yao et al., 2008; Marjanović et al., 2011; Xu et al., 2012; San, 2014; Pham et al., 2016b; Shirzadi et al., 2017; Pawluszek et al., 2018), and Linear regression (LR) (Onagh et al., 2012a; 2012b). Analysis of the literature reveals that every model has its benefits and limitations conditional on the characteristics of the study area and the variation of used datasets. The behavior also fluctuates accordingly among different models. Therefore, comparisons among different models are highly desired to assess landslide susceptibility.

Muzaffarabad district, situated in the state of Azad Jammu and Kashmir and falls in the lower Himalayas of Northern Pakistan, is encompassed geologically by Hazara–Kashmir

Syntax. The main boundary thrust (MBT) and Bagh-Balakot and Fault, recognized for tectonic uplift and crustal deformation, dissect this region (Kazmi and Jan, 1997; Saba et al., 2010). In Muzaffarabad city and the areas around the city, the 2005 earthquake disrupted several slopes and prompted 158 landslides (Kamp et al., 2008; Khan et al., 2011). Previously, the region has been subjected to numerous earthquakes of various extents (Rossetto and Peiris, 2009). In the future, there is a chance for a high-magnitude earthquake (Wallace et al., 2005; Raghukanth, 2008). Therefore, for activating the landslides in this region, rainfalls and earthquakes are regarded as the two major contributory processes (Owen et al., 2008).

There have been a few studies targeting this region in the past concerning the mapping of landslides. Most of the studies are confined to the landslides that resulted from the 2005 earthquake, or they just targeted the 2005 earthquake region. Moreover, most of these studies have used conventional statistical or decision-making methods to map landslide susceptibility. For example, Kamp et al. (2008) conducted a study for mapping landslide susceptibility in the 2005 earthquake region using a GIS-based multi-criteria evaluation method by exploiting eight landslide triggering factors. A few other studies that involved the assessment of landslide hazards targeting the same area are Owen et al. (2008); Khattak et al. (2010); Saba et al. (2010). Therefore the present study tried to fill the research gap by using conventional decision-making techniques and compared them with the most prevalent ML techniques.

The current research aims to present the landslide susceptibility analysis of the Muzaffarabad district using Multi-Criteria Decision Making (MCDM) and Machine Learning (ML) techniques. The methods used involves two MCDM techniques, AHP and TOPSIS, and three ML techniques, explicitly LGR, LR, and SVM. The purpose of using these various techniques is to assess the performance of each technique for the designated area. So far, several studies have been carried out using a single or two techniques, and no comparative studies have been carried out using five techniques in the targeted area. Also, this study used a set of multiple datasets derived from the latest available data; hence it provides the latest landslide susceptibility mapping. Ultimately, this research provides novel Landslide Susceptibility Maps (LSMs) and identifies the results to see how much aerial overlap between the models by susceptibility type. How much do these models geographically agree? Do these areas overlap at all?

2 Study area

Muzaffarabad district is situated in the Pakistan-administered territory of Azad Jammu and Kashmir. The district has a very hilly terrain and is located on the banks of the Neelum and Jhelum rivers. Muzaffarabad is the capital city of the state of Azad Jammu and Kashmir having geographical coordinates as 34° 21′ 30″ N and 73° 28′ 20″ E and covers an area of 20665 m^2. The Mansehra and Abbottabad district of Khyber Pakhtunkhwa bounds the district on the Western side, the Baramullah and Kupwara districts of the Indian-administered Jammu and Kashmir are on the East, and the North and South sides face the Neelum and Bagh Districts of Azad Kashmir. The district of Muzaffarabad geologically lies in the lower Himalayan region of Pakistan. The district is well known for its deadliest 7.5 magnitude earthquake in 2005, killing more than 80000 people (Kamp et al., 2008; Owen et al., 2008; Saba et al., 2010). The climate of the district varies considerably.

December, January, and February happen to be cold months. While June, July, and August are relatively warmer. The mean maximum and minimum temperatures during January are 16°C and 3°C, respectively, and the mean maximum and minimum temperature during July are about 35°C and 23°C, respectively. The annual average high and low temperatures are 22.3°C and 11.1°C, respectively. The average annual precipitation of the district is 1,242.8 mm. During the monsoon spell from June to September, the region receives the highest amount of precipitation as in the rest of the months. July is the wettest, with an average precipitation of 328.7 mm, followed by August, which has an average of 229.9 mm. The region receives slight rainfall from October to December, with the lowest average observed in November (37.2 mm). The Muzaffarabad region has experienced plenty of landslides yearly, especially after the Kashmir 2005 earthquake, especially during the rainy monsoon season in July and August (Kamp et al., 2008; Owen et al., 2008; Khattak et al., 2010). Thus, taking immediate and effective measures to counter landslide happenings is imperative. Therefore, this study tried to focus on assessing landslide susceptibility in the area, thus, paving the way for policymakers to take precautionary measures to alleviate the destruction caused by landslides (Figure 1).

3 Materials

3.1 Constructing a database of landslide conditioning factors in Muzaffarabad

Because of the development and the complex nature of landslides, there is no explicit agreement on their exact origins (Hong et al., 2016a; Bui et al., 2016). However, several conditioning factors, such as geological and topographical, besides climatic conditions, and their association with landslides have been studied by many scientists in the past (Hong et al., 2017). Anthropogenic activities also greatly influence the geological environment (Yang et al., 2017). Consequently, established on former landslide susceptibility investigations (Saha et al., 2005; Owen et al., 2008; Khattak et al., 2010; Saba et al., 2010; Pourghasemi et al., 2012;

Kanwal et al., 2017; Ali et al., 2019) and examination of the features of the Muzaffarabad region (Kamp et al., 2008; Owen et al., 2008; Khan et al., 2019), 15 landslide inducing factors including slope, aspect, elevation, lithology, curvature, plan curvature, profile curvature, flow direction, fault lines, precipitation, Normalized Difference Water Index (NDWI), Normalized Difference Vegetation Index (NDVI), distance from roads, earthquake, and distance from waterways were considered in this study.

In this study, the ASTER DEM with 30 m × 30 m resolution was used. Six geomorphometric factors, like curvature, slope, aspect, plan curvature, profile curvature, and elevation, were extracted using the DEM. The factors of NDVI and NDWI were extracted from Landsat 8 images with a spatial resolution of 30 × 30 m. Landsat 8 images were downloaded from https://earthexplorer.usgs.gov/(June 2022). NDVI was calculated using infrared (IR) and red (R) bands with the help of the following formula (Hong et al., 2016a; Chen et al., 2018b):

$$NDVI = \frac{IR - R}{IR + R} \quad (1)$$

NDWI was derived from green (G) and near-infrared (NIR) channels. NDWI was calculated using the formula (Xu, 2006):

$$NDWI = \frac{G - NIR}{G + NIR} \quad (2)$$

Geological maps of Pakistan, at a scale of 1:2,000,000, were used to produce the thematic maps of faults, earthquakes, and lithology, and fault distance was calculated using proximity analysis (Pavelsky and Smith, 2008). Pakistan Meteorological Department (PMD) station data was used to construct the precipitation map. The precipitation from the available data was calculated using the following formula (Arnoldus, 1980):

$$P = \sum_{i=1}^{12} \left(1.735 \times 10^{1.5 \times \log \frac{p_i^2}{p} - 0.8188} \right) \quad (3)$$

Where p is the average yearly rainfall while p_i represents average monthly rainfall. The annual precipitation was used to calculate rainfall erosivity in this research. The reason for using rainfall erosivity instead of direct rainfall was because rainfall erosivity highlights the area which may be affected the most due to rainfall. Topographic maps of Pakistan were used for the thematic maps of distance to roads and distance to the waterway.

The standardization and normalization of all the factors were done. All the maps of landslide trigging factors were transformed into raster format with a resolution of 30 m × 30 m Lastly, all the rasterized maps were reclassified based on the level of susceptibility for inducing landslides into five categories. To each category, a value was assigned, such as very high influence was ranked as 5, the high influence was ranked as 4, the medium influence was ranked as 3, the low influence was ranked as 2, and very low influence was ranked as 1. For categorical data like lithology, the reclassification was still based on the rating of 1–5 in such a way that every class was assigned a score based on their influence. Since all the factors were reclassified into 1 to 5 classes, the weights were obtained for each factor from the methods multiplied by its subclass weight to get the total landslide susceptibility score to produce the LSMs.

3.2 Landslide inventory and data distribution

The formulation of the aerial distribution of present landslide areas is the primary phase in landslide susceptibility mapping (Cevik and Topal, 2003). For probabilistic analysis of landslide susceptibility, precise recognition of the landslide's locality is very significant. To find the landslide distribution over the area and to produce a statistical database of landslides for the individual division of the landslide activating factors, a landslide inventory map was generated. Several researchers' used satellite and aerial photographs to prepare the landslide inventory map (Pradhan et al., 2009; Pradhan, 2010; Choi et al., 2012; Umar et al., 2014). In the current study, the past landslide areas (from 2000 to 2021) were marked using satellite data (Landsat), and historical records from official data of Pakistan. A similar methodology as of Aslam et al. (2022) was adopted for the inventory preparation.

To implement the ML techniques, both landslide and non-landslide locations are needed to produce the LSMs (Ballabio and Sterlacchini, 2012; Chen et al., 2017). Therefore, 606 past landslide locations (the center points of landslide polygons) were marked as "1," and the same number of randomly sampled non-landslide locations was marked as "0". Moreover, for the implementation of ML models, landslide inventory is split into testing and training datasets. The training dataset is used to build the model. The models examine the factors such as topographical, lithological, and hydrological from the training dataset. The testing data is used to validate the training of the model. This whole procedure, as a result, assists in proposing the weightage of individual factors. A total of 1212 datasets were used, which were randomly divided into the ratio of 2/3 and 1/3, which means 70% of the dataset was arbitrarily designated as training samples. The remaining 30% was used for testing purposes. The ratio of 70/30 is a generally accepted way of splitting data (Wang et al., 2016; Chen et al., 2018a; Wang et al., 2019).

4 Methodology

For the specified objective various topographical, geomorphological, lithological, and hydrogeological factors were used, which were selected relying on the studies that were conducted formerly and the study area's characteristics. Historical data, satellite images, and official data from the state departments were exercised to formulate a landslide conditioning

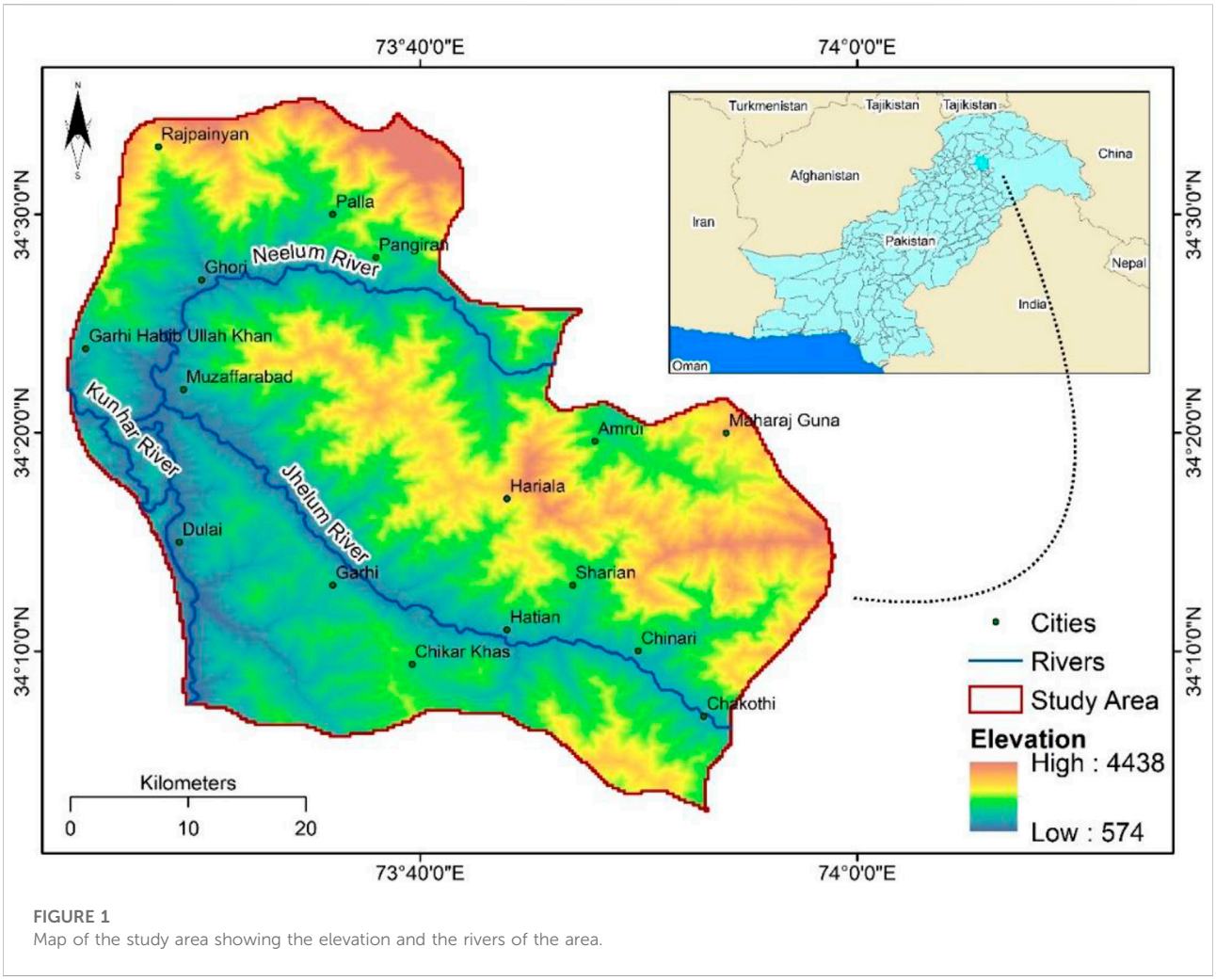

FIGURE 1
Map of the study area showing the elevation and the rivers of the area.

factors database for the study area. The LR, SVM, and LGR models were constructed using the training dataset. R programming language was used for the implementation of ML techniques. The models were constructed using 10 cross folds to prevent over-fitting and reduce inconsistency. Tuning of models was done to increase the accuracy of models. The accuracy was calculated among the predicted and actual points in testing datasets for all three ML models. The weights of individual factors were the outcome of the ML models. The weights were also obtained from the two MCDM methods. These weights were then used to prepare the final LSMs in ArcGIS using weighted overlay analysis. The produced LSMs were reclassified into five susceptibility classes, i.e., very high, high, moderate, low, and very low. These classes were generated based on equal intervals for each class. This was done based on the field visit and considering the landslides from the past. A correlation was also computed between the LSMs and the historical landslide locations to check for the accuracies of LSMs. A comprehensive overview of the methodology is shown in Figure 2. The practiced methods are discussed as follows:

4.1 Multicollinearity analysis

Multicollinearity analysis was used to evaluate the correlation among landslide conditioning factors. It is a statistical phenomenon in which a high-level relationship exists between two or more variables in a multiple regression model (O'brien, 2007). To detect multicollinearity among conditioning factors, the tolerance (TOL) and variance inflation factor (VIF) was utilized in this study. Let X = {X1, X2, . . ., XN} describe a given independent variable set and R_j^2 signify the coefficient of determination when the *jth* independent variable Xj is regressed on all other variables in the model. The following Eq. 2 was used for the computation of the VIF value:

$$VIF = \frac{1}{1 - R_j^2} \quad (4)$$

The reciprocal of the VIF value gives the TOL value. The TOL value signifies the degree of linear correlation between

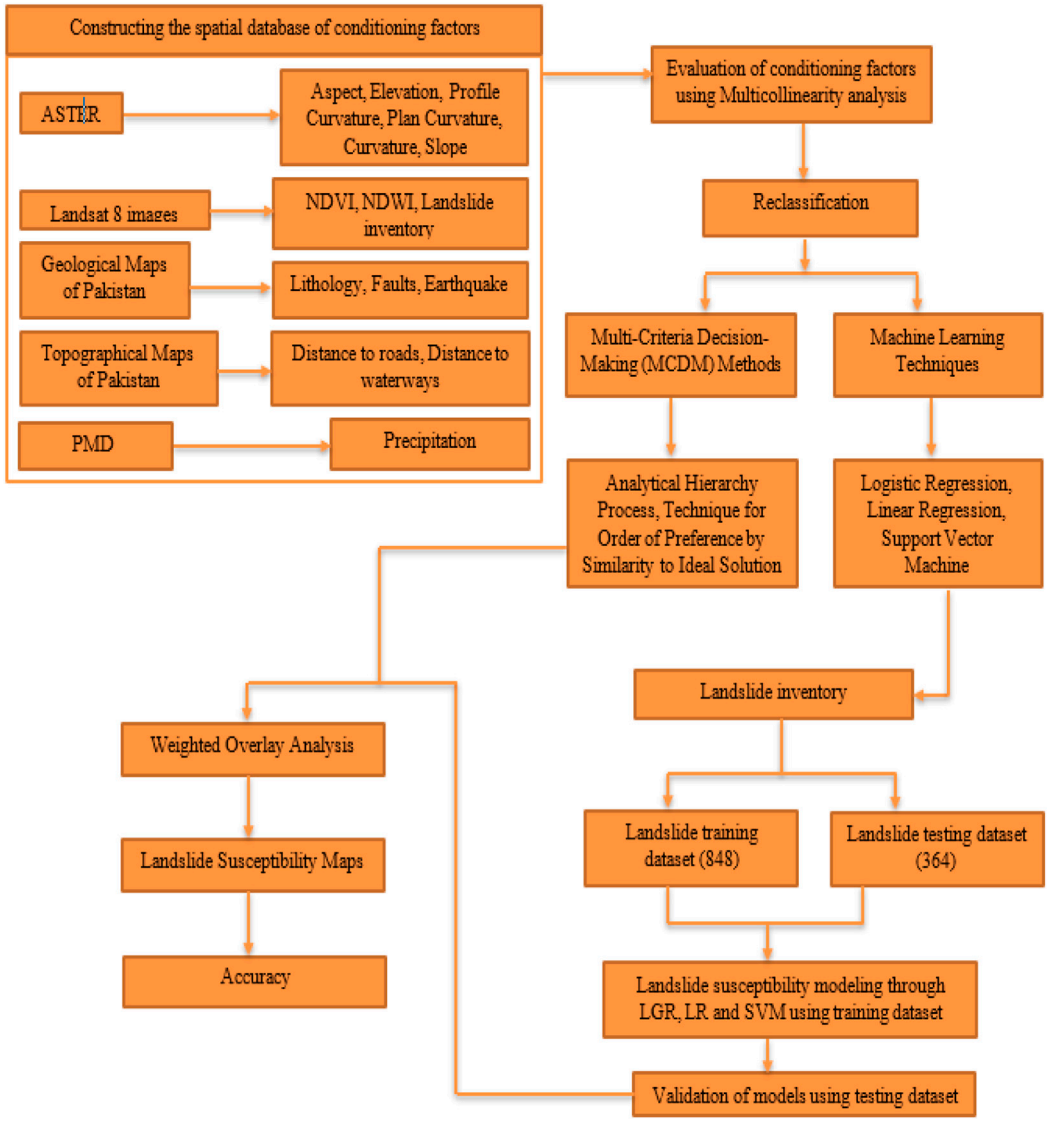

FIGURE 2
Methodology flow chart.

independent variables. If the TOL value is less than 0.1 and the VIF value is greater than 10, the corresponding factors show multicollinearity and ought to be eliminated from further analysis (Wang et al., 2019).

4.2 Support vector machine

The basic theory for SVM is the statistical learning theory (Cortes and Vapnik, 1995). The SVM reduces together model complications and the error test. SVM uses support vectors to define the margin of the hyperplane. The number of support vectors held from the first dataset is information subordinate. It differs, considering the information unpredictability caught by the information dimensionality and class distinguishableness. SVM used different kernel functions to map the data into higher dimensional space. The most popular kernel functions are linear, polynomial, radial, and sigmoid kernel functions. However, the present study used the radial basis function. The used kernel function is shown in Eq. 3 below:

$$\text{Radial basis Function: } K(x_i y_i) = e^{-\gamma\left(x_i - x_j^2\right)} \quad (5)$$

Where, r is the bias term, d is the polynomial degree, and r is the gamma term.

4.3 Logistic regression

It is a classification algorithm that assigns observations to a discrete set of classes using the logistic or sigmoid function to transform its output. Its concept is based on probability and predictive analysis algorithms. A relationship between some dependent factors and a categorical variable is clarified by this model, which might be categorical, binary, or continuous variables (Hong et al., 2016a). Using the algorithm has the advantage that there is no need for the normal distribution of variables (Pradhan and Lee, 2010). Binomial, multinomial, and ordinal are types of LGR. Independent variables that denote the landslide presence and absence in the LGR were designated as 1 and 0, respectively. The equation used for LGR is shown below (Hong et al., 2016a; Aslam et al., 2022):

$$Y = b_0 + b_1x_1 + b_2x_2 + \ldots + b_nx_n \quad (6)$$

where, Y is the dependent variable (landslide occurrence), b_0 is the intercept, all the b's are expectation of the target variable (weights), and all the x's are the independent variables. This study used a sigmoid activation function.

4.4 Linear regression

It is a supervised ML algorithm with a constant slope and is used to predict a continuous output. It reveals how the changing standard deviation of predictors and independent variables changes the dependent variable. The used equation for LR is shown below (Onagh et al., 2012a; Aslam et al., 2022):

$$L = b_0 + b_1X_1 + b_2X_2 + b_3X_3 \ldots + b_mX_m + \varepsilon \quad (7)$$

where, L is the occurrence of landslides, all the X's represent the independent variables (factors), all the b's represent the estimated coefficients (weights), and ϵ represents the model error. The used LR type in this study was multiple linear regression. The best fit line during the implementation of LR was computed using mean squared error.

4.5 Analytical hierarchy process

AHP is an MCDM technique comprising a pair-wise assessment of numerous factors contributing towards a certain cause and establishing ranks of these factors. A pair-wise comparison matrix is developed as proposed by Saaty (1990) and Saaty and Vargas (2001) for estimating the weights of different factors for solving a problem. Another tempting attribute of the AHP is the aptitude to appraise pair-wise rating variation. It allows the pair-wise relative comparison between every factor, and afterward values from 1 to 9 are assigned based on the relative importance. The following steps are very important to execute AHP: 1) to break the composite problem into different parts; 2) to assemble the conditioning factors into hierarchic order; 3) to allocate the numerical values to evaluate the comparative significance of each conditioning factor; 4) to constitute a comparison matrix and provide weights to every factor (Saaty, 1990). The implementation of the AHP was adopted from Maqsoom et al. (2021).

4.6 Technique for order of preference by similarity to ideal solution

Hwang and Yoon (1981) introduced TOPSIS, an MCDM technique that assesses the dilemma in an n × m matrix (m criteria and n alternatives). This method is founded on the notion that each designated factor must have the maximum detachment from the negative ideal (the least important factor) and the least detachment from the positive ideal (the most critical factor) (Lin and Wu, 2004). The basic principle of TOPSIS is that the decision would be the nearest to the best result and remotest from the non-ideal result. It assumes that each factor is uniformly increasing or decreasing, making it visually easy to locate the best and worst selection. Normalization is important because the factors are inconsistent in dimensions. After normalization, positive and negative ultimate results are measured. Then the detachment from the ultimate result is calculated. Lastly, the preference value is assigned to each factor (Rao and Davim, 2008; Krohling and Pacheco, 2015; Najafabadi et al., 2016; Razavi and Shirani, 2019). The implementation of the TOPSIS method was adopted from Najafabadi et al. (2016).

4.7 Model validation

It is essential to evaluate the validity of the used models in landslide susceptibility analysis since they, without validation, lack scientific significance (Pradhan and Kim, 2016). The ML models were validated by calculating their accuracy using their confusion matrixes (Deng et al., 2016; Maria Navin and Pankaja, 2016). However, for checking the logical consistency in pair-wise comparisons, the AHP method integrates an operative practice. Consistency Ratio (CR) (Saaty, 1980) is a tool that articulates the compatibility of the matrix of paired comparisons of all the parameters involved. The CR value less than 0.1 indicates that the matrix outcomes are satisfactory (Saaty, 1980); otherwise, the judgments need to be reviewed. Moreover, a logical procedure was adopted for the performance assessment of the TOPSIS method. The relative closeness coefficient (cli+) to the ideal solution was calculated for each alternative. The best alternatives are those with higher values (Krohling and Pacheco, 2015; Najafabadi et al., 2016).

TABLE 1 Outcomes of Multicollinearity analysis.

Landslide conditioning factors	Statistics	
	TOL	VIF
Aspect	0.276	3.623
Curvature	0.962	1.04
Earthquake	0.892	1.121
Elevation	0.722	1.385
Flow	0.803	1.245
Lithology	0.727	1.376
NDVI	0.596	1.678
NDWI	0.753	1.328
Plane Curvature	0.587	1.704
Precipitation	0.793	1.261
Profile Curvature	0.817	1.224
Slope	0.275	3.636
Faults	0.316	3.165
Roads	0.243	4.115
Waterways	0.461	2.16

5 Results

5.1 Relative importance analysis of conditioning factors

The importance of all the landslide conditioning factors was assessed utilizing the training set centered on multicollinearity analysis. The outcomes of the multicollinearity analysis of landslide conditioning factors are presented in Table 1. The factor of roads was found to have a VIF value that is considerably larger than the rest of the factors, but still, it is less than 10. None of the factors were found to have a VIF value larger than the threshold value of 10. Therefore, none of the factors was removed from the further processes.

5.2 Thematic maps of conditioning factors

The aspect was classified into Flat, North, Northeast, East, Southeast, South, Southwest, West, and Northwest (Figure 3A). Most of the exploratory area lies in the Northern and Southward orientations. The value of −0.0000001 is all the flat or no aspect pixels, 45 breaks between North and East, 135 breaks between East and South, 225 breaks between South and West, and 315 breaks between West and North. These orientations were reclassified into five categories to understand better the contribution level in triggering landslides. Based on the reclassification, the class intervals of −1 to −0.00000001 were weighted as 1, 0–45, and 315–360 equal to 2, 45–135 equivalent to 3, 135 to 225 equal to 4, and 225–315 equal to 5. Furthermore, the elevation was divided into five classes, from the lowest class of 575–1000 m to higher elevated areas of 1000–2000 m, 2000–3000 m, 3000–4000 m, and 4000–4438 m (Figure 3B). It can be observed that the Southwest area is low elevated while the Northeast has a higher elevation.

This region is seismically very active and has several faults in the region. Areas nearer to the fault lines have a higher potential for landslides, while as the remoteness from the fault line increases, the level of landslide susceptibility also decreases gradually. So, a buffer of 0–300 m was ranked as 5 since this region has a higher potential of landslide susceptibility while 300–600 m as 4, 600–900 m as 3, 900–1200 m as 2, 1200–1500, and >1500 m as 1 (Figure 3C). In addition to the faults, the flow direction is also among the key contributing factors in landslide susceptibility because it shows which direction the soil slush will flow. The higher the flow direction value, the higher the susceptibility potential, and vice versa. So based on this fact, it was divided into five categories depending on the possibility of susceptibility. 64–128 was ranked as 5 while 32–64 as 4, 8–32 as a 3, 2–8 as 2, and 1–2 as 1 (Figure 3D). The Northward flow has a higher susceptibility. In the considered study area, the flow is from North to South. Thus, more slopes are cut to Northward flow, resulting in higher landslide susceptibility.

The slope is also a foremost contributing factor in the landslide because steeper slope areas have a higher chance of rockfall than the gentle slope area. Hence five categories depending on the potential of susceptibility were established. >16° slopes were ranked as 5 while 12°–16° as 4, 8°–12° as 3, 4°–8° as 2, and <4° as 1 (Figure 3E). Additionally, the level of precipitation in the area increases gradually from North to South. Since higher levels of precipitation have a greater potential of triggering landslides than lower levels of precipitation, therefore the region was categorized based on the precipitation potential as 1259–1323 mm is ranked as 5 while 1203–1259 mm as 4, 1136–1203 mm as 3, 1070–1136 mm as 2, and 983–1070 mm as 1 (Figure 3F). Moreover, just like faults, areas nearer to the roads have a higher potential for landslides because the roads are constructed by cutting the toes of slopes, making them unstable. As the remoteness from the roads increases, the level of susceptibility also declines gradually. So, a buffer of 0–300 m was ranked as 5 while 300–600 m as 4, 600–900 m as 3, 900–1200 m as 2, and 1200–1500 and >1500 m as 1 (Figure 3G).

Soil moisture has a direct influence on soil compactness and rock strength. Higher soil moisture has the potential to cause landslides as compared to lesser moisture. Thus, the area with a higher NDWI value was ranked the highest (a rating of 5) and vice versa (Figure 3H). Like faults and roads, areas nearer to the water bodies have a higher potential for landslides. At the same time, as the distance increases from the water bodies, the level of

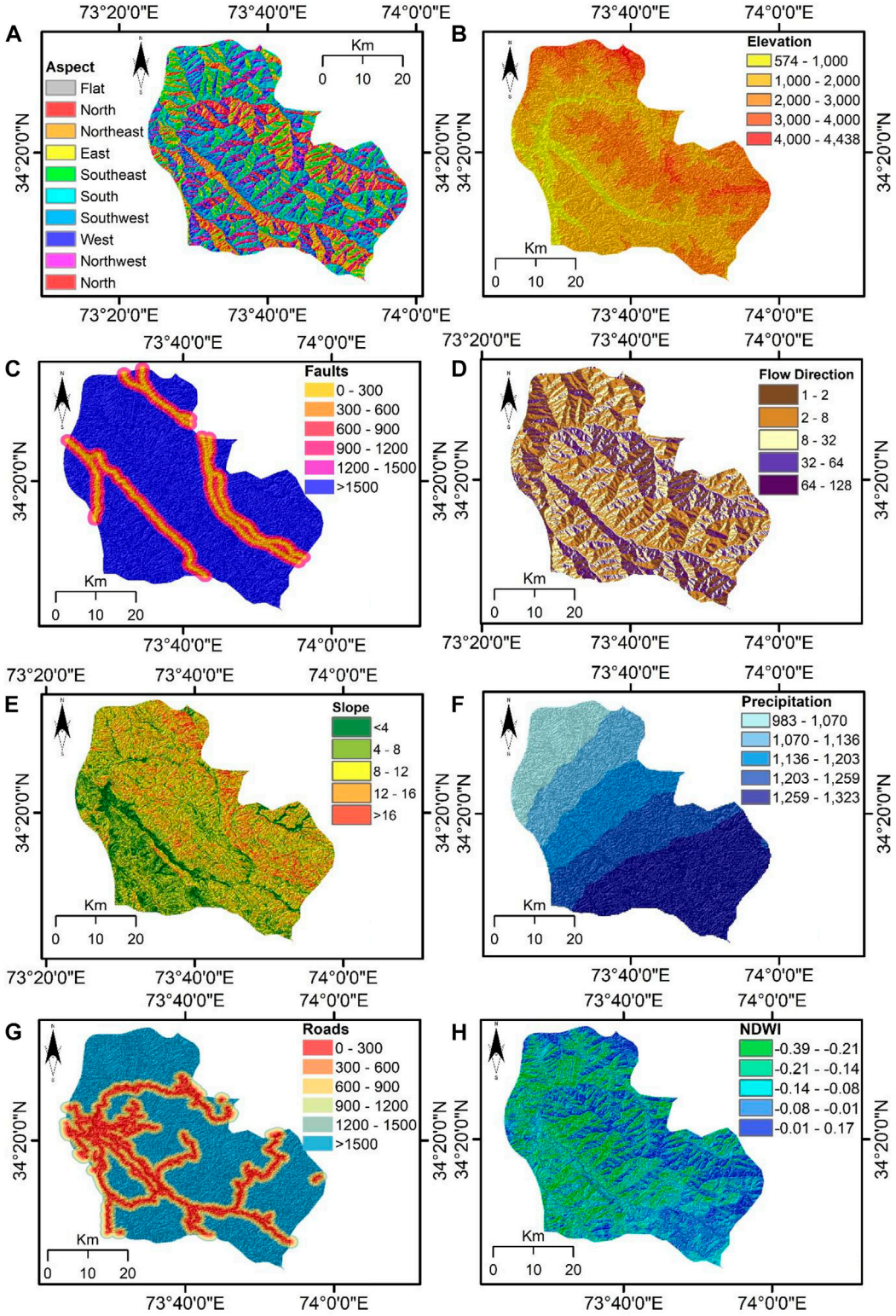

FIGURE 3
Input derived datasets: **(A)** aspects, **(B)** elevation, **(C)** faults, **(D)** flow direction, **(E)** slope, **(F)** precipitation, **(G)** roads, **(H)** NDWI, **(I)** waterways, **(J)** earthquake, **(K)** lithology, **(L)** NDVI, **(M)** plan curvature, **(N)** profile curvature, **(O)** curvature.

TABLE 2 Resulted weights of the contributing factors from different techniques.

Dataset	SVM	LGR	LR	AHP	TOPSIS
Aspect	5	4	6	8	4
Curvature	8	10	9	5	8
Earthquake	3	5	4	6	7
Elevation	11	12	12	12	12
Flow direction	10	9	11	8	10
Lithology	10	8	10	12	11
NDVI	5	7	6	5	9
NDWI	8	10	9	8	7
Plane Curvature	4	6	5	4	3
Precipitation	13	10	10	11	14
Profile Curvature	2	1	1	1	1
Slope	12	13	9	13	10
Faults	5	2	4	3	1
Roads	2	2	2	2	2
Waterways	2	1	2	2	1
Total	100	100	100	100	100

susceptibility also decreases gradually. So, a buffer of 0–300 m was ranked as 5 while 300–600 m as 4, 600–900 m as 3, 900–1200 m as 2, and 1200–1500 and >1500 m as 1 (Figure 3I). Furthermore, earthquakes have a direct role in causing landslides, as landslides occur after ground shaking. The region is in a subduction zone where seismicity is very high. The Northern portion of the exploratory area lies in a highly high seismic zone. Since this region receives larger magnitude earthquakes hence this region was classified as very high (a rating of 5), high (a rating of 4), and medium only (a rating of 3) (Figure 3J).

A larger part of the study area comprises limestone, and other prominent lithologies are slate, volcanic rock, and quartzite (Figure 3K). Limestone and slate are an example of weak lithologies. Based on the strength, these lithologies were ranked from 1 to 5 during the reclassification. The positive NDVI value shows a high concentration of vegetation, while the negative value depicts no vegetation. High vegetation covers on the slope surface reduce soil erosion and slope failure. In contrast, no vegetation on the slope increases the chances of failure as it is exposed to the atmosphere. This logic was adopted

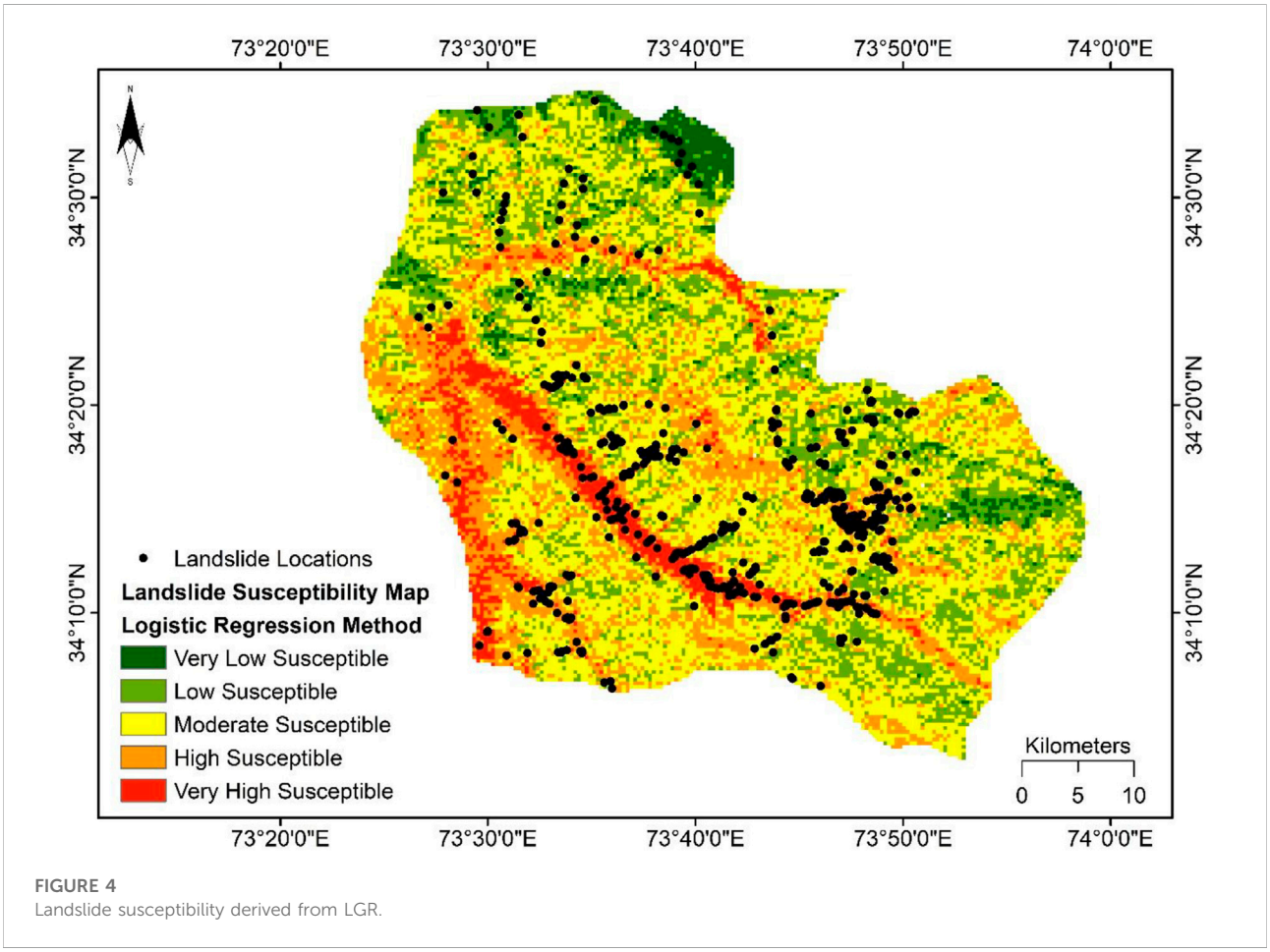

FIGURE 4
Landslide susceptibility derived from LGR.

TABLE 3 Division of different landslide susceptibility classes for different methods.

Model type		Susceptibility class				
		Very low	Low	Moderate	High	Very high
LGR	Area m^2	834	4726	8892	4819	1394
	Area %	4.04%	22.87%	43.03%	23.32%	6.75%
LR	Area m^2	404	3457	9431	6164	1209
	Area %	1.95%	16.73%	45.64%	29.83%	5.85%
SVM	Area m^2	219	2624	8713	7446	1663
	Area %	1.06%	12.70%	42.16%	36.03%	8.05%
AHP	Area m^2	1892	5353	7538	4275	1607
	Area %	9.16%	25.90%	36.48%	20.69%	7.78%
TOPSIS	Area m^2	1786	6465	7204	4030	1180
	Area %	8.64%	31.28%	34.86%	19.50%	5.71%

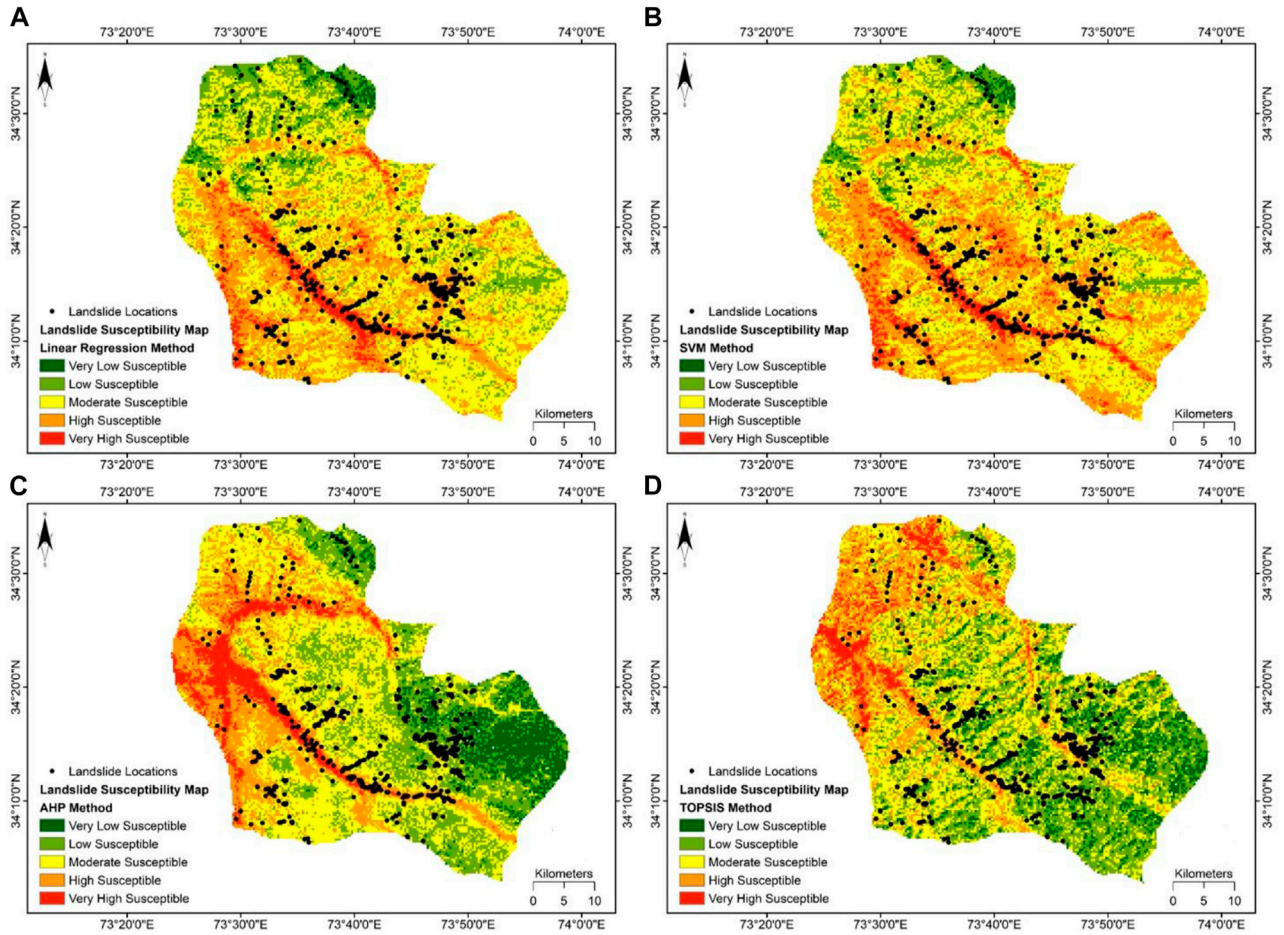

FIGURE 5
Landslide susceptibility maps derived from **(A)** LR **(B)** SVM **(C)** AHP and **(D)** TOPSIS.

TABLE 4 Confusion matrixes for Machine Learning models.

Confusion matrix for logistic regression

	0	1
0	481	111
1	125	495

Confusion matrix for linear regression

	0	1
0	435	135
1	171	471

Confusion matrix for support vector machine

	0	1
0	445	161
1	116	490

during the reclassification process. The NDVI value for most of the study area is high, which is consistent with the high vegetation coverage observed for the mountainous area (Figure 3L).

The curvature value represents the morphology of topography. The curvature proposes information about the flow's divergent or convergent and accelerated or deaccelerated character. The convexity (positive curvature) or concavity (negative curvature) of the earth's surface greatly influences the soil's moisture-holding capacity, which in turn affects the slope stability. This fact was based for the reclassification of different curvature types. For plan curvature, the concave surfaces are shown by the positive values, and the convex character of the surfaces is signified by the negative values (Figure 3M). However, for profile curvature, the negative curvature value relates to the concave slope, and the positive curvature value relates to the convex slope (Figure 3N). The research area is diversely dominated by convex, straight, and concave slopes. The convex slope is related to the positive curvature value, and the concave slope is associated with the negative curvature value (Figure 3O).

TABLE 5 Validation results of Machine Learning models.

Model type	Validation accuracy
LGR	80%
LR	75%
SVM	84%

5.3 The comparative significance of conditioning factors for considered models

From Table 2, it can be perceived that a similar controlling element can have a varied influence according to distinct models. For the SVM model, flow direction, elevation, and precipitation have the highest contributions of 13%, 12%, and 12%. As per the SVM model, the remaining conditioning factors contribute less. For the LGR, LR, AHP, and TOPSIS models, the influences of the landslide controlling elements are very much alike. Flow direction, elevation, lithology, precipitation, and slope have extreme impacts based on these four models, but the effects of the remaining factors varied slightly.

5.4 Landslide susceptibility maps

The developed LSM (Figure 4) of the considered area after the application of the LGR model illustrates that an area of 4.04% is classed as very low and 22.87% as low susceptible zones, predominantly located on the Northeast side of the region. The moderate susceptible area covers 43.03% of the total area, and 23.32% of the total area is sorted as a high susceptible zone, as evident from Table 3. The very high susceptible area is 6.75%, and these zones are mainly located in the Southwest of the region. Whereas the LR model's generated LSM (Figure 5A) shows that the very low susceptibility class encompasses 1.95%, and the low susceptibility class covers 16.73% of the considered area, which is less than the LGR model's respective classes. 29.83% and 5.85% of the explorative area come under the high and very high susceptibility classes, respectively, and these zones are primarily located in the central and southwest parts of the area. An area of 45.64% falls in the moderate susceptibility class, which is slightly higher than the moderate class area of both other ML models, as can be seen from Table 3. SVM-based susceptibility map shows that 42.16% of the area is under moderate susceptibility (Figure 5B). It can be viewed from the SVM model generated LSM that the very high susceptibility class comprises 8.05% of the considered area, and it is more as compared to all other used models. The high and low susceptibility classes encompass 36.03% and 12.70% of the explorative area. The percentage of the research area that accounts for very low susceptibility is 1.06%, and it is the least percentage of area in this class than other models, as shown in Table 3. The zones in the extreme North of the region have the lowest susceptibility. The spatial distribution of the susceptible areas according to the ML models produced LSMs is somewhat the same, but it differs in proportions of area.

The LSM (Figure 5C) generated by exercising the AHP technique illustrates that 9.16% of the area is very low, whereas 25.90% is under low susceptibility. These two classes are mainly concentrated on the Southeast side of the region,

TABLE 6 Accuracy assessment of produced landslide susceptibility maps.

Model type	Map accuracy (%)
LGR	79
LR	83
SVM	87
AHP	80
TOPSIS	78

which is different from the results of ML models in which these two classes are majorly positioned in the extreme North. The moderate susceptibility class encompasses 36.48% of the deliberated area. Besides this, 20.69% of the research area accounts for the high susceptibility, and the very high susceptibility represents 7.78% of the total area. Both these classes are concentrated on the central and Northwest sides of the region. The pattern of susceptibility classes is comparatively different from the results of ML models. As portrayed in Table 3, the results of the AHP show that the percentage of the exploratory area subjected to high susceptibility is more than the results of the TOPSIS. The generated LSM (Figure 5D) by the TOPSIS technique also exhibits similar trends as the AHP method LSM. The very low susceptibility class represents 8.64% of the research area. The low and moderate susceptibility classes comprise 31.28% and 34.86% of the study area, respectively. Finally, 19.50% of the considered area comes under the high susceptibility class, and the portion of the investigative area falls into the very high susceptibility class is 5.71%.

5.5 Validation of models

In the current research, the obtained value of CR was less than 0.1, which validated the AHP technique. For TOPSIS technique, the values of cli + ranged from 0 to 1. An option with a score close to 1 was considered the best. For all three ML models, SVM, LGR, and LR, the accuracy was calculated using the predicted and actual results for the testing dataset. The higher accuracy value demonstrates that the model calculations are precise. The confusion matrixes used to calculate the accuracy of all three models are shown in Table 4.

The results of the LGR model showed that out of 1212 points, 481 non-landslide and 495 landslide points were accurately predicted. In comparison, 125 non-landslide and 111 landslide points are wrongly predicted by the model. As seen from Table 4, out of 1212 points, the LR model accurately predicted 435 non-landslide and 471 landslide points, while 135 non-landslide and 171 landslide points were wrongly predicted. The confusion matrix for the SVM model reveals that, out of 1212 points, the SVM model accurately predicted 445 non-landslide and 490 landslide points, while 161 non-landslide and 116 landslide points were wrongly predicted. The calculated accuracy of the models based on the confusion matrix is presented in Table 5. The accuracy of the SVM model (84%) is more than the remaining two models, followed by LGR with 80% and LR with 75% accuracy (Table 5).

6 Discussion

The Muzaffarabad district of Azad Kashmir in Pakistan has been subjected to devastating landslides. There is a risk of future landslides due to the high precipitation levels, steeper slopes, high mountains composed of weaker lithology, etc. Therefore, it is vital to assess the landslide susceptibility of the region. In this study, for mapping the landslide susceptibility in the area, the landslide susceptibility maps (LSMs) were generated by exercising three ML techniques: SVM, LR, and LGR, besides two MCDM techniques: TOPSIS and AHP. Based on the literature review and the geographical setting of the area, 15 influencing factors were selected for mapping the landslide susceptibility.

Insights into the relative importance of inducing factors as a landslide susceptibility indicator are essential. Table 2 shows that all the models have marked slope and elevation as the most significantly impacting factors on landslide occurrence, followed by lithology, precipitation, flow direction, and NDWI. The elevation of an area controls the profile curvature, slope angle, and aspect of a geographical area. Thus, it is an important parameter. Slope plays an essential role in initiating landslides. Therefore, it is used frequently to prepare LSMs (Lee, 2005; Saha et al., 2005; Pourghasemi et al., 2012). According to the produced LSMs, landslide susceptible regions are majorly those with elevations ranging from 575 to 2000 m and steep slopes.

Precipitation is a crucial landslide triggering factor, and this region receives a significant amount of precipitation over a year, varying from an average of 983–1323 mm at different places. Precipitation triggers unexpected floods, which also produce shallow landslides. Water infiltrates rapidly into the soil due to higher levels of precipitation and thus increases the degree of saturation of the soil (Mandal and Mandal, 2018). Saturated soil has the potential to slide easily. NDWI is the amount of moisture in the soil which has a more significant role in initiating landslides. Soil water content disturbs soil cohesion and thus changes the shear strength of the soil (Del Gaudio et al., 2013; von Ruette et al., 2013). When the moisture increases, the material composition of the slope becomes loose, and the risk of slipping increases.

Lithology offers material support for the incident of landslides and forms the foundation of landslide development. Many studies have considered lithological features as an influencing factor for landslide susceptibility mapping

(Pourghasemi et al., 2012; Chen et al., 2016b; Wang et al., 2016). The weaker lithologies are responsible for causing landslides because they do not possess enough strength to withstand the higher precipitations and can easily slip away. The pondered area in this research receives a considerable amount of rainfall, and most of the landslides that have occurred were positioned near the rivers and were debris flow (Saba et al., 2010). The Jhelum river drains the study area and its two tributaries, the Neelum and Kunhar rivers. These rivers flow North to the West, developing profound antecedent valleys before gushing Southwards alongside wider ones valleys to the Indo-Gangetic Plain (Kamp et al., 2008). The flow of the rivers is very swift owing to the area's topography, thus cutting the slopes and causing debris flow while flowing from North to South. This makes the flow direction a critical factor for mapping landslide susceptibility. All these factors are related, and their combined effect can cause landslides in areas where they are present.

For every produced map as an application of the five methods, it can be seen that for landslide susceptibility, the categorized five classes vary in their percentages and locations in the area (Figures 4, 5). Overall, the spatial distribution of landslide susceptibility zones reveals vital training data selection. Table 3 displays the comprehensive outcomes of all the practiced models in statistical form. The accuracy of the produced LSMs was assessed using the data of previous landslide locations. The established data of landslide locations were compared with the LSMs for performing the accuracy assessment. The results disclosed acceptable conformity amid the LSMs and the previously present data on landslide positions, as evident from Table 6. For the landslide susceptibility mapping, the SVM model based LSM outperformed the other models. The SVM model based LSM accomplished the maximum implementation accuracy, which is 87%, followed by the LR model (83%), AHP (80%), LGR model (79%), and lastly, TOPSIS (78%).

In general, the performance of ML techniques was better than the performance of MCDM techniques. The results are quite like the results of different studies carried out previously in different parts of the world using a range of ML and MCDM models. For mapping landslide susceptibility at the Haraz watershed, Iran Pourghasemi et al. (2012) applied two MCDM techniques, Fuzzy Logic, and AHP, and evaluated the performance of both models. The results showed that the Fuzzy Logic model, with an accuracy of 89.7%, performed better than AHP, which showed an accuracy of 81.1%. The results of both MCDM techniques are considerably different in the mentioned study. But in the present case, there is a marginal difference between the two practiced MCDM techniques. This can be due to conditioning factors, as the study area's geographic location controls them. Erener et al. (2016) used the GIS-based MCDM method (AHP), Association Rule Mining (ARM), and LGR to carry out a comparative study for landslide susceptibility mapping for Şavşat in Artvin Province (NE Turkey). The authors found that ARM and LGR methods are more accurate than GIS-based MCDM for landslide susceptibility mapping. These results are as per the results of this study. In the present study, the LGR model also performs better than AHP. Razavi and Shirani (2019) used Frequency Ratio (FR), entropy methods, and an MCDM method (TOPSIS) for landslide hazard zoning for the Fahliyan basin, Fars. The results exhibited that the statistical methods entropy (91%) and FR (87.7%) have better accuracy than TOPSIS (84%). In the current analysis the accuracy of TOPSIS also turns out to be the least as compared to the other models.

In another study by Tsangaratos and Ilia (2016), a comparison between the performances of NB and LGR was made for the landslide susceptibility mapping in Greece, and the validation results showed an accuracy for NB at 82.61% and LGR at 87.50%. The study conducted by Pham et al. (2016a) for the evaluation of the performance of five ML methods SVM, LGR, NB, Fisher's Linear Discriminant Analysis (FLDA), and Bayesian Network (BN) applied for landslide susceptibility assessment demonstrated that SVM has the highest accuracy compared to the other methods. Goetz et al. (2015) used multiple statistical and ML techniques for the landslide hazard mapping of the province of Lower Austria. They used LGR, SVM, WOE, RF, Bootstrap Aggregated Classification Trees (bundling) with Penalized Discriminant Analysis (BPLDA) and Generalized Additive Model (GAM) method. The authors found that all methods gave similar accuracy and results, but the BPLDA, WOE, and RF had marginally better accuracy.

In these previously mentioned two studies, SVM performed better in one, but in the other study, the accuracy of SVM was marginally less. So, it can be concluded that the performance varies from location to location and depends on the conditioning factors. The results of previous studies also show that the ML techniques perform better than the MCDM techniques. Thus, indicating that the generated results of this study are acceptable. Even though the employed models in this research produced reasonable results; however, it must be perceived that the landslide position statistics, that is, the landslide inventory map, directly affect the reliability of the results.

An essential aspect of data-driven methods is that they are most prevailing for landslide susceptibility mapping since they contain less subjectivity. The accuracy of the SVM can be affected by the training sample selection, indicated by the fact that the best hyperplane is fitted by the SVM model that can detach non-landslides from landslides efficiently, even though specific complexity could come across for non-detachable landslide factors in fitting the hyperplane (Ballabio and Sterlacchini, 2012; Bui et al., 2016). High-dimensional data does not affect the workability of SVM, which means that it can handle the high number of landslide conditioning factors (Mountrakis et al., 2011; Kavzoglu et al., 2014). SVM accuracy is less affected by categorical influences, for instance, lithology and land use. The purpose is that the number of designated landslides might not differ among different classes when deciding on different landslide training data subsets. However, more effects can be

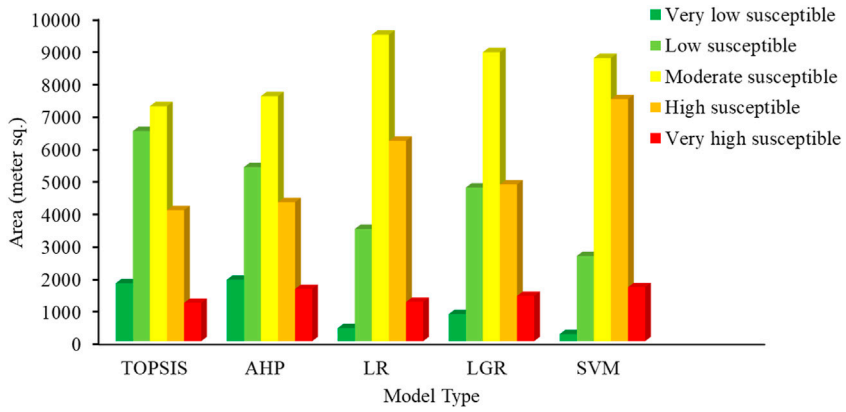

FIGURE 6
Landslide susceptibility class division in terms of area for different methods.

witnessed in continuous elements such as slope and altitude as the values differ relentlessly.

In contrast, for training data selection, the LGR model was observed to be less complex. To the landslide inventory data, the LGR model strives to fit a linear location and might usually place the landslide sites among classes as high and very high susceptibility. It was determined that the LGR model undoubtedly highlights the interrelation present between the occurrence of landslides and instability factors. Besides the SVM and LGR, the LR method has been used due to the ease of data attainment and examination and less time consumption.

TOPSIS and AHP are the most rational and extensively used among all the MCDM methods (Rao and Davim, 2008; Achour et al., 2017; RAZAVI and Shirani, 2019; Bahrami et al., 2020; Maqsoom et al., 2021). An optimal result can be produced by their combination, provided that the strengths of one model can offset the weaknesses of another model (Rao and Davim, 2008). Unfortunately, TOPSIS is unreliable in its valuation of decisions and lacks weights, according to the stated purpose, to determine the relative importance of different indicators; this technique requires a workable procedure. The AHP method also delivers such a practice (Rao and Davim, 2008). A rating system based on expert opinion is used for the conventional AHP model. In fact, for solving composite problems like landslides, expert opinion is very beneficial. However, to some extent, views may be imperiled by cognitive restrictions with partiality and vagueness. They may vary for every individual expert. Therefore, the analysis of spatial relationships is important amongst landslide locations and the landslide activating factors. Though the AHP technique is primarily centered on professional judgment, it is supposed that the choice of landslide activating factors based on landslide incidences can neutralize the partiality perception in this technique (Achour et al., 2017; Maqsoom et al., 2021).

A detailed comparison of the results in terms of area under different susceptibility classes, as shown by the susceptibility maps, is provided in Figure 6. In contrast with all the other methods, the LR model's generated LSM shows that the maximum area is in the moderate susceptibility class (>9000 m^2). The SVM model outcomes show that the least area is under the very low susceptibility class compared to the other models. The representation shows that the area under low susceptibility is higher for the TOPSIS model (>6000 m^2) than the area of other models. However, the area under the high and very high susceptibility class of SVM is considerably higher than the results of TOPSIS and AHP. The overall results of the models indicate that primarily the investigative area has moderate landslide susceptibility, which comprises approximately 40% of the considered area.

All the LSMs (Figures 4, 5) show that the high and very high susceptibility classes are in the lower elevation areas, including the floodplains of the main rivers. This is because most of the landslides in the study area occur along the rivers and are debris flows. Due to this, the models have predicted high susceptibility in the lower elevation areas, including the floodplains of main rivers. Moreover, the practiced models in this research have computed very low or low susceptibility in the Northern region with a cluster of landslide points. This shows the limitation of the practiced conventional ML and MCDM techniques. Therefore, it is suggested that future researchers should practice contemporary deep learning techniques the evaluate the landslide potential in this study area.

7 Conclusion

There are several advised practices for landslide susceptibility mapping. However, in this study, to assess the

landslide susceptibility of the Muzaffarabad district, a comparison was made between the results of three ML techniques, LGR, LR, and SVM, and the results of two MCDM techniques, TOPSIS and AHP. Based on the landslide's physical mechanics in the study area and other related knowledge, selected slope, profile curvature, aspect, plan curvature, elevation, lithology, curvature, flow direction, fault lines, precipitation, NDWI, NDVI, distance from roads, earthquake, and distance from waterways as landslides inducing factors for this study. A total of 1212 data points, 606 landslide locations, and 606 randomly selected non-landslide locations were used for the analysis. 70% of the data was used as training and 30% as testing data. The training data was used to train the ML models, and the testing data was used for checking the validity of trained SVM, LGR, and LR models. All the methods ranked slope, precipitation, elevation, flow direction, and lithology as the most critical landslide-inducing factors, but the assigned weights differed. The accuracy assessment of produced maps showed that the performance of all the methods was relatively decent. Still, the accuracy of the SVM model-produced map was somewhat higher (85%), followed by LR (83%), AHP (80%), LGR (79%), and TOPSIS (78%). By offering the LSMs, this study provides a baseline for decision-makers for effective countermeasures that can be practiced for the study areas' susceptible zones, including drainage measures, revetments, stabilizing piles, anchor bolts, and long-term monitoring. This can, as a result, help reduce the loss of life and property in diverse situations.

Data availability statement

The raw data supporting the conclusions of this article will be made available by the authors, without undue reservation.

Author contributions

Conceptualization, UK and BA; methodology, UK, II, and BA; software, II, IU, and BA; validation, UK, IU, and BA; formal analysis, AT; investigation, II and AT; resources, II, BA, and IU; data curation, BA and IU; writing—original draft preparation, UK and BA; writing—review and editing, UK, BA, IU, and AT; visualization, II and AT; supervision, AT and SQ; project administration, AT and SQ; funding acquisition, SQ. All authors have read and agreed to the published version of the manuscript.

Funding

The research is financially supported by the National Key Research and Development Program of China (2021YFC3200301), National Natural Science Foundation of China Youth Fund (52209068), Postdoctoral Research Foundation of China (2020M682477), and the Fundamental Research Funds for the Central Universities (2042021kf0053).

Conflict of interest

The authors declare that the research was conducted in the absence of any commercial or financial relationships that could be construed as a potential conflict of interest.

Publisher's note

All claims expressed in this article are solely those of the authors and do not necessarily represent those of their affiliated organizations, or those of the publisher, the editors and the reviewers. Any product that may be evaluated in this article, or claim that may be made by its manufacturer, is not guaranteed or endorsed by the publisher.

References

Abella, E. C., and Van Westen, C. (2007). Generation of a landslide risk index map for cuba using spatial multi-criteria evaluation. *Landslides* 4 (4), 311–325. doi:10.1007/s10346-007-0087-y

Achour, Y., Boumezbeur, A., Hadji, R., Chouabbi, A., Cavaleiro, V., and Bendaoud, E. A. (2017). Landslide susceptibility mapping using analytic hierarchy process and information value methods along a highway road section in constantine, algeria. *Arab. J. Geosci.* 10 (8), 194–216. doi:10.1007/s12517-017-2980-6

Ali, S., Biermanns, P., Haider, R., and Reicherter, K. (2019). Landslide susceptibility mapping by using a geographic information system (GIS) along the china–pakistan economic corridor (Karakoram Highway), pakistan. *Nat. Hazards Earth Syst. Sci.* 19 (5), 999–1022. doi:10.5194/nhess-19-999-2019

Arnoldus, H. M. J. (1980). *An approximation of the rainfall factor in the universal soil loss equation*, Editor M. De Boodt and D. Gabriels (New York: Assessment of Erosion, John Wiley and Sons), 127–132.

Aslam, B., Maqsoom, A., Khalil, U., Ghorbanzadeh, O., Blaschke, T., Farooq, D., et al. (2022). Evaluation of different landslide susceptibility models for a local scale in the Chitral District, Northern Pakistan. *Sensors* 22 (9), 3107. doi:10.3390/s22093107

Azareh, A., Rahmati, O., Rafiei-Sardooi, E., Sankey, J. B., Lee, S., Shahabi, H., et al. (2019). Modelling gully-erosion susceptibility in a semi-arid region, Iran: Investigation of applicability of certainty factor and maximum entropy models. *Sci. Total Environ.* 655, 684–696. doi:10.1016/j.scitotenv.2018.11.235

Baeza, C., Lantada, N., and Moya, J. (2010). Influence of sample and terrain unit on landslide susceptibility assessment at La Pobla de Lillet, Eastern Pyrenees, Spain. *Environ. Earth Sci.* 60 (1), 155–167. doi:10.1007/s12665-009-0176-4

Bahrami, Y., Hassani, H., and Maghsoudi, A. (2020). *Landslide susceptibility mapping using AHP and fuzzy methods in the Gilan province, Iran*. Rasht: GeoJournal, 1

Ballabio, C., and Sterlacchini, S. (2012). Support vector machines for landslide susceptibility mapping: The staffora river basin case study, Italy. *Math. Geosci.* 44 (1), 47–70. doi:10.1007/s11004-011-9379-9

Bragagnolo, L., da Silva, R. V., and Grzybowski, J. M. V. (2020). Landslide susceptibility mapping with r. landslide: A free open-source GIS-integrated tool based on artificial neural networks. *Environ. Model. Softw.* 123, 104565. doi:10.1016/j.envsoft.2019.104565

Bui, D. T., Nguyen, Q. P., Hoang, N.-D., and Klempe, H. (2017). A novel fuzzy K-nearest neighbor inference model with differential evolution for spatial prediction of rainfall-induced shallow landslides in a tropical hilly area using GIS. *Landslides* 14 (1), 1–17. doi:10.1007/s10346-016-0708-4

Bui, D. T., Tuan, T. A., Klempe, H., Pradhan, B., and Revhaug, I. (2016). Spatial prediction models for shallow landslide hazards: A comparative assessment of the efficacy of support vector machines, artificial neural networks, kernel logistic regression, and logistic model tree. *Landslides* 13 (2), 361–378. doi:10.1007/s10346-015-0557-6

Capitani, M., Ribolini, A., and Bini, M. (2013). The slope aspect: A predisposing factor for landsliding? *Comptes Rendus Geosci.* 345 (11-12), 427–438. doi:10.1016/j.crte.2013.11.002

Cevik, E., and Topal, T. (2003). GIS-based landslide susceptibility mapping for a problematic segment of the natural gas pipeline, Hendek (Turkey). *Environ. Geol.* 44 (8), 949–962. doi:10.1007/s00254-003-0838-6

Chen, W., Ding, X., Zhao, R., and Shi, S. (2016a). Application of frequency ratio and weights of evidence models in landslide susceptibility mapping for the Shangzhou District of Shangluo City, China. *Environ. Earth Sci.* 75 (1), 64. doi:10.1007/s12665-015-4829-1

Chen, W., Panahi, M., Tsangaratos, P., Shahabi, H., Ilia, I., Panahi, S., et al. (2019b). Applying population-based evolutionary algorithms and a neuro-fuzzy system for modeling landslide susceptibility. *Catena* 172, 212–231. doi:10.1016/j.catena.2018.08.025

Chen, W., Pourghasemi, H. R., Kornejady, A., and Zhang, N. (2017). Landslide spatial modeling: Introducing new ensembles of ANN, MaxEnt, and SVM machine learning techniques. *Geoderma* 305, 314–327. doi:10.1016/j.geoderma.2017.06.020

Chen, W., Pourghasemi, H. R., and Naghibi, S. A. (2018a). Prioritization of landslide conditioning factors and its spatial modeling in shangnan county, china using GIS-based data mining algorithms. *Bull. Eng. Geol. Environ.* 77 (2), 611–629. doi:10.1007/s10064-017-1004-9

Chen, W., Wang, J., Xie, X., Hong, H., Van Trung, N., Bui, D. T., et al. (2016b). Spatial prediction of landslide susceptibility using integrated frequency ratio with entropy and support vector machines by different kernel functions. *Environ. Earth Sci.* 75 (20), 1344. doi:10.1007/s12665-016-6162-8

Chen, W., Zhang, S., Li, R., and Shahabi, H. (2018b). Performance evaluation of the GIS-based data mining techniques of best-first decision tree, random forest, and naïve Bayes tree for landslide susceptibility modeling. *Sci. total Environ.* 644, 1006–1018. doi:10.1016/j.scitotenv.2018.06.389

Chen, W., Zhao, X., Shahabi, H., Shirzadi, A., Khosravi, K., Chai, H., et al. (2019a). Spatial prediction of landslide susceptibility by combining evidential belief function, logistic regression and logistic model tree. *Geocarto Int.* 34 (11), 1177–1201. doi:10.1080/10106049.2019.1588393

Choi, J., Oh, H.-J., Lee, H.-J., Lee, C., and Lee, S. (2012). Combining landslide susceptibility maps obtained from frequency ratio, logistic regression, and artificial neural network models using ASTER images and GIS. *Eng. Geol.* 124, 12–23. doi:10.1016/j.enggeo.2011.09.011

Cortes, C., and Vapnik, V. (1995). Support-vector networks. *Mach. Learn.* 20 (3), 273–297. doi:10.1007/bf00994018

Del Gaudio, V., Wasowski, J., and Muscillo, S. (2013). New developments in ambient noise analysis to characterise the seismic response of landslide-prone slopes. *Nat. Hazards Earth Syst. Sci.* 13 (8), 2075–2087. doi:10.5194/nhess-13-2075-2013

Deng, X., Liu, Q., Deng, Y., and Mahadevan, S. (2016). An improved method to construct basic probability assignment based on the confusion matrix for classification problem. *Inf. Sci.* 340, 250–261. doi:10.1016/j.ins.2016.01.033

Devkota, K. C., Regmi, A. D., Pourghasemi, H. R., Yoshida, K., Pradhan, B., Ryu, I. C., et al. (2013). Landslide susceptibility mapping using certainty factor, index of entropy and logistic regression models in GIS and their comparison at Mugling–Narayanghat road section in Nepal Himalaya. *Nat. Hazards (Dordr).* 65 (1), 135–165. doi:10.1007/s11069-012-0347-6

Erener, A., Mutlu, A., and Düzgün, H. S. (2016). A comparative study for landslide susceptibility mapping using GIS-based multi-criteria decision analysis (MCDA), logistic regression (LR) and association rule mining (ARM). *Eng. Geol.* 203, 45–55. doi:10.1016/j.enggeo.2015.09.007

Fall, M., Azzam, R., and Noubactep, C. (2006). A multi-method approach to study the stability of natural slopes and landslide susceptibility mapping. *Eng. Geol.* 82 (4), 241–263. doi:10.1016/j.enggeo.2005.11.007

Flentje, P., and Chowdhury, R. (2018). Resilience and sustainability in the management of landslides. *Proceedings of the institution of Civil engineers-engineering sustainability* 171 (1), 3–14.

Froude, M. J., and Petley, D. N. (2018). Global fatal landslide occurrence from 2004 to 2016. *Nat. Hazards Earth Syst. Sci.* 18 (8), 2161–2181. doi:10.5194/nhess-18-2161-2018

Girma, F., Raghuvanshi, T., Ayenew, T., and Hailemariam, T. (2015). Landslide hazard zonation in Ada Berga District, Central Ethiopia–a GIS based statistical approach. *J. Geom.* 9, 25–38.

Goetz, J., Brenning, A., Petschko, H., and Leopold, P. (2015). Evaluating machine learning and statistical prediction techniques for landslide susceptibility modeling. *Comput. geosciences* 81, 1–11. doi:10.1016/j.cageo.2015.04.007

Hong, H., Chen, W., Xu, C., Youssef, A. M., Pradhan, B., and Tien Bui, D. (2017). Rainfall-induced landslide susceptibility assessment at the Chongren area (China) using frequency ratio, certainty factor, and index of entropy. *Geocarto Int.* 32 (2), 1–16. doi:10.1080/10106049.2015.1130086

Hong, H., Naghibi, S. A., Pourghasemi, H. R., and Pradhan, B. (2016a). GIS-based landslide spatial modeling in Ganzhou City, China. *Arab. J. Geosci.* 9 (2), 112. doi:10.1007/s12517-015-2094-y

Hong, H., Pourghasemi, H. R., and Pourtaghi, Z. S. (2016b). Landslide susceptibility assessment in lianhua county (China): A comparison between a random forest data mining technique and bivariate and multivariate statistical models. *Geomorphology* 259, 105–118. doi:10.1016/j.geomorph.2016.02.012

Hwang, C., and Yoon, K. (1981). *Multi-objective decision making–methods and application. A state-of-the-art study*. New York: Springer-Verlag.

Kamp, U., Growley, B. J., Khattak, G. A., and Owen, L. A. (2008). GIS-based landslide susceptibility mapping for the 2005 Kashmir earthquake region. *Geomorphology* 101 (4), 631–642. doi:10.1016/j.geomorph.2008.03.003

Kanwal, S., Atif, S., and Shafiq, M. (2017). GIS based landslide susceptibility mapping of northern areas of Pakistan, a case study of Shigar and Shyok Basins. *Geomatics, Nat. Hazards Risk* 8 (2), 348–366. doi:10.1080/19475705.2016.1220023

Kavzoglu, T., Sahin, E. K., and Colkesen, I. (2014). Landslide susceptibility mapping using GIS-based multi-criteria decision analysis, support vector machines, and logistic regression. *Landslides* 11 (3), 425–439. doi:10.1007/s10346-013-0391-7

Kazmi, A. H., and Jan, M. Q. (1997). *Geology and tectonics of Pakistan*. Wollongong, Australia: Graphic publishers.

Khan, A. N., Collins, A. E., and Qazi, F. (2011). Causes and extent of environmental impacts of landslide hazard in the himalayan region: A case study of murree, Pakistan. *Nat. Hazards (Dordr).* 57 (2), 413–434. doi:10.1007/s11069-010-9621-7

Khan, H., Shafique, M., Khan, M. A., Bacha, M. A., Shah, S. U., and Calligaris, C. (2019). Landslide susceptibility assessment using Frequency Ratio, a case study of northern Pakistan. *Egypt. J. Remote Sens. Space Sci.* 22 (1), 11–24. doi:10.1016/j.ejrs.2018.03.004

Khattak, G. A., Owen, L. A., Kamp, U., and Harp, E. L. (2010). Evolution of earthquake-triggered landslides in the Kashmir Himalaya, northern Pakistan. *Geomorphology* 115 (1-2), 102–108. doi:10.1016/j.geomorph.2009.09.035

Krohling, R. A., and Pacheco, A. G. (2015). A-TOPSIS–an approach based on TOPSIS for ranking evolutionary algorithms. *Procedia Comput. Sci.* 55, 308–317. doi:10.1016/j.procs.2015.07.054

Lee, S. (2005). Application of logistic regression model and its validation for landslide susceptibility mapping using GIS and remote sensing data. *Int. J. Remote Sens.* 26 (7), 1477–1491. doi:10.1080/01431160412331331012

Lin, C., and Wu, W.-W. (2004). A fuzzy extension of the DEMATEL method for group decision making. *Eur. J. Operational Res.* 156, 445–455. doi:10.1016/S0377-2217(02)00914-1

Mandal, B., and Mandal, S. (2018). Analytical hierarchy process (AHP) based landslide susceptibility mapping of Lish river basin of eastern Darjeeling Himalaya, India. *Adv. Space Res.* 62 (11), 3114–3132. doi:10.1016/j.asr.2018.08.008

Maqsoom, A., Aslam, B., Khalil, U., Kazmi, Z. A., Azam, S., Mehmood, T., et al. (2021). Landslide susceptibility mapping along the China Pakistan Economic Corridor (CPEC) route using multi-criteria decision-making method. *Model. Earth Syst. Environ.* 8, 1519–1533. doi:10.1007/s40808-021-01226-0

Maria Navin, J., and Pankaja, R. (2016). Performance analysis of text classification algorithms using confusion matrix. *Int. J. Eng. Tech. Res. (IJETR)* 6, 75–78.

Marjanović, M., Kovačević, M., Bajat, B., and Voženílek, V. (2011). Landslide susceptibility assessment using SVM machine learning algorithm. *Eng. Geol.* 123 (3), 225–234. doi:10.1016/j.enggeo.2011.09.006

Mountrakis, G., Im, J., and Ogole, C. (2011). Support vector machines in remote sensing: A review. *ISPRS J. Photogrammetry Remote Sens.* 66 (3), 247–259. doi:10.1016/j.isprsjprs.2010.11.001

Najafabadi, R. M., Ramesht, M. H., Ghazi, I., Khajedin, S. J., Seif, A., Nohegar, A., et al. (2016). Identification of natural hazards and classification of urban areas by TOPSIS model (case study: Bandar Abbas city, Iran). *Geomatics, Nat. Hazards Risk* 7 (1), 85–100. doi:10.1080/19475705.2013.871353

O'brien, R. M. (2007). A caution regarding rules of thumb for variance inflation factors. *Qual. Quant.* 41 (5), 673–690. doi:10.1007/s11135-006-9018-6

Onagh, M., Kumra, V., and Rai, P. K. (2012b). Application of multiple linear regression model in landslide susceptibility zonation mapping the case study narmab basin Iran. *Int. J. Geol. Earth Environ. Sci.* 2 (2), 87

Onagh, M., Kumra, V., and Rai, P. K. (2012a). Landslide susceptibility mapping in a part of Uttarkashi district (India) by multiple linear regression method. *Int. J. Geol. Earth Environ. Sci.* 2 (2), 102

Owen, L. A., Kamp, U., Khattak, G. A., Harp, E. L., Keefer, D. K., and Bauer, M. A. (2008). Landslides triggered by the 8 october 2005 Kashmir earthquake. *Geomorphology* 94 (1-2), 1–9. doi:10.1016/j.geomorph.2007.04.007

Pavelsky, T. M., and Smith, L. C. (2008). RivWidth: A software tool for the calculation of river widths from remotely sensed imagery. *IEEE Geosci. Remote Sens. Lett.* 5 (1), 70–73. doi:10.1109/lgrs.2007.908305

Pawluszek, K., Borkowski, A., and Tarolli, P. (2018). Sensitivity analysis of automatic landslide mapping: Numerical experiments towards the best solution. *Landslides* 15 (9), 1851–1865. doi:10.1007/s10346-018-0986-0

Pham, B. T., Bui, D. T., Dholakia, M., Prakash, I., and Pham, H. V. (2016b). A comparative study of least square support vector machines and multiclass alternating decision trees for spatial prediction of rainfall-induced landslides in a tropical cyclones area. *Geotech. Geol. Eng. (Dordr).* 34 (6), 1807–1824. doi:10.1007/s10706-016-9990-0

Pham, B. T., Pradhan, B., Bui, D. T., Prakash, I., and Dholakia, M. (2016a). A comparative study of different machine learning methods for landslide susceptibility assessment: A case study of uttarakhand area (India). *Environ. Model. Softw.* 84, 240–250. doi:10.1016/j.envsoft.2016.07.005

Pourghasemi, H. R., Pradhan, B., and Gokceoglu, C. (2012). Application of fuzzy logic and analytical hierarchy process (AHP) to landslide susceptibility mapping at Haraz watershed, Iran. *Nat. Hazards (Dordr).* 63 (2), 965–996. doi:10.1007/s11069-012-0217-2

Pradhan, A., and Kim, Y. (2016). Evaluation of a combined spatial multi-criteria evaluation model and deterministic model for landslide susceptibility mapping. *Catena* 140, 125–139. doi:10.1016/j.catena.2016.01.022

Pradhan, B. (2013). A comparative study on the predictive ability of the decision tree, support vector machine and neuro-fuzzy models in landslide susceptibility mapping using GIS. *Comput. Geosciences* 51, 350–365. doi:10.1016/j.cageo.2012.08.023

Pradhan, B. (2010). Landslide susceptibility mapping of a catchment area using frequency ratio, fuzzy logic and multivariate logistic regression approaches. *J. Indian Soc. Remote Sens.* 38 (2), 301–320. doi:10.1007/s12524-010-0020-z

Pradhan, B., Lee, S., and Buchroithner, M. F. (2009). Use of geospatial data and fuzzy algebraic operators to landslide-hazard mapping. *Appl. Geomat.* 1 (1-2), 3–15. doi:10.1007/s12518-009-0001-5

Pradhan, B., and Lee, S. (2010). Landslide susceptibility assessment and factor effect analysis: Backpropagation artificial neural networks and their comparison with frequency ratio and bivariate logistic regression modelling. *Environ. Model. Softw.* 25 (6), 747–759. doi:10.1016/j.envsoft.2009.10.016

Raghukanth, S. (2008). Ground motion estimation during the Kashmir earthquake of 8th October 2005. *Nat. Hazards (Dordr).* 46 (1), 1–13. doi:10.1007/s11069-007-9178-2

Raghuvanshi, T. K., Ibrahim, J., and Ayalew, D. (2014). Slope stability susceptibility evaluation parameter (SSEP) rating scheme–an approach for landslide hazard zonation. *J. Afr. Earth Sci.* 99, 595–612. doi:10.1016/j.jafrearsci.2014.05.004

Rao, R. V., and Davim, J. P. (2008). A decision-making framework model for material selection using a combined multiple attribute decision-making method. *Int. J. Adv. Manuf. Technol.* 35 (7-8), 751–760. doi:10.1007/s00170-006-0752-7

Razavi, S., and Shirani, K. (2019). *Landslide hazard zoning using frequency ratio, entropy methods and TOPSIS decision making methods (Case study: Fahliyan basin. Fars).*

Rossetto, T., and Peiris, N. (2009). Observations of damage due to the Kashmir earthquake of October 8, 2005 and study of current seismic provisions for buildings in Pakistan. *Bull. Earthq. Eng.* 7 (3), 681–699. doi:10.1007/s10518-009-9118-5

Ruff, M., and Czurda, K. (2008). Landslide susceptibility analysis with a heuristic approach in the Eastern Alps (Vorarlberg, Austria). *Geomorphology* 94 (3-4), 314–324. doi:10.1016/j.geomorph.2006.10.032

Saaty, T. L. (1990). *Decision making for leaders: The analytic hierarchy process for decisions in a complex world.* RWS publications.

Saaty, T. L., and Vargas, L. G. (2001). "How to make a decision," in *Models, methods, concepts & applications of the analytic hierarchy process* (Springer), 1

Saaty, T. (1980). *The analytic hierarchy process*, 70. New York: Mcgraw Hill Agricultural Economics Review.

Saba, S. B., van der Meijde, M., and van der Werff, H. (2010). Spatiotemporal landslide detection for the 2005 Kashmir earthquake region. *Geomorphology* 124 (1-2), 17–25. doi:10.1016/j.geomorph.2010.07.026

Saha, A. K., Gupta, R. P., Sarkar, I., Arora, M. K., and Csaplovics, E. (2005). An approach for GIS-based statistical landslide susceptibility zonation—With a case study in the Himalayas. *Landslides* 2 (1), 61–69. doi:10.1007/s10346-004-0039-8

Saito, H., Nakayama, D., and Matsuyama, H. (2009). Comparison of landslide susceptibility based on a decision-tree model and actual landslide occurrence: The akaishi mountains, Japan. *Geomorphology* 109 (3-4), 108–121. doi:10.1016/j.geomorph.2009.02.026

San, B. T. (2014). An evaluation of SVM using polygon-based random sampling in landslide susceptibility mapping: The candir catchment area (Western antalya, Turkey). *Int. J. Appl. earth observation geoinformation* 26, 399–412. doi:10.1016/j.jag.2013.09.010

Shahabi, H., and Hashim, M. (2015). Landslide susceptibility mapping using GIS-based statistical models and Remote sensing data in tropical environment. *Sci. Rep.* 5 (1), 9899–9915. doi:10.1038/srep09899

Shahabi, H., Khezri, S., Ahmad, B. B., and Hashim, M. (2014). Retracted: Landslide susceptibility mapping at central zab basin, Iran: A comparison between analytical hierarchy process, frequency ratio and logistic regression models. *Catena* 115, 55–70. doi:10.1016/j.catena.2013.11.014

Shano, L., Raghuvanshi, T. K., and Meten, M. (2020). Landslide susceptibility evaluation and hazard zonation techniques–a review. *Geoenvironmental Disasters* 7 (1), 18–19. doi:10.1186/s40677-020-00152-0

Shirzadi, A., Shahabi, H., Chapi, K., Bui, D. T., Pham, B. T., Shahedi, K., et al. (2017). A comparative study between popular statistical and machine learning methods for simulating volume of landslides. *Catena* 157, 213–226. doi:10.1016/j.catena.2017.05.016

Süzen, M. L., and Kaya, B. Ş. (2012). Evaluation of environmental parameters in logistic regression models for landslide susceptibility mapping. *Int. J. Digital Earth* 5 (4), 338–355. doi:10.1080/17538947.2011.586443

Trigila, A., Iadanza, C., Esposito, C., and Scarascia-Mugnozza, G. (2015). Comparison of logistic regression and random Forests techniques for shallow landslide susceptibility assessment in giampilieri (NE sicily, Italy). *Geomorphology* 249, 119–136. doi:10.1016/j.geomorph.2015.06.001

Tsangaratos, P., and Ilia, I. (2016). Comparison of a logistic regression and naïve bayes classifier in landslide susceptibility assessments: The influence of models complexity and training dataset size. *Catena* 145, 164–179. doi:10.1016/j.catena.2016.06.004

Tsangaratos, P., Ilia, I., Hong, H., Chen, W., and Xu, C. (2017). Applying Information Theory and GIS-based quantitative methods to produce landslide susceptibility maps in Nancheng County, China. *Landslides* 14 (3), 1091–1111. doi:10.1007/s10346-016-0769-4

Umar, Z., Pradhan, B., Ahmad, A., Jebur, M. N., and Tehrany, M. S. (2014). Earthquake induced landslide susceptibility mapping using an integrated ensemble frequency ratio and logistic regression models in west Sumatera Province, Indonesia. *Catena* 118, 124–135. doi:10.1016/j.catena.2014.02.005

von Ruette, J., Lehmann, P., and Or, D. (2013). Rainfall-triggered shallow landslides at catchment scale: Threshold mechanics-based modeling for abruptness and localization. *Water Resour. Res.* 49 (10), 6266–6285. doi:10.1002/wrcr.20418

Wang, L.-J., Guo, M., Sawada, K., Lin, J., and Zhang, J. (2015). Landslide susceptibility mapping in mizunami city, Japan: A comparison between logistic regression, bivariate statistical analysis and multivariate adaptive regression spline models. *Catena* 135, 271–282. doi:10.1016/j.catena.2015.08.007

Wang, Q., Li, W., Xing, M., Wu, Y., Pei, Y., Yang, D., et al. (2016). Landslide susceptibility mapping at gongliu county, china using artificial neural network and weight of evidence models. *Geosci. J.* 20 (5), 705–718. doi:10.1007/s12303-016-0003-3

Wang, Y., Fang, Z., and Hong, H. (2019). Comparison of convolutional neural networks for landslide susceptibility mapping in yanshan county, china. *Sci. total Environ.* 666, 975–993. doi:10.1016/j.scitotenv.2019.02.263

Wallace, K., Bilham, R., Blume, F., Gaur, V. K., and Gahalaut, V. (2005). Surface deformation in the region of the 1905 Kangra Mw = 7.8 earthquake in the period 1846–2001. *Geophys. Res. Lett.* 32, L15307. doi:10.1029/2005GL022906

Xu, C., Dai, F., Xu, X., and Lee, Y. H. (2012). GIS-based support vector machine modeling of earthquake-triggered landslide susceptibility in the Jianjiang River watershed, China. *Geomorphology* 145, 70–80. doi:10.1016/j.geomorph.2011.12.040

Xu, H. (2006). Modification of normalised difference water index (NDWI) to enhance open water features in remotely sensed imagery. *Int. J. remote Sens.* 27 (14), 3025–3033. doi:10.1080/01431160600589179

Yang, Z., Qiao, J., Uchimura, T., Wang, L., Lei, X., and Huang, D. (2017). Unsaturated hydro-mechanical behaviour of rainfall-induced mass remobilization in post-earthquake landslides. *Eng. Geol.* 222, 102–110. doi:10.1016/j.enggeo.2017.04.001

Yao, X., Tham, L., and Dai, F. (2008). Landslide susceptibility mapping based on support vector machine: A case study on natural slopes of Hong Kong, China. *Geomorphology* 101 (4), 572–582. doi:10.1016/j.geomorph.2008.02.011

Yoshimatsu, H., and Abe, S. (2006). A review of landslide hazards in Japan and assessment of their susceptibility using an analytical hierarchic process (AHP) method. *Landslides* 3 (2), 149–158. doi:10.1007/s10346-005-0031-y

Youssef, A. M., Al-Kathery, M., and Pradhan, B. (2015). Landslide susceptibility mapping at Al-Hasher area, Jizan (Saudi Arabia) using GIS-based frequency ratio and index of entropy models. *Geosci. J.* 19 (1), 113–134. doi:10.1007/s12303-014-0032-8

Zhang, Y., Liao, J., Long, Y., An, J., Xu, S., and Wang, X. (2018). Dating reservoir deposits to reconstruct sediment yields from a small limestone catchment in the yimeng mountain region, China. *Catena* 166, 1–9. doi:10.1016/j.catena.2018.03.012

Zhu, A.-X., Miao, Y., Yang, L., Bai, S., Liu, J., and Hong, H. (2018). Comparison of the presence-only method and presence-absence method in landslide susceptibility mapping. *Catena* 171, 222–233. doi:10.1016/j.catena.2018.07.012

frontiers | Frontiers in Earth Science

TYPE Original Research
PUBLISHED 19 September 2022
DOI 10.3389/feart.2022.957506

OPEN ACCESS

EDITED BY
Biswajeet Pradhan,
University of Technology Sydney, Australia

REVIEWED BY
Avirut Chinkulkijniwat,
Suranaree University of Technology, Thailand
Bing Bai,
Beijing Jiaotong University, China
Wuwei Mao,
Tongji University, China
Luqi Wang,
Chongqing University, China

*CORRESPONDENCE
Hsin-Fu Yeh,
hfyeh@mail.ncku.edu.tw

SPECIALTY SECTION
This article was submitted to Geohazards and Georisks, a section of the journal Frontiers in Earth Science

RECEIVED 31 May 2022
ACCEPTED 30 August 2022
PUBLISHED 19 September 2022

CITATION
Yang Y-S, Yeh H-F, Ke C-C, Chen N-C and Chang K-C (2022), Assessment of probability of failure on rainfall-induced shallow landslides at slope scale using a physical-based model and fuzzy point estimate method.
Front. Earth Sci. 10:957506.
doi: 10.3389/feart.2022.957506

Assessment of probability of failure on rainfall-induced shallow landslides at slope scale using a physical-based model and fuzzy point estimate method

Ya-Sin Yang[1], Hsin-Fu Yeh[1]*, Chien-Chung Ke[2], Nai-Chin Chen[2] and Kuo-Chin Chang[3]

[1]Department of Resources Engineering, National Cheng Kung University, Tainan, Taiwan, [2]Geotechnical Engineering Research Center, Sinotech Engineering Consultants, Inc., Taipei, Taiwan, [3]Nantou Branch, Soil and Water Conservation Bureau, Council of Agriculture, Executive Yuan, Nantou, Taiwan

Shallow hillslope failure caused by rainfall is characterized by complex soil hydrology and mechanical behavior. It is important to understand the hydraulic behavior of hillslopes and quantify the effect of the uncertainty of mechanical parameters on hillslope stability for forewarning and hillslope management. Intra-hole deformation and displacement were record for the hillslope of the Babaoliao collapse site in the Chiayi County, as a case study. The fuzzy point estimation method and physical-based model were combined with the local factor of safety (LFS) theory to calculate the internal local factor of safety of the hillslope. A reliability analysis was then performed to determine the failure probability at different depths. Historical rainfall events were used to validate the model and predict the development of the failure probability for different rainfall patterns with the same warning rainfall. The results revealed that the failure probability model could effectively predict the area of hillslope instability and its changes over time and space. Different rainfall patterns affected the infiltration flux, leading to the difference in hillslope failure time. The delayed rainfall pattern had a significant impact on the time of slope instability, and shallow collapse was most likely to occur earlier. This study can be used as a reference for developing future hillslope warnings.

KEYWORDS

shallow landslide, fuzzy point estimation method, physical-based model, local factor of safety, failure probability

Highlights

- Uncertainty propagation is handled through physical-based model
- Fuzzy method can respond to the uncertainties inherent in practical landslide
- The proposed framework was applied to practical hillslope to verify its feasibility

Introduction

Landslides are geomorphic processes occurring globally in areas with hillslopes, covering different climatic zones and soil materials, and can potentially result in environmental and economic loss (Tiranti and Cremonini 2019). Rainfall is the most common landslide trigger (Iverson 2000). When rainfall infiltrates into the unsaturated soil of a hillslope, the increased water content of the soil leads to a loss of matric suction and an increase in soil weight (Lacerda 2007; Godt et al., 2009; Augusto Filho and Fernandes 2019), leading to hillslope instability and failure. Usually, rainfall-induced hillslope failure occurs preferentially at shallow depths. In contrast, a single high-intensity rainfall event may cause rapid and deep failure, while slow and deep hillslope failure requires long hydrological processes (Sidle and Bogaard 2016). The internal hydrological processes, timing, and location of failures caused by rainfall on hillslopes remain a complex and ongoing research problem. Bogaard and Greco (2016) defined the hydrological processes that trigger hillslope failure as landslide hydrology and noted that storage and flux measurements are essential for understanding and quantifying landslide failure. The evolution of transient unsaturated groundwater flow and local stress can be considered based on physical models to effectively describe rainfall-induced internal hydrological and mechanical changes and failure mechanisms of hillslopes (Zhang J. et al., 2018).

As the physical model can combine hydrological and mechanical mechanisms, it can describe the internal hydrological and mechanical changes and the failure mechanisms of hillslopes caused by transient rainfall. Moreover, the model has a high predictive capability for quantifying the effects of various parameters on the hillslope stability (Corominas et al., 2014). Common hillslope stability analysis usually based on limit equilibrium analysis (e.g., Fellenius, 1936; Janbu, 1954; Bishop, 1955; Morgentern and Price, 1965) or shear strength reduction techniques (Matsui and San 1992; Dawson et al., 1999; Cai and Ugai 2004; Cheng et al., 2007). In addition, research on developed constitutive models that consider soil stress state variables, such as suction stress (Lu and Likos 2006; Lu 2020) and thermal and chemical processes (Nuth and Laloui 2008; Zhang et al., 2012; Bai et al., 2019; Bai et al., 2021), has gradually become prevalent. However, using a single stability index (factor of safety, Fs) for the hillslope makes it challenging to describe the spatiotemporal evolution of the hillslope unstable surface. Recently, Lu et al. (2012) proposed the local factor of safety (LFS) theory. Based on the Mohr-Coulomb failure criterion, the finite element method was used to solve the transient variably saturated flow and stress state, thereby analyzing the local safety factor of each position inside the hillslope. This method can capture the evolution of the stress state and failure surface with rainfall infiltration without the prior condition of the potential failure surface, thereby overcoming the challenges of limit equilibrium analysis. This method has also been applied to study the evolution of hillslope failure surfaces caused by changes in water content dynamics (Moradi et al., 2018) and the change in infiltration characteristics on embankment stability over time and space (Hinds et al., 2019). However, because the physical model relies on an extensive database of *in situ* or laboratory parameters, the quality and quantity of the database are major issues in this analysis, indicating that the model is susceptible to uncertainties arising from measurement errors, spatial variability, and incomplete data (Phoon and Kulhawy 1999). The geotechnical parameters of hillslope material, such as cohesion and friction angle, are inherently heterogeneous in space and these data are often limited in acquisition (Baecher and Christian 2005). The uncertainty of the input model parameters is the main factor that causes the deviation of the hillslope stability analysis results from reality (Burton et al., 1998).

Probabilistic analysis has been widely applied to quantify the uncertainty in hillslope stability analysis (El-Ramly et al., 2002; Griffiths and Fenton 2004; Xiao et al., 2017; Zhang L. et al., 2018; Li et al., 2020). As physical-based slope stability analysis is highly dependent on reliable estimates of soil parameters, the reliability of slopes for soil variables has been increasingly investigated (Jiang et al., 2014; Liu et al., 2019; Johari & Fooladi 2020). However, Nawari and Liang (2000) and Giasi et al. (2003) suggested that probability analysis requires a sufficient number of reliable observations to construct a reasonable probability density function. In addition, the uncertainty of the parameters may be non-stochastic (Juang et al., 1998; Nawari and Liang 2000). When data are limited and insufficient to define the probability density function, fuzzy set theory based on cognitive origin seems to be more suitable for analyzing the uncertainty of geotechnical parameters (Luo et al., 2011; Beer et al., 2013). In some case, this theory has been applied to hillslope stability analysis (Dodagoudar and Venkatachalam 2000; Park et al., 2012; Gong et al., 2014; Xu et al., 2014; Park et al., 2017, 2019; Zhou et al., 2019; Habibagahi et al., 2021).

In this study, by combining the fuzzy theory and hydraulic coupling model to quantify the uncertainty of mechanical parameters (cohesion and internal friction angle), we evaluated the internal hydrological and mechanical processes of hillslopes under rainfall conditions, the two-dimensional spatial distribution of hillslope stability and failure probability, and the impact and evolution of different rainfall patterns on the failure surface using the existing hillslope as an example.

Study methods

The fuzzy theory was used to establish the dependence functions of the soil mechanics parameters, namely cohesion and internal friction angle. The fuzzy point estimation method combined with the finite element analysis model HYDRUS2D and the Slope Cube Module effectively described the changes in

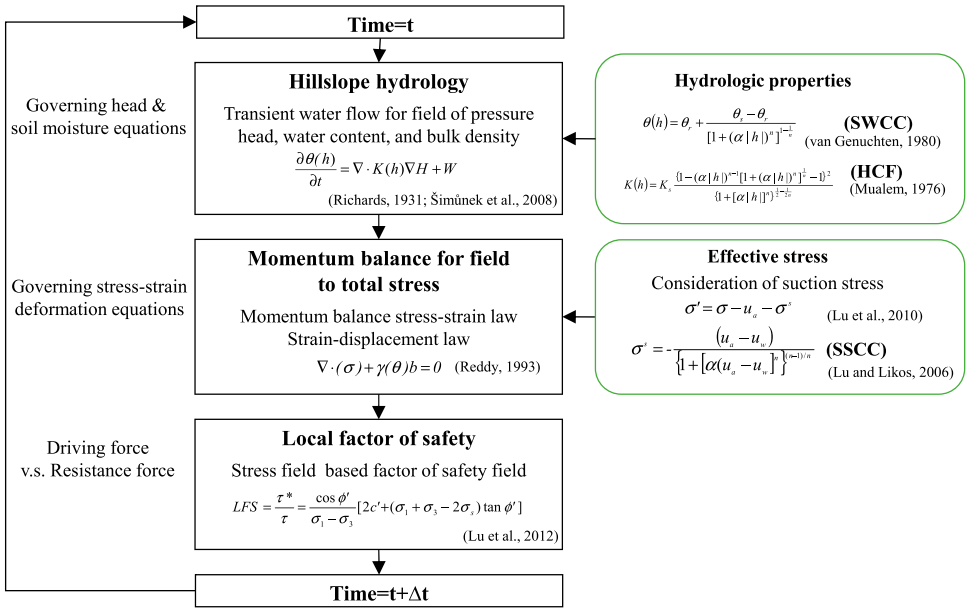

FIGURE 1
Flowchart of one way coupled hydro-mechanical calculation in this study.

the soil hydraulic behavior of the unsaturated layer affected by rainfall infiltration. HYDRUS 2D is a hydrological model that is widely used to simulate the movement of soil water (Bufon et al., 2012; Dabach et al., 2013; Kanda et al., 2020), heat (Wang et al., 2013; Nakhaei and Šimůnek, 2014), and solute (Pang et al., 2000) in variably saturated soils. The Slope Cube Module is a supplemental package of HYDRUS 2D to simulate the transient fields of soil suction, suction stress, and local factor of safety (LFS). Finally, the failure probability was calculated using reliability analysis. The hydraulic analysis process is illustrated in Figure 1, and each method is explained as follows.

Hydrological model

The two-dimensional HYDRUS2D seepage control equation is a transient unsaturated layer seepage control equation developed by Šimůnek et al. (2008) based on Richards' equation (Richards 1931).

$$\frac{\partial\theta(h)}{\partial t}=\nabla\cdot K(h)\nabla H+W \tag{1}$$

where t denotes the time [T]; W, the source or sink [T^{-1}]; H, the total head [L]; $K(h)$, the hydraulic conductivity function (HCF) [LT^{-1}]; and $\theta(h)$, the volumetric water content [L^3L^{-3}]. Soil water characteristic curve (SWCC) links the relationships between matric suction and volumetric water content, and is of great importance for exploring the hydraulic and mechanical behavior of unsaturated soils. In this study, the SWCC model proposed by van Genuchten (1980) and the HCF proposed by Mualem (1976) were used to describe the water retention capacity and hydraulic conductivity coefficients of unsaturated soil, as shown in Eqs 2, 3:

$$\theta(h)=\theta_r+\frac{\theta_s-\theta_r}{[1+(\alpha|h|)^n]^{1-\frac{1}{n}}} \tag{2}$$

$$K(h)=K_s\frac{\{1-(\alpha|h|)^{n-1}[1+(\alpha|h|)^n]^{\frac{1}{n}}-1\}^2}{\{1+[\alpha|h|]^n\}^{\frac{1}{2}-\frac{1}{2n}}} \tag{3}$$

where θ_s denotes the saturated soil water content [L^3L^{-3}]; θ_r, the residual soil water content [L^3L^{-3}]; h, the pressure head [L]; α [1/L] and n [-], the fitted parameters of SWCC [-]; and$K$, the saturated hydraulic conductivity [LT^{-1}].

Stress-strain deformation model

The Hillslope Cube Module adopts the two-dimensional finite element code FEM2D (Reddy 1985) to solve the stress distribution at each point within the hillslope based on the momentum balance. The method is based on plane stress linear elasticity to simulate the stress change caused by the change in transient unit weight, and applies suction stress in the computation of effective stress and displacement. The control equation is expressed as follows:

$$\nabla\cdot(\sigma)+\gamma b=0 \tag{4}$$

where σ denotes the three independent stress variables (i.e., σ_{xx}, σ_{yy}, σ_{xy}) [$ML^{-1}T^{-2}$]; γ, the bulk unit weight of the hillslope soil material [$ML^{-2}T^{-2}$]; and b, the unit vector of body forces [-]. Therefore, the elastic modulus $E = \sigma/\varepsilon$ [$ML^{-1}T^{-2}$] and Poisson's ratio ν [-] can be used to solve the stress and displacement.

The unified effective stress developed and validated by Lu and Likos (2004,2006), and Lu et al. (2010) was adopted.

$$\sigma' = \sigma - u_a - \sigma^s \tag{5}$$

where u_a is the pore-air pressure [$ML^{-1}T^{-2}$] and σ^s is the suction stress [$ML^{-1}T^{-2}$], representing all the physical and chemical mechanisms that can occur between soil particles, expressed as follows:

$$\sigma^s = -\sigma_c = -\sigma_{cap} - \sigma_{pc} - S(u_a - u_w) \tag{6}$$

where σ_c is the Born repulsive force [$ML^{-1}T^{-2}$]; σ_{cap}, the capillary force [$ML^{-1}T^{-2}$]; σ_{pc}, the combination of van der Waals attractive force and electric double-layer force [$ML^{-1}T^{-2}$]; S, the soil saturation [-]; and $(u_a - u_w)$, the matric suction [$ML^{-1}T^{-2}$], where u_w is the pore-water pressure [$ML^{-1}T^{-2}$]. The matric suction, capillary, van der Waals, and electric double-layer force of the soil balance each other out with the Born repulsive force, but the effects of van der Waals and electric double-layer force can be neglected as the grain size of the soil increases. Lu et al. (2010) used thermodynamic theory to consider suction as the energy stored in a unit soil as each stress component of soil can be expressed as a function of matric suction, saturation, and water content, and since soil suction is mainly controlled by soil water content. The suction stress characteristic curve can be estimated from the same set of parameters from the SWCC model. The formula can be expressed as follows:

$$\begin{aligned} \sigma^s &= -(u_a - u_w) && u_a - u_w \le 0 \\ \sigma^s &= -\frac{(u_a - u_w)}{\{1 + [\alpha(u_a - u_w)]^n\}^{(n-1)/n}} && u_a - u_w > 0 \end{aligned} \tag{7}$$

Hillslope stability model

The LFS theory developed by Lu et al. (2012) was used to assess the internal stability of the hillslopes. The LFS is based on the Mohr-Coulomb failure criterion and represents the process of changing the soil stress state toward the direction of failure owing to rainfall infiltration. LFS is defined as the ratio of shear strength to shear stress at any point inside the slope, as follows:

$$LFS = \frac{\tau^*}{\tau} = \frac{\cos\phi'}{\sigma'_{II}}\left(c' + \sigma'_I \tan\phi'\right) \tag{8}$$

where τ^* is the shear strength, also known as potential Coulomb stress [$ML^{-1}T^{-2}$]; τ, the shear stress, also known as current Coulomb stress [$ML^{-1}T^{-2}$];c', effective cohesion [$ML^{-1}T^{-2}$]; andϕ', the effective internal friction angle [°]. σ'_I [$ML^{-1}T^{-2}$] and σ'_{II}[$ML^{-1}T^{-2}$] are the positions of the center and radius of the Mohr circle in two dimensions and can be expressed as follows:

$$\begin{aligned} \sigma_I &= \frac{\sigma'_1 + \sigma'_3}{2} = \frac{\sigma_1 + \sigma_3}{2} - \sigma^s \\ \sigma_{II} &= \frac{\sigma'_1 + \sigma'_3}{2} = \frac{\sigma_1 - \sigma_3}{2} - \sigma^s \end{aligned} \tag{9}$$

Substituting Eq. 9 into Eq. 8, LFS can be expressed as follows:

$$LFS = \frac{\cos\phi'}{\sigma_1 - \sigma_3}\left[2c' + (\sigma_1 + \sigma_3 - 2\sigma^s)\tan\phi'\right] \tag{10}$$

This study calculated the suction stress by combining the water content, matric suction, and total stress changes. The LFS was then calculated using the unified effective stress based on suction stress. This linear theory-based computational mechanics framework solves the stresses and displacements of statically admissible fields, regardless of the complex elastoplastic theory. The redistribution of pressure or displacement caused by a hillslope failure is defined by the static allowable stress field as that satisfies the equilibrium differential equation (Malvern 1969). Therefore, an LFS of less than one indicates the location of potential hillslope failure (Lu et al., 2012), which can be used to indicate the location of potential failure areas. This model and finite element analysis can be used to analyze the stability of soil elements at different locations or depths of the hillslope affected by changes in water content or suction stress, overcoming the challenges of conventional hillslope stability analysis.

Fuzzy set theory

The traditional set rationality defines whether an element x belongs to set A, and its characteristic function is expressed as follows:

$$\mu_A(\mathrm{x}) = \begin{cases} 1, \mathrm{x} \in \mathrm{A} \\ 0, \mathrm{x} \notin \mathrm{A} \end{cases} \tag{11}$$

When x belongs to A,$\mu_A(\mathrm{x}) = 1$; when x does not belong to A, $\mu_A(\mathrm{x}) = 0$. There are only two cases of 0–1. Zadeh (1965) proposed the fuzzy theory to represent the uncertainty and fuzzy phenomenon, also known as the fuzzy set theory. The characteristic function is extended into a continuous value function $\mu_A(\mathrm{x})$ in the interval [0,1], called the membership function. The value of the membership function indicates the degree to which element x belongs to set A. The most significant difference between a fuzzy set and a traditional set is that a traditional set has only a unique characteristic function. In contrast, a fuzzy set has an infinite number of membership functions to represent. Common membership functions include a triangular shape, trapezoid shape, Gaussian shape, S function, and Z function. Triangular and trapezoid functions are less computationally intensive and highly adoptable

(Dodagoudar and Venkatachalam 2000). Fuzzy theory is also known as fuzzy set theory, and the fuzzy number is a special case of fuzzy set, its characteristic is that the shape of the membership function is unimodal, and at least one degree of membership is 1. If there is no specific assumption (under the condition of lack of data), the fuzzy number can be assumed to be a triangle, expressed as $TFN[a, m, b]$, including upper bound (a), lower bound (b), and peak value (m). In general, the peak value is usually estimated from the average of the available data (Luo et al., 2011). This study used cohesion and internal friction angle as analysis variables. We used the mean value of cohesion and friction angle from the laboratory test as the peak value of their fuzzy numbers. Upper and lower bounds were determined using an estimated approach of the standard deviation of uncertain parameters. Therefore, the triangular fuzzy number of cohesion and friction angle can be expressed as follows:

$$\begin{aligned} x_c &= TFN[m_c - k\sigma_c, m_c, m_c + k\sigma_c] \\ x_\phi &= TFN\left[m_\phi - k\sigma_\phi, m_\phi, m_\phi + k\sigma_\phi\right] \end{aligned} \tag{12}$$

The value of k depends on the actual conditions of the hillslope project and ranges from 0.5 to 3. When the value of k is larger, the distribution of the mechanical parameters is larger and the selected parameter is less reliable, and vice versa. Luo et al. (2011) and Park et al. (2017) considered it reasonable to estimate the upper and lower bounds using the mean value of $\pm 2\sigma$. Therefore, the value of k in this study was considered to be 2 cv is the coefficient of variation, which indicates the degree of parameter variation ($cv = \sigma/\mu$):$cv$of cohesion is 25–30%, and that of the internal friction angle is 10–20% (Phoon & Kulhawy 1999; Hsiao et al., 2008; Park et al., 2013).

The fuzzy point estimation method combines the fuzzy vertex and the point estimation methods. The fuzzy vertex method was proposed by Dong and Shah (1987) and is based on α- intercept set and interval analysis to obtain the vertex combinations of variables and replace the membership functions as input variables. Thus, there are vertex combinations for N membership functions as the input variables2^N. Rosenblueth (1975) proposed a point estimation method to evaluate the uncertainty parameters of a performance function. Two points estimate the mean and standard deviation of the performance function, and the upper bounds of the variables obtained through α- intercept set are $(c_-^{\alpha_i}, c_+^{\alpha_i})$ and $(\phi_-^{\alpha_i}, \phi_+^{\alpha_i})$, respectively. In this study, the α-intercept set took nine membership degrees from 0.1 to 0.9 to reduce the dispersion of the analysis results. Each α- intercept set can cut out a range of two points and obtain four sets of vertex combinations, and four sets of output values were obtained through simulation $(LFS_{--}, LFS_{-+}, LFS_{+-}, LFS_{++})$. When considering the difference in the contribution of each α- intercept set to the results, this study used the concept of fuzzy weighted average, and the mean and standard deviation of the fuzzy weighted factor of safety is expressed as follows.

$$E[LFS] = \frac{\sum_{i=1}^{M} \alpha_i LFS_{\alpha_i}}{\sum_{i=1}^{M} \alpha_i} \tag{13}$$

$$\sigma_{LFS} = \sqrt{E[LFS^2] - (E[LFS])^2} \tag{14}$$

$M$is the number of α- intercept sets. The failure probability is obtained from the reliability index. Assuming that the factor of safety is normally distributed, the reliability index is a standard normal distribution. The reliability indexβ and failure probability (P_f) are expressed as follows:

$$\beta = \frac{E[LFS] - 1}{\sigma_{LFS}} \tag{15}$$

$$P_f = 1 - \Phi(\beta) = \Phi(-\beta) \tag{16}$$

Study site

Background of the study site

Located at the collapse site of Babaoliao in the Dongxing Village, Zhongpu Township, Chiayi County, the topography of the study site is low-altitude hilly terrain with elevations ranging from 420–580 m. The slopes of the area are Grade 5 and Grade 6 (slope >40°), and the slope direction decreases from north to south, followed by southeast, southwest, and west. The rocks belong to the western piedmont belt geological area, and the exposed strata are of Miocene to Pleistocene age. As shown in Figure 2, the regional geological unit contained the main stratum of the collapse site—the beak layer (Niaotsui Formation, Nt), with a lithology of muddy sandstone, sandy shale, and thick sandstone. The Yunshuichi Formation (Yh) was first exposed and was composed to shale, sandy shale, and mudstone on the west side of the collapse site. The Liuchungchi Formation (Lu), with silt-layered shales, sandy shales, or interbedded muddy sandstones, is exposed on the west side of the collapse site. Tangenshan sandstone (Tn), located on the eastern side of the collapse site, is dominated by thickly bedded gray to massive mudstone sandstone, occasionally interbedded with sandstone or thin shale. The Changchikeng Formation (Cc) is dominated by greenish-grey fine-grained sandstone, muddy sandstone, and thick grey sand shale, commonly interbedded with mound-like laminations. In the geological structure, the Liuchungchi Fault passes through the southern side of the collapsed area, while the Chukou and Lunhou Faults are the main fault structures in the area. The collapse site was mainly located on the back-slope axis (anticline axis) and its eastern flank slope. The northeastern portion of the collapse site presents a localized oblique structure. This complex geological condition is one factor contributing to the higher collapse

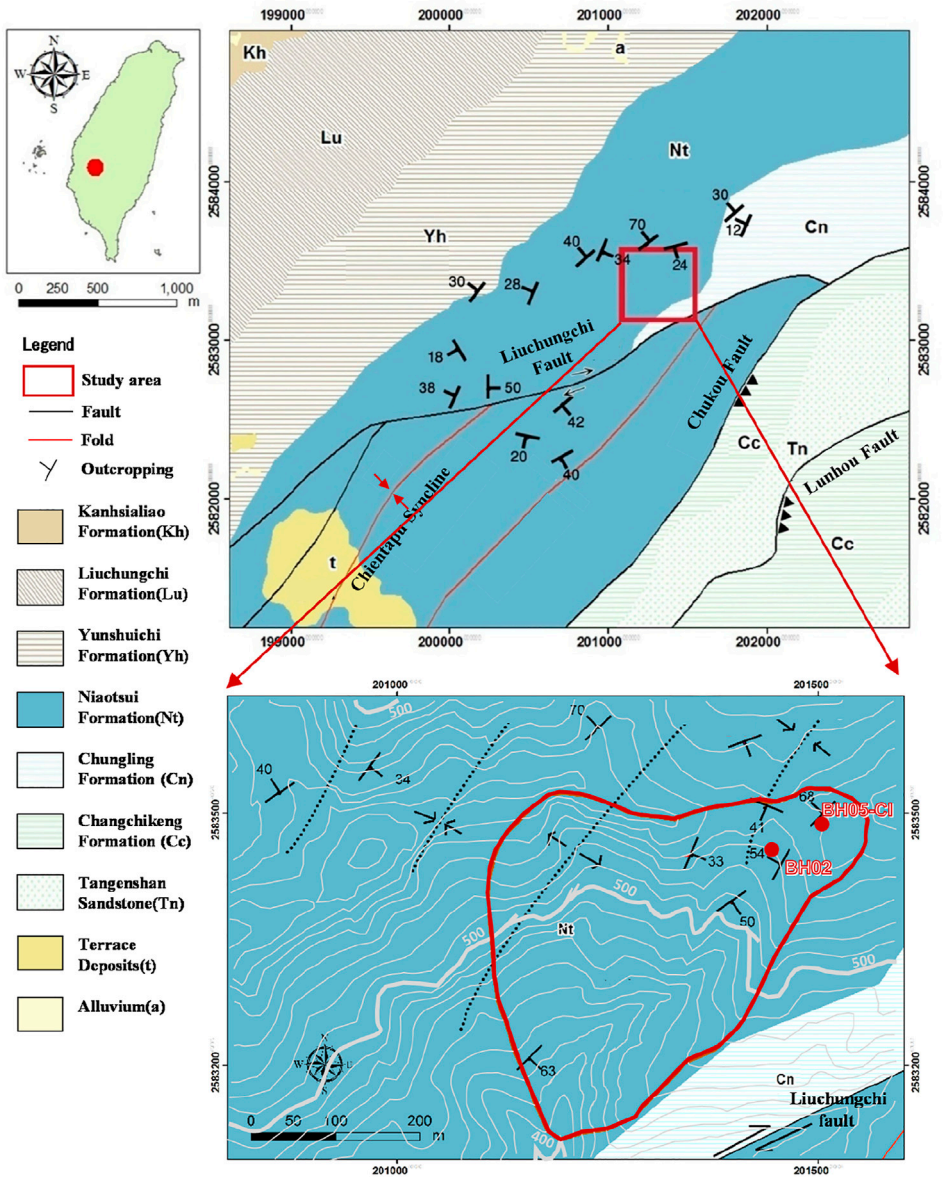

FIGURE 2
Schematic diagram of geology and geological structure in Babaoliao area.

potential of the area. Since the formation of the collapse site in November 2011, the landslide area has continued to expand owing to heavy rains and typhoons, and there are signs of continuous sliding. The potential collapse area is 11.31 ha, with a risk of shallow collapse and deep sliding. Systematic surveys have been conducted since 2017. To date, the collapse site has undergone integrated analysis such as field surveys, geophysical/chemical investigations, sampling and analysis, observation system construction, UAV interpretation, and application models. Related observations are ongoing, and the investigation strategy is being revised in response to spatiotemporal changes to clarify the sliding mechanism of the potential landslide and formulate countermeasures (Branch, 2018).

Hydrogeological assessment

The internal factor of the Babaoliao collapse mechanism was regional geological fragmentation, and the external

TABLE 1 Hydraulic and mechanical parameters of three geological materials.

Hydraulic parameters

Materials	θr [-]	θs [-]	α [m^{-1}]	n [-]	e [-]	Ks [mm/h]
Soil	0.00001	0.350	0.21	1.158	0.56	32.4
Regolith	0.0000124	0.486	0.63	1.125	1.05	3.24
Bedrock	0.031	0.467	3.64	1.121	0.19	5.90×10^{-03}

Mechanical parameters

Materials	Gs[-]	c'[kPa]	ϕ'[degree]	E[kPa]	possion ratio[-]
Soil	2.72	17.16	23	20000	0.33
Regolith	2.61	34.33	23	20000	0.33
Bedrock	2.64	68.65	23	40000	0.33

triggering factor was mainly rainfall. When rainfall infiltrates into shallow soil or generates fracture -advantageous water flow on the sliding surface, it may cause hillslope instability. Therefore, we conducted soil sampling and indoor test analysis on the collapse site to understand the internal hydraulic behavior of hillslope soils due to rainfall and its effect on stability. The test items included the general physical property test of soil (unit weight, porosity ratio, specific gravity, and saturation), general physical property test of rock (water content, porosity, durability, unit weight, and specific gravity), triaxial water permeability test of soil, pressure cooker test of soil, and direct shear test of rock. The tests were performed by the geotechnical engineering test laboratory of Sinotech Engineering Consultants with TAF certification. The hydro-mechanical properties of geological materials are listed in Table 1 and reported in detail in SWCB (2018). The results and parameters of the tests were used as references for subsequent conceptual modeling of the collapse site. The soil composition of the fine particles was mainly fine sand to powder soil, whereas the coarse particles with relatively high content are mainly medium sand. The results of the soil permeability test showed that the permeability values ranged from 1.64×10^{-7}–8.99×10^{-6} cm/s at 20°C under different compression pressure. The test

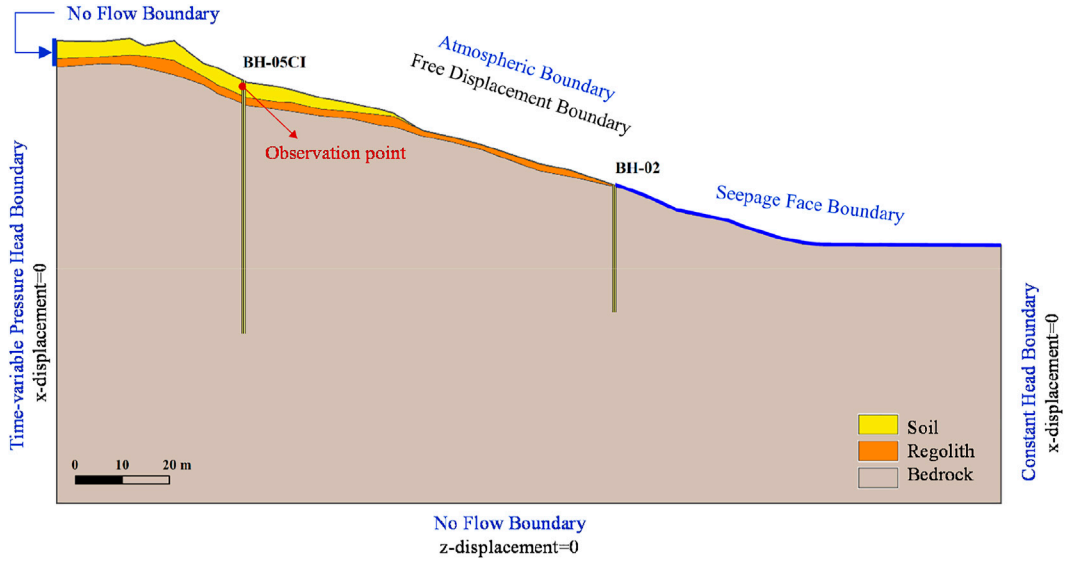

FIGURE 3
Conceptual model of slope geometry and boundary conditions.

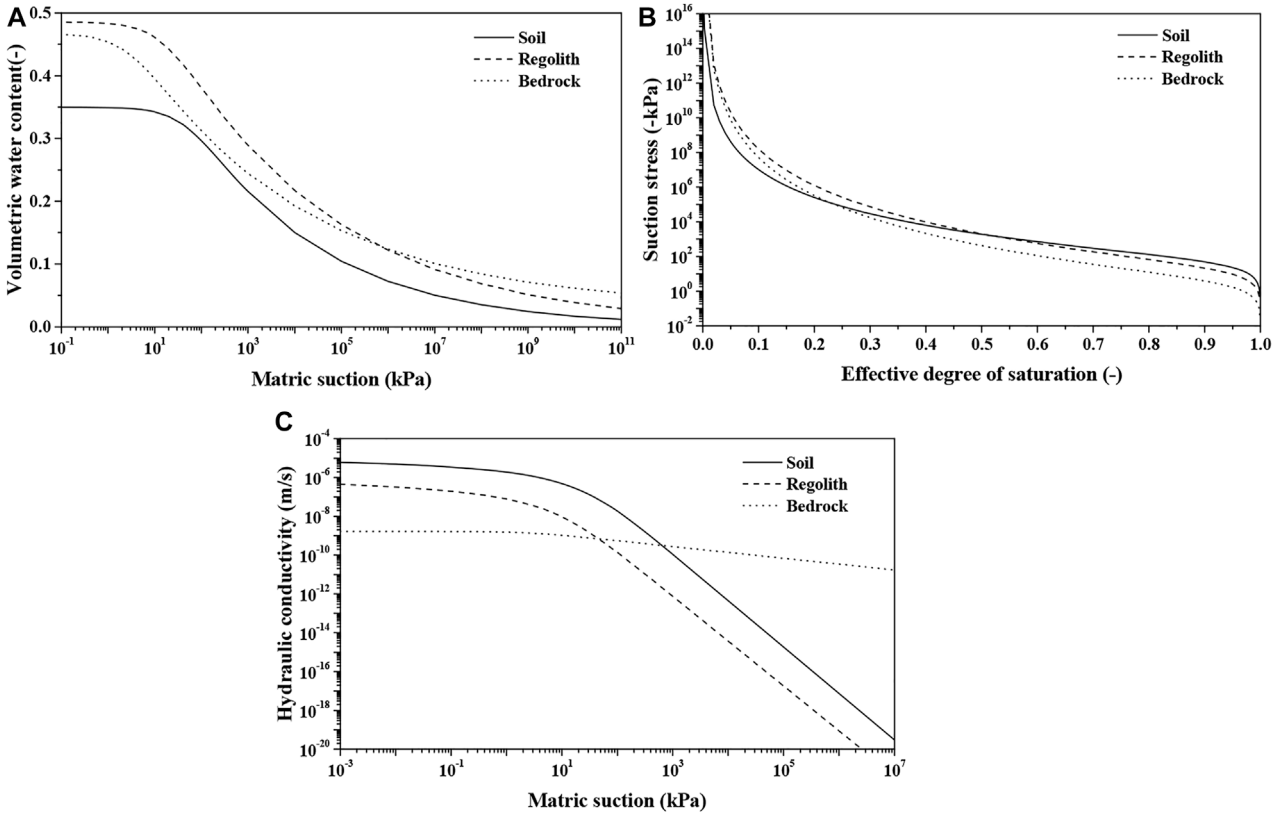

FIGURE 4
Hydraulic properties of materials **(A)** SWCC **(B)** SSCC **(C)** HCF.

results showed that the unit weight of the rock sample was 2.37–2.69 t/m^3, water content was 1.9–8.7%, specific gravity was 2.68–2.73, porosity was 0.08–0.19, and water absorption rate was 2.7–12.8%.

Conceptual modeling of hillslopes

This study used the section from BH05-CI to BH-02 on the upper slope of the disaster-prone area at the Babaoliao collapse site as an example. The soil thickness of this section ranges from 3.8 to 7.2 m, and the rock plate is muddy sandstone. On-site surveys have shown that the surface soil has undergone erosion caused by rainfall events, forming several eroded pits and trenches, and is prone to disasters such as rock chippings. BH-05CI established an automatic observation record of in-hole deformation in July 2018, and obvious deformation was observed during the rainfall period from 08/23/2018 to 08/24/2018. This study adopted a rainfall event (hereafter referred to as the 0823 rainfall event) for subsequent numerical simulations. In this study, the geological conceptual model from BH05-CI to BH-02 was first established based on the results of previous field surveys and tests, as shown in Figure 3, and the actual

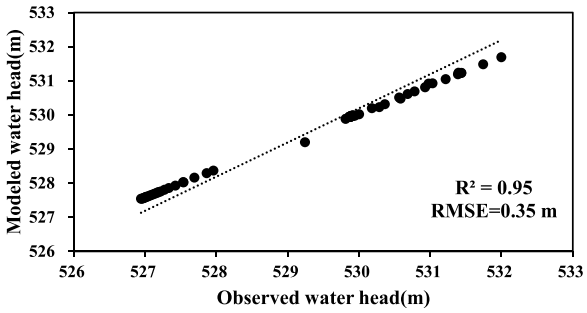

FIGURE 5
Validation of simulated value against observed values at BH05-CI.

elevation of the slope before the rainfall event was used for the surface elevation. According to the experimental parameters of the test (Table 1), we adopted the best-fitting SWCC, HCF, and estimated SSCC through Eq. 7, as shown in Figure 4.

Stratification was used as the mesh refinement unit in this study. The soil layer was set to 0.8 m, and the weathered rock

TABLE 2 The value of cohesion and friction angle of three geological materials in this study.

α-cut	Soil				Regolith				Bedrock			
	c-	c+	ϕ-	ϕ+	c-	c+	ϕ-	ϕ+	c-	c+	ϕ-	ϕ+
0.1	7.89	26.43	14.72	31.28	15.79	52.87	14.72	31.28	31.58	105.72	14.72	31.28
0.2	8.92	25.40	15.64	30.36	17.85	50.81	15.64	30.36	35.70	101.60	15.64	30.36
0.3	9.95	24.37	16.56	29.44	19.91	48.75	16.56	29.44	39.82	97.48	16.56	29.44
0.4	10.98	23.34	17.48	28.52	21.97	46.69	17.48	28.52	43.94	93.36	17.48	28.52
0.5	12.01	22.31	18.40	27.60	24.03	44.63	18.40	27.60	48.06	89.25	18.4	27.6
0.6	13.04	21.28	19.32	26.68	26.09	42.57	19.32	26.68	52.17	85.13	19.32	26.68
0.7	14.07	20.25	20.24	25.76	28.15	40.51	20.24	25.76	56.29	81.01	20.24	25.76
0.8	15.10	19.22	21.16	24.84	30.21	38.45	21.16	24.84	60.41	76.89	21.16	24.84
0.9	16.13	18.19	22.08	23.92	32.27	36.39	22.08	23.92	64.53	72.79	22.08	23.92

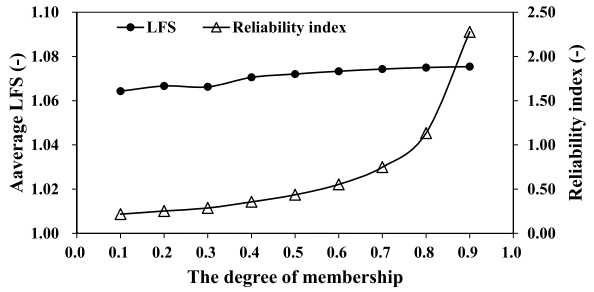

FIGURE 6
Variation of average LFS, reliability index with the degree of membership.

debris layer was 1.6 m. The farther the grid distance from the set stratification, the larger the size, and the system automatically optimizes the target grid size to 5.6 m; that is, the grid distribution to the target grid size stops. The overall grid was divided into 2,453 nodes and 5,032 elements. The hydrological boundary is the atmospheric boundary on the slope, seepage surface boundary on the slope below BH-02, constant head boundary on the right side, time-varying head boundary on the left side, and zero-flow boundary at the bottom. The mechanical boundary is the free displacement boundary on the slope, the zero-displacement boundary in the *x*-direction on the left and right sides, and the zero-displacement boundary in the *z*-direction at the bottom. The simulation of the 0823 rainfall events included the complete rainfall events. To include the complete rainfall event, the simulation time used in this study was 60 h, and the iterative convergence conditions are 0.001 water content tolerance and 0.01 m pressure head tolerance. The simulation results showed that the root mean square error of water level was ~0.35 m, and the coefficient of determination R^2 was ~0.95 at the BH05-CI, as shown in Figure 5, indicating the reasonableness of the model.

Establishment of cohesion and internal friction angle fuzzy numbers

In this study, the cohesion force and internal friction angle were considered triangular fuzzy numbers, and the values in Table 1 were considered the mean values. The maximum coefficient of variation was used to establish the triangular fuzzy numbers, which were 30% of the cohesion coefficient of variation and 20% of the internal friction angle coefficient of variation. The top sets of cohesion and internal friction angle were obtained by intercepting nine affiliations from 0.1 to 0.9. A total of 36 input variables were obtained, as listed in Table 2. After the model calculation, 36 sets of output variables were obtained, subsequently, the hillslope failure probability was obtained by calculating Eqs 13–15.

Results and discussion

Analysis of failure probability of historical rainfall events

This study used the 0823 rainfall event as the analysis period. We obtained different combinations of parameters with varying degrees of affiliation through the intercept set without considering the correlation between cohesion and angle of internal friction. We considered an observation point at a depth of 1 m for BH-05CI and the 48th hour of rainfall as an example. The results show that the reliability index increased as the degree of affiliation increased. The

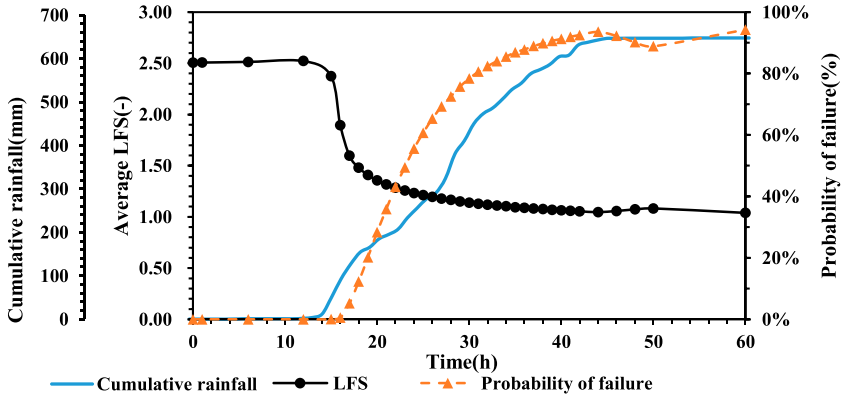

FIGURE 7
Temporal variation in accumulation rainfall, fuzzy weighted average LFS and probability of failure at observation point.

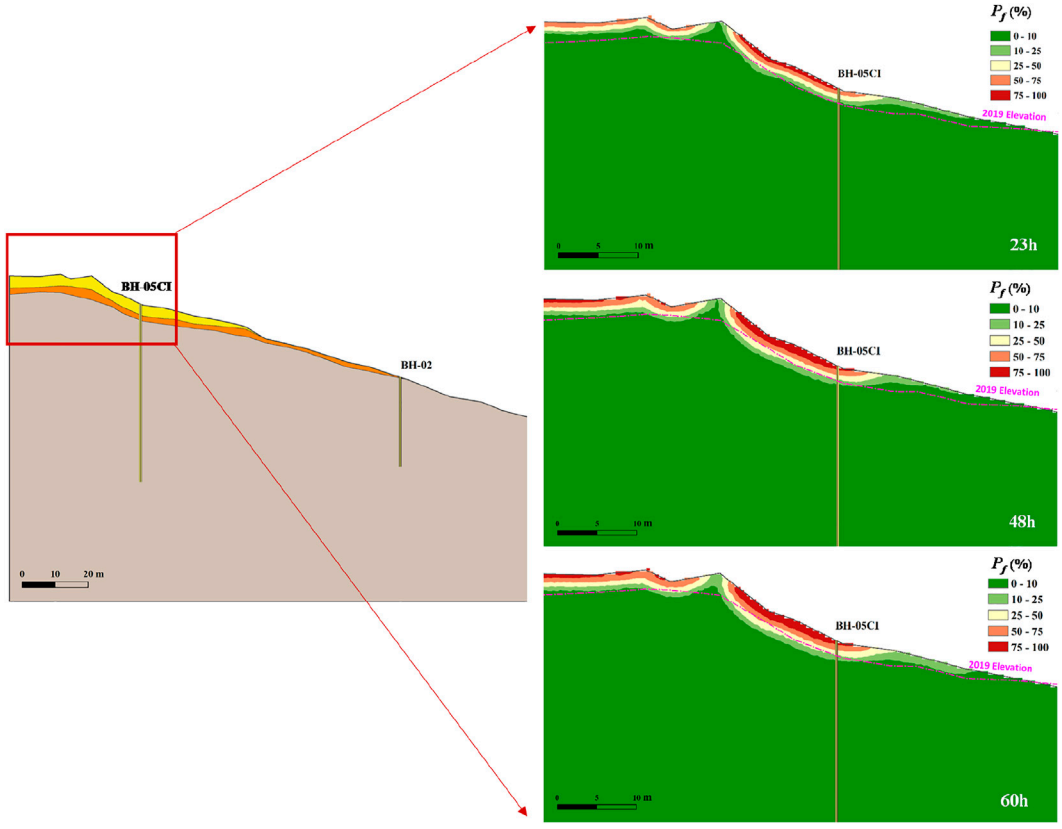

FIGURE 8
Distribution of probability of failure at 23, 48, and 60 h at the top of slope.

average local safety coefficient at this location varied from [1.064, 1.075] to [0.217, 2.278], as shown in Figure 6. The fuzzy weighted average local safety factor considering the degree of membership was 1.073. The change in the fuzzy weighted average local safety factor over time is shown in Figure 7. According to the rainfall data, continuous heavy rainfall began at the 15th hour. The BH-05CI observation deformation records in the wellbore show that the position started to deform by 0.54 mm at the 23rd hour, the

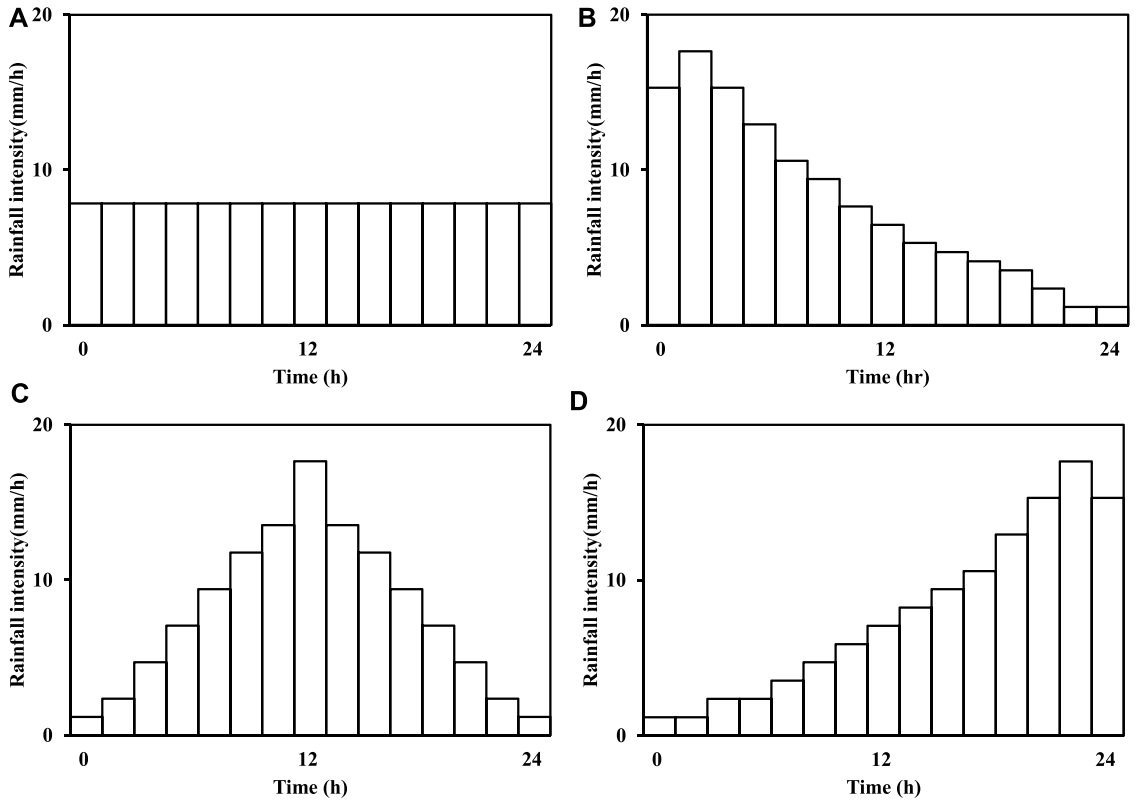

FIGURE 9
Four rainfall patterns with the same accumulated rainfall, 200 mm: **(A)** uniform rainfall pattern, **(B)** delayed rainfall pattern, **(C)** normal rainfall pattern, **(D)** advanced rainfall pattern.

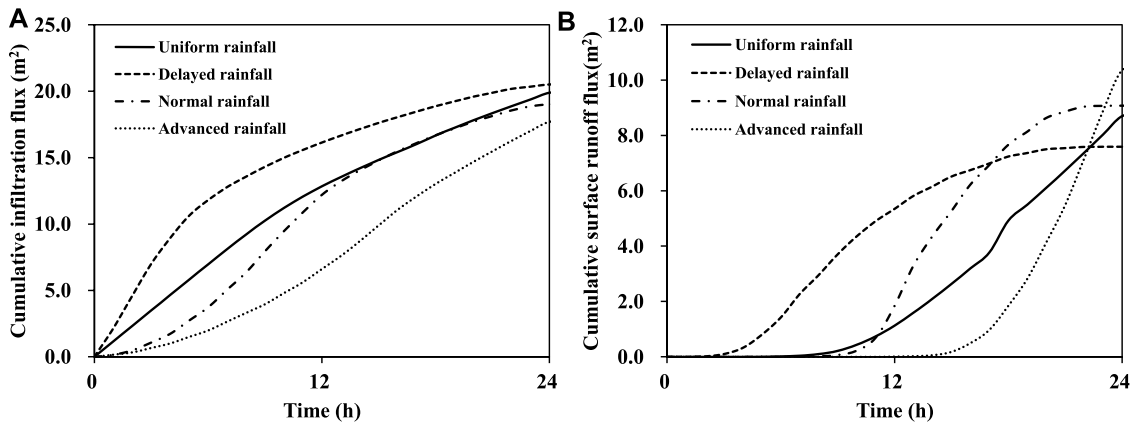

FIGURE 10
Result of flux analysis on atmospheric boundary condition under four rainfall pattern**(A)**cumulative infiltration flux and **(B)** cumulative surface runoff flux.

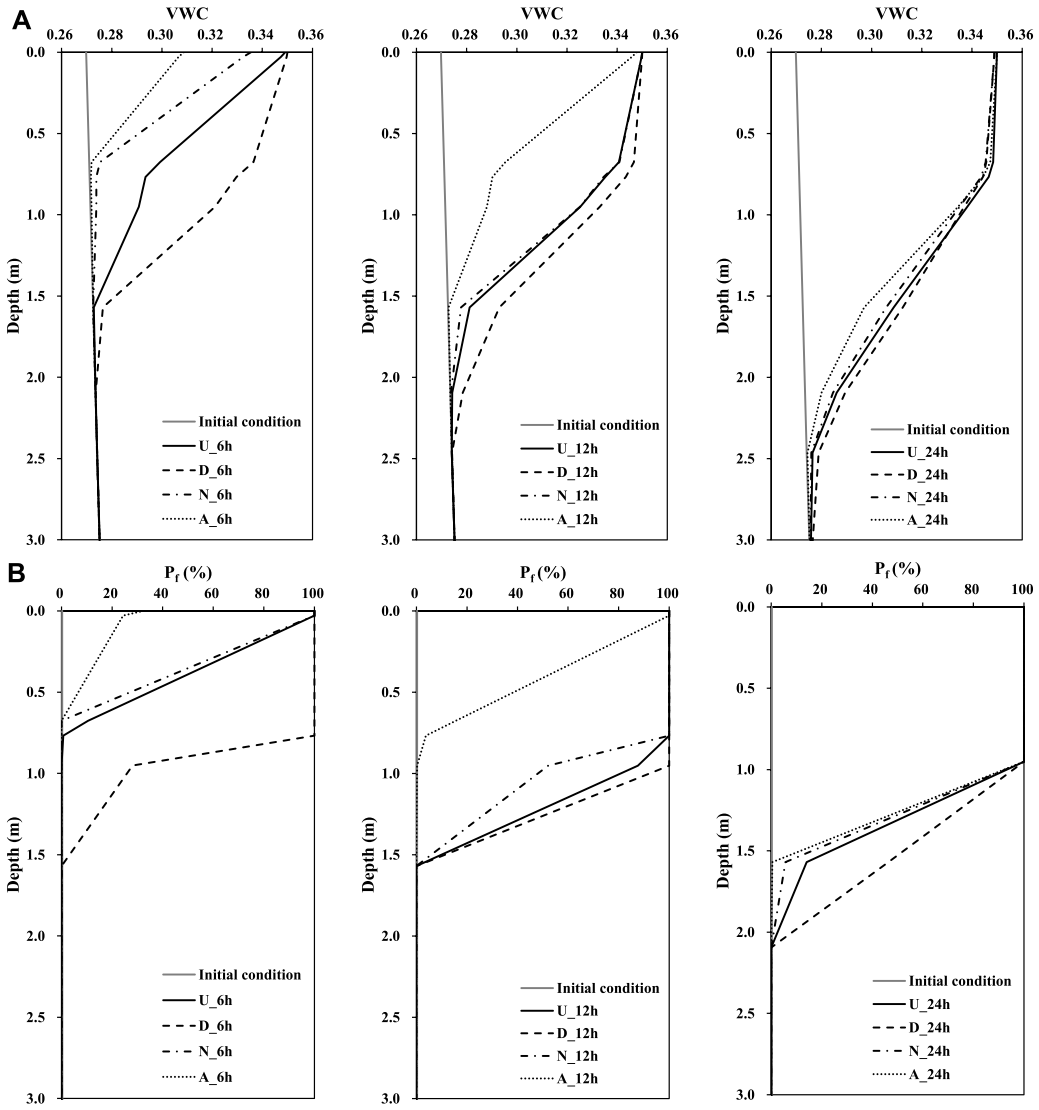

FIGURE 11
Result of **(A)** volumetric water content and **(B)** probability of failure change with depth at 6, 12 and 24 h (U: Uniform rainfall pattern; D: Delayed rainfall pattern; N: Normal rainfall pattern; A: Advanced rainfall pattern).

deformation increased by more than 1 mm per hour, and the maximum deformation was 25.04 mm at the 32nd hour. Therefore, the LFS (LFS = 1.258) at the 23rd hour was considered a critical value in this study. The change in the failure rate of this observation point with time showed that the LFS decreased with the increase in cumulative rainfall, and the failure rate increased with it. The failure rates were 50% at the 23rd hour, 90% at the 48th hour, and 94% at the 60th hour. The spatial distribution of the failure rate was mainly concentrated around BH-05CI, indicating that the unstable area of the slope extended from the surface to the bottom as the rainfall infiltration increased. A failure rate of 50% was used as an indicator of instability. The instability depth was ~1.5 m at the 23rd hour, 1.8 m at the 48th hour, and 2 m at the 60th hour. As shown in Figure 8, the areas with a failure rate of over 50% were consistent with the interface of elevation loss, indicating that the model can predict the area of slope instability and its change over time and space.

Analysis of rainfall pattern failure probability

In this study, regarding the warning management benchmark of Babaoliao, the cumulative rainfall of the yellow warning in the area was 200 mm, and the average rainfall intensity was 20 mm/h (SWCB, 2018). Therefore, in this study, four rainfall patterns were

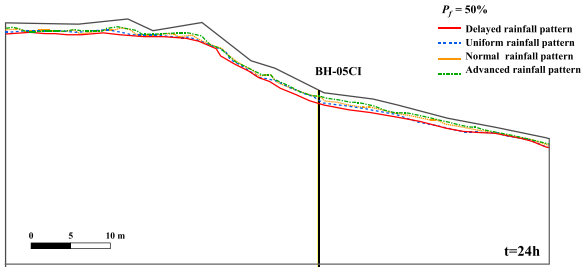

FIGURE 12
Distribution of 50% probability of failure at 24 h at the top of slope.

designed based on the principle of 24-h cumulative rainfall of 200 mm, namely, uniform, delayed, normal, and advanced rainfall patterns (Rahimi et al., 2011), as shown in Figure 9, to investigate the effect of different rainfall patterns on the hydraulic behavior and stability of the hillslope.

This study first analyzed the cumulative runoff and infiltration flux of the atmospheric boundary at the surface of the slope under four rainfall patterns. Surface runoff analysis showed that the retrogressive rain pattern was third in rainfall time owing to the strong initial rainfall intensity. Surface runoff occurs in hours, and surface runoff occurred at the latest in the progressive rain pattern of ~ the 14th hour, as shown in Figure 10A. The cumulative infiltration flux shows that the overall cumulative infiltration flux of the delayed rainfall pattern was higher than that of the other rainfall patterns in each time period, as shown in Figure 10B. This study evaluated the changes in the volumetric water content of the surface soil with depth in different time periods under four rainfall conditions on the BH-05CI vertical profile. The delayed rainfall pattern caused the soil surface to reach saturation in a short time (the sixth hour as an example). Furthermore, the wet zone had a deep advancing depth, and the water content response depth was ~2 m. Advanced rainfall patterns had little initial and accumulated rainfall intensity, so the water content response depth was ~0.7 m, and the surface layer was saturated. As shown in Figure 11A, at the 12th hour, the water content reaction states of the homogeneous and normal types were similar. After the 24th hour, the surface layer reached a saturated state, and the depth of the saturation zone was ~0.7 m. The water content response changed below the saturation zone in the order of delayed rainfall pattern> uniform rainfall pattern> normal rainfall pattern> advanced rainfall pattern. The soil water content was affected by the rainfall pattern and accumulated rainfall. In the process of rainfall infiltration, rainfall intensity affected the development of the shallow saturation profile, revealing the important influence of vertical seepage on shallow hydrological responses. Chinkulkijniwat et al. (2016) conducted experiments to evaluate the hydrological response of different shallow slope and showed similar findings. The slope soil was unstable owing to rainfall infiltration, which was affected by the change and distribution of soil water content. The analysis of the probability of failure shows that in the sixth hour, except for the advanced rainfall pattern, other rainfall patterns caused instability of the surface soil. Along with the vertically downward direction of the saturation zone, the instability range also developed in the deep soil, as shown in Figure 11B; in the 24th hour, the location with a 100% probability of failure was ~1 m below the surface.

Under the four rainfall conditions, the spatial variability of the hillslope failure probability was affected by the boundary flux and hillslope topography, as shown in Figure 12. The spatial distribution of the failure probability of 50% was presented at the end of the rainfall time (24th hour) as the basis of analysis, which showed that different rainfall patterns would lead to different degrees of development of the unstable area for the same cumulative rainfall of 200 mm. At the end of the rainfall event, the delayed rainfall pattern had the largest instability area, followed by the uniform and normal types. In contrast, the advancing rain type had the smallest instability area. The variation in stability over time was evaluated at the observation

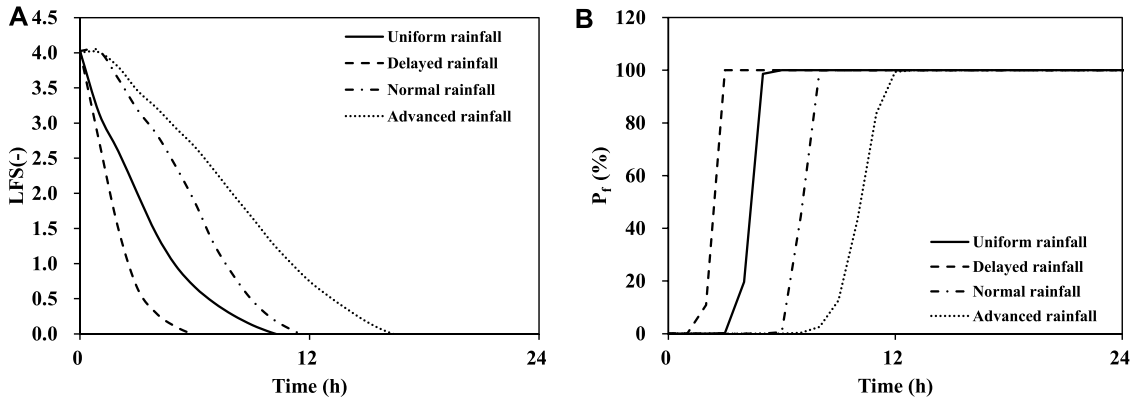

FIGURE 13
Result of **(A)** slope stability analysis and **(B)** probability of failure under four rainfall patterns.

point of BH-05CI at a depth of 1 m. When considering the time variability, this study considered the observation point at a depth of 1 m at BH-05CI as an example to evaluate the changes in stability over time under the four different rainfall patterns, as shown in Figure 13. The average local safety factor of the delayed rainfall pattern had a large decreasing slope, reaching a failure probability of 100% in the third hour, followed by a uniform rainfall pattern at the sixth hour, a normal rainfall pattern at the ninth hour, and an advanced rainfall pattern at the 13th hour. This shows that even if the accumulated rainfall over 24-h was 200 mm, depending on the rainfall intensity, the overall infiltration flux of the slope changes dynamically, affecting the time of slope instability. Among them, the delayed rainfall pattern significantly impacted on the time of slope instability, and shallow collapse was most likely to occur earlier. Rahimi et al. (2011) showed that the delayed rainfall pattern occurred earlier and exhibited similar results. It should be noted that this study only considered the effects of different rainfall patterns on the boundary fluxes, slope hydraulic behavior, and stability for the same 24-h rainfall. When the rainfall is of the long-delay, high-intensity continuous type, deeper slope failure may occur after the shallow collapse, which is not included in the scope of this study. The type and scale of slope failure are controlled by slope hydraulic behavior, geomaterial properties, and slope structure. Shallow failures are usually the priority soil-sand hazards caused by rainfall, indicating the importance of evaluating shallow soil hydraulic behavior and failure mechanisms.

Conclusion

This study considered uncertainties in the mechanical parameters. The fuzzy theory was combined with the hydraulic coupling model and the LFS theory was used to evaluate the LFS at different depths of the shallow slope. Reliability analysis was then used to calculate the failure rate of the slope at different depths. To verify the rationality of the analytical model, this study used a case study of the Babaoliao hillslope, which has a record of in-hole deformation and observed displacements, to simulate the 0823 rainfall event, analyze of the simulation results, calculate the failure probability, and compare the instability range.

The observation of 1 m underground displacement in BH-05CI, and the time of the beginning of displacement after the 23rd h was used as the benchmark. The local safety factor at this time was regarded as the critical value (LFS = 1.258), and the underground factor was calculated—the change in the probability of failure with time. The results showed that the failure rate was 50% at the 23rd hour, 90% at the 48th hour, and 94% at the 60th hour. Spatial analysis showed that the change in the failure rate was mainly concentrated around BH-05CI, and the relative instability area is consistent with the elevation loss interface, indicating that the model could effectively describe the development and distribution of the slope instability area with *in situ* observation data.

We evaluated the effect of different rainfall patterns on hillslope stability concerning yellow alert rainfall (24-h cumulative rainfall of 200 mm), which is the benchmark value of the Babaoliao alert management. The results showed that the boundary flux controls the overall infiltration of water into the slope and affects the change in soil water content, which in turn causes slope instability. Delayed rainfall causes early slope instability, therefore, special attention should be paid to this type of rainfall pattern. According to the occurrence sequence of soil-sand disasters, shallow landslides and soil-rock flows are usually the priority soil-sand disasters. They are influenced by the internal hydraulic behavior of the slope, the characteristics of the geological material, and the structure that controls the type and scale of slope failure, indicating that shallow failure is one of the precursors of large-scale collapse. Therefore, evaluating the hydraulic behavior and failure mechanisms of shallow soils is crucial.

Data availability statement

The original contributions presented in the study are included in the article/supplementary material, further inquiries can be directed to the corresponding author.

Author contributions

Material preparation, investigation, data collection and curation were performed by C-CK, N-CC, and K-CC. Conceptualization, data analysis, visualization and the original draft was performed by Y-SY. Supervision and Writing-reviewing and editing was performed by H-FY. All authors commented on previous versions of the manuscript and approved the final manuscript.

Conflict of interest

C-CK and N-CC were employed by the company Sinotech Engineering Consultants, Inc.

The remaining authors declare that the research was conducted in the absence of any commercial or financial relationships that could be construed as a potential conflict of interest.

Publisher's note

References

Augusto Filho, O., and Fernandes, M. A. (2019). Landslide analysis of unsaturated soil slopes based on rainfall and matric suction data. *Bull. Eng. Geol. Environ.* 78 (6), 4167–4185. doi:10.1007/s10064-018-1392-5

Baecher, G. B., and Christian, J. T. (2005). *Reliability and statistics in geotechnical engineering*. John Wiley & Sons.

Bai, B., Yang, G. C., Li, T., and Yang, G. S. (2019). A thermodynamic constitutive model with temperature effect based on particle rearrangement for geomaterials. *Mech. Mat.* 139, 103180. doi:10.1016/j.mechmat.2019.103180

Bai, B., Zhou, R., Cai, G., Hu, W., and Yang, G. (2021). Coupled thermo-hydro-mechanical mechanism in view of the soil particle rearrangement of granular thermodynamics. *Comput. Geotech.* 137, 104272. doi:10.1016/j.compgeo.2021.104272

Beer, M., Zhang, Y., Quek, S. T., and Phoon, K. K. (2013). Reliability analysis with scarce information: Comparing alternative approaches in a geotechnical engineering context. *Struct. Saf.* 41, 1–10. doi:10.1016/j.strusafe.2012.10.003

Bishop, A. W. (1955). The use of the slip circle in the stability analysis of slopes. *Géotechnique* 5 (1), 7–17. doi:10.1680/geot.1955.5.1.7

Bogaard, T. A., and Greco, R. (2016). Landslide hydrology: From hydrology to pore pressure. *WIREs Water* 3 (3), 439–459. doi:10.1002/wat2.1126

Branch, N. (2018), Large-scale collapse investigation and monitoring plan in the Babaoliao area - evaluation and correlation of key factors of multi-scale sliding signs in collapse (in Chinese)). *Soil and water conservation bureau council of agriculture*. Executive Yuan.

Bufon, V. B., Lascano, R. J., Bednarz, C., Booker, J. D., and Gitz, D. C. (2012). Soil water content on drip irrigated cotton: Comparison of measured and simulated values obtained with the hydrus 2-D model. *Irrig. Sci.* 30 (4), 259–273. doi:10.1007/s00271-011-0279-z

Burton, A., Arkell, T. J., and Bathurst, J. (1998). Field variability of landslide model parameters. *Environ. Geol.* 35 (2-3), 100–114. doi:10.1007/s002540050297

Cai, F., and Ugai, K. (2004). Numerical analysis of rainfall effects on slope stability. *Int. J. Geomech.* 4 (2), 69–78. doi:10.1061/(asce)1532-3641(2004)4:2(69)

Cheng, Y. M., Lansivaara, T., and Wei, W. (2007). Two-dimensional slope stability analysis by limit equilibrium and strength reduction methods. *Comput. Geotech.* 34 (3), 137–150. doi:10.1016/j.compgeo.2006.10.011

Chinkulkijniwat, A., Yubonchit, S., Horpibulsuk, S., Jothityangkoon, C., Jeeptaku, C., and Arulrajah, A. (2016). Hydrological responses and stability analysis of shallow slopes with cohesionless soil subjected to continuous rainfall. *Can. Geotech. J.* 53 (12), 2001–2013. doi:10.1139/cgj-2016-0143

Corominas, J., van Westen, C., Frattini, P., Cascini, L., Malet, J. P., Fotopoulou, S., et al. (2014). Recommendations for the quantitative analysis of landslide risk. *Bull. Eng. Geol. Environ.* 73 (2), 209–263. doi:10.1007/s10064-013-0538-8

Dabach, S., Lazarovitch, N., Šimůnek, J., and Shani, U. (2013). Numerical investigation of irrigation scheduling based on soil water status. *Irrig. Sci.* 31 (1), 27–36. doi:10.1007/s00271-011-0289-x

Dawson, E., Roth, W., and Drescher, A. (1999). Slope stability analysis by strength reduction. *Geotechnique* 49 (6), 835–840. doi:10.1680/geot.1999.49.6.835

Dodagoudar, G., and Venkatachalam, G. (2000). Reliability analysis of slopes using fuzzy sets theory. *Comput. Geotech.* 27 (2), 101–115. doi:10.1016/S0266-352X(00)00009-4

Dong, W., and Shah, H. C. (1987). Vertex method for computing functions of fuzzy variables. *Fuzzy Sets Syst.* 24 (1), 65–78. doi:10.1016/0165-0114(87)90114-X

El-Ramly, H., Morgenstern, N., and Cruden, D. (2002). Probabilistic slope stability analysis for practice. *Can. Geotech. J.* 39 (3), 665–683. doi:10.1139/t02-034

Fellenius, W. (1936). Paper presented at the transactions, *Calculation of stability of earth dam*. Washington, DC. 2nd Congress Large Dams.

Giasi, C., Masi, P., and Cherubini, C. (2003). Probabilistic and fuzzy reliability analysis of a sample slope near Aliano. *Eng. Geol.* 67 (3-4), 391–402. doi:10.1016/S0013-7952(02)00222-3

Godt, J. W., Baum, R. L., and Lu, N. (2009). Landsliding in partially saturated materials. *Geophys. Res. Lett.* 36 (2). doi:10.1029/2008GL035996

Gong, W., Wang, L., Khoshnevisan, S., Juang, C. H., Huang, H., and Zhang, J. (2014). Robust geotechnical design of Earth slopes using fuzzy sets. *J. Geotech. Geoenviron. Eng.* 141 (1), 04014084. doi:10.1061/(ASCE)GT.1943-5606.0001196

Griffiths, D., and Fenton, G. A. (2004). Probabilistic slope stability analysis by finite elements. *J. Geotech. Geoenviron. Eng.* 130 (5), 507–518. doi:10.1061/(asce)1090-0241(2004)130:5(507)

Habibagahi, G., Shahgholian, R., and Sahraeian, S. M. S. (2021). Stochastic analysis of rock slope stability: Application of fuzzy sets theory. *Iran. J. Sci. Technol. Trans. Civ. Eng.* 45, 851–863. doi:10.1007/s40996-020-00525-3

Hinds, E., Lu, N., Mirus, B., and Wayllace, A. (2019). Effects of infiltration characteristics on spatial-temporal evolution of stability of an interstate highway embankment. *J. Geotech. Geoenviron. Eng.* 145 (9), 05019008. doi:10.1061/(ASCE)GT.1943-5606.0002127

Hsiao, E. C., Schuster, M., Juang, C. H., and Kung, G. T. (2008). Reliability analysis and updating of excavation-induced ground settlement for building serviceability assessment. *J. Geotech. Geoenviron. Eng.* 134 (10), 1448–1458. doi:10.1061/(asce)1090-0241(2008)134:10(1448)

Iverson, R. M. (2000). Landslide triggering by rain infiltration. *Water Resour. Res.* 36 (7), 1897–1910. doi:10.1029/2000WR900090

Janbu, N. (1954). "Application of composite slip surface for stability analysis," in Paper presented at the Proceedings of European Conference on Stability of Earth Slopes (Sweden.

Jiang, S. H., Li, D. Q., Zhang, L. M., and Zhou, C. B. (2014). Slope reliability analysis considering spatially variable shear strength parameters using a non-intrusive stochastic finite element method. *Eng. Geol.* 168, 120–128. doi:10.1016/j.enggeo.2013.11.006

Juang, C., Jhi, Y.-Y., and Lee, D.-H. (1998). Stability analysis of existing slopes considering uncertainty. *Eng. Geol.* 49 (2), 111–122. doi:10.1016/S0013-7952(97)00078-1

Kanda, E. K., Senzanje, A., and Mabhaudhi, T. (2020). Soil water dynamics under Moistube irrigation. *Phys. Chem. Earth Parts A/B/C* 115, 102836. doi:10.1016/j.pce.2020.102836

Lacerda, W. A. (2007). Landslide initiation in saprolite and colluvium in southern Brazil: Field and laboratory observations. *Geomorphology* 87 (3), 104–119. doi:10.1016/j.geomorph.2006.03.037

Li, T., Liu, G., Wang, C., Wang, X., and Li, Y. (2020). The probability and sensitivity analysis of slope stability under seepage based on reliability theory. *Geotech. Geol. Eng.* 38, 3469–3479. doi:10.1007/s10706-020-01226-4

Liu, L., Zhang, S., Cheng, Y.-M., and Liang, L. (2019). Advanced reliability analysis of slopes in spatially variable soils using multivariate adaptive regression splines. *Geosci. Front.* 10 (2), 671–682. doi:10.1016/j.gsf.2018.03.013

Lu, N., Godt, J. W., and Wu, D. T. (2010). A closed-form equation for effective stress in unsaturated soil. *Water Resour. Res.* 46 (5). doi:10.1029/2009WR008646

Lu, N., and Likos, W. J. (2006). Suction stress characteristic curve for unsaturated soil. *J. Geotech. Geoenviron. Eng.* 132 (2), 131–142. doi:10.1061/(asce)1090-0241(2006)132:2(131)

Lu, N., and Likos, W. J. (2004). *Unsaturated soil mechanics*. Wiley.

Lu, N., Şener Kaya, B., Wayllace, A., and Godt, J. W. (2012). Analysis of rainfall-induced slope instability using a field of local factor of safety. *Water Resour. Res.* 48 (9), 2012WR011830. doi:10.1029/2012WR011830

Lu, N. (2020). Unsaturated soil mechanics: Fundamental challenges, breakthroughs, and opportunities. *J. Geotech. Geoenviron. Eng.* 146 (5), 02520001. doi:10.1061/(ASCE)GT.1943-5606.0002233

Luo, Z., Atamturktur, S., Juang, C. H., Huang, H., and Lin, P. S. (2011). Probability of serviceability failure in a braced excavation in a spatially random field: Fuzzy finite element approach. *Comput. Geotech.* 38 (8), 1031–1040. doi:10.1016/j.compgeo.2011.07.009

Malvern, L. E. (1969). *Introduction to the mechanics of a continuous medium*.

Matsui, T., and San, K.-C. (1992). Finite element slope stability analysis by shear strength reduction technique. *Soils Found.* 32 (1), 59–70. doi:10.3208/sandf1972.32.59

Moradi, S., Huisman, J., Class, H., and Vereecken, H. (2018). The effect of bedrock topography on timing and location of landslide initiation using the local factor of safety concept. *Water* 10 (10), 1290. doi:10.3390/w10101290

Morgentern, N., and Price, V. (1965). The analysis of stability of general slip surface. *Geotechnique* 15 (1), 79–93.

Mualem, Y. (1976). A new model for predicting the hydraulic conductivity of unsaturated porous media. *Water Resour. Res.* 12 (3), 513–522. doi:10.1029/WR012i003p00513

Nakhaei, M., and Šimůnek, J. (2014). Parameter estimation of soil hydraulic and thermal property functions for unsaturated porous media using the HYDRUS-2D code. *J. Hydrol. Hydromech.* 62 (1), 7–15. doi:10.2478/johh-2014-0008

Nawari, N., and Liang, R. (2000). Fuzzy-based approach for determination of characteristic values of measured geotechnical parameters. *Can. Geotech. J.* 37 (5), 1131–1140. doi:10.1139/t00-025

Nuth, M., and Laloui, L. (2008). Effective stress concept in unsaturated soils: Clarification and validation of a unified framework. *Int. J. Numer. Anal. Methods Geomech.* 32 (7), 771–801. doi:10.1002/nag.645

Pang, L., Close, M. E., Watt, J. P., and Vincent, K. W. (2000). Simulation of picloram, atrazine, and simazine leaching through two New Zealand soils and into groundwater using HYDRUS-2D. *J. Contam. Hydrol.* 44 (1), 19–46. doi:10.1016/S0169-7722(00)00091-7

Park, H. J., Jang, J. Y., and Lee, J. H. (2017). Physically based susceptibility assessment of rainfall-induced shallow landslides using a fuzzy point estimate method. *Remote Sens. (Basel).* 9 (5), 487. doi:10.3390/rs9050487

Park, H. J., Jang, J. Y., and Lee, J. H. (2019). Assessment of rainfall-induced landslide susceptibility at the regional scale using a physically based model and fuzzy-based Monte Carlo simulation. *Landslides* 16 (4), 695–713. doi:10.1007/s10346-018-01125-z

Park, H. J., Lee, J. H., and Woo, I. (2013). Assessment of rainfall-induced shallow landslide susceptibility using a GIS-based probabilistic approach. *Eng. Geol.* 161, 1–15. doi:10.1016/j.enggeo.2013.04.011

Park, H. J., Um, J.-G., Woo, I., and Kim, J. W. (2012). Application of fuzzy set theory to evaluate the probability of failure in rock slopes. *Eng. Geol.* 125, 92–101. doi:10.1016/j.enggeo.2011.11.008

Phoon, K. K., and Kulhawy, F. H. (1999). Characterization of geotechnical variability. *Can. Geotech. J.* 36 (4), 612–624. doi:10.1139/t99-038

Rahimi, A., Rahardjo, H., and Leong, E. C. (2011). Effect of antecedent rainfall patterns on rainfall-induced slope failure. *J. Geotech. Geoenviron. Eng.* 137 (5), 483–491. doi:10.1061/(ASCE)GT.1943-5606.0000451

Reddy, J. N. (1985). *An introduction to the finite element method*, 2. New York: McGraw-Hill.

Richards, L. A. (1931). Capillary conduction of liquids through porous mediums. *Physics* 1 (5), 318–333. doi:10.1063/1.1745010

Rosenblueth, E. (1975). Point estimates for probability moments. *Proc. Natl. Acad. Sci. U. S. A.* 72 (10), 3812–3814. doi:10.1073/pnas.72.10.3812

Sidle, R. C., and Bogaard, T. A. (2016). Dynamic Earth system and ecological controls of rainfall-initiated landslides. *Earth. Sci. Rev.* 159, 275–291. doi:10.1016/j.earscirev.2016.05.013

Šimůnek, J., van Genuchten, M. T., and Šejna, M. (2008). Development and applications of the HYDRUS and STANMOD software packages and related codes. *Vadose zone J.* 7 (2), 587–600. doi:10.2136/vzj2007.0077

Tiranti, D., and Cremonini, R. (2019). Editorial: Landslide hazard in a changing environment. *Front. Earth Sci.* 7, 3. doi:10.3389/feart.2019.00003

van Genuchten, M. T. (1980). A closed-form equation for predicting the hydraulic conductivity of unsaturated soils. *Soil Sci. Soc. Am. J.* 44 (5), 892–898. doi:10.2136/sssaj1980.03615995004400050002x

Wang, J., Gong, S., Xu, D., Juan, S., and Mu, J. (2013). Numerical simulations and validation of water flow and heat transport in a subsurface drip irrigation system using HYDRUS-2D. *Irrig. Drain.* 62 (1), 97–106. doi:10.1002/ird.1699

Xiao, T., Li, D. Q., Cao, Z. J., and Tang, X. S. (2017). Full probabilistic design of slopes in spatially variable soils using simplified reliability analysis method. *Georisk Assess. Manag. Risk Eng. Syst. Geohazards* 11 (1), 146–159. doi:10.1080/17499518.2016.1250279

Xu, C., Wang, L., Tien, Y. M., Chen, J.-M., and Juang, C. H. (2014). Robust design of rock slopes with multiple failure modes: Modeling uncertainty of estimated parameter statistics with fuzzy number. *Environ. Earth Sci.* 72 (8), 2957–2969. doi:10.1007/s12665-014-3201-1

Zadeh, L. A. (1965). Fuzzy sets. *Inf. Control* 8 (3), 338–353. doi:10.1016/S0019-9958(65)90241-X

Zhang, J., Li, J., and Lin, H. (2018). Models and influencing factors of the delay phenomenon for rainfall on slope stability. *Eur. J. Environ. Civ. Eng.* 22 (1), 122–136. doi:10.1080/19648189.2016.1179682

Zhang, L., Li, J., Li, X., Zhang, J., and Zhu, H. (2018). *Rainfall-induced soil slope failure: Stability analysis and probabilistic assessment*. Boca Raton, USA: CRC Press.

Zhang, S., Leng, W., Zhang, F., and Xiong, Y. (2012). A simple thermo-elastoplastic model for geomaterials. *Int. J. Plast.* 34, 93–113. doi:10.1016/j.ijplas.2012.01.011

Zhou, X., Li, J., Liu, Z., and Tang, Y. (2019). Analysis of slope stability with imprecise soil properties using uncertain sets. *Math. Probl. Eng.* 2019, 1–9. doi:10.1155/2019/1062347

frontiers | Frontiers in Physics

TYPE Original Research
PUBLISHED 18 November 2022
DOI 10.3389/fphy.2022.1006840

OPEN ACCESS

EDITED BY
Irasema Alcántara-Ayala,
National Autonomous University of Mexico, Mexico

REVIEWED BY
Lei Wang,
Beihang University, China
Zeng Meng,
Hefei University of Technology, China

*CORRESPONDENCE
X. B. Gu,
15823405952@163.com

SPECIALTY SECTION
This article was submitted to Interdisciplinary Physics, a section of the journal Frontiers in Physics

RECEIVED 29 July 2022
ACCEPTED 02 November 2022
PUBLISHED 18 November 2022

CITATION
Li Y, Wang YH, Wu QH and Gu XB (2022), The risk assessment of landslide hazards in the Badong section of Three Gorges using the variable fuzzy set theory. *Front. Phys.* 10:1006840. doi: 10.3389/fphy.2022.1006840

The risk assessment of landslide hazards in the Badong section of Three Gorges using the variable fuzzy set theory

Y. Li[1], Y. H. Wang[2], Q. H. Wu[1] and X. B. Gu[3]*

[1]School of Architecture and Civil Engineering, Chengdu University, Chengdu, Sichuan, China, [2]School of Civil Engineering, Sichuan University of Science and Engineering, Zigong, China, [3]School of Civil Engineering, Nanyang Institute of Technology, Nanyang, Henan, China

The risk assessment of landslide hazards has a tremendous influence on people's lives and property safety; therefore, its investigation is significant. The stratigraphic lithology, degree of weathering, relationship between the structural plane and slope direction, cohesive force, angle of internal friction, severity, average slope degree, height of slope, and type of landslide are adopted as the evaluation factors first. Second, an assessment model is developed based on the variable fuzzy set theory. In addition, the proposed model is utilized to assess the landslide hazards in the Badong section of Three Georges in China. Finally, the results demonstrate that the results derived from the proposed model are consistent with the current specifications; the accuracy rate reaches 83%. The method can determine the risk level of landslide hazards and provide an alternative scheme. Hence, this study can accurately present a new approach for assessing landslide hazards in the future.

KEYWORDS

risk assessment, landslide hazards, variable fuzzy sets, Three Gorges Reservoir area, evaluation index

1 Introduction

A landslide is a disaster that frequently occurs [1]. Its area of impact can be extensive and very destructive [2]. Landslides can cause massive damage to local infrastructure and even threaten the safety of people [3, 4].

Landslide hazards often occur in the Three Gorges Reservoir area. Until November 2003, landslide hazards occurred 4,638 times, and several thousand landslide hazards could not be controlled according to the relevant statistics [5, 6]. Therefore, how to lessen the economic losses and casualties arising from landslide hazards has become an important issue [2, 7]. The accurate risk level of landslide hazards in the Three Gorges Reservoir area is significant.

Research on the risk assessment and prediction of landslide hazards has become a hot issue [8]. For example, slope, precipitation, and human activities are adopted as the assessment index. Gao et al. [9] assessed the risk level of landslide hazards in the Wanzhou zone, Chongqing, China. Wang et al. [10] established three nonlinear

prediction models based on the weight of the joint prediction model to assess the risk level of the Qinglong landslide in Guizhou. Liu et al. [11] performed an investigation on the risk and vulnerability evaluation of landslide hazards in the bank section of the reservoir. Men et al. [12] investigated the reasons for and mechanisms of the Baijia Bao landslide based on geological surveys and rainfall data using numerical simulations in combination with actual monitoring data. Shi et al. [13] analyzed the risk assessment of landslide hazards using GIS technology with existing applications to improve the precision of the evaluation method. Spatial prediction of landslide hazards was investigated using the information model and quantitative analysis, multifactor regression analysis model, and fuzzy discriminant analysis model by Huang et al. [14]. Gu et al. [15] analyzed the landslide hazards in Shiwangmiao, Chongqing, using the intuitionistic fuzzy set-TOPSIS model.

With the development of science and technology, many methods have been used to evaluate landslide hazards, such as the catastrophe theory model [16, 17], neural network model [18], fuzzy comprehensive evaluation, and gray correlation analysis model [19]. The aforementioned methods have fostered the development of an evaluation model for landslide hazards. However, deficiencies still exist [20, 21], such as the complex calculation process and the quantitative or qualitative analytical results [22–24].

To conquer the insufficiency of the aforementioned theories, the variable fuzzy set theory is introduced to assess the risk level of landslide hazards. The method has many merits, such as its algorithm is precise, its operability is very strong in reality, and the grading standards, which are interval forms, can be solved well. For the proposed model, the construction of the relative difference function is depicted as quantitative tools of variable fuzzy sets. It describes the essence for contradictions and unity of opposites of movement and the change criterion about the objective things. The theory confirms the principle of dialectics of nature; therefore, the model improves the traditional fuzzy set model enormously.

This paper is organized as follows: in Section 2, the study area is correlated first; Section 3 presents a new assessment model based on the proposed method ; Section 4 explores the construction of the evaluation model of landslide hazards; Section 5 presents the analysis of the evaluation results derived from the proposed method; and Section 6 summarizes the conclusions.

FIGURE 1
Survey area.

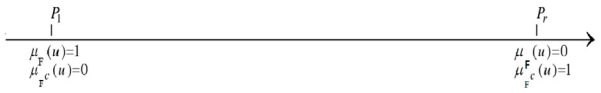

FIGURE 2
Dynamic variables.

2 Study area

The Three Gorges Reservoir area is located at 28°32′~31°44′ North and 105°44′~31°44′ East. The total length of backwater in the mainstream is 662.9 km. It includes Badong County on the Yangtze River. Badong County is located in southwestern Hubei Province in China and contains the middle and upper streams of the Yangtze River watershed. It is located in Enshi Tujia and Miao Autonomous Prefecture. Its width from east to west is 10.3 km; its length from north to south is 135 km; its total area reaches 3,354 km^2; and the survey area is shown in Figure 1.

The soil material in the landslide is mainly silty clay with crushed stone and crushed stone soil distributed in the whole slide body. The slippage soil is mainly silty clay with gravel breccia. The thickness of the slip band is 0.2 cm. The extraordinary phenomenon of deep slip zone soil is not apparent, but it has less breccia.

The material of the slide bed consists mainly of feldspar quartz sandstone and mudstone of the Jurassic Badong Formation. The occurrence of the bedrock is 260° < 30°. The bedrock surface undulates little and is close to the ground. According to the strata, the slope is reversed.

3 Methodology

Entropy theory and the variable fuzzy set assessment method are combined to develop a comprehensive approach for land hazard assessment. It can depict the inconsistent conception and implication of membership and non-membership functions dynamically; therefore, it is the significant optimization of traditional fuzzy sets.

3.1 The basic definition

Assuming that F belongs to the domain **U**, at any $u \in U$, the number $\mu_F^0(u)$ can be determined in the closed interval. The absolute membership relationship is defined as the relation between U and F, which can be expressed as follows [25]:

$$\begin{matrix} \mu_F^0 \colon \mathbf{U} \to [0,1]. \\ u \mid \to \mu_F^0 \end{matrix} \tag{1}$$

In the domain **U**, $u \in \mathbf{U}$, there are two opposite fuzzy numbers: F and F^c. For any variable u, there are two determined numbers, $\mu_F(u)$ and $\mu_{F^c}(u)$, and the relative membership degree of u to F and F^c is defined as

$$\begin{matrix} \mu_F, \mu_{F^c} \colon \mathbf{U} \to [0,1] \\ u \mid \to \mu_F(u), \mu_{F^C}(u) \in [0,1] \end{matrix}. \tag{2}$$

Figure 2 depicts the dynamic variable of any number in any closed interval as follows:

The relative membership degree of F and F^c meet with $\mu_F(u) + \mu_{F^c} = 1$, $0 \le \mu_F(u) \le 1$, and $0 \le \mu_{F^c}(u) \le 1$, and they can be expressed as follows:

$$\underset{\sim}{\mathbf{F}} = \{u, \mu_F(u), \mu_{F^C}(u) | u \in U\}, \tag{3}$$

where $\underset{\sim}{F}$ is the opposite fuzzy set. Figure 3 shows its definition.

The attractive and repelled sets $\mu_F(u)$ and $\mu_{F^c}(u)$ can likewise be defined as follows:

$$D_F(u) = \mu_F(u) - \mu_{F^c}(u). \tag{4}$$

When $\mu_F(u) > \mu_{F^c}(u)$, $0 \le D_F(u) \le 1$, and when $\mu_F(u) = \mu_{F^c}$, $D_F(u) = 0$, but when $\mu_F(u) < \mu_{F^c}(u)$, $-1 \le D_F(u) \le 0$. The mapping of the relative difference function $D_F(u)$ can be expressed as follows:

$$\begin{matrix} D \colon \mathbf{U} \to [0,1] \\ u \mid \to D_F(u) \in [-1,1]. \end{matrix} \tag{5}$$

Figure 4 shows the relative difference function of u to F.

3.2 Determining the relative membership degree

X is a sample set, which is expressed as follows :

$$X = \left(x_{ij}\right), \tag{6}$$

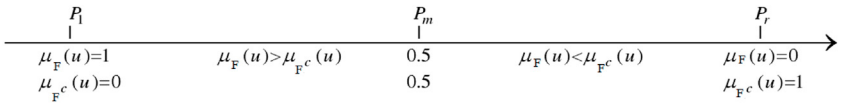

FIGURE 3
Diagram of opposite fuzzy sets.

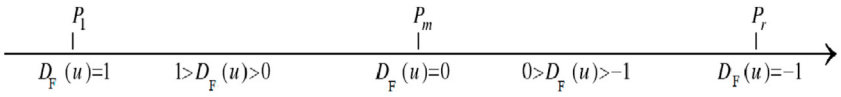

FIGURE 4
Relative difference function.

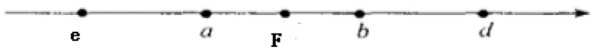

FIGURE 5
Drawing of the position relationship.

where x_{ij} is the eigenvalue of the index $\boldsymbol{i}$ of sample j, $i = 1, 2, ..., m$; $j = 1, 2, ...c$. c represents the grade of the index; the attractive domain I_{ab} can be obtained in Eq. 7.

$$\mathbf{I_{ab}} = \left(\left|a_{ij}, b_{ij}\right|\right). \tag{7}$$

When we enlarge the set I_{ab} according to the upper and lower bounds of its adjacent intervals, set I_{de} is expressed as follows:

$$\mathbf{I}_{de} = \left(\left|d_{ij}, e_{ij}\right|\right). \tag{8}$$

Based on the relevant Ref. [26], the level standard F of the index is depicted as follows:

$$\mathbf{F} = \begin{bmatrix} \mathbf{F_{11}} & ... & \mathbf{F_{1j}} \\ ... & ... & ... \\ \mathbf{F_{i1}} & ... & \mathbf{F_{ij}} \end{bmatrix}, \tag{9}$$

where the element F_{ij} is depicted as follows:

$$F_{ij} = \frac{c-j}{c-1}a_{ij} + \frac{j-1}{c-1}b_{ij}, \tag{10}$$

when $j = 1$, $F_{i1} = a_{i1}$; when $j = c$, then, $F_{ij} = b_{ic}$; and when $j = \frac{c+1}{2}$, then, $F_{ij} = \frac{a_{ij}+b_{ij}}{2}$.

$X_0(a, b)$ is defined as the attractive domain, namely, when $0 \le D_F(u) \le 1$, $X = [d, e]$, and it belongs to the upper and lower domain intervals of X_0 ($X_0 \subset X$). Figure 5 shows their position relationship.

Therefore, their relative membership degree is depicted in Eqs. 11, 12.

$$\begin{cases} \mu_F(u) = 0.5\left[1 + \left(\frac{x-a}{F-a}\right)^{\beta}\right]; x \in [a, F] \\ \mu_F(u) = 0.5\left[1 - \left(\frac{x-a}{d-a}\right)^{\beta}\right]; x \in [d, a] \end{cases}. \tag{11}$$

$$\begin{cases} \mu_F(u) = 0.5\left[1 + \left(\frac{x-b}{F-b}\right)^{\beta}\right]; x \in [F, b] \\ \mu_F(u) = 0.5\left[1 - \left(\frac{x-b}{e-b}\right)^{\beta}\right]; x \in [b, e]. \end{cases} \tag{12}$$

3.3 Determining index weights

(1) It is assumed that sample set X can be depicted as follows:

$$X = \begin{bmatrix} x_{11} & x_{12} & ... & x_{1m} \\ x_{21} & x_{22} & ... & x_{2m} \\ ... & ... & ... & ... \\ x_{n1} & x_{n2} & ... & x_{nm} \end{bmatrix}. \tag{13}$$

(2) Sample set X_{ij} is normalized.

3.3.1 The positive index:

$$x'_{ij} = \frac{x_{ij} - \min\left\{x_{ij}, ..., x_{nj}\right\}}{\max\left\{x_{1j}, ..., x_{nj}\right\} - \min\left\{x_{ij}, ..., x_{nj}\right\}} \tag{14}$$

3.3.2 The negative index:

$$x'_{ij} = \frac{\min\left\{x_{ij}, ..., x_{nj}\right\} - x_{ij}}{\max\left\{x_{1j}, ..., x_{nj}\right\} - \min\left\{x_{ij}, ..., x_{nj}\right\}} \tag{15}$$

where i is the number of evaluation schemes, j is the number of evaluation indices, and x_{ij} is the corresponding magnitude.

(3) Determining the proportion of the assessment index.

$$b_{ij} = \frac{x_{ij}}{\sum_{i=1}^{n} x_{ij}}. \tag{16}$$

(4) The entropy is calculated in Eq. 17:

$$s_j = -k\sum_{i=1}^{n} b_{ij} \ln\left(b_{ij}\right). \tag{17}$$

(5) The final weight can be depicted in Eq. 18:

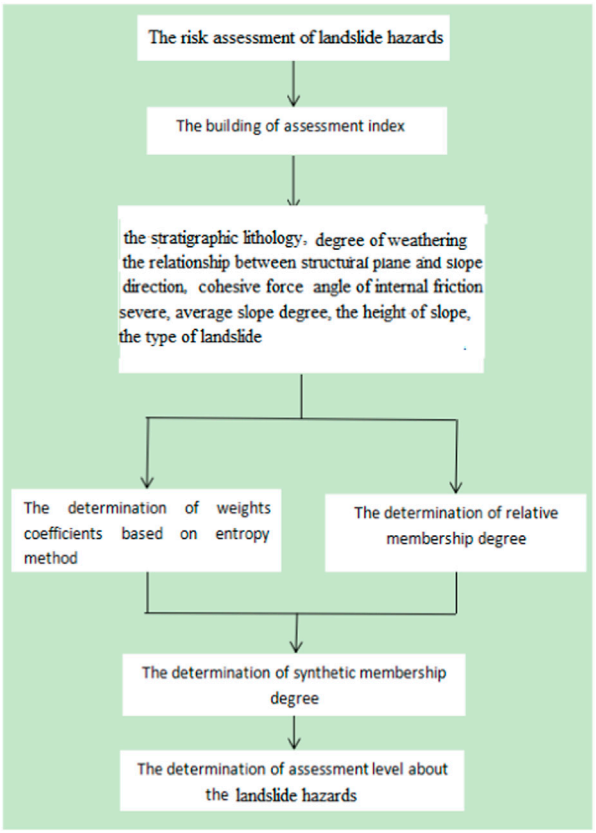

FIGURE 6
Risk assessment process of landslide hazards.

$$\omega_j = \frac{1 - s_j}{n - \sum_{j=1}^{n} s_j}. \tag{18}$$

3.4 Determining the evaluation grade

According to Eqs. 11, 12, and 18 and in combination with the relevant Ref. [26], a synthetic membership degree is shown in Eq. 19:

$$\mathrm{v}_F(\mathrm{u})_j = \frac{1}{1 + \left(\frac{\sum_{i=1}^{m} \left[\omega_i \left(1 - \mu_F(u)_{ij}\right)\right]^l}{\sum_{i=1}^{m} \left[\omega_i \mu_F(u)_{ij}\right]^l} \right)^{\frac{k}{l}}}. \tag{19}$$

Based on Eq. 19, the synthetic membership degree is calculated as follows:

$$V = \left(\mathrm{v}'\right), \tag{20}$$

where

$$v' = \frac{v_F(u)_j}{\sum_{j=1}^{m} v_F(u)_j}. \tag{21}$$

The evaluation grade R is expressed in Eq. 22.

$$R = (1, 2, ..., \mathrm{c}) \bullet V. \tag{22}$$

3.5 The calculative step and the flow chart

Its calculative process is correlated as follows:

(1) According to the specific data and evaluation standard, the eigenvalue matrix X and classification matrix Y are constructed.
(2) The attractive domain I_{ab}, range matrix I_{de}, and point value matrix F are constructed.
(3) Based on Eqs. 11, 12, the relative membership degree is calculated.
(4) The weights of the landslide hazards using the proposed model are calculated.
(5) The grade eigenvalues R based on the relevant equations are calculated. If $n - 0.5 \le H \le n + 0.5$, then the risk grade is n (n is a nonnegative integer).

Its flow chart is plotted in Figure 6. First, a complete evaluation index system should be constructed before the risk level of landslide hazards is evaluated. Second, entropy–weight theory is adopted to calculate the weight of each evaluation index. Third, the relative membership degree is defined based on the proposed model. Then, the proposed model can determine the risk level of landslide hazards.

4 Construction of the evaluation model

4.1 Determining evaluation indices

The Caofang River landslide, Leijia Ping landslide, Daping landslide, Lijia Wan landslide, Zhujia Dian landslide, and Jiaojia Wan landslide in the Badong sections of the Three Gorges Reservoir area are selected as the assessment objects. According to the characteristics of landslides in the Three Gorges Reservoir area, the stratigraphic lithology (X_1), degree of weathering (X_2), relationship between the structural plane and slope direction (X_3), cohesive force (X_4), angle of internal friction (X_5), severity (X_6), average slope degree (X_7), height of slope (X_8), and type of landslide (X_9) are selected as assessment indices. Their original values are shown in Table 1 [27].

It can be found in Table 1 that X_1, X_2, X_3, and X_9 are qualitative and the other indices are quantitative. To assess

TABLE 1 Data of different assessment indices.

Name of the landslide	Assessment index								
	X_1	X_2	X_3	X_4	X_5	X_6	X_7	X_8	X_9
Caofang River landslide	Semihard rocks	A slight or moderate weathering	162° < 34°, consequent slope	25.0	18	22.5	12.5	160	Hydrodynamic pressure
Leijia Ping landslide	Semihard rocks	A slight or moderate weathering	172° < 48°, reverse slope	33.0	17.75	21.70	33	210	Hydrodynamic pressure
Daping landslide	Softer–harder rocks	Strong weathering–moderate weathering	350° < 20°, reverse slope	14.0	20.0	21.5	17	240	Hydrodynamic pressure + rainfall
Lijia Wan landslide	Softer–harder rocks	A slight or moderate weathering	222° < 35°, consequent slope	25.5	18.2	21.7	32.5	200	Hydrodynamic pressure
Zhujia Dian landslide	Hard and semihard rocks	Moderate weathering–weak weathering	276° < 61°, reverse slope	24.0	18.0	20.46	37.5	420	Hydrodynamic pressure + rainfall
Jiaojia Wan landslide	Softer–harder rocks	A slight or moderate weathering	160° < 30°, consequent slope	34.5	17.5	21.7	32.5	150	Hydrodynamic pressure

TABLE 2 Comparison sequence of the evaluation index.

Name of the landslide	Assessment index								
	X_1	X_2	X_3	X_4	X_5	X_6	X_7	X_8	X_9
Caofang River landslide	4.5	4.0	3.0	25.0	18	22.5	12.5	160	3
Leijia Ping landslide	4.5	3.5	4.5	33.0	17.75	21.70	33	210	3
Daping landslide	2.0	3.0	4.0	14.0	20.0	21.5	17	240	2
Lijia Wan landslide	2.5	3.5	2.5	25.5	18.2	21.7	32.5	200	3
Zhujia Dian landslide	4.5	2.5	5.0	24.0	18.0	20.46	37.5	420	2
Jiaojia Wan landslide	3.0	4.0	2.0	34.5	17.5	21.7	32.5	150	3

TABLE 3 Classification of the assessment index.

Risk level	X_1	X_2	X_3	X_4	X_5	X_6	X_7	X_8	X_9
I	[4.5)	[4.5)	[4.5)	[30.35]	[33.38)	[23.24)	[0.15)	[0.170)	[4.5)
II	[3.4)	[3.4)	[3.4)	[25.30)	[28.33)	[22.23)	[15.25)	[170,200)	[3.4)
III	[2.3)	[2.3)	[2.3)	[20.25)	[23.28)	[21.22)	[25.35)	[200,230)	[2.3)
IV	[1.2)	[1.2)	[1.2)	[15.20)	[18.23)	[20.21)	[35.45)	[230,260)	[1.2)
V	(0.1)	(0 1)	(0.1)	[0.15)	[0.18)	[0.20)	[45.90)	[260,500)	[0.1)

the risk level of landslides, the quantitative indices should be transformed into qualitative indices. According to the hierarchy method, the quantitative indices are divided into five groups: excellent, good, moderate, bad, and very bad. The five grades are 5, 4, 3, 2, and 1, respectively. Table 2 is as follows:

According to extensive statistics and analysis and in combination with the geological conditions of assessment objects [16, 28], the risk level of landslides is classified into five classes: safe (I), mildly dangerous (II), dangerous (III), more dangerous (IV), and hazardous (V). Their classification standards are shown in Table 3.

4.2 Determination of the risk level of the landslide hazard

(1) The construction of the attractive domain, range matrix, and point value matrix.

According to Table 3 and in combination with Eq. 7, the attractive domain I_{ab} is depicted as follows:

$$\mathbf{I_{ab}} = \begin{bmatrix} [5\ 4] & [4\ 3] & [3\ 2] & [2\ 1] & [1\ 0] \\ [5\ 4] & [4\ 3] & [3\ 2] & [2\ 1] & [1\ 0] \\ [5\ 4] & [4\ 3] & [3\ 2] & [2\ 1] & [1\ 0] \\ [35\ 30] & [30\ 25] & [25\ 20] & [20\ 15] & [15\ 0] \\ [38\ 33] & [33\ 28] & [28\ 23] & [23\ 18] & [18\ 0] \\ [24\ 23] & [23\ 22] & [22\ 21] & [21\ 20] & [20\ 0] \\ [0\ 15] & [15\ 25] & [25\ 35] & [35\ 45] & [45\ 90] \\ [0\ 170] & [170\ 200] & [200\ 230] & [230\ 260] & [260\ 500] \\ [5\ 4] & [4\ 3] & [3\ 2] & [2\ 1] & [1\ 0] \end{bmatrix}$$

Based on Eq. 8, the matrix I_{de} can be expressed as follows:

$$\mathbf{I_{de}} = \begin{bmatrix} [5\ 3] & [5\ 2] & [4\ 1] & [3\ 0] & [2\ 0] \\ [5\ 3] & [5\ 2] & [4\ 1] & [3\ 0] & [2\ 0] \\ [5\ 3] & [5\ 2] & [4\ 1] & [3\ 0] & [2\ 0] \\ [35\ 25] & [35\ 20] & [30\ 15] & [25\ 0] & [20\ 0] \\ [38\ 28] & [38\ 23] & [33\ 18] & [28\ 0] & [23\ 0] \\ [24\ 22] & [24\ 21] & [23\ 20] & [22\ 0] & [21\ 0] \\ [0\ 25] & [0\ 35] & [15\ 45] & [25\ 90] & [35\ 90] \\ [0\ 200] & [0\ 230] & [170\ 260] & [200\ 500] & [230\ 500] \\ [5\ 3] & [5\ 2] & [4\ 1] & [3\ 0] & [2\ 0] \end{bmatrix}$$

Based on Eq. 10, the point value matrix F can be depicted as follows:

$$\mathbf{F} = \begin{bmatrix} 5 & 3.75 & 2.5 & 1.25 & 0 \\ 5 & 3.75 & 2.5 & 1.25 & 0 \\ 5 & 3.75 & 2.5 & 1.25 & 0 \\ 35 & 28.75 & 27.5 & 16.25 & 0 \\ 38 & 31.75 & 25.5 & 19.25 & 0 \\ 24 & 22.75 & 21.5 & 20.25 & 0 \\ 0 & 19.5 & 30 & 42.5 & 90 \\ 0 & 177.5 & 215 & 252.5 & 500 \\ 5 & 3.75 & 2.5 & 1.25 & 0 \end{bmatrix}$$

(2) Determining the relative membership degree

Based on Table 2 and in combination with Eqs. 11, 12, we should decide whether the evaluation magnitudes are to the left or the right of point F. The data of the Caofang River landslide are adopted for an examination. If $i = 1$, then, $[a\ \ b]_{1j}$, $[d\ \ e]_{1j}$, and F can be depicted as follows:

$$[a\ \ b]_{1j} = ([5\ 4]\ \ [4\ 3]\ \ [3\ 2]\ \ [2\ 1]\ \ [1\ 0]),$$
$$[d\ \ e]_{1j} = ([5\ 3]\ \ [5\ 2]\ \ [4\ 1]\ \ [3\ 0]\ \ [2\ 0]),$$
$$F_{1j} = [5\ \ 3.75\ \ 2.5\ \ 1.25\ \ 0].$$

When $x_1 = 4.5$, $a_{11} = 5$, $b_{11} = 4$, $d_{11} = 5$, $e_{11} = 3$, and $F_{11} = 5$, then x_1 is located in the interval $[F_{11}\ \ b_{11}]$; thus, $\mu_F(u_{11}) = 0.75$; when $a_{12} = 4$, $b_{12} = 3$, $d_{12} = 5$, $e_{12} = 2$, and $F_{12} = 3.75$, then x_1 is located in the interval $[d_{11}\ \ a_{11}]$; thus, $\mu_F(u_{12}) = 0.25$; when $a_{13} = 3$, $b_{13} = 2$, $d_{13} = 4$, $e_{13} = 1$, and $F_{13} = 2.5$, then x_1 is located in the out of intervals; thus, $\mu_F(u_{13}) = 0$.

In the same way, the relative membership degree matrix of the Caofang River landslide can be obtained as follows:

$$\mu_F(u_{1j}) = \begin{bmatrix} 0.75 & 0.25 & 0 & 0 & 0 \\ 0.5 & 0.5 & 0 & 0 & 0 \\ 0 & 0.5 & 0.5 & 0 & 0 \\ 0 & 0.5 & 0.5 & 0 & 0 \\ 0 & 0 & 0 & 0.5 & 0.5 \\ 0.25 & 0.833 & 0.25 & 0 & 0 \\ 0.583 & 0.417 & 0 & 0 & 0 \\ 0.529 & 0.471 & 0 & 0 & 0 \\ 0 & 0.5 & 0.5 & 0 & 0 \end{bmatrix}$$

(3) Determining weight coefficients

Based on Table 2 and in combination with Eq. 16, Table 4 shows the parameter matrix.

According to Table 4 and Eq. 17, the entropy matrix can be shown in Table 5.

According to Eq. 18, the weight coefficients are shown in Table 6.

(4) Determination of the comprehensive relative membership degree

Based on Eq. 19 and $\mu_F(\mu_{1j})$, the results are calculated in Table 7.

Based on Eqs. 20, 21, the comprehensive relative membership degree matrix is normalized in Table 8.

(5) Determining the risk level of the landslide hazards.

According to Eq. 22 and Table 8, the ranking value of the Caofang River landslide is shown in Table 9.

Similarly, the feature values of the other five landslides are shown in Table 10.

The results obtained from different methods are contrasted in Table 11.

The variable fuzzy set assessment method is used to evaluate the risk level of landslide hazards. Their complete results are shown in Table 10. Table 10 shows that the risk levels of landslide hazards of six different landslides are different. The risk level of the Daping landslide and Lijia Wan landslide is III and that of the rest of the landslides is II. This indicates that the risk level of the Daping landslide and Lijia Wan landslide is dangerous and that of the rest of the landslides is mildly dangerous. Therefore, the necessary consolidation measurements should be performed at the Daping landslide and Lijia Wan landslide. The qualified rate of landslide hazards in all the Badong section of Three Gorges is 67%.

Based on the analytical results of the evaluation method in Table 11, the conclusions obtained from the proposed model are consistent with the site investigations of the five landslides, except for the Zhujia Dian landslide. Its accuracy is 83% in the proposed model, which is higher than that (50%) while using the gray fuzzy comprehensive evaluation theory [27] and that

TABLE 4 Synthetic parameters of landslide hazards.

Name of the landslide	X_1	X_2	X_3	X_4	X_5	X_6	X_7	X_8	X_9
Caofang River landslide	0.2143	0.1951	0.1429	0.1603	0.1645	0.1737	0.0758	0.1159	0.1875
Leijia Ping landslide	0.2143	0.1707	0.2143	0.2115	0.1622	0.1675	0.2	0.1522	0.1875
Daping landslide	0.0952	0.1463	0.1905	0.0897	0.1827	0.1659	0.103	0.1739	0.125
Lijia Wan landslide	0.119	0.1707	0.119	0.1635	0.1663	0.1675	0.197	0.1449	0.1875
Zhujia Dian landslide	0.2143	0.122	0.2381	0.1538	0.1645	0.1579	0.2273	0.3043	0.125
Jiaojia Wan landslide	0.1429	0.1951	0.0952	0.2212	0.1599	0.1675	0.197	0.1087	0.1875

TABLE 5 Entropy weight matrix.

Index	X_1	X_2	X_3	X_4	X_5	X_6	X_7	X_8	X_9
Weight coefficients	0.9742	0.993	0.9727	0.9801	0.9995	0.9998	0.9646	0.962	0.9908

TABLE 6 Weight coefficient matrix.

Index	X_1	X_2	X_3	X_4	X_5	X_6	X_7	X_8	X_9
Weight coefficients	0.1587	0.0431	0.1669	0.1219	0.0034	0.0013	0.2169	0.2325	0.0561

TABLE 7 Comprehensive relative membership.

kandl	$v_F(u)_1$				
$k = 1, l = 1$	0.39	0.4344	0.1726	0.0017	0.0017
$k = 1, l = 2$	0.4505	0.4341	0.2227	0.0041	0.0041
$k = 2, l = 1$	0.2902	0.371	0.0417	0	0
$k = 2, l = 2$	0.4019	0.3705	0.0759	0	0

TABLE 8 Normalization of the comprehensive relative membership degree vector.

kandl	v'				
$k = 1, l = 1$	0.3899	0.4342	0.1726	0.0017	0.0017
$k = 1, l = 2$	0.4038	0.3892	0.1997	0.0036	0.0036
$k = 2, l = 1$	0.4129	0.5278	0.0594	0	0
$k = 2, l = 2$	0.4738	0.4367	0.0895	0	0

while using level-based weight assessment (67%). In comparison with gray fuzzy comprehensive evaluation theory, the variable fuzzy set assessment method can accurately transmit the risk degree of landslide hazards. Therefore, the conclusions indicate that estimating the risk level of landslide hazards is feasible using the proposed method. Accurate results and details of landslide hazards were obtained. For example, the cohesive force of the Lijia Ping landslide is 33, which should be Grade I based on Table 3. In addition, the membership degree of the other indices obtained by the proposed method is Grade II; therefore, the grade probability of the Lijia Ping landslide at Grade II is more extensive than that at Grades I, IV, III, and V. The risk level probability of the Lijia Ping landslide must be Level II and almost impossible is Level I, IV, III, and V. The risk grade of the Zhujia Dian landslide possibly belongs to Grade III, which is more than that of the Lijia Wan landslide, because the mean ranking feature value (3.1773) of the Zhujia Dian landslide, Level III, is higher than that of the Lijia Wan landslide (2.8162). The conclusions obtained using the proposed method demonstrate the accuracy of the risk level and further determine the ranking of landslide hazards for different landslides at the same grade.

5 Discussion

5.1 Comparison with existing studies

The variable fuzzy set method is provided to assess the risk level of landslide hazards, and the results are good. However, due

TABLE 9 Feature values.

Sample number	Ranking feature value				
	$k = 1, l = 1$	$k = 1, l = 2$	$k = 2, l = 1$	$k = 2, l = 2$	Mean value
1	1.7912	1.814	1.6465	1.6158	1.7169

TABLE 10 Values of the assessment model for the other five landslides.

Name of the landslide	Ranking feature value				
	$k = 1, l = 1$	$k = 1, l = 2$	$k = 2, l = 1$	$k = 2, l = 2$	Mean value
Caofang River landslide	1.7912	1.814	1.6465	1.6158	1.7169
Leijia Ping landslide	2.315	2.4558	2.194	2.426	2.3477
Daping landslide	3.0176	2.9759	3.1403	2.9991	3.0332
Lijia Wan landslide	2.7825	2.8046	2.8213	2.8564	2.8162
Zhujia Dian landslide	3.1051	3.1683	3.1211	3.3146	3.1773
Jiaojia Wan landslide	2.4033	2.4402	2.38	2.384	2.4019

TABLE 11 Comparison of results from the different models.

Name of the landslide	Method in the text	Current specification	Gray fuzzy comprehensive evaluation method	Level-based weight assessment
Caofang River landslide	II	II	II	II
Leijia Ping landslide	II	II	I	I
Daping landslide	III	III	III	III
Lijia Wan landslide	III	III	III	III
Zhujia Dian landslide	III	II	I	II
Jiaojia Wan landslide	II	II	I	I

to a lack of information, the uncertain human mind, and time complexity, decision experts (DEs) cannot provide accurate results for subjective methods such as the gray fuzzy comprehensive evaluation method and level-based weight assessment (LBWA). While the proposed model addresses this concern, it not only considers the unreliability or reliability of the problem but also solves some degrees of uncertainty and ambiguity of the data. Therefore, it has significant advantages over these subjective methods.

5.2 The advantages and limitations of the proposed model

In comparison with the traditional models, the advantages of the variable fuzzy set theory are analyzed as follows:

(1) The variable fuzzy set method can accurately demonstrate the risk degree of landslide hazards using the eigenvalue of level H.
(2) Interval-oriented evaluation, not point assessment, is applied in the proposed model; therefore, the reliability of evaluation outcomes is enhanced, and the quality state of landslide hazards can be discovered with effect.

6 Conclusion

Considering the stratigraphic lithology (X_1), degree of weathering (X_2), relationship between the structural plane and slope direction (X_3), cohesive force (X_4), angle of internal friction (X_5), severity (X_6), average slope degree (X_7), height of slope (X_8), and type of landslide (X_9), the

variable fuzzy set theory is applied to evaluate the risk level of landslide hazards in the study.

The conclusions demonstrate that the outcomes obtained using the proposed model are consistent with the site investigations; its accuracy rate reaches 83%. The acceptance rate of landslide hazards for all landslides in the Badong section of Three Gorges is 67%. The proposed method further determines the risk ranking of landslide hazards of different landslides at the same grade. It can accurately demonstrate the risk degree of landslide hazards. Relative to the conventional model, its evaluation process is more reliable and efficient. However, it still has some drawbacks, such as complicated calculation and necessary multiple variable parameters; therefore, it still has significant room for improvement in the future.

In summary, the variable fuzzy set model could offer an alternate route to precisely evaluate the risk grade of landslide hazards.

Data availability statement

The original contributions presented in the study are included in the article/Supplementary Material; further inquiries can be directed to the corresponding author.

Author contributions

YL provided the method and wrote the manuscript; Y-HW provided Figures 1, 2; Q-HW provided Figure 3. X-BG provided the rest work.

Funding

This work is supported by the mineral resources project of Sichuan province (SCKCZY2022-ZC003), the cross project in the Nanyang Institute of Technology (520009), the start-up Foundation (510126), the Sichuan Science and Technology Program (No: 2020YJ0424), Regional Innovation Cooperation Programs of Sichuan Province (2021YFQ0050), Guizhou Provincial Science and Technology Projects [No. (2020) 2004], the Scientific and Technological Projects of Henan Province (No: 222102320296), and the Opening Project of Sichuan Province University Key Laboratory of Bridge Non-destruction Detecting and Engineering Computing (2022QYJ02).

Conflict of interest

The authors declare that the research was conducted in the absence of any commercial or financial relationships that could be construed as a potential conflict of interest.

Publisher's note

All claims expressed in this article are solely those of the authors and do not necessarily represent those of their affiliated organizations, or those of the publisher, the editors, and the reviewers. Any product that may be evaluated in this article, or claim that may be made by its manufacturer, is not guaranteed or endorsed by the publisher.

References

1. Gu XB, Wu ST, Ji XJ, Zhu YH. The risk assessment of debris flow hazards in Banshanmen gully based on the entropy weight normal cloud method. *Adv Civil Eng* (2021) 2021:1–11. doi:10.1155/2021/8841310

2. Gu XB, Wu QH. Seismic stability analysis of waterfront rock slopes using the modified pseudo-dynamic method. *Geotech Geol Eng* (2019) 37(3):1743–53. doi:10.1007/s10706-018-0718-1

3. Gu X-B, Wang L, Wu Q-H. The risk assessment of debris flow in the duba river watershed using intuitionistic fuzzy sets: TOPSIS model. *Math Probl Eng* (2022) 2022:1–12. Article ID 2031907, 12 pages. doi:10.1155/2022/2031907

4. Chen J, Shou Y, Zhou X. Implementation of the novel perfectly matched layer element for elastodynamic problems in time-domain finite element method107054. *Soil Dyn Earthquake Eng* (2022) 152.

5. Gu XB, Wu QH, Zhu YH. The experimental investigation on the propagation process of crack for brittle rock similar material. *Geotech Geol Eng* (2019) 37(6): 4731–40. doi:10.1007/s10706-019-00934-w

6. Gu XB, Shao JL, Wu ST, Wu QH, Bai H. The risk assessment of debris flow hazards in zhouqu based on the projection pursuit classification model. *Geotech Geol Eng (Dordr)* (2021) 8:1267–79. doi:10.1007/s10706-021-01961-2

7. Gu X-B, Wu Q-H, Ma Y. Risk assessment of the rockburst intensity in a hydraulic tunnel using an intuitionistic fuzzy sets-TOPSIS model. *Adv Mater Sci Eng* (2022) 2022:1–14. doi:10.1155/2022/4774978

8. Gu CZ, Yang HF, Hu XW. Analysis of energy conversion of earthquake-induced landslide based on fuzzy synthetic evaluation. *Rock Soil Mech* (2012) 33(S1):297–302.

9. Gao C, Cui X. Landslide risk assessment based on multi-index weighted grey target decision model[J]. *J Cent South Univ* (2018) 47(2):524–5292007.

10. Wang W-d, Qu X, Liu P. Prediction on landslide displacement using a combination model with optimal weight. *[J] J Catastrophology* (2018) 33(1):59–64. doi:10.3969/j.issn.1000-811X.2018.01.012

11. liu L. *Assessment of landslide risk along Wanzhou area in three Georges Reservoir[D]*. Wuhan,China: China University of Geosciences (2016).

12. Men M. Analysis of deformation mechanism of baijiabao landslide in three Georges reservoir area[J]. *J China Three Georges Univ* (2017) 39:243–7.

13. Shi J, Xu R, Shi L. ETM+ imagery and GIS-based landslide susceptibility mapping for the regional area of Geheyan reservoir on the Qingjiang River, Hubei Province, China. *EarthScience Front* (2007) 14(6):119–28.

14. Huang ZM, Fu B, Chen Y. Aeration and hydrodynamic pressure characteristics for outer convex step in steep slope section. *J Water ResourcesWater Eng* (2018) 29(3):138–43. In Chinese.

15. Gu XB, Ma Y, Wu QH, Ji XJ, Bai H. The risk assessment of landslide hazards in Shiwangmiao based on intuitionistic fuzzy sets-Topsis model. *Nat. Hazards* (2022) 111(1):283–303.

16. Zhou XP, Zhang YX, Ha QL, Zhu KS. Micromechanical modelling of the complete stress–strain relationship for crack weakened rock subjected to compressive loading. *Rock Mech Rock Eng* (2008) 41(5):747–769. doi:10.1007/s00603-007-0130-2

17. Zhou XP, Gu XB, Qian QH. Seismic bearing capacity of shallow foundations resting on rock masses subjected to seismic loads. *KSCE J Civ Eng* (2016) 20(1): 216–28. doi:10.1007/s12205-015-0283-6

18. Wang XT, Li SC, Ma XY, Xue YG, Hu J, Li Z. Risk assessment of rockfall hazards in a tunnel portal section based on normal cloud model. *Pol J Environ Stud* (2017) 26:2295–306. doi:10.15244/pjoes/68427

19. Ye BM, Li XW, Zhang JH. Study on artificial network method of surrounding rocks classification for hydraulic tunnel. *Water resource & Hydropower of Northeast* (2003) 8:53–5. (in Chinese).

20. Zhao Y, Bi J, Wang C, Liu P. Effect of unloading rate on the mechanical behavior and fracture characteristics of sandstones under complex triaxial stress conditions. *Rock Mech Rock Eng* (2021) 54:4851–66. doi:10.1007/s00603-021-02515-x

21. Gu XB, Wu QH. The application of nonordinary, state-based peridynamic theory on the damage process of the rock-like materials. *Math Probl Eng* (2016) 3(8):1–9. doi:10.1155/2016/9794605

22. Wang L, Liu Y, Li M. Time-dependent reliability-based optimization for structural-topological configuration design under convex-bounded uncertain modeling. *Reliability Eng Syst Saf* (2022) 221:108361. doi:10.1016/j.ress.2022.108361

23. Wang L, Liu J, Yang C, Wu D. A novel interval dynamic reliability computation approach for the risk evaluation of vibration active control systems based on PID controllers. *Appl Math Model* (2021) 92:422–46. doi:10.1016/j.apm.2020.11.007

24. Liu Y, Wang L, Gu K, Li M. Artificial neural network (ANN) - bayesian probability framework (BPF) based method of dynamic force reconstruction under multi-source uncertainties,Knowledge-based systems (2022) 237, 107796.

25. Wang Wc., Xu DM, Lei KW, Lei GJ. *Assess river Water Qual based Theor variable fuzzy sets fuzzy binary comparison methodWater Resour Manage* (2014) 28(12):4183–200.

26. Wang YK, Sheng D, Wang D, Ma H, Wu J, Xu F. Variable fuzzy set theory to assess water quality of the meiliang bay in taihu lake basin. *Water Resour Manage* (2014) 28(3):867–80. doi:10.1007/s11269-014-0521-6

27. Wang C, Li W. Application of grey relational fuzzy comprehensive evaluation method to landslide risk assessment in Badong section of three Georges reservoir area[J]. *Water Resour Power* (2019) 37(4):131–5.

28. Zhou XP, Zhang JZ, Louis W, Yuen N. Experimental study on the growth, coalescence and wrapping behaviors of 3D cross-embedded flaws under uniaxial compression. *Rock Mech Rock Eng* (2018) 51(5):137928–400. doi:10.1007/s00603-018-1406-4

frontiers | Frontiers in Earth Science

TYPE Original Research
PUBLISHED 06 February 2023
DOI 10.3389/feart.2022.1032438

OPEN ACCESS

EDITED BY
Eric Josef Ribeiro Parteli,
University of Duisburg-Essen, Germany

REVIEWED BY
Alfredo Reder,
Ca' Foscari University of Venice, Italy
Yacine Achour,
University of Bordj Bou Arréridj, Algeria

*CORRESPONDENCE
Anil Yildiz,
yildiz@mbd.rwth-aachen.de

SPECIALTY SECTION
This article was submitted to Geohazards and Georisks, a section of the journal Frontiers in Earth Science

RECEIVED 30 August 2022
ACCEPTED 28 December 2022
PUBLISHED 06 February 2023

CITATION
Yildiz A, Zhao H and Kowalski J (2023), Computationally-feasible uncertainty quantification in model-based landslide risk assessment.
Front. Earth Sci. 10:1032438.
doi: 10.3389/feart.2022.1032438

Computationally-feasible uncertainty quantification in model-based landslide risk assessment

Anil Yildiz*, Hu Zhao and Julia Kowalski

Methods for Model-based Development in Computational Engineering, RWTH Aachen University, Aachen, Germany

Introduction: Increasing complexity and capacity of computational physics-based landslide run-out modelling yielded highly efficient model-based decision support tools, e.g. landslide susceptibility or run-out maps, or geohazard risk assessments. A reliable, robust and reproducible development of such tools requires a thorough quantification of uncertainties, which are present in every step of computational workflow from input data, such as topography or release zone, to modelling framework used, e.g. numerical error.

Methodology: Well-established methods from reliability analysis such as Point Estimate Method (PEM) or Monte Carlo Simulations (MCS) can be used to investigate the uncertainty of model outputs. While PEM requires less computational resources, it does not capture all the details of the uncertain output. MCS tackles this problem, but creates a computational bottleneck. A comparative study is presented herein by conducting multiple forward simulations of landslide run-out for a synthetic and a real-world test case, which are used to construct Gaussian process emulators as a surrogate model to facilitate high-throughput tasks.

Results: It was demonstrated that PEM and MCS provide similar expectancies, while the variance and skewness differ, in terms of post-processed scalar outputs, such as impact area or a point-wise flow height. Spatial distribution of the flow height was clearly affected by the choice of method used in uncertainty quantification.

Discussion: If only expectancies are to be assessed then one can work with computationally-cheap PEM, yet MCS has to be used when higher order moments are needed. In that case physics-based machine learning techniques, such as Gaussian process emulation, provide strategies to tackle the computational bottleneck. It can be further suggested that computational-feasibility of MCS used in landslide risk assessment can be significantly improved by using surrogate modelling. It should also be noted that the gain in compute time by using Gaussian process emulation critically depends on the computational effort needed to produce the training dataset for emulation by conducting simulations.

KEYWORDS

landslides, debris flows, natural hazards risk assessment, susceptibility maps, numerical simulations, computational geosciences

1 Introduction

Computational landslide run-out models can predict the spatial evolution of depth and velocity of the failed mass, which is crucial for landslide risk assessment and mitigation, especially for flow-like landslides due to their rapid nature (Cepeda et al., 2013; McDougall, 2017). Utilising computational landslide run-out models for model-based decision support requires a well-defined, transparent and modular setup of the complete computational value-chain. Such a chain consists of many links, including a digital representation of the topography, the underlying physics-based process model, a numerical solution scheme, the approach to parameter calibration along with the training data it relies on, and concepts used for sensitivity analyses and uncertainty quantification. Challenges in the technical realisation of such integrated workflows have been successfully addressed in the past (Dalbey et al., 2008; Aaron et al., 2019; Sun X. P. et al., 2021b; Zhao et al., 2021; Aaron et al., 2022; Zhao and Kowalski, 2022). It will be of crucial importance in the future to increase the efficiency, sustainability and, hence, acceptance of such orchestrated workflows for landslide risk assessment by improving their robustness, reliability and computational-feasibility.

It will be particularly important to assess the reliability of landslide risk assessment by quantifying and managing uncertainties throughout the workflow. This is a challenging task, which requires to consider and structure the *landscape of uncertainties* affecting various steps of the decision-making process. Relevant uncertainty originates from uncertain model input—such as the digital elevation model representing the topography (Zhao and Kowalski, 2020) or release area and volume—and rheological parameters (Quan Luna et al., 2013). Furthermore, process uncertainty can result from numerical modelling schemes (Schraml et al., 2015) or calibration methods (Aaron et al., 2019; 2022). All relevant uncertainties in the computational workflow include aleatoric aspects due to the intrinsic randomness of the process, as well as epistemic uncertainty that is of systemic nature, and might be due to a lack of data. A comprehensive, integrated uncertainty analysis within a georisk assessment framework is an important reminder of the limitations of the knowledge about processes involved, and the need to improve data collection and quality (Eidsvig et al., 2014).

Different methods of reliability analysis have been used in the recent decades both in geohazards research and its practical implementation, to assess the output uncertainty in landslide run-out models due to uncertain input parameters, or to quantify the uncertainty of derived metrics such as the Factor of Safety (FoS). Point Estimate Method (PEM) (Przewlocki et al., 2019), First Order Second Moment method (FOSM) (Kaynia et al., 2008), First Order Reliability Method (FORM) (Sun X. et al., 2021a), and Monte Carlo Simulations (MCS) (Cepeda et al., 2013; Liu et al., 2019; Brezzi et al., 2021) are examples of such methods. Dalbey et al. (2008) presented several standard and new methods for characterising the effect of input data uncertainty on model output for hazardous geophysical mass flows.

PEM is a simple way to determine the expectation (mean), variance, and skewness of a variable that depends on a random input, by evaluating the function at a low number of pre-selected values. Additionally, MCS grants access to the complete probability distribution even in complex problems (Fenton and Griffiths, 2008). However, it requires a large number of model evaluations, so-called realisations, at randomly selected inputs following a pre-determined statistical distribution. Przewlocki et al. (2019) used PEM to conduct a probabilistic slope stability analysis of a sea cliff in Poland, and compared the moment estimates with results from MSC. Mean and standard deviation values of FoS yielded similar results, and PEM was favoured as it required a lower number of model realisations, hence lower computational costs for a seemingly similar information outcome. Tsai et al. (2015) also obtained similar estimations by comparing PEM and MSC, but pointed out the effects of correlation between input variables. Earlier works also highlighted the limited feasibility of PEM for an increasing number of input variables, as 2^n estimations are required for n input variables (Christian and Baecher, 1999; 2002). Therefore, it is more feasible to handle problems characterised by a low-dimensional input parameter space with PEM, while high-dimensional problems quickly become computationally infeasible.

MCS has also been widely used for practical uncertainty quantification owing to its simplicity of implementation. Liu et al. (2019) and Ma et al. (2022) used MCS to quantify uncertainty in landslide run-out distance due to uncertain soil properties. Brezzi et al. (2021) performed uncertainty quantification of the Sant'Andrea landslide using MCS. They assumed the two friction parameters (Coulomb friction and turbulent friction) in a depth-averaged Voellmy-Salm type approach to follow independent Gaussian distributions, and then studied the induced uncertainty in deposit heights. The major challenge of using MCS for uncertainty quantification in landslide run-out modelling is the high computational cost, as pointed out by many researchers (Dalbey et al., 2008; McDougall, 2017; Aaron et al., 2022; Zhao and Kowalski, 2022).

As PEM relies on a much lower number of sampling points compared to MCS, the probability distribution function (PDF) of the output cannot be reliably approximated for a general non-linear process model, such as a landslide run-out model in complex topography. MCS provides an approximation of the PDF, but it creates a computational bottleneck when the forward-model is complex and subject to long runtimes. Physics-based machine learning, i.e. creating a surrogate by training a data-driven model with results from a physics-based simulation, can overcome the computational bottleneck of highly-throughput tasks such as uncertainty quantification. The surrogate model can be sampled, instead of the sampling from the forward model, and hence the PDF of the quantity of interest can be calculated efficiently. An example of physics-based machine learning techniques proven to be effective in many applications related to geohazards is Gaussian Process Emulation, with successful demonstrations in landslide run-out models (Zhao et al., 2021; Zhao and Kowalski, 2022) and stability of infrastructure slopes (Svalova et al., 2021).

This study aims at demonstrating how an uncertainty quantification workflow can be set up effectively, and how this affects the model-based landslide risk assessment. A test case with a synthetic topography and a test case with a real world problem are designed. Multiple forward simulations of both cases are conducted to construct Gaussian process emulators to facilitate MCS. The objectives are (i) comparing the results of PEM-based simulations and MCS conducted with emulators trained based on datasets from a limited number of simulations in terms of three moments, (ii) investigating the effects of topographic complexity, i.e. synthetic topography vs. the topography of a real-world problem, on the PEM - MCS comparison,

and (iii) demonstrating the applicability of emulation techniques for uncertainty quantification.

2 Materials and methods

2.1 Modelling approach

Existing physics-based landslide run-out models can be divided into three groups: lumped mass models, particle models, and continuum models. Lumped mass models treat the flow mass as a condensed mass point without spatial variation. This process idealisation greatly reduces the complexity of the problem, but the trade-off is losing spatial variation of flow dynamics, such as internal deformation of the flowing mass. Particle models treat the flow mass as an assembly of particles and simulate the movement of each particle and their interactions in order to characterise flow dynamics. They can directly account for three-dimensional flow behaviours, including an internal re-distribution of mass. Computational realisation of a particle model relies on the definition of conceptual particles, whose size is chosen based on available computational resources, and is often much larger than actual material particles in the landslide. This is beneficial from an implementation point of view, yet requires special attention, when formulating necessary interaction forces which are often challenging to justify and validate. Continuum models treat the flow mass as continuum material, for which governing equations are derived from balance laws closed by tailored, complex constitutive relations. Implementing these in a general three-dimensional context is very challenging and uses a lot of computational resources. A majority of particularly relevant continuum models for practical landslide run-out modelling are formulated within a depth-averaging framework. Depth-averaged continuum models balance computational efficiency, accuracy and interpretability. They can account for internal deformation of the flow material, and provide spatial variation of flow dynamics. Eqs. 1–3 describe the governing system of an idealised depth-averaged landslide run-out model:

$$\partial_t h + \partial_x \left(h u_x\right) + \partial_y \left(h u_y\right) = 0, \tag{1}$$

$$\partial_t \left(h u_x\right) + \partial_x \left(h u_x^2 + g_n \frac{h^2}{2}\right) + \partial_y \left(h u_x u_y\right) = g_x h - S_{fx}, \tag{2}$$

$$\partial_t \left(h u_y\right) + \partial_x \left(h u_x u_y\right) + \partial_y \left(h u_y^2 + g_n \frac{h^2}{2}\right) = g_y h - S_{fy}. \tag{3}$$

The equations are derived from the mass balance (Eq. 1) and momentum balance (Eqs. 2, 3). The flow height h and the depth-averaged surface tangent flow velocities u_x and u_y are the state variables. g_x, g_y, and g_n are components of the gravitational acceleration along surface tangent and in normal directions. The friction terms S_{fx} and S_{fy} depend on the chosen basal rheology. In terms of the Voellmy rheological model, they are defined as:

$$S_{fi} = \frac{u_i}{\|\mathbf{u}\|}\left(\mu g_n h + \frac{g}{\xi}\|\mathbf{u}\|^2\right), \quad i \in \{x, y\}, \tag{4}$$

where $\|\mathbf{u}\|$ denotes the magnitude of the flow velocity; μ and ξ are the dry-Coulomb friction coefficient and turbulent friction coefficient respectively.

Many numerical solvers for depth-averaged landslide run-out models have been developed in the past decades, and McDougall (2017) provides a comprehensive review. A GIS-based open source computational tool developed by Mergili et al. (2017), r.avaflow v2.3, is used in this study. It implements a high-resolution total variation diminishing non-oscillatory central differencing scheme to solve Eqs. 1–4 given topographic data, initial mass distribution, and Voellmy parameters. It runs on Linux systems, and employs the GRASS GIS software, together with the programming languages Python and C, and the statistical software R. A Digital Elevation Model (DEM) and a release height map are given as input as raster files.

2.2 Case studies

2.2.1 Synthetic case

A simple topography has been created in Python—similar to the topography generation in AvaFrame (D'Amboise et al., 2022) — which is denoted as *synthetic case* herein. Topography consists of a parabolic slope starting at $x = 0$ at an altitude of 1332 m, and connecting to a flat land at $x = 3000$ at an altitude of 0 m. Extent of the area in x and y directions are 5000 m and 4000 m, respectively, whereas the resolution is 20 m. Release zone was defined as an elliptic cylinder, of which the centre is located at $(x, y) = (600, 2000)$ with a minor axis of 100 m and a major axis of 200 m. Height at each point within the ellipse was defined as 20 m, which generates a total release volume of 1.432 x 10^6 m^3. **Figure 1A** illustrates the maximum flow height map from a simulation of synthetic case, while **Figure 1B** shows the deposit height from the same simulation.

2.2.2 Acheron rock avalanche

A real-world case is chosen to compare the differences in uncertainty quantification with the synthetic case. Radiocarbon testing dates the occurrence of Acheron rock avalanche—located near Canterbury, New Zealand—approximately 1100 years before present, and it may have been triggered by seismic activity (Smith et al., 2006). The deposit area was estimated to be .72 x 10^6 m^2 using a GPS outline of the deposit, while the deposit volume was estimated as 8.9 x 10^6 m^3 using an estimated mean depth derived from observed and estimated thicknesses for different morphological zones (Smith et al., 2012). DEM file and the release height map are obtained from Mergili and Pudasaini (2014–2021)[1], which gives an initial release volume of 6.4 x 10^6 m^3. **Figure 2** presents the shaded relief of the area, together with a map of maximum flow height (see **Figure 2A**) and deposit height (see **Figure 2B**) from a random simulation of Acheron rock avalanche.

2.3 Gaussian process emulation

The main problem of applying MCS for uncertainty quantification in landslide run-out modelling is its high computational cost. The runtime of the landslide run-out model is one of the key drivers of computational cost in classical MCS, as it scales with the number of

1 Mergili, M., Pudasaini, S.P., 2014–2021. r.avaflow—The mass flow simulation tool. https://www.avaflow.org. Accessed on 2022-07-12.

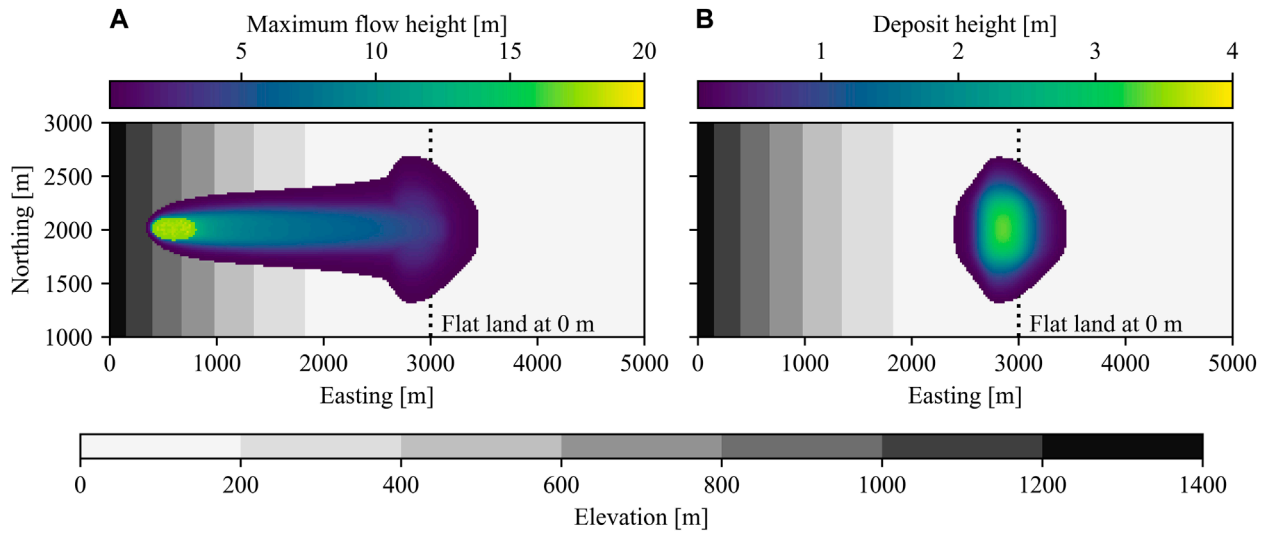

FIGURE 1
(A) Maximum flow height and **(B)** deposit height from a simulation of the synthetic case.

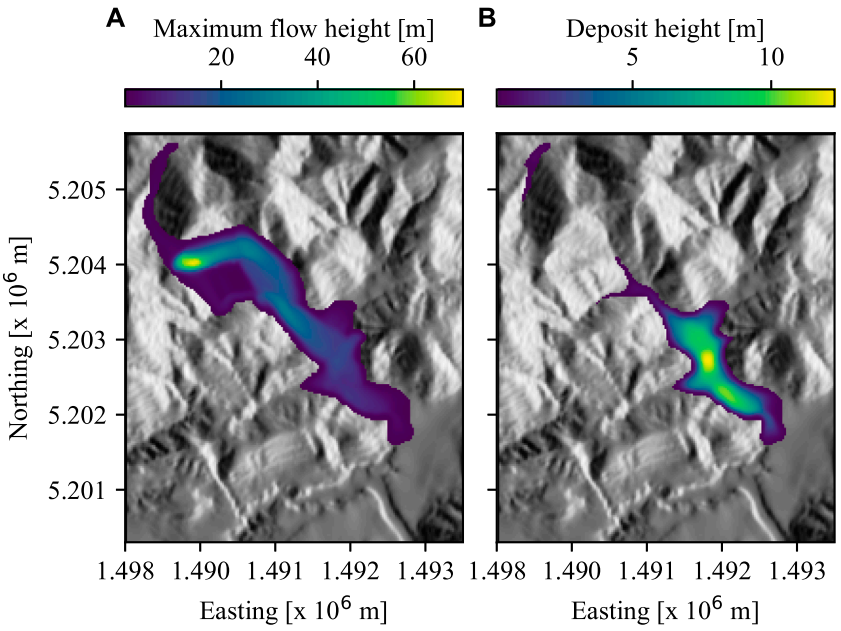

FIGURE 2
(A) Maximum flow height and **(B)** deposit height from a simulation of Acheron rock avalanche.

forward evaluations. Gaussian process emulation has been used in recent years to build cheap-to-evaluate emulators to replace expensive-to-evaluate computational models in the framework of uncertainty quantification, such as Sun X. P. et al. (2021b), Zeng et al. (2021), and Zhao and Kowalski (2022). A Gaussian process emulator is a statistical approximation of a simulation model, built based on input and output data of a small number of simulation runs. Once an emulator is constructed, it provides prediction of simulation output at a new input point almost instantly, together with an assessment of the prediction uncertainty. This emulator-induced uncertainty can be taken into account in the framework of uncertainty quantification.

Let $y = f(\mathbf{x})$ denote a simulator where y represents a scalar output depending on a p-dimensional input $\mathbf{x}$. Assuming that the simulator is a realisation of a Gaussian process with a mean function $m(\cdot)$ and a

kernel function $k(\cdot,\cdot)$, namely

$$f(\cdot)\sim\mathcal{N}(m(\cdot),k(\cdot,\cdot)), \tag{5}$$

A Gaussian process emulator can be built based on the input-output data $\mathcal{D}$ of n simulation runs, namely $\mathcal{D}=\{\mathbf{x}_i,y_i\}_{i=1}^{n}$. At any new input point $\mathbf{x}^\star$, the approximated output $y^\star$ follows a Gaussian distribution given by

$$y^*\sim\mathcal{N}\left(m'\left(\mathbf{x}^*\right),k'\left(\mathbf{x}^*,\mathbf{x}^*\right)\right), \tag{6}$$

$$m'\left(\mathbf{x}^*\right)=m\left(\mathbf{x}^*\right)+\mathbf{k}^T\left(\mathbf{x}^*\right)\mathbf{K}^{-1}(y_1-m(\mathbf{x}_1),\ldots,y_n-m(\mathbf{x}_n))^T, \tag{7}$$

$$k'\left(\mathbf{x}^*,\mathbf{x}^*\right)=k\left(\mathbf{x}^*,\mathbf{x}^*\right)-\mathbf{k}^T\left(\mathbf{x}^*\right)\mathbf{K}^{-1}\mathbf{k}\left(\mathbf{x}^*\right). \tag{8}$$

The symbol $\mathbf{K}$ denotes the $n\times n$ covariance matrix of which the (i,j)-th entry $\mathbf{K}_{ij}=k(\mathbf{x}_i,\mathbf{x}_j)$ and the symbol $\mathbf{k}(\mathbf{x}^*)=\left[k(\mathbf{x}^*,\mathbf{x}_1),\ldots,k(\mathbf{x}^*,\mathbf{x}_n)\right]^T$.

RobustGaSP package developed by Gu et al. (2019) is used in this study to build emulators. It provides robust Gaussian process emulation for both single-variate (Gu et al., 2018), i.e. one simulation producing one scalar output, and multi-variate simulators (Gu and Berger, 2016), i.e. one simulation producing high-dimensional output. Training and validation datasets of each case were generated from outputs of both cases simulated with r. avaflow 2.3. 100 simulations for training, and 20 additional simulations for validation of vector emulators were run for synthetic case and Acheron rock avalanche separately. Dry-Coulomb friction coefficient (μ), turbulent friction coefficient (ξ), and release volume (v_o) were chosen as uncertain input variables. The friction coefficients are rather conceptual than physical (Fischer et al., 2015) and rely on back-analysing past events where field data are available. The calibrated results are often ranges (Zhao et al., 2021) or probability density functions (Quan Luna et al., 2013). In this study, ranges of friction coefficients were chosen as $\mu=[.02,.3]$, $\xi=[100,2200]$ m/s^2 according to Zhao et al. (2021). The release volume of a future landslide event is hardly predictable. Uncertainty in v_o were defined by multiplying the release height map with a coefficient k, which is assumed to vary between .5 and 1.5 in this study. Parameter combinations were generated using Latin Hypercube sampling by maximising the minimum distance between points. Datasets were extracted from simulation results after training, and scalar outputs, e.g. impact area, deposit area, deposit volume, and vector outputs, e. g flow height or flow velocity in each cell, were defined.

2.4 Uncertainty analysis

2.4.1 Point estimate method

Any scalar output $y(\mathbf{s},t)$ — either aggregated, such as impact area, deposit area or deposit volume, or point-wise flow height, flow velocity, or flow pressure—in space $(\mathbf{s})$ and time (t), from the landslide run-out simulations can be expressed as a function of three uncertain input variables as shown in Eq. 9.

$$y(\mathbf{s},t)=f(\mu,\xi,v_o) \tag{9}$$

Assuming that the input variables are not correlated and skewness is 0, locations of sampling points of each variable correspond to mean ± standard deviation. This results in eight sampling points with equal weights for three input variables to evaluate the output function y and calculate the three moments of the output, i.e. mean, variance, skewness. PEM were executed three times with different coefficient of variation (*COV*), i.e. 10%, 25% and 50%. **Table 1** shows the assumed mean, which was chosen as the central point of the ranges defined in **Section 2.3**, and standard deviations for the input variables used in the analyses, PEM 1, PEM 2, and PEM 3.

2.4.2 Monte Carlo Simulations

Parameter combinations for MCS were sampled from truncated multivariate normal distribution using the R package, *tmvtnorm* (Wilhelm and Manjunath, 2010). Points of truncation were chosen as the ranges given in **Section 2.3**. Three sets of MCS were conducted similarly to the PEM, i.e. mean value is the central point of the range and *COV* is chosen arbitrarily as 10% (MCS 1), 25% (MCS 2), and 50% (MCS 3) to represent different levels of uncertainty in input variables. 10,000 parameter sets were generated for each MCS analysis, and the outputs are estimated using the emulators defined in **Section 2.3**.

3 Results

Simulation outputs used in this study can be found in Yildiz et al. (2022a), and the general workflow, as well as the scripts to reproduce the figures can be found in the Git repository presented in Yildiz et al. (2022b).

3.1 r.avaflow simulations

A total of 100 simulations of the synthetic case and a separate 100 simulations for Acheron rock avalanche have been used to calculate the scalar outputs, and to extract vector outputs. Quantities of interest (*QoI*) derived from the simulations are impact area, deposit area and deposit volume. In addition to the derived ones, direct simulation outputs, i.e. maximum flow height (h_{max}) and maximum flow velocity (v_{max}) at a predefined cell, are extracted from the simulations. Point of extraction was chosen arbitrarily as (x,y) = (1000, 2000) for the synthetic case, and as (1490100, 5204100) for Acheron rock avalanche. These points were picked among those which had a value higher than a threshold, e.g. a maximum flow height of .1 m, from all simulations.

Evolution of a simulation in synthetic case can be summarised as a rather constrained flow, with a limited lateral spread at the upper section of the slope, and a more pronounced lateral spread close to the transition to the flat land (See **Figure 1A**). As no stopping criteria was defined, the failed mass accumulates mostly around the toe of the slope (See **Figure 1B**). Mean values ± standard deviations of the impact area, deposit area and deposit volume were (2.39 ± .37) x 10^6 m^2, (1.22 ± .22) x 10^6 m^2 and (1.37 ± .41) x 10^6 m^3, respectively. Ranges of v_{max} and h_{max} at (x,y) = (1000, 2000) are 24.9–63.4 m/s and 7.18–14.4 m, with mean values of 47.7 m/s and 11.0 m, respectively.

Flow path of Acheron rock avalanche can be generalised based on the simulations conducted in this paper as an initially relatively straight path, followed by a sharp turn and extending into the valley (See **Figure 2A**). Similar to synthetic case, 100 simulations of Acheron rock avalanche were run, and the same scalar outputs were calculated or extracted. Mean values ± standard deviations of the impact area, deposit area and deposit volume were (2.78 ± .91) x 10^6 m^2, (1.45 ±

TABLE 1 Mean and standard deviation values of the input variables used in the Point Estimate Method (PEM) analysis of the synthetic case and Acheron rock avalanche. Same values of Dry-Coulomb and turbulent friction coefficients are used for both cases.

	Unit	PEM 1 (COV = 10%)		PEM 2 (COV = 25%)		PEM 3 (COV = 50%)	
		mean	Std. dev.	mean	Std. dev.	mean	Std. dev.
Dry-Coulomb friction coefficient	-	.160	.016	.160	.040	.160	.080
Turbulent friction coefficient	m/s^2	1150	115.0	1150	287.5	1150	575.0
Release volume - Synthetic	x 10^6 m^3	1.432	.143	1.432	.358	1.432	.716
Release volume - Acheron	x 10^6 m^3	6.40	.64	6.40	1.60	6.40	3.20

TABLE 2 Coefficient of determination, R^2, mean absolute percentage error, *MAPE*, and normalised root mean squared error *nRMSE* for the emulators trained with scalar outputs from synthetic case and Acheron rock avalanche.

Output	Synthetic case			Acheron rock avalanche		
	R^2 [-]	*MAPE* [%]	*nRMSE* [%]	R^2 [-]	*MAPE* [%]	*nRMSE* [%]
Impact area	.999	.468	.606	.997	1.294	1.900
Deposit area	.996	.864	1.173	.988	2.530	3.100
Deposit volume	.999	.553	.717	.999	.541	.752
Maximum velocity	.999	.592	.731	.967	2.802	3.473
Maximum height	.989	1.609	1.996	.965	2.084	2.828

.42) x 10^6 m^2 and (6.28 ± 1.83) x 10^6 m^3, respectively. v_{max} and h_{max} at (x, y) = (1490100, 5204100) have mean values of 32.2 m/s and 42.2 m, with standard deviations of 6.2 m/s and 6.4 m.

3.2 Emulation

Gaussian process emulation has been used in this study in order to facilitate the prediction of many scalar outputs for MCS analysis. Once the training datasets consisting of scalar outputs described in **Section 3.1** are generated, the trained emulators are first validated with leave-one-out cross-validation technique. **Table 2** presents the validation results of scalar emulators, i.e. mean absolute percentage error (*MAPE*), normalised root-mean-square error (*nRMSE*), and coefficient of determination (R^2) values for both cases. Emulators trained for synthetic case produced very low percentage-based errors, i.e. maximum *MAPE* and *nRMSE* was 1.609% and 1.996%, respectively, while the R^2 values were around .99. The lowest prediction quality was obtained for maximum flow height at (x, y) = (1000, 2000) in synthetic case. Emulators trained with derived scalar outputs, i.e. impact area, deposit area and deposit volume, of Acheron rock avalanche yielded similar model performance as the synthetic case. Relatively lower R^2 values, approximately .97, and higher *MAPE* and *nRMSE* values were obtained for v_{max} and h_{max} at (x, y) = (1490100, 5204100). Lowest prediction performance for Acheron rock avalanche was for maximum flow velocity at the given point.

Prediction quality of the vector emulators both for synthetic case and Acheron rock avalanche has been evaluated using testing data from additional 20 simulations. P_{CI}(95%), defined by Gu and Berger (2016), is chosen as the diagnostic for vector emulators. It represents the proportion of testing outputs that lie in emulator-based 95% credible intervals. P_{CI}(95%) of the vector emulator for point-wise maximum flow height is 83.8% and 85.3% for synthetic case and Acheron rock avalanche respectively; P_{CI}(95%) of the vector emulator for point-wise maximum flow velocity is 86.3% and 89.1% for synthetic case and Acheron rock avalanche respectively.

3.3 Uncertainty analysis

Uncertainty of model outputs were investigated by conducting PEM and MCS with three different *COV*, a comparison has been made in terms of the three moments, i.e. mean, variance, and skewness, of the scalar outputs. **Figure 3** presents the comparison for the synthetic case. If the uncertainty of the model outputs is assessed *via* PEM, similar mean values are obtained even though the *COV* is varied from 10% up to 50%. Differences were higher for v_{max} and h_{max} (See **Figures 3D, E**). An increase of variance with increasing *COV* is evident for all outputs produced by PEM, whereas no clear relationship can be defined for skewness. For example, the skewness of impact area and deposit area increased with increasing *COV*, whereas the deposit volume, v_{max} and h_{max} had nearly no skewness if analysed by PEM.

Similar to PEM, MCS at all *COV* produced similar mean values and increasing variance with increasing *COV* for all scalar outputs. No overall trend can be observed in skewness of the outputs generated *via* MCS. If both techniques are compared, no significant difference is present in mean values. PEM produced higher variances especially at the highest *COV*, while—similar to previous comparisons—no generalisations can be made for skewness. It should be noted that there is a change from a slightly positive skewness to negative skewness for v_{max} and h_{max}, if the method is switched from PEM to MCS. Other scalar outputs had rather arbitrary changes between methods, even though slightly lower values are observed for impact area and deposit area.

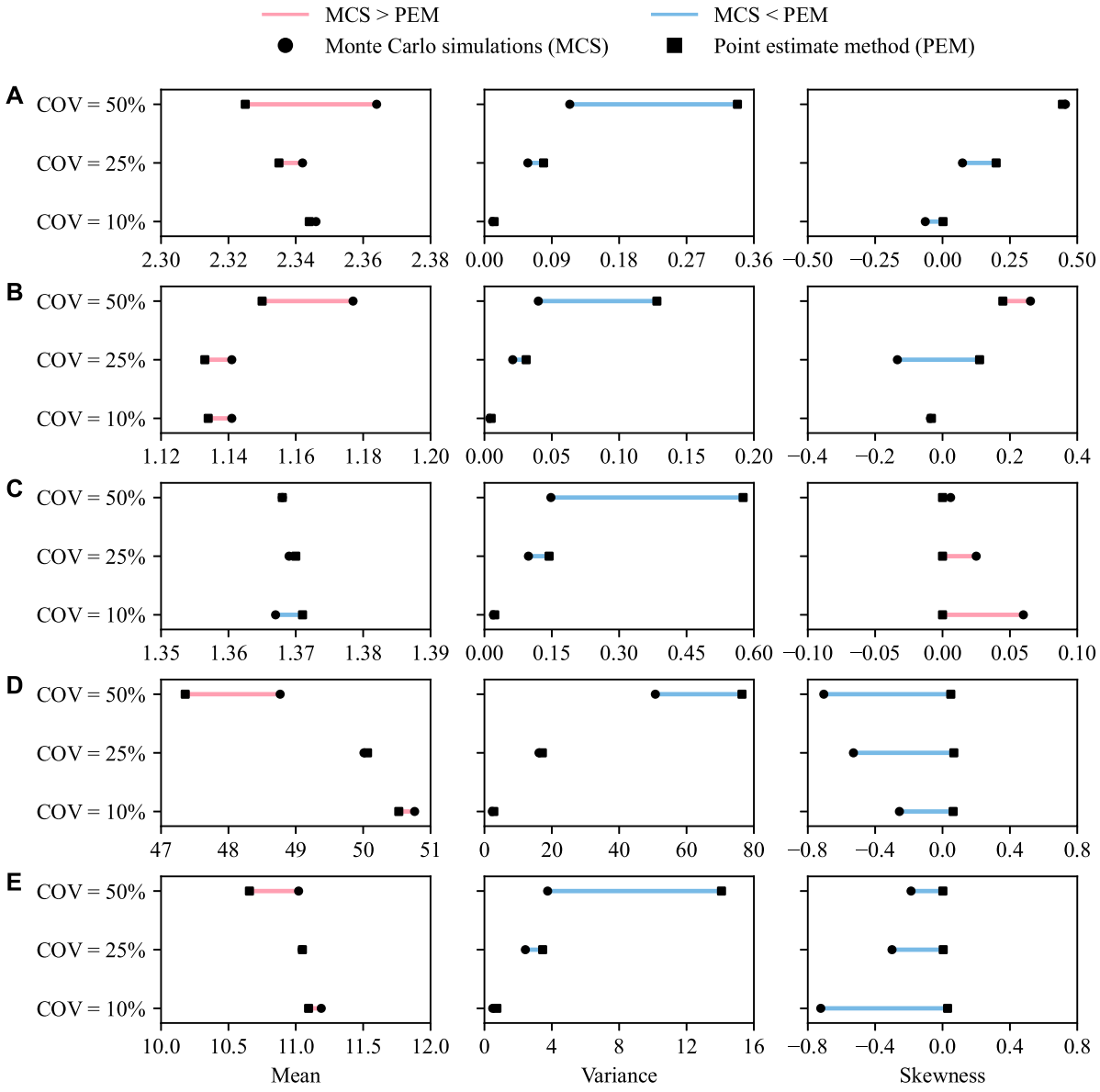

FIGURE 3
Three moments (mean, variance and skewness) of **(A)** impact area (in x10^6 m^2), **(B)** deposit area (in x10^6 m^2), **(C)** deposit volume (in x10^6 m^3), **(D)** maximum flow velocity (in m/s) and **(E)** maximum flow height (in m) at (x,y) = (1000, 2000) obtained from synthetic case with Monte Carlo simulations (MCS) and point estimate method (PEM).

Figure 4 presents three moments of the same scalar outputs from Acheron rock avalanche. Similar patterns to data from synthetic case are observed in Figure 4. Mean values of the outputs are similar between different methods and levels of *COV*. Variance increases in both methods with increasing *COV*, while the values obtained from MCS is lower than those from PEM.

Figure 5 illustrates the synthetic case results of the MCS analysis at *COV* of 50% in terms of the five scalar outputs–the impact area, deposit area, deposit volume, v_{max} and h_{max} at (x,y) = (1000, 2000). The first three columns show the relationships of the scalar outputs with respect to the three uncertain parameters. The last column shows the histograms of each scalar output. Figure 6 presents the corresponding results of Acheron rock avalanche. Observations from Figures 5, 6 can be generalised as follows.

- the impact area and deposit area decrease with increasing dry-Coulomb friction coefficient and increases with increasing release volume (see Figures 5A, B, 6A, B),
- the deposit volume is proportional to the release volume and has almost no dependence on the dry-Coulomb and turbulent friction coefficients (see Figures 5C, 6C),

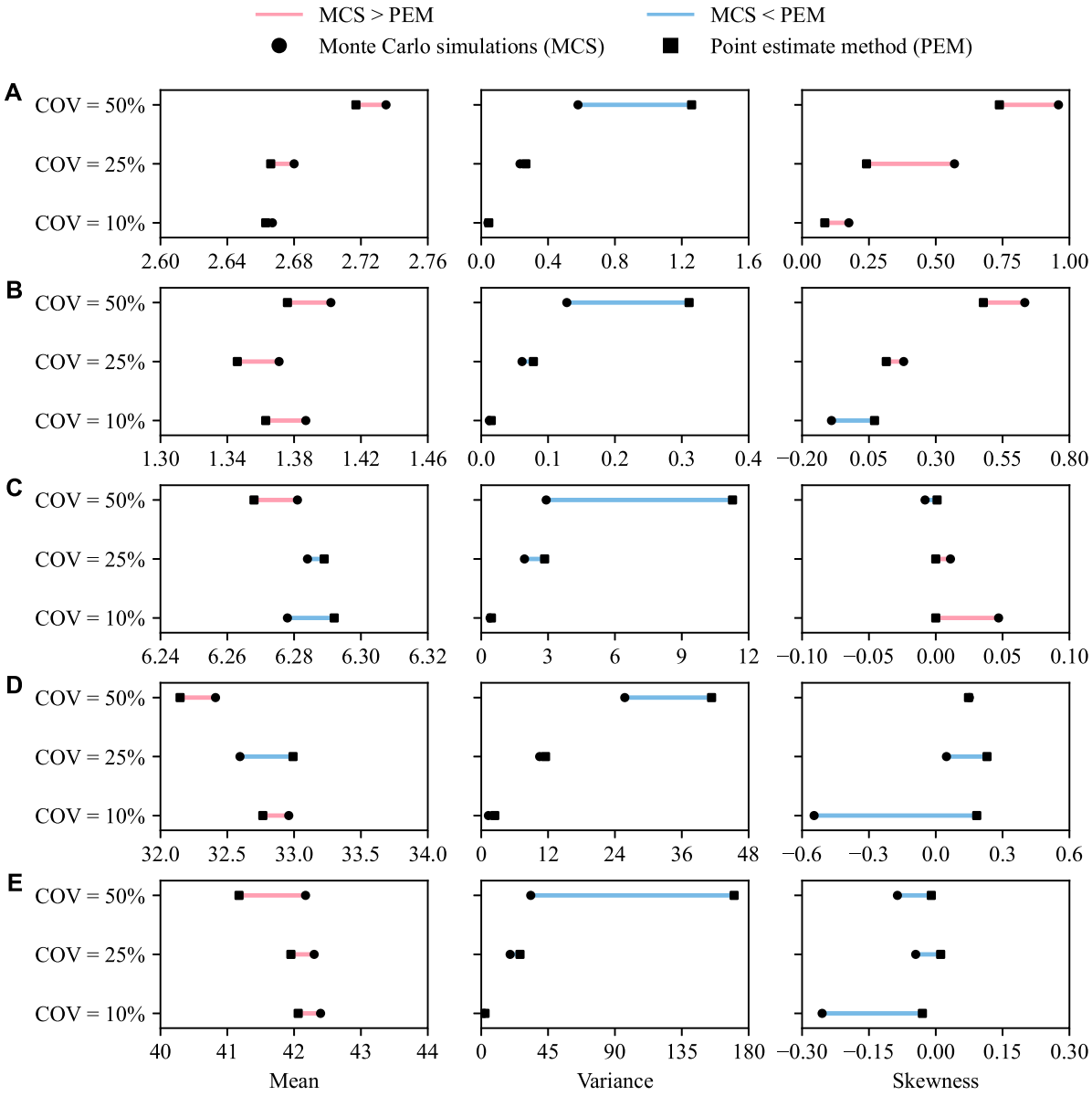

FIGURE 4
Three moments (mean, variance and skewness) of **(A)** impact area (in x10^6 m^2), **(B)** deposit area (in x10^6 m^2), **(C)** deposit volume (in x10^6 m^3), **(D)** maximum flow velocity (in m/s) and **(E)** maximum flow height (in m) at (x,y) = (1490100, 5204100) obtained from Acheron rock avalanche with Monte Carlo simulations (MCS) and point estimate method (PEM).

- the point-wise maximum flow velocity decreases with increasing dry-Coulomb friction coefficient and has little dependence on the release volume (see Figures 5D, 6D),
- the point-wise maximum flow height increases with increasing release volume and has little dependence on the dry-Coulomb and turbulent friction coefficient (see Figures 5E, 6E).

Differences between the two cases can be noted as (1) the deposit area has a clear negative relationship with the dry-Coulomb friction coefficient in Acheron rock avalanche, but the trend is hardly visible for the synthetic case; (2) the point-wise maximum velocity increases with the turbulent friction coefficient in the synthetic case, but the relationship is vague in Acheron rock avalanche.

Figures 7, 8 show the comparison of spatial distribution of maximum flow height from synthetic case and Acheron rock avalanche, respectively. Results given in the figures, mean and standard deviation of h_{max} in each cell as well as their differences, are from the PEM and MCS analyses conducted at $COV = 50\%$. A visual comparison of mean values (See Figures 7A, B, 8A, B) look nearly identical, but the difference map shows that flow heights at the central section of the flow path in both cases are higher in MCS analysis, while

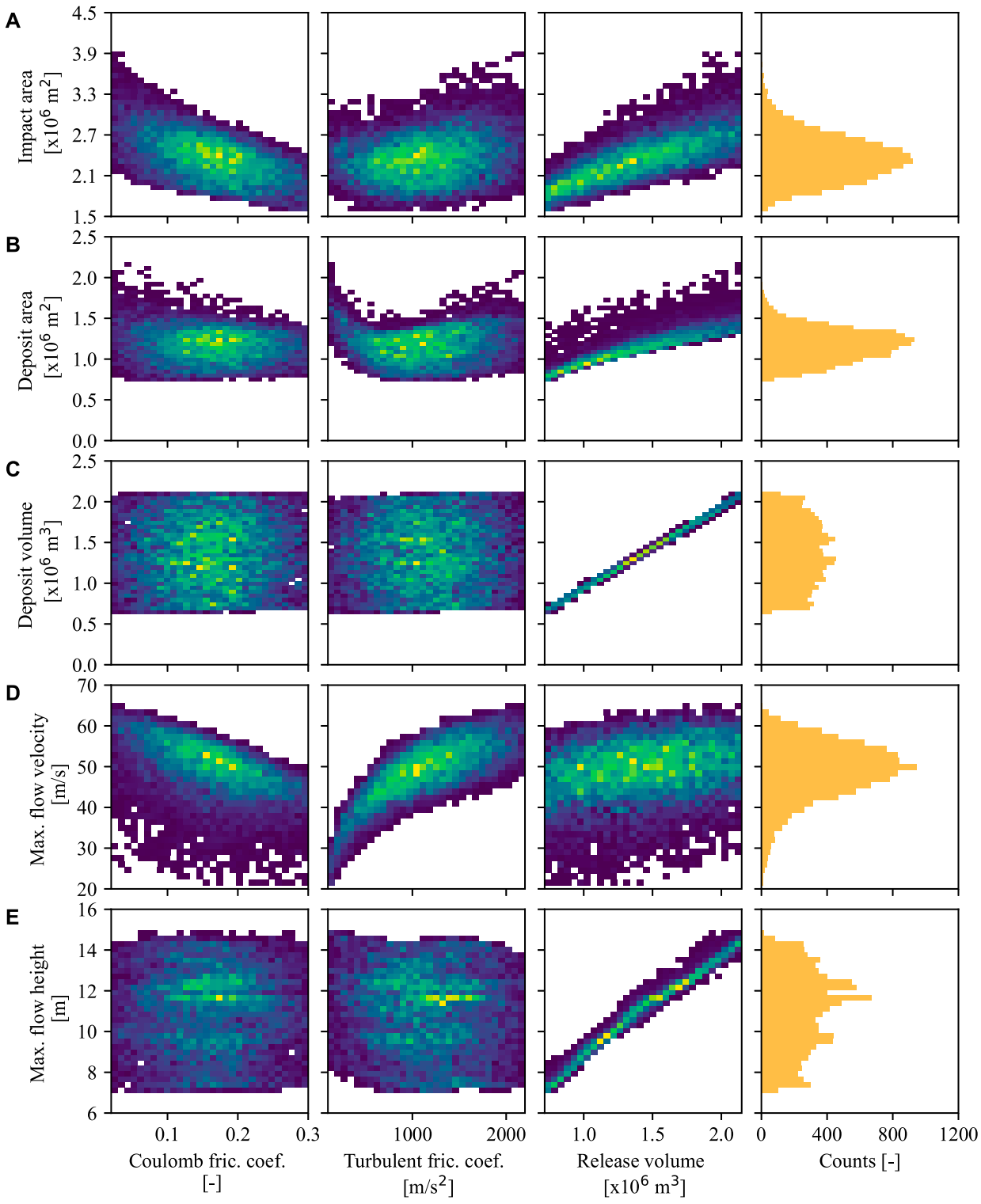

FIGURE 5
Relationships and histograms of **(A)** impact area, **(B)** deposit area, **(C)** deposit volume, **(D)** maximum flow velocity and **(E)** maximum flow height at (x,y) = (1000, 2000) from synthetic case with uncertain parameters used in the Monte Carlo analysis with coefficient of variation of 50%.

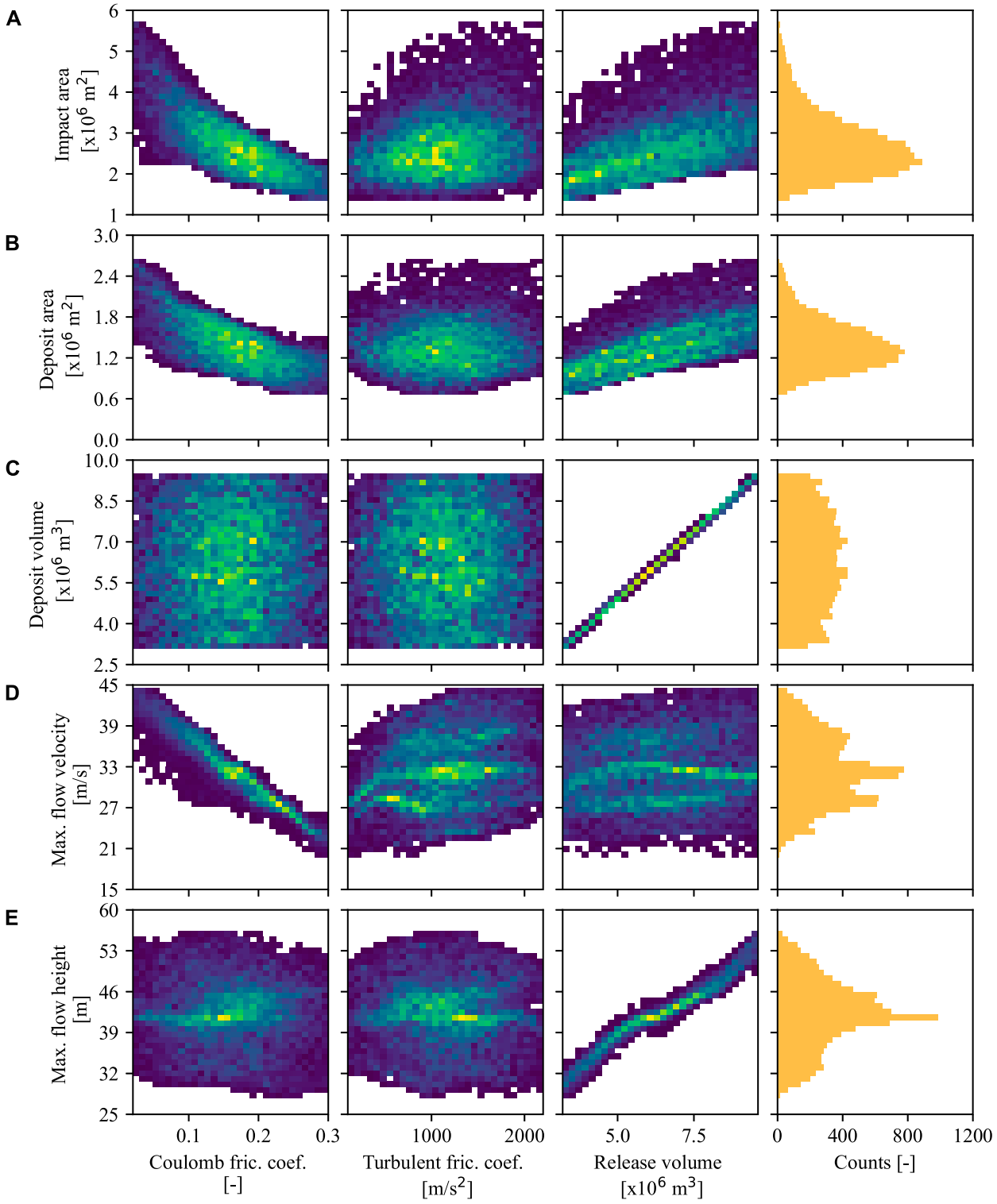

FIGURE 6
Relationships and histograms of **(A)** impact area, **(B)** deposit area, **(C)** deposit volume, **(D)** maximum flow velocity and **(E)** maximum flow height at (*x*,*y*) = (1490100, 5204100) from Acheron rock avalanche with uncertain parameters used in the Monte Carlo analysis with coefficient of variation of 50%.

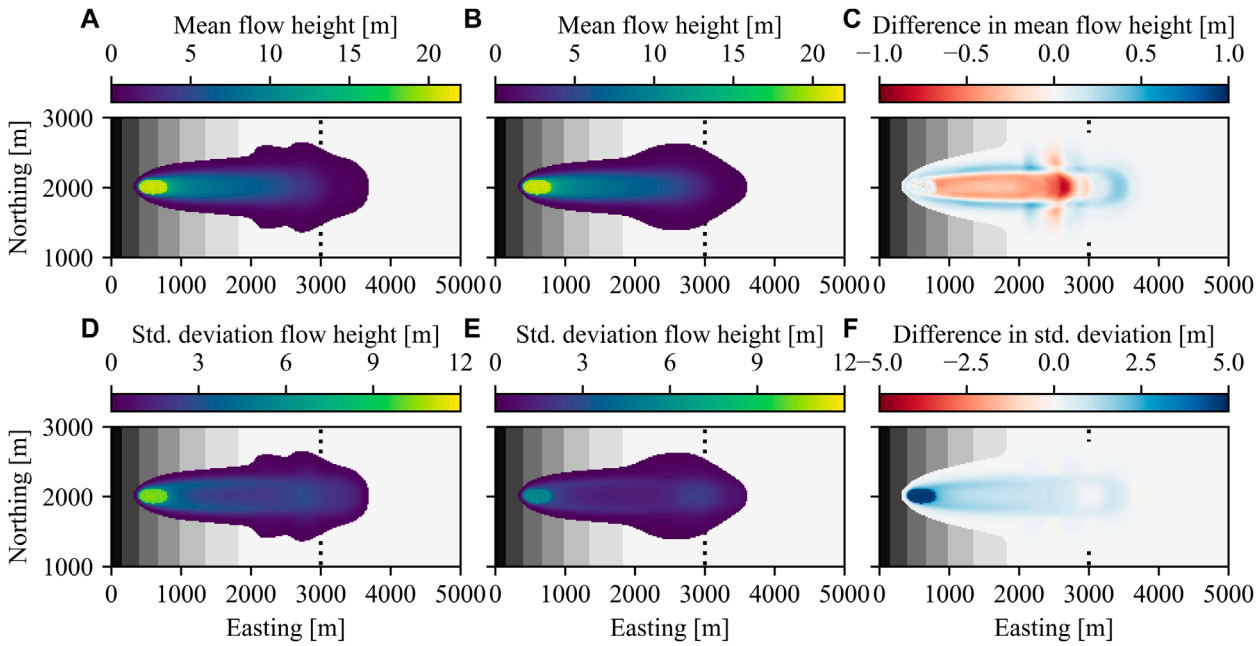

FIGURE 7
Spatial distribution of mean and standard deviations of maximum flow height (h_{max}) from synthetic case obtained with **(A, D)** Point Estimate Method (PEM) and **(B, E)** Monte Carlo Simulations (MCS) at 50% coefficient of variation. Differences of **(C)** mean value and **(F)** standard deviation are plotted by subtracting MCS results from PEM results.

TABLE 3 Correlation of input variables with location (x_L) and the length (L_{max}) of maximum lateral spread in synthetic case.

	x_L	L_{max}
Dry-Coulomb friction coefficient	.99***	.33***
Turbulent friction coefficient	*No correlation*	.50***
Release volume	*No correlation*	.80***

***$p < .001$

the edges of the flow path have higher flow heights in the PEM analysis. Similar to the results in **Figures 3**, **4**, MCS produced lower standard deviation than PEM at the majority of cells, i. e approximately 200 cells out of 6600 for synthetic case, and 830 cells out of 9800 cells for Acheron rock avalanche.

4 Discussion

Risk for a single landslide scenario has three main components: the landslide hazard, the exposure of the elements at risk, and their vulnerability. Conducting a quantitative risk analysis enables the researchers or practitioners to obtain the probability of a given level of loss and the corresponding uncertainties of these components (Corominas et al., 2014; Eidsvig et al., 2014). The hazard in a model-based landslide risk assessment is generally evaluated by simulating various scenarios with an underlying physics-based computational model. A probabilistic approach to this assessment and the quantification of associated uncertainty inevitably create a computational bottleneck—especially for large-scale applications (Strauch et al., 2018; Jiang et al., 2022). One can opt for a simple technique to quantify uncertainty, i.e. PEM in this study, to reduce the number of simulations required, or use a technique necessitating high number of simulations, for instance MCS techniques.

The computational challenge of MCS has been well-recognised in the field of landslide modelling, which results from the large number of model realisations at randomly selected input values (Dalbey et al., 2008; McDougall, 2017). MCS can be very computationally intensive, since it typically requires tens of thousands of model runs to achieve reasonable accuracy (Salciarini et al., 2017). This is often not feasible in model-based landslide risk assessment, as a single model run may take minutes to hours. A solution to overcome this problem has been demonstrated in this study by utilising recent development of GP emulation (Gu and Berger, 2016; Gu et al., 2018; Gu et al., 2019). GP emulators are built for each case based on only 100 model runs. Then, MCS with 10,000 randomly generated inputs is conducted using the emulators, which means no further model runs are needed. Moreover, diagnostics of built GP emulators are analysed to evaluate their performance. High R^2 values and low *MAPE*s and *nRMSE*s (See **Table 2**) suggests that the scalar emulators can be used with confidence for predictions of a singular output from an input parameter combination. All P_{CI}(95%) values for the vector emulators are close to 95%, which justify their usage as a surrogate to the computational model (Gu et al., 2019). The corresponding results of GP emulation-based MCS are therefore close to results of a classical MCS, but the computational time is significantly reduced by introducing GP emulation. This demonstrates the

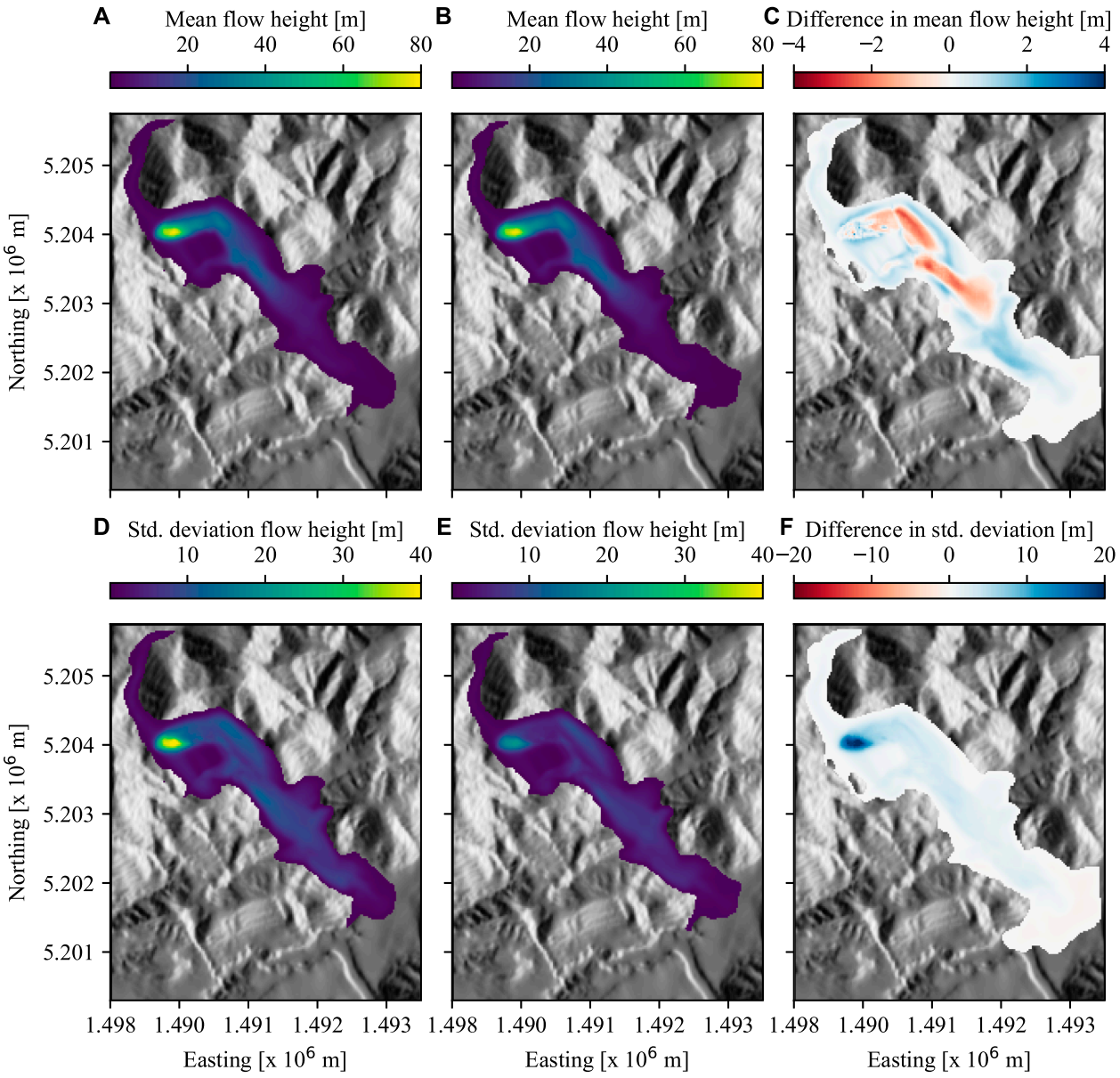

FIGURE 8
Spatial distribution of mean and standard deviations of maximum flow height (h_{max}) from Acheron rock avalanche obtained with **(A, D)** Point Estimate Method (PEM) and **(B, E)** Monte Carlo Simulations (MCS) at 50% coefficient of variation. Differences of **(C)** mean value and **(F)** standard deviation are plotted by subtracting MCS results from PEM results.

applicability of GP emulation for uncertainty quantification of landslide run-out models. A similar methodology applied to landslide generated waves was also found promising to perform probabilistic hazard analysis based on computationally intensive models (Snelling et al., 2020).

Comparative studies in landslide research showed that similar mean values of the QoI can obtained with PEM or MCS (Tsai et al., 2015; Przewlocki et al., 2019). As shown in **Figures 3**, **4**, when an aggregated (e.g. impact area, deposit area, deposit volume) or point-wise (velocity and height at a predetermined coordinate) output is calculated, PEM and MCS yielded similar expectancies (mean values) in this study. In addition, both PEM and MCS lead to similar variance values for relatively low COV, i.e. 10% and 25%. This implies that if one only aims at computing low-order moments in comparative topographic settings, PEM can achieve reasonable results (Fanelli et al., 2018). PEM is particularly computationally appealing for low-dimensional problems due to the requirement of 2^n realisations, where n is the dimension of the input parameter space. However, as pointed out by Christian and Baecher (2002), caution should be used in approximating skewness or other higher order moments based on PEM. This is supported by the large difference between PEM- and MCS-based skewness results as shown in **Figures 3**, **4**. Christian and Baecher (2002) also pointed out that the results deviate significantly, when the *COV* of uncertain inputs is

large, which is confirmed by the large difference between the variance computed by PEM and MCS in the cases of $COV = 50\%$ as shown in **Figures 3**, **4**. Comparing **Figures 3**, **4**, it can be seen that the complexity of topography, which refers to the real topography of Acheron rock avalanche in comparison to the parabolic slope of the synthetic case, seems to have limited impact on the general trend of moments based on PEM and MCS, especially mean and variance. It may imply the transferability of the trends described above to different topographies.

When input uncertainty is high and the input parameter space is high-dimensional, MCS is clearly favourable over PEM to compute desired statistics of the output of interest. The benefit of GP-integrated MCS is that it can not only compute the desired statistics, but it also provides the PDF (Marin and Mattos, 2020). Cepeda et al. (2013) recommends a stochastic approach for uncertainty quantification such as MCS to be part of the routine of any landslide hazard risk assessment, and Hussin et al. (2012) denotes the frequency distributions of model outputs important as a first step to assess the spatial probability in future debris flow hazard assessments. The workflow of GP emulation-based uncertainty quantification in this study is therefore expected to improve landslide risk assessment. It should be noted that the number of model runs to train GP emulators are effected by the dimension of input parameter space even though the number of model runs of MCS is independent. Due to this limitation, the gain of computational efficiency by using GP emulation decreases with increasing dimension of input parameter space. If the dimension is too high, other emulation techniques or dimension reduction can be considered (Liu and Guillas, 2017).

Histograms plotted in **Figures 5**, **6** can be used to infer on the complexity of the output functions, see Eqs. **9**. Input parameters were assumed to be normally distributed in MCS analysis. It can be seen that the deposit volume (see **Figures 5C**, **6C**) is the only parameter that has the shape of the truncated normal distribution with nearly no skewness. Other scalar outputs result in skewed and even bi-modal distributions that clearly deviate from the initial Gaussian distribution of the corresponding input parameter. Both cases show a nearly perfect correlation between deposit and release volume with no effects of the friction coefficient indicating parameter-independent mass conservation. It should be noted that the deposit volume was calculated considering cells in which height exceeded .1 m at the last simulation time step. As there was no stopping criteria defined and no entrainment was considered, the deposit volume was nearly equal to the release volume. Highly linear function of deposit volume and release volume translates into the deposit volume having a Gaussian distribution, as the linear transformation of a Gaussian distribution is also a Gaussian distribution. However, the non-linearity of the other functions that can be used the express the scalar outputs—except deposit volume—results in distributions different than those of the input parameters. For example, Cepeda et al. (2013) fitted Gamma distributions for flow height and velocity in two different cases.

Patterns observed in **Figures 7C**, **8C** can be explained by analysing the effects of input variables on the general shape of the flow path. Hence, the simulation in a synthetic topography is an ideal example due to its simplicity. As explained in **Section 3.1** and shown in **Figure 1A**, the flow path of the synthetic case can be described as a concentrated central flow superposed by lateral spread at the toe of the slope. It can be seen in **Figure 7A** that the mean flow height has two pronounced *dents* in its spatial distribution obtained with PEM. These correspond to the initiation of the lateral spread at different configurations of the input variables are considered. More specifically, PEM analysis is run only at few discrete values in parameter space chosen at a distance of one standard deviation away from the mean. When the friction coefficient is chosen at a $COV = 50\%$ with a mean of .16, PEM simulations are characterised by a lateral spread very early in the flow path, or a lateral spread that kicks in much further downstream. Therefore, the *dents* in the maximum flow height map (See **Figure 7A**) is a direct consequence of the coarse discretisation of the parameter space in the PEM approach. In contrast, MCS yields a homogeneously distributed maximum flow height map at the toe of the slope as expected in this almost linear setting. As a consequence, flow heights at the upper sections of the lateral spread are higher in PEM, whereas MCS yields higher values at the mid-section of the lateral spread (See **Figure 7C**).

To recognise patterns between the location (x_L) and the magnitude ($L_{\max}$) of the maximum lateral spread with the input variables, linear regression analysis was conducted. **Table 3** shows that the location is controlled dominantly by the dry-Coulomb friction coefficient with a negative correlation, i.e. higher the friction coefficient earlier the lateral spread starts, and how much the flow spreads in y-axis is mostly controlled by the release volume, even though the friction coefficients affect to a certain extent.

5 Conclusion

Uncertainty quantification is a computationally demanding task for designing and developing a model-based landslide risk assessment. Classical MCS is often computationally infeasible due to the large number of required forward evaluations of the computational model. It has been demonstrated that GP emulation-based MCS can greatly improve the computational efficiency which makes GP-integrated MCS applicable for landslide run-out modelling. One clear advantage of using GP emulation-based MCS is the ability to sample parameter uncertainty in a dense way, as evaluation time of the forward simulation is no longer a computational bottleneck. As a consequence, the output's probability distribution reflecting the propagated uncertainty is captured at high accuracy and provides additional information about skewness and possible multi-modality. In contrast to this PEM provides only limited information on the output's probability distribution. A comparative study between PEM and GP emulation-based MCS has been conducted based on the three moments of the probability distribution, i.e. mean, variance, and skewness. The simpler approach, PEM, yielded a similar expectancy values to GP emulation-based MCS. However, PEM and MCS differed in higher order moments, such as variances and skewness, hence also in the respective spatial distribution of the flow path, and the subsequent hazard map. This finding is of high practical relevance: While a computationally cheap PEM based workflow predicts the mean of a probabilistic landslide risk assessment well, it is in general cases not suitable to assess the reliability of the prediction, for instance in the sense of a probabilistic simulation's standard deviation. The latter requires a MCS approach, which often is computationally infeasible. GP-emulated MCS overcome this limitations by introducing a surrogate model trained based on an empirical error control. It can be suggested that highly uncertain and

high-dimensional input parameter spaces, e.g. complex topographies, advanced material models, models with empirical parameters, inevitably requires an uncertainty quantification workflow that is able to account for non-Gaussian, potentially multi-modal distributions. It should be noted that the gain in compute time by using GP emulation critically depends on the computational effort needed to train the GP emulator. This means that computational resources significantly increase, as the dimension of the input parameter space increases. Alternative techniques will have to be incorporated if the input dimension is too high.

Data availability statement

The datasets generated for this study can be found on Figshare as a collection titled "Uncertainty quantification in landslide runout simulations" (doi: 10.6084/m9.figshare.c.6172702). General workflow can be accessed as a Python package in a compressed format hosted on Figshare (doi: 10.6084/m9.figshare.20730871), also as a Git repository (https://github.com/yildizanil/frontiers_yildizetal).

Author contributions

Contributions are defined according to CRediT author statement. AY: Conceptualisation, Methodology, Software, Formal analysis, Investigation, Writing—Original Draft, Writing—Review and Editing, Visualization. HZ: Methodology, Software, Formal analysis, Investigation, Writing—Original Draft, Writing—Review and Editing. JK: Conceptualisation, Methodology, Writing—Review and Editing, Supervision, Funding acquisition.

Funding

This work was partially funded by Deutsche Forschungsgemeinschaft (DFG) within the framework of the research project *OptiData*: Improving the Predictivity of Simulating Natural Hazards due to Mass Movements – Optimal Design and Model Selection (Project no. 441527981).

Acknowledgments

The authors would like to thank Prof. Florian Amann, whose comments initiated a discussion which led to preparation of this manuscript.

Conflict of interest

The authors declare that the research was conducted in the absence of any commercial or financial relationships that could be construed as a potential conflict of interest.

Publisher's note

References

Aaron, J., McDougall, S., Kowalski, J., Mitchell, A., and Nolde, N. (2022). Probabilistic prediction of rock avalanche runout using a numerical model. *Landslides* 19, 2853–2869. doi:10.1007/s10346-022-01939-y

Aaron, J., McDougall, S., and Nolde, N. (2019). Two methodologies to calibrate landslide runout models. *Landslides* 16, 907–920. doi:10.1007/s10346-018-1116-8

Brezzi, L., Carraro, E., Gabrieli, F., Santa, G. D., Cola, S., and Galgaro, A. (2021). Propagation analysis and risk assessment of an active complex landslide using a Monte Carlo statistical approach. *IOP Conf. Ser. Earth Environ. Sci.* 833, 012130. doi:10.1088/1755-1315/833/1/012130

Cepeda, J., Luna, B. Q., and Nadim, F. (2013). "Assessment of landslide run-out by Monte Carlo simulations," in *Proceedings of the 18th International Conference on Soil Mechanics and Geotechnical Engineering* (Paris, France: Presses des Ponts), 2157.

Christian, J. T., and Baecher, G. B. (1999). Point-estimate method as numerical quadrature. *J. Geotechnical Geoenvironmental Eng.* 125, 779–786. doi:10.1061/(asce)1090-0241(1999)125:9(779)

Christian, J. T., and Baecher, G. B. (2002). The point-estimate method with large numbers of variables. *Int. J. Numer. Anal. Methods Geomechanics* 26, 1515–1529. doi:10.1002/nag.256

Corominas, J., van Westen, C., Frattini, P., Cascini, L., Malet, J.-P., Fotopoulou, S., et al. (2014). Recommendations for the quantitative analysis of landslide risk. *Bull. Eng. Geol. Environ.* 73, 209–263. doi:10.1007/s10064-013-0538-8

Dalbey, K., Patra, A. K., Pitman, E. B., Bursik, M. I., and Sheridan, M. F. (2008). Input uncertainty propagation methods and hazard mapping of geophysical mass flows. *J. Geophys. Res.* 113, B05203. doi:10.1029/2006JB004471

D'Amboise, C. J. L., Neuhauser, M., Teich, M., Huber, A., Kofler, A., Perzl, F., et al. (2022). Flow-py v1.0: A customizable, open-source simulation tool to estimate runout and intensity of gravitational mass flows. *Geosci. Model Dev.* 15, 2423–2439. doi:10.5194/gmd-15-2423-2022

Eidsvig, U., Papathoma-Köhle, M., Du, J., Glade, T., and Vangelsten, B. (2014). Quantification of model uncertainty in debris flow vulnerability assessment. *Eng. Geol.* 181, 15–26. doi:10.1016/j.enggeo.2014.08.006

Fanelli, G., Salciarini, D., and Tamagnini, C. (2018). "A comparison between probabilistic approaches for the evaluation of rainfall-induced landslide susceptibility at regional scale," in *Landslides and engineered slopes. Experience, theory and practice*. Editors S. Aversa, L. Cascini, L. Picarelli, and C. Scavia (CRC Press), 879. doi:10.1201/9781315375007-93

Fenton, G. A., and Griffiths, D. V. (2008). *Risk assessment in geotechnical engineering*. John Wiley & Sons.

Fischer, J.-T., Kofler, A., Fellin, W., Granig, M., and Kleemayr, K. (2015). Multivariate parameter optimization for computational snow avalanche simulation. *J. Glaciol.* 61, 875–888. doi:10.3189/2015JoG14J168

Gu, M. Y., and Berger, J. O. (2016). Parallel partial Gaussian process emulation for computer models with massive output. *Ann. Appl. Statistics* 10, 1317–1347. doi:10.1214/16-AOAS934

Gu, M. Y., Palomo, J., and Berger, J. O. (2019). Robustgasp: Robust Gaussian stochastic process emulation in R. *R J.* 11, 112–136. doi:10.32614/RJ-2019-011

Gu, M. Y., Wang, X. J., and Berger, J. O. (2018). Robust Gaussian stochastic process emulation. *Ann. Statistics* 46, 3038–3066. doi:10.1214/17-AOS1648

Hussin, H. Y., Luna, B. Q., van Westen, C. J., Christen, M., Malet, J.-P., and van Asch, T. W. J. (2012). Parameterization of a numerical 2-d debris flow model with entrainment: A case study of the faucon catchment, southern French alps. *Nat. Hazards Earth Syst. Sci.* 12, 3075–3090. doi:10.5194/nhess-12-3075-2012

Jiang, S.-H., Huang, J., Griffiths, D., and Deng, Z.-P. (2022). Advances in reliability and risk analyses of slopes in spatially variable soils: A state-of-the-art review. *Comput. Geotechnics* 141, 104498. doi:10.1016/j.compgeo.2021.104498

Kaynia, A., Papathoma-Köhle, M., Neuhäuser, B., Ratzinger, K., Wenzel, H., and Medina-Cetina, Z. (2008). Probabilistic assessment of vulnerability to landslide: Application to the village of lichtenstein, baden-württemberg, Germany. *Eng. Geol.* 101, 33–48. doi:10.1016/j.enggeo.2008.03.008

Liu, X., and Guillas, S. (2017). Dimension reduction for Gaussian process emulation: An application to the influence of bathymetry on tsunami heights. *SIAM/ASA J. Uncertain. Quantification* 5, 787–812. doi:10.1137/16M1090648

Liu, X., Wang, Y., and Li, D. Q. (2019). Investigation of slope failure mode evolution during large deformation in spatially variable soils by random limit equilibrium and material point methods. *Comput. Geotechnics* 111, 301–312. doi:10.1016/j.compgeo.2019.03.022

Ma, G. T., Rezania, M., Nezhad, M. M., and Hu, X. W. (2022). Uncertainty quantification of landslide runout motion considering soil interdependent anisotropy and fabric orientation. *Landslides* 19, 1231–1247. doi:10.1007/s10346-021-01795-2

Marin, R. J., and Mattos, Á. J. (2020). Physically-based landslide susceptibility analysis using Monte Carlo simulation in a tropical mountain basin. *Georisk Assess. Manag. Risk Eng. Syst. Geohazards* 14, 192–205. doi:10.1080/17499518.2019.1633582

McDougall, S. (2017). 2014 Canadian geotechnical colloquium: Landslide runout analysis — Current practice and challenges. *Can. Geotechnical J.* 54, 605–620. doi:10.1139/cgj-2016-0104

Mergili, M., Fischer, J.-T., Krenn, J., and Pudasaini, S. P. (2017). r.avaflow v1, an advanced open-source computational framework for the propagation and interaction of two-phase mass flows. *Geosci. Model Dev.* 10, 553–569. doi:10.5194/gmd-10-553-2017

Przewlocki, J., Zabuski, L., and Winkelmann, K. (2019). Reliability analysis of sea cliff slope stability by point estimate method. *IOP Conf. Ser. Mater. Sci. Eng* 471, 042003. doi:10.1088/1757-899X/471/4/042003

Quan Luna, B., Cepeda, J., Stumpf, A., van Westen, C. J., Remaître, A., Malet, J., et al. (2013). Analysis and uncertainty quantification of dynamic run-out model parameters for landslides, in *Landslide science and practice: Volume 3: Spatial analysis and modelling*. Editors C. Margottini, and P. Canuti, doi:10.1007/978-3-642-31310-3_42

Salciarini, D., Fanelli, G., and Tamagnini, C. (2017). A probabilistic model for rainfall—Induced shallow landslide prediction at the regional scale. *Landslides* 14, 1731–1746. doi:10.1007/s10346-017-0812-0

Schraml, K., Thomschitz, B., McArdell, B. W., Graf, C., and Kaitna, R. (2015). Modeling debris-flow runout patterns on two alpine fans with different dynamic simulation models. *Nat. Hazards Earth Syst. Sci* 15, 1483–1492. doi:10.5194/nhess-15-1483-2015

Smith, G., Bell, D., and Davies, T. (2012). The acheron rock avalanche deposit, canterbury, New Zealand: Age and implications for dating landslides. *N. Z. J. Geol. Geophys.* 55, 375–391. doi:10.1080/00288306.2012.733947

Smith, G. M., Davies, T. R., McSaveney, M. J., and Bell, D. H. (2006). The acheron rock avalanche, canterbury, New Zealand—Morphology and dynamics. *Landslides* 3, 62–72. doi:10.1007/s10346-005-0012-1

Snelling, B., Neethling, S., Horsburgh, K., Collins, G., and Piggott, M. (2020). Uncertainty quantification of landslide generated waves using Gaussian process emulation and variance-based sensitivity analysis. *Water* 12, 416. doi:10.3390/w12020416

Strauch, R., Istanbulluoglu, E., Nudurupati, S. S., Bandaragoda, C., Gasparini, N. M., and Tucker, G. E. (2018). A hydroclimatological approach to predicting regional landslide probability using landlab. *Earth Surf. Dyn.* 6, 49–75. doi:10.5194/esurf-6-49-2018

Sun, X. P., Zeng, P., Li, T. B., Wang, S., Jimenez, R., Feng, X. D., et al. (2021b). From probabilistic back analyses to probabilistic run-out predictions of landslides: A case study of heifangtai terrace, gansu province, China. *Eng. Geol.* 280, 105950. doi:10.1016/j.enggeo.2020.105950

Sun, X., Zeng, P., Li, T., Zhang, T., Feng, X., and Jimenez, R. (2021a). Run-out distance exceedance probability evaluation and hazard zoning of an individual landslide. *Landslides* 18, 1295–1308. doi:10.1007/s10346-020-01545-w

Svalova, A., Helm, P., Prangle, D., Rouainia, M., Glendinning, S., and Wilkinson, D. J. (2021). Emulating computer experiments of transport infrastructure slope stability using Gaussian processes and bayesian inference. *Data-Centric Eng.* 2, e12. doi:10.1017/dce.2021.14

Tsai, T.-L., Tsai, P.-Y., and Yang, P.-J. (2015). Probabilistic modeling of rainfall-induced shallow landslide using a point-estimate method. *Environ. Earth Sci.* 73, 4109–4117. doi:10.1007/s12665-014-3696-5

Wilhelm, S., and Manjunath, B. G. (2010). Tmvtnorm: A package for the truncated multivariate normal distribution. *R J.* 2, 25–29. doi:10.32614/RJ-2010-005

Yildiz, A., Zhao, H., and Kowalski, J. (2022a). Uncertainty quantification in landslide run-out simulations. doi:10.6084/m9.figshare.c.6172702

Yildiz, A., Zhao, H., and Kowalski, J. (2022b). Uncertainty quantification workflow in landslide risk. doi:10.6084/m9.figshare.20730871

Zeng, P., Sun, X. P., Xu, Q., Li, T. B., and Zhang, T. L. (2021). 3D probabilistic landslide run-out hazard evaluation for quantitative risk assessment purposes. *Eng. Geol.* 293, 106303. doi:10.1016/j.enggeo.2021.106303

Zhao, H., Amann, F., and Kowalski, J. (2021). Emulator-based global sensitivity analysis for flow-like landslide run-out models. *Landslides* 18, 3299–3314. doi:10.1007/s10346-021-01690-w

Zhao, H., and Kowalski, J. (2022). Bayesian active learning for parameter calibration of landslide run-out models. *Landslides* 19, 2033–2045. doi:10.1007/s10346-022-01857-z

Zhao, H., and Kowalski, J. (2020). Topographic uncertainty quantification for flow-like landslide models via stochastic simulations. *Nat. Hazards Earth Syst. Sci.* 20, 1441–1461. doi:10.5194/nhess-20-1441-2020

Frontiers in Earth Science

Investigates the processes operating within the major spheres of our planet

Advances our understanding across the earth sciences, providing a theoretical background for better use of our planet's resources and equipping us to face major environmental challenges.

Discover the latest Research Topics

See more →

Frontiers

Avenue du Tribunal-Fédéral 34
1005 Lausanne, Switzerland
frontiersin.org

Contact us

+41 (0)21 510 17 00
frontiersin.org/about/contact